Hybrid CFD simulations of two-phase flows in inline flow splitters

Hanane Atmani

THÈSE

En vue de l'obtention du

DOCTORAT DE L'UNIVERSITÉ DE TOULOUSE

Délivré par :

Institut National Polytechnique de Toulouse (Toulouse INP)

Discipline ou spécialité :

Dynamique des fluides

Présentée et soutenue par :

Mme HANANE ATMANI

le mardi 15 février 2022

Titre :

Hybrid CFD simulations of two-phase flows in inline flow splitters

---

Ecole doctorale :

Mécanique, Energétique, Génie civil, Procédés (MEGeP)

Unité de recherche :

Institut de Mécanique des Fluides de Toulouse (IMFT)

Directeur(s) de Thèse :

M. DOMINIQUE LEGENDRE

M. RÉMI ZAMANSKY

Rapporteurs :

M. FRANÇOIS XAVIER DEMOULIN, UNIVERSITE DE ROUEN

M. STEPHANE VINCENT, UNIVERSITE GUSTAVE EIFFEL

Membre(s) du jury :

M. UWE HAMPEL, TECHNISCHE UNIVERSITAT DRESDEN, Président

M. DOMINIQUE LEGENDRE, TOULOUSE INP, Membre

M. ERIC CLIMENT, TOULOUSE INP, Invité(e)

M. ERIC LAMBALLAIS, UNIVERSITE DE POITIERS, Membre

M. LUIS PORTELA, UNIVERSITE DE DELFT, Membre

MME MARIA VITTORIA SALVETTI, UNIVERSITA DI PISA, Membre

M. RÉMI ZAMANSKY, TOULOUSE INP, Membre

Summary

The current PhD work is part of the European project TOMOCON which joins 12 international academic institutions and 15 industry partners who work together in the emerging field of industrial process control using smart tomographic sensors. Four industrial processes are investigated experimentally and numerically, inter alia, inline fluid separation. This recent technology for oil/gas extraction makes use of a static swirl element installed inside the pipeline and which has a bullet form with deflected blades on its surface to transform part of the incoming axial momentum into a tangential one. This flow splitter can generate centrifugal forces up to 100 times the gravitational acceleration and separate the phases leaving the heavy phase next to the wall and the light one in the center to be recovered at the outlet by a pick-up tube.

In the present work, we are interested in developing CFD methods in the IMFT in-house code JADIM to simulate the two-phase flow separation. Since the scales are ranging from meters the length of the device (pipe, swirl element) to a millimeter which is the size of the smallest bubbles and drops, the numerical strategy needs to combine Eulerian and Lagrangian schemes. First, because of the complexity of the separator geometry, we use Immersed Boundary Method (IBM) for solid/fluid interaction to simulate the pipe, the swirl element and the pick-up tube. The flow being highly turbulent that Direct Numerical Simulation (DNS) is not possible, Large Eddy Simulation (LES) is considered and the turbulence is modeled using mixed dynamic Smagorinsky model. Then the Lagrangian solver is used to track the dispersed phase (drops/bubbles). Once the separation is done and the accumulation of the dispersed phase takes place leading to large volume of gas/oil compared to the mesh size, we switch to the Volume of Fluid (VoF) method to simulate the core inside the heavy phase. Finally, the exit control of the light core extraction is done through the flow straightner placed between the pipe and the pick-up tube using Immersed Boundary Method.

To ensure a good interaction/communication between the CFD methods considered here, a coupling of the solvers is needed. Therefore, to be able to use Large Eddy Simulation (LES) on a coarse mesh and avoid the constraint of mesh refinement next to the IB wall, an original stochastic wall model is developed for hybrid LES/IBM and validated through the study of the classical turbulent pipe flow. The Lagrangian Tracking solver is also coupled to Immersed Boundary Method to enable the rebound of the bubbles/drops on the surface of the IB solids via a collision model. The hybrid Lagrangian Tracking/Volume of Fluid consists in moving the bubbles/drops in contact with a VoF cell or those which have migrated to the separator center from the Lagrangian framework to the Eulerian one and updating the phase fraction with their corresponding volume. The method is validated by simulating bubbles accumulation in a rotating flow.

The numerical strategy based on the coupling of these different methods makes possible accurate simulations of the inline separation with limited CPU cost. A full description of single-phase flow in the separator is done, the velocity and pressure profiles are plotted, a swirl number is calculted and its evolution in the streamwise direction is fitted with a previous experimental correlation. Two-phase flow separation is then simulated, the bubble migration is descibed and the gas core is characterized. The effect of the Reynolds number and the condition at the pick-up tube are also studied. The numerical simulations help fixing the physical parameters which influence the separation and control the efficiency and validating models with experimental data from TU Delft, HZDR and TU Lodz.

Keys words: CFD, Inline fluid separation, Swirl, IBM, LES, VoF, Lagrangian Tracking.

Résumé

Ces travaux de thèse s'inscrivent dans le cadre du projet européen TOMOCON qui réunit 12 institutions académiques internationales et 15 partenaires industriels. Ensemble, ils travaillent dans le domaine émergent de l'apport de la tomographie au contrôle des processus industriels. Dans le cadre du projet TOMOCON, quatre processus industriels sont étudiés expérimentalement et numériquement, et cette thèse s'applique à la séparation en ligne des écoulements diphasiques. Cette technologie récemment proposée pour l'extraction du pétrole et du gaz naturel utilise un obstacle muni d'ailettes mettant en rotation l'écoulement conduisant à une force centrifuge jusqu'à 100 fois l'accélération gravitationnelle et permet de séparer deux phases . La phase lourde est poussée vers la paroi du pipeline et la phase légère reste au centre pour être récupérée par la suite à la sortie du séparateur par un tube collecteur. Pour être efficace, ce processus nécessite un contrôle en temps réel de la pression d'aspiration du collecteur basé sur le champ de taux de gaz obtenu par un capteur tomographique de type "wire mesh sensors". La prédiction numérique de l'écoulement dans un tel dispositif est un élément clé pour la mise en place d'une telle boucle de régulation.
Dans le présent travail, nous nous intéressons au développement de méthodes CFD (Computational Fluid Dynamics) dans JADIM, un code de CFD developpé à l'IMFT, pour pouvoir simuler la séparation de l'écoulement diphasique. Cependant, puisque les échelles vont de 1 m la longueur du dispositif de séparation à 10^{-6}m qui est la taille des plus petites bulles ou gouttes, la stratégie numérique doit donc combiner des méthodes eulériennes et lagrangiennes. Tout d'abord, en raison de la complexité de la géométrie du séparateur, nous utilisons la méthode 'Immersed Boundary Method (IBM)' pour l'interaction solide/fluide pour simuler toutes les parties solides du séparateur. De plus, l'écoulement étant fortement turbulent, la Simulation Numérique Directe (DNS) n'est pas envisageable, et la Simulation à Grandes Echelles (LES) est considérée et la turbulence de sous-maille est modélisée à l'aide du modèle dynamique mixte de Smagorinsky. Un solveur lagrangien est utilisé pour suivre la phase dispersée (gouttes/bulles) en résolvant l'équation de trajectoire pour chaque bulles ou gouttes. La migration de la phase dispersée conduisent à former des volumes de gaz/huile grands par rapport à la taille de la maille, que nous simulons grâce à la méthode Volume of Fluid (VoF). Finalement, le contrôle de la condition sur la vanne qui agit sur le tube collecteur pour aspirer le cœur est fait via le redresseur de l'écoulement placé entre le pipeline et le tube collecteur, ce redresseur est modélisé par l'IBM.
Il est donc évident que pour assurer une bonne interaction/communication entre les méthodes CFD considérées ici, un couplage des solveurs est nécessaire. De ce fait, pour pouvoir utiliser la simulation des grandes Echelles (LES) sur un maillage grossier et éviter la contrainte du raffinement de maillage dans la sous-couche

visqueuse à proximité de la paroi, un nouveau modèle de paroi stochastique est développé pour la simulation LES/IBM hybride et validé à travers l'étude d'un écoulement turbulent en tube. Le solveur du suivi lagrangien est également couplé à la méthode IBM pour permettre le rebond des bulles/gouttes sur la surface des solides IB via un modèle de collision. En ce qui concerne la méthode hybride de suivi lagrangien/Volume de Fluide, elle consiste à transformer les bulles/gouttes en contact avec une cellule VoF ou celles ayant migré au centre du séparateur vers le VoF et à mettre à jour la fraction de volume en tenant compte du volume de la phase dispersée transformée au VoF. Cette méthode est validée par la simulation de l'accumulation des bulles dans un écoulement en rotation.
La stratégie numérique hybride basée sur le couplage de ces différentes méthodes permet de réaliser des simulations précises de la séparation en ligne à un coût de CPU raisonnable. En premier, l'écoulement monophasique dans le séparateur est analysé et comparé aux résultats expérimentaux obtenus précédemment. La séparation de l'écoulement diphasique est ensuite simulée, la migration de la phase dispersée est decrite le cœur gazeux est caractérisé. L'effet du nombre de Reynolds et de la condition au niveau du tube collecteur est également étudié. Pour conclure, les simulations numériques permettent de déterminer les paramètres physiques qui influencent la séparation et contrôlent l'efficacité de la séparation et de valider les modèles CFD développés avec des données expérimentales de TU Delft, HZDR et TU Lodz.

Mot clés: CFD, séparation, écoulement diphasique, force centrifuge, IBM, LES, VoF, suivi lagrangien.

Acknowledgements

The work presented in this thesis was carried out with the support and guidance of many people i would like to thank.
Many thanks go to my three supervisors Dominique Legendre, Rémi Zamansky and Eric Climent, first for making me part of such interesting and huge project TOMOCON, for their clear explanations when needed and most importantly, for giving me an exemple of a good researcher. Thank you for being patient, available and supportive during all ups and downs.
I would like to thank Pr. Stéphance Vincent and Pr. François-Xavier Demoulin for accepting to be my thesis referees and for their efforts and time to evaluate this work. I am also grateful to my academic and industrial supervisors: Gregory Lecrivain from HZDR, Peter Veenstra from SHELL and Johanna Bos from Frames who helped and guided me during my secondments and introduced me to industrial research.
From IMFT, i would like to thank the cosinus group in the person of Annaig Pedrono and Pierre Elyakime for their help with JADIM and last but not least thanks to all my friends and collegues who i have met and worked with either in IMFT or within the TOMOCON project.
In the spirit of saving the best for last, it is time to give some heart-felt thanks to my family for all their support.

****

This work is done within the TOMOCON project which has received funding from the European Union's Horizon 2020 research and innovation program under the Marie Sklodowska Curie grant agreement No 764902.
The numerical simulations were performed using high-performance computing resources from CALMIP at the University of Toulouse (under the project P0910) as well as the computing resources from CINES (under the project imf7400).

Contents

List of Figures

List of Tables

Nomenclature

Greek symbols

α_{def}	Deflection angle of the swirl element
α_h	Stochastic wall model parameter
α_{IBM}	Solid volume fraction
Δ	Mesh size $[m]$
Δt	Time step $[s]$
ν^T	Turbulent viscosity $[m^2/s]$
Ω	Vorticity $[s^{-1}]$
ω	The rotation rate $[s^{-1}]$
$\overline{\Delta}$	Filter size $[m]$
Φ	auxiliary potential $[Pa]$
σ	Surface tension $[N/m]$
τ^*	Mean wall shear $[Pa]$
τ^{SGS}	Sub-grid stress tensor $[m/s^2]$
$\widetilde{\Delta}$	Second filter's size $[m]$
μ	Dynamic viscosity $[Pa.s]$
ν	Kinematic viscosity $[m^2/s]$
ρ	Density $[kg/m^3]$

Latin symbols

$< u^* >$	Mean friction velocity $[m/s]$
$\overline{G}$	Filtering operator
$\mathbf{g}$	Gravity $[m/s^2]$
$\mathbf{n}_{IBM}$	Normal vector to IB surface

$\mathbf{v}_d$ Velocity vector of the dispersed phase $[m/s]$

$\widehat{u}$ Intermediate velocity $[m/s]$

A Area $[m^2]$

Bo Bond number

C Volume fraction for VoF

C_D Drag coefficient

C_{ij} Cross-term tensor $[m^2/s^2]$

C_L Lift coefficient

C_M Virtual mass coefficient

C_{sw} Swirl decay coefficient

C_s Dynamic Smagorinsky coefficient

Ca_{max} Capillary number

D Pipe diameter $[m]$

d_d Diameter of the dispersed phase $[m]$

e Restitution coefficient

eff Efficiency of separation

f^{IBM} IBM volumetric force $[m/s^2]$

F_C The bulk velocity $[N]$

f_σ Surface tension force $[N]$

F_B Buoyancy and weight of the dispersed phase $[N]$

F_D Drag force $[N]$

F_H History force $[N]$

F_L Lift force $[N]$

F_{Tchen} Tchen force $[N]$

F_{VM} Virtual mass force $[N]$

FS Flow split

l^* Wall unit $[m]$

l_1 Averaged spurious velocity $[m/s]$

l_∞ Maximum spurious velocity $[m/s]$

$L_{c\theta}$ Turbulent spanwise characteristic length $[m]$

L_{cx} Turbulent streamwise characteristic length $[m]$

L_{ij} Leonard tensor $[m^2/s^2]$

La Laplace number

m Mass $[kg]$

p' Unresolved pressure $[Pa]$

Q_{HPO} Flow rate at the Heavy Phase Outlet (HPO) $[m^3/s]$

Q_{inlet} Inlet flow rate $[m^3/s]$

Q_{LPO} Flow rate at the Light Phase Outlet (LPO) $[m^3/s]$

R Pipe radius $[m]$

r Radial coordinate $[m]$

r^* Bubble radial position $[m]$

r^+ Distance from the wall in wall units

r_d Radius of the dispersed phase $[m]$

R_{ij} Reynolds tensor $[m^2/s^2]$

R_{int} Internal radius of the swirl element $[m]$

R_{pt} Radius of the pick-up tube $[m]$

Re Reynolds number

Re^* Friction Reynolds number

Re_d Reynolds number for the dispersed phase

S Swirl number

S_{ij} Strain rate tensor $[m/s^2]$

t_σ Capillary time scale $[s]$

T_c Correlation time $[s]$

u' Unresolved velocity $[m/s]$

u^* Friction velocity $[m/s]$

U^+ Normalized mean velocity

u_b The bulk velocity $[m/s]$

u_θ^+ Normalized azimuthal rms velocity

u_{adv} Advection velocity $[m/s]$

u_b bulk velocity $[m/s]$

u_r^+ Normalized radial rms velocity

u_x^+ Normalized axial rms velocity

V Volume $[m^3]$

v_s Local velocity of the IB object $[m/s]$

We Weber number

x Coordinate in the x-direction $[m]$

y Coordinate in the x-direction $[m]$

z Coordinate in the z-direction $[m]$

$\overline{p}$ Resolved pressure $[Pa]$

$\overline{u}$ Resolved velocity $[m/s]$

$\mathbf{f}$ Volumetric force $[m/s^2]$

$\mathbf{u}$ Velocity vector $[m/s]$

DNS Direct Numerical Simulation

IBM Immersed Boundary Method

LES Large Eddy Simulation

LT Lagrangian Tracking

p Pressure $[Pa]$

$RANS$ Reynolds Averaged Navier-Stokes

rms Root mean square

T Viscous stress tensor $[Pa]$

VoF Volume of Fluid

Subscripts

c Continuous phase

d Dispersed phase

Chapter 1

Introduction

1.1 TOMOCON Project

The European Training Network "Smart tomographic sensors for advanced industrial process control (TOMOCON)" is an EU research project financially funded by the European Union's Horizon 2020 research and innovation program under the Marie Sklodowska Curie grant agreement 764902. It started in March 2018 (see Fig.1.1) and will end in September 2021.
The project joins 12 international academic institutions and 15 industrial partners who work together in the emerging field of industrial process control using smart tomographic sensors. The network shall set the scientific and technological fundamentals of using imaging sensors for industrial controlled processes and demonstrate its operating feasibility on lab and pilot-scale applications.

Figure 1.1: Kick off meeting in HZDR, Dresden, Germany

Together with their supervisors and industry partners, 15 early stage researchers ESRs (PhD students) are engaged in multi-disciplinary research on various fields: tomographic imaging and sensors, control system theory and design, multi-physics modelling and simulation. The 15 ESRs are working in 4 groups, each group is focusing on an industrial process:
- Inline fluid separation.
- Microwave drying.
- Continuous casting.

- Batch crystallization.

For each of the above processes, CFD models are developed and simulations to understand the flow are done, experiments using tomographs are conducted and finally a controller is built. Thus, interdisciplinary within each group is displayed to prepare for the final demonstration which serves as a proof of concept for the use of process tomography in process control. The current PhD work is part of the inline fluid separation study and more specifically the CFD development and simulation of this process.

In addition, the project does also ensure a good public communication of the results through publications, participation to conferences and the organization of workshops and summer schools (see Fig.1.2) on both the technical topics of control theory, tomographs and sensors, multiphase flow modelling as well as the soft skills (problem-oriented thinking, career development, patents, entrepreneurship, marketing, project management, team building, dissemination and open science ...)

(a) Virtual workshop organized by UEF, Kuopio, Finland

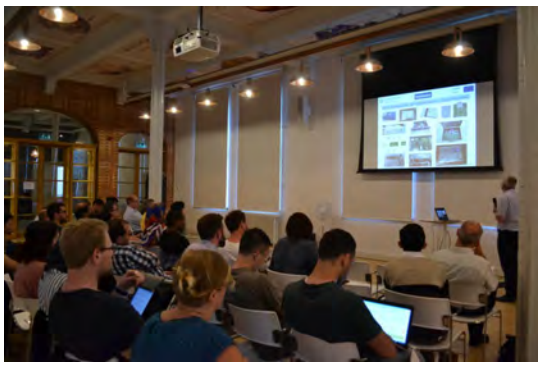

(b) Summer school in TUD, Delft, Netherlands

(c) Workshop in TUL, Lodz, Poland

Figure 1.2: TOMOCON's workshops and summer schools

Moreover, the project provides scientific and industrial trainings for the ESRs during short visits and stays (secondments) to academic and industry partners over a total period up to 8 months. The objective is to help the ESRs to develop the specific skills of research and innovation both in academia and industry. For instance, i spent 2 months in HZDR learning about and taking part in the two-phase flow separation experiments [8], 2 months in Shell Technology Centre Amsterdam (STCA) doing numerical simulations of single-phase flow in the separator using the open source

CFD code Openfoam and 1 month in Frames simulating a two-phase flow pretreater (results are confidential) using the commercial CFD code Star CCM+ (see Fig.1.3). The secondments in both companies were also opportunities to discover the research work in an industrial environment in the sector of petroleum and energy production and to broaden my experience and knowledge in that domain.

(a) Secondment at HZDR

(b) Secondment at Frames

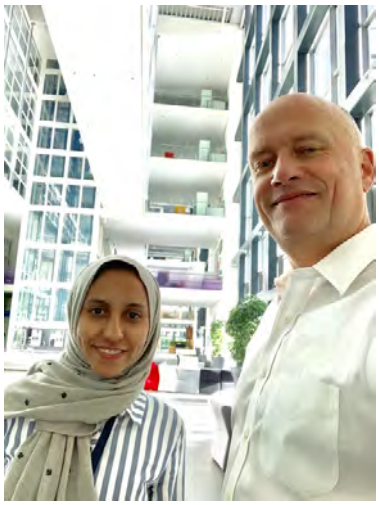

(c) Secondment at Shell (STCA)

Figure 1.3: TOMOCON Secondments

1.2 Two-phase flow separation

1.2.1 Petroleum engineering

When the living organisms die and as the time goes by, they are buried in the ground by more and more layers of sediment pushing them further from the earth's crust by a few meters to a few hundred meters every million years or so. During this process, temperature and pressure increase, the nitrogen, sulfur and phosphorus atoms are gradually converted into kerogen. At a depth of about 2 km, when the temperature is around 100C, kerogen releases hydrocarbons. Wether it will be oil or natural gas, it all depends on the temperature and the organic debris. For instance more heat produces natural gas and animal source rock gives more oil than gas. With an estimated average sedimentation of 50 meters every million years, it takes 60 million

years for dead animals to become liquid hydrocarbons.
Oil and gas have mostly been recovered by drilling. The latter is carried out after studies of structural geology, sedimentary basin analysis, and reservoir characterisation. The whole procedure is thus time and money demanding, that is why the concerned industries are constantly working on new technologies to recover the maximum amount of gas/oil and extend the economic lifespan of the wells both on offshore and onshore fields. One can find various separation techniques which are used and still under development to insure a good quality, a big quantity and minimum production fees.

1.2.2 Gravity separator

It is the common type of separators. The concept of gravity separators is based on exploiting the density difference between two fluids, as they are naturally separated by buoyancy. The separators could either be vertical or horizontal. A vertical separator could be used to save space on a topside facility, and is mostly used to separate gas/liquid. The horizontal gravity separator is the most common separator for liquid/liquid emulsion. This kind of separators needs time and large vessels to increase the efficiency. Other components are usually added (coalescing packs, weir reduction ...) to prevent certain operating problems during the process.

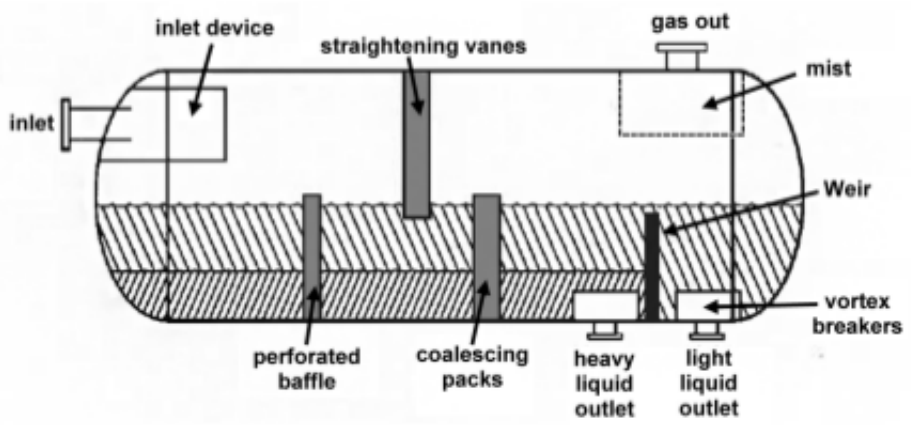

Figure 1.4: Sketch of three-phase flow gravity separator [1]

1.2.3 Cyclones

It is a vertical pipe with a tangential/horizontal inlet and two outlets: one at the top and the other at the bottom, which uses the centrifugal separation technology. The mixture of two fluids flows through the inlet into the cyclone separator. A strong swirling flow field is formed causing the light phase to migrate to the center line and the heavy phase towards the wall. Different cyclones were subjects to many studies [9], [10], [11].

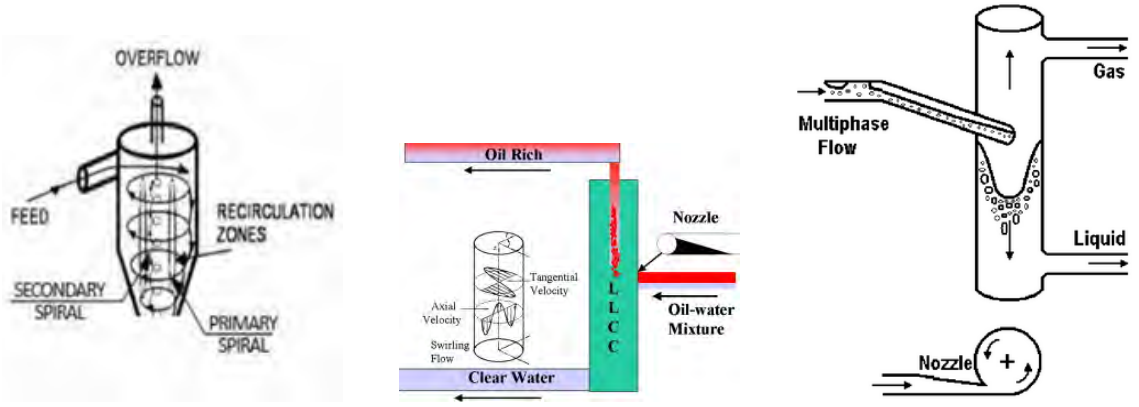

(a) Conical Liquid Hydrocyclone [9]

(b) Liquid Liquid Cylindrical Cyclone [10]

(c) Gas Liquid Cylindrical Cyclones [11]

Figure 1.5: Sketch of three types of cyclones

1.2.4 Inline fluid separator: swirl element

Based on similar principles. The swirl element is a device used to separate a dispersed phase from a continuous phase based on a centrifugal force. It has a bullet shape with deflected blades on its surface (see Fig.1.6) and remains static inside the pipe. When the axial flow injected at the inlet of the pipe goes through the non moving swirl blades, part of the axial momentum is transformed into an azimuthal momentum, which is the origin of the centrifugal force. Following this swirling motion, the two phases are separated, the heavy phase is pushed towards the wall and the light one to the center of the pipe to be recoverd afterwards by a pick-up tube placed at the outlet of the pipe.

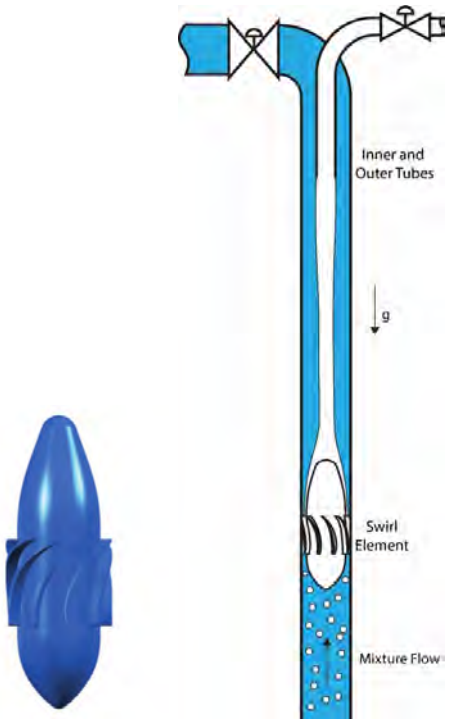

Figure 1.6: Sketch of the inline separator

This represents a new technology developed to reduce the residence time, the investment cost and the installation weight.
A few studies were conducted on this geometry. Dirkzwager [12] designed an inline swirl element different from the traditional cyclone to reduce the turbulence production and pressure drop. Based on experiments, a swirl number was introduced. However, his research was limited to single-phase flow only and was more focusing on the design itself. Then, the inline separator was further developed and investigated numerically by Delfos [13]. Later, Campen [5] measured the axial and azimuthal velocities using LDA for single-phase flow, pressure drop and the swirl number. He also made some experiments for oil/water separation to determine the physical parameters which control the efficiency of separation. Simultaneously, Slot [1] reshaped the swirl element, three geometries were defined: weak, large and strong swirl elements, RANS simulations were done for the strong element using Ansys CFX and oil/water separation was simulated using the Euler-Euler model. His numerical results were compared to the measurements of Campen [5]. The present work is based on one of the geometries previously designed by Slot [1] and focuses on developing advanced CFD models for the simulations and the investigation of gas/water separation.

1.3 Present work

1.3.1 Project objectives

As mentionned before, being part of the inline fluid separation team, our aim is to develop exclusively the concept of tomography controlled inline gas/water separator [14]. The latter is investigated experimentally in the large-scale Delft Inline Separator Facility (DISE) in TU Delft and is equiped with high-speed cameras, pressure transducers. A wire mesh sensor (WMS) developed in HZDR is placed upstream to measure the phase fraction and an electrical resistance tomography sensor (ERT) developed in TU Lodz is placed downstream after the swirl element to measure the gas core diameter (see Fig.1.7). Getting real time data from both sensors, the controller acts on the valve pressure at the pick-up tube to insure a high separation efficiency. The feedback loop for the controller is built based on the flow physics from both experiments and CFD simulations [15].

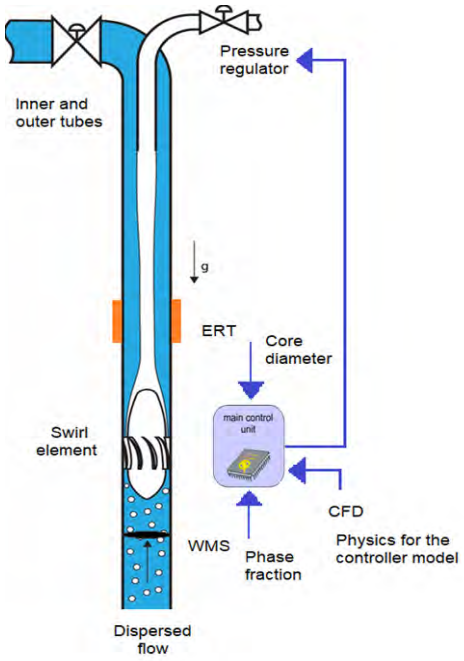

Figure 1.7: Tomography controlled inline separator

1.3.2 Why using CFD for inline fluid separation

Computational Fluid Dynamics (CFD), in general, have a great ability to describe flows in a detailed manner. Any flow parameter can be calculated at each position and time. Information that experiments are lacking since the measurements are limited to the available experimental tools and their space-time resolution. Additionaly, even in terms of cost, CFD are in most cases cheaper than building rigs and conducting experiments, this is why, campanies are becoming more and more interested in first investigating the flow of industrial processes using CFD before moving to the prodution stage.
For the inline fluid separation, the interest of using CFD comes from the complexity of the flow and if we want to control the process of the separation, we need as much information as possible about the bubble dynamics and the core stability to various conditions on the valve at the pick-up tube. The question now is how to choose the adequat approach to simulate the process since CFD proposes an arsenal of methods to model the flow features. In the next subsection 1.3.3, we introduce the flow characteristics in the inline fluid separator and the brought CFD challenges.

1.3.3 Problem description

The CFD work, which is the subject of this thesis, is highly challenging because of the flow features present in the separator. In fact, the flow is highly turbulent, the geometry of the swirl element is complex and the scales are ranging from meters, the length of the device down to the smallest bubble or drop at millimeters.
Since we need a precise description of the flow to evaluate correctly the separation efficiency, we will have to carefully build the CFD approach in a way to get all the details of fluid dynamics with an affordable computation cost. For instance, avoiding complicated and irregular meshing for the complex geometry of the swirl element,

going for turbulence modelling instead of Direct Numerical Simulations which is impossible considering the high Reynolds numbers. Finally for the two-phase flow modelling, choosing an approach which can capture the bubble/droplet migration as well as the behaviour of the core interface. In the next subsection 1.3.4, we present the existing CFD methods commonly used in two-phase flow separation simulations.

1.3.4 CFD state of art

Two-phase flow separation can be easily found in diverse industrial processes such as atomization, cyclones, cavitation ... They all represent similar challenges because of the encountered interface length scales. Two approaches exist to describe those scales:
- Euler methods in which each fluid properties are written as a function of time and space. Within this Eulerian framework, one can distinguish between 'one fluid model' in which only one Navier-Stokes equation and one continuity equation are solved such as Volume of Fluid (VoF), and 'two-fluid model' which consists in solving a Navier-Stokes and a continuity equations for each phase and incorporate the interaction between them through a momentum exchange term. The advantge of this model is its simplicity in implementation but the drawback is that it does not adequately solve the details of interactions dispersed phase/dispersed phase and dispersed phase/continuous phase.
-Lagrange methods in which one phase properties are determined by tracking the movement of its fluid particles in time. This model consists in defining a continuous phase solved using an Eulerian description and tracking the dispersed phase during time through the force balance. Thus, the interaction between the two phases is well resolved but the simulation is computationally expensive.
In the current study, we are interested in the dynamics of the dispersed phase during the migration and by the core stability after the separation. Therefore, we will implement a hybrid approach detailed in subsection 1.3.5.

1.3.5 Proposed numerical approach

We propose a hybrid approach based on a Navier-Stokes solver that makes possible accurate simulations with coarse spatial resolution.
First, Immersed Boundary Method (IBM) is used to simulate both the pipe, the pick-up tube and the complex geometry of the swirl element on a simple regular Cartesian mesh. Turbulence is modelled with the mixed dynamic Smagorinsky subgrid model in Large Eddy Simulation (LES) with an original stochastic wall law coupled to the IBM allowing to avoid the need for mesh refinement close to the wall. A Lagrangian Tracking (LT) method is used to solve the dispersed flow, it is coupled to Immersed Boundary Method via a collision model to ensure the rebound of the dispersed phase in contact with the IB walls and is also coupled to a Volume of Fluid (VoF) to switch from the Lagrangian framework to the Eulerian one once the accumulation of the dispersed phase takes place and the light core is formed. Finally, the control of the core extraction is achieved by imposing the valve condition at the pick-up tube through a flow straightner placed between the pipe and the pick-up tube using Immersed Boundary Method.
This hybrid approach [16] allows a pertinent description of this swirling flow es-

pecially that the experiments are constrained to time and cost and helps with the needed physics for the controller.
We should note that the coupling between LES and VoF is not within the scope of this thesis, but remains an interesting subject in modelling the turbulence in two phase-flows [17] and represents one of the perspectives for this PhD work.

1.4 Thesis outline

In chapter 2, the CFD methods are presented in details. The IMFT in-house code JADIM used for the simulations is introduced. We provide a full description of the discretization and the resolution of Navier-Stokes equations, the IBM solver, the LES solver, the Lagrangian Tracking and the VoF solver as they have been already developed and validated in JADIM. The new CFD developments and their validations are also presented to wit: the use of IBM for CAD complex geometries, the coupling of IBM/LT and LT/VoF. The coupling of LES/IBM and the development and validation of the stochastic wall model is detailled in chapter 3.
Chapter 4 presents the results of the numerical simulations of single-phase flow including a description of swirling flow in the separator, a study of the effect of the Reynolds number and the effect the pick-up tube outlet condition. In chapter 5, two-phase flow in the separator is studied, the migration of a bubble in the separator is described using Lagrangian Tracking and simulations for the core formation are presented. Finally, conclusions are made and perspectives for further research are given in chapter 6.

Chapter 2

CFD developments and validations

2.1 Introduction

As previously described in 1.3.3 and 1.3.5, the inline fluid separation is a complex process to simulate since many flow features are present. The hybrid approach proposed here involves Large Eddy Simulation (LES) because the flow is highly turbulent, Immersed Boundary Method (IBM) because the geometry is complex, Lagrangian Tracking (LT) to efficiently follow the trajetory of the dispersed phase, Volume of Fluid (VoF) to simulate the evolution of the light phase core and the coupling between them.
In this chapter, the IMFT in-house CFD code JADIM used for the simulations is introduced, the four existing solvers in JADIM for LES, IBM, Lagrangian Tracking and VoF are detailed and the new CFD developements done within the framework of this PhD work are presented and validated namely the use of IBM for complex geometries, the collision model for LT/IBM and the hybrid LT/VoF as for the wall model for hybrid LES/IBM, a whole chapter 3 is dedicated to model description and validation.

2.2 CFD code: JADIM

JADIM is a CFD code developed at IMFT since 1991 through the work of many researchers and PhD students. Beside a main part for the resolution of Navier-Stokes equations of incompressible, unsteady, Newtonian and three dimensional flows in curvilinear orthogonal coordinates [18, 19]. The code has many solvers: Large Eddy Simulation (LES), Immersed Boundary Method (IBM), Lagrangian Tracking (LT), thermal model, Volume of Fluid (VoF), Level Set (LS) and was validated in various previous studies [18, 19, 20, 21, 22, 23, 24, 25].

2.2.1 The Navier-Stokes system of equations

The mass and momentum conservation equations in a differential form are expressed as:

$$\nabla.\mathbf{u} = 0 \tag{2.1}$$

$$\frac{\partial \mathbf{u}}{\partial t} + \mathbf{u}.\nabla \mathbf{u} = -\frac{1}{\rho}\nabla p + \frac{1}{\rho}\nabla \cdot \mathbf{T} + \mathbf{f} \tag{2.2}$$

with $\mathbf{u}$ is the velocity field, p is the pressure, ρ is the density , $\mathbf{T} = \mu(\nabla \mathbf{u} +^t \nabla \mathbf{u})$ is the viscous stress tensor , $\mathbf{f}$ is the sum of any external volumetric force applied to the fluid.
In the following, a focus is made on the solver considered during this PhD work. First the Navier-Stokes solver is presented.

2.2.2 Spatial and temporal discretization

The equations 2.1 and 2.2 are solved using a finite volume method on an offset mesh. The pressure p and the volume fraction C for VoF are calculated in the center of each cell while the components of the velocity $\mathbf{u}$ are defined on the facets of the cell. Figure 2.1 shows the positioning of the variables on a 3D cell.

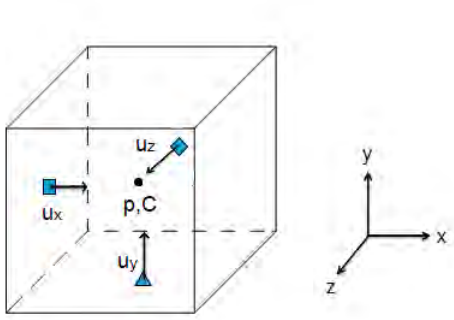

Figure 2.1: Representation of the variables on a 3D cell: the pressure p, the volume fraction C and the velocities u_x, u_y and u_z in the x, y and z directions respectively

In a Cartesian formulation and using Einstein notation, equations 2.1 and 2.2 are expressed as:

$$\frac{\partial u_i}{\partial x_i} = 0 \tag{2.3}$$

$$\frac{\partial u_i}{\partial t} + \frac{\partial u_i u_j}{\partial x_i} = -\frac{1}{\rho}\frac{\partial p}{\partial x_i} + \nu \frac{\partial^2 u_i}{\partial x_i \partial x_j} + f_i \tag{2.4}$$

with u_i $(i = x, y, z)$ and p the velocity and pressure fields, respectively. f_i is the sum of any imposed volumetric force applied to the fluid in the direction i.
The integration of each unknown variable is done on a corresponding volume. The spatial derivatives are calculated using a second order centered schemes $O(\Delta^2)$ with Δ is the mesh size. The diffusive term is solved using a semi implicit Crank Nicolson (CN) scheme, when the other terms are treated explicitly by a Runge-Kutta 3 (RK3) procedure.

$$\frac{\widehat{u}_i^k - \widehat{u}_i^{k-1}}{\Delta t} = SM_i^k \tag{2.5}$$

with

$$SM_i^k = \gamma_k N(\widehat{u}_i^{k-1}) + \xi_k N(\widehat{u}_i^{k-2}) + \alpha_k L(\widehat{u}_i^{k-1}) \\ +\beta_k L(\widehat{u}_i^k) + (\alpha_k + \beta_k)[f_i - \frac{1}{\rho^{n+1/2}} \nabla p^{n-1/2}] \tag{2.6}$$

where γ_k, α_k, ξ_k, β_k are the Runge-Kutta coefficients summerized in table 2.1. N (resp. L) is a non-linear (resp. linear) operator containing the advective and viscous terms:

$$N(u_i) = \nu \frac{\partial^2 u_j}{\partial x_j \partial x_i} - \frac{\partial}{\partial x_j}(u_i u_j) \tag{2.7}$$

$$L(u_i) = \nu \frac{\partial^2 u_i}{\partial x_j \partial x_i} \tag{2.8}$$

k	α_k	β_k	γ_k	ξ_k
1	4/15	4/15	8/15	0
2	1/15	1/15	5/12	-17/60
3	1/6	1/6	3/4	-5/12

Table 2.1: Values of the Runge-Kutta 3 coefficients

In terms of the stability of the integration algorithm, the hybrid RK/CN have advantages from both numerical schemes. In fact, RK3 applied to a pure advection equation, when the spatial derivatives are calculated using a second order centered schemes $O(\Delta^2)$, is stable for CFL number under $\sqrt{3}$ and precise to the third order $O(\Delta t^3)$. CN, being semi-implicit, is unconditionally stable and is second order accurate $O(\Delta t^2)$. Therefore, the over-all algorithm is second order precise and the only stability condition on the time step is the following:

$$\Delta t \leq \sqrt{3} min \left(\frac{\Delta_x \Delta_y \Delta_z}{u_{xmax} \Delta_y \Delta_z + u_{ymax} \Delta_x \Delta_z + u_{zmax} \Delta_x \Delta_y} \right) \tag{2.9}$$

where Δ_i with $i = x, y, z$ is the cell size and u_{imax} is the maximum velocity in the i direction.

2.2.3 Projection method

At the end of the RK3 loop, the velocity $\widehat{u}_i^{n+1} = \widehat{u}_i^3$ resulting from the previous integration is not divergence free, to satisfy the incompressibility condition, the projection method [26, 27] is applied.
The auxiliary potential Φ^{n+1} is introduced as:

$$\frac{\partial \Phi^{n+1}}{\partial x_i} = \frac{\rho}{\Delta t}(u_i^{n+1} - \widehat{u}_i^{n+1}) \tag{2.10}$$

By taking the divergence of this equation and knowing that $\partial u_i^{n+1} / \partial x_i = 0$ we end up with a Poisson equation:

$$\frac{\partial^2 \Phi^{n+1}}{\partial x_i \partial x_i} = \frac{\rho}{\Delta t} \frac{\partial \widehat{u}_i^{n+1}}{\partial x_i} \tag{2.11}$$

To get Φ^{n+1}, the linear system of the Poisson equation is solved by a Jacobi preconditioned conjugate gradient technique (PETSc Library) for three-dimensional cases while a multifrontal direct method (MUMPS Library) is used in two-dimensional situations. The final divergence-free velocity and pressure are finally obtained:

$$u_i^{n+1} = \tilde{u}_i^{n+1} - \frac{\Delta t}{\rho}\frac{\partial \Phi^{n+1}}{\partial x_i} \tag{2.12}$$

$$p^{n+1/2} = p^{n-1/2} + \Phi^{n+1} \tag{2.13}$$

2.3 Large Eddy Simulation (LES)

2.3.1 Introduction

Like most of flows present both in nature and in industrial applications, the swirling flow in the inline separator is characterized by a high Reynolds number resulting in a turbulent regime. A precise description both in time and space of such flows requires Direct Numerical Simulation (DNS) which consists in solving all temporal and spatial scales. To do so on a three dimentional realistic configuration, one can estimate the number of cells needed for that to $O(Re^{9/4})$ for a homogeneous isotropic turbulence and even more cells for confined flows to resolve the boundary layer. In short, DNS is highly demanding in terms of computational resources that are in most of the cases beyond the actual capacity of even the most powerful supercomputers. To overcome this limitation, two common methods are used: Reynolds Averaged Navier-Stokes (RANS) equations and Large Eddy Simulation (LES). While the former is based on an ensemble averaging which gives only the mean velocity. LES, on the other hand, resolves the large scales thanks to an appropriate modelling of small scale (unresolved) dynamics and is able to provide both the mean and the fluctuations of the velocity close to the DNS results [28].
When the local Reynolds number is high, one expect the small scale to be universal because of the local homogeneity assumptio. However, in the case of significant shear, typically close to a wall, the modelling of the sub-grid scale needs to be adapted. And within Large Eddy Similation, different methods have been proposed [29] such as constant Smagorinsky model, dynamic Smagorinsky model, Bardina model, Chollet-Lesieur model, WALE ...
The choice of the adequate method depends mainly on the flow conditions. And since we are dealing with confined flows, we have chosen the mixed dynamic Smagorinsky model [18] described in the following subsection 2.3.2. It is also worth mentionning that using this method still requires a mesh refinement close to the wall to capture the viscous-sublayer by putting four to five cells in there. This condition can become constraining for highly turbulent flows and one solution to avoid it is the implementation of a wall model. In the current PhD work, an original wall model for LES on IB walls is proposed and validated in chapter 3.

2.3.2 Mixed dynamic Smagorinsky model

Mass and momentum equations result from a spatial filtering of the equations 2.3 and 2.3. We use a uniform grid spacing Δ yielding the filter length to be $\overline{\Delta} = \Delta$, the filtering operator is then noted $\overline{G}$. The advantage of using a regular mesh is to be

able to commute the filtering and the differentiation operation because otherwise, commutation errors rise [29].
Now by applying $\overline{G}$, the velocity and pressure fields are decomposed as $u_i = \overline{u}_i + u'_i$ and $p = \overline{p} + p'$ where $\overline{u}_i$ (resp. u'_i) and $\overline{p}$ (resp. p') are the resolved (resp. unresolved) contributions. The governing equations in the LES approach are then:

$$\frac{\partial \overline{u}_i}{\partial x_i} = 0 \tag{2.14}$$

$$\frac{\partial \overline{u}_i}{\partial t} + \frac{\partial \overline{u}_i \overline{u}_j}{\partial x_i} = -\frac{1}{\rho}\frac{\partial \overline{p}_i}{\partial x_i} + \nu \frac{\partial^2 \overline{u}_i}{\partial x_i \partial x_j} - \frac{\partial \tau_{ij}^{SGS}}{\partial x_j} + \overline{f}_i \tag{2.15}$$

where ν is the kinematic viscosity of the fluid, $\overline{f}_i$ is the sum of the filtered volumetric force and $\tau_{ij}^{SGS} = \overline{u_i u_j} - \overline{u}_i \overline{u}_j$ is the sub-grid stress tensor (SGS) expressed as the sum of these three terms: L_{ij}, C_{ij} and R_{ij} such as:

$$L_{ij} = \overline{\overline{u}_i \overline{u}_j} - \overline{\overline{u}}_i \overline{\overline{u}}_j \tag{2.16}$$

$$C_{ij} = \overline{\overline{u}_i u'_j} + \overline{\overline{u}_j u'_i} - \overline{\overline{u}}_i \overline{u'}_j - \overline{\overline{u}}_j \overline{u'}_i \tag{2.17}$$

$$R_{ij} = \overline{u'_i u'_j} - \overline{u'}_i \overline{u'}_j \tag{2.18}$$

The Leonard term L_{ij} is calculted explicitly.

$$\tau_{ij}^{SGS} - \frac{1}{3}\tau_{kk}^{SGS}\delta_{ij} = -2\nu_T \overline{S}_{ij} + L_{ij} - \frac{1}{3}L_{kk}\delta_{ij} \tag{2.19}$$

where $\overline{S}_{ij}$ is the strain rate tensor calculated from the resolved velocity field and the turbulent viscosity ν_T is given by:

$$\nu_T = C_s \overline{\Delta}^2 (2\overline{S}_{ij}\overline{S}_{ij})^{\frac{1}{2}} \tag{2.20}$$

with $\overline{\Delta}$ is the filter length. C_s is a local parameter calculated at each time step.
Assuming scale similarity of τ_{ij}^{SGS} and by the same old dynamic procedure [30], (2.15) is refiltered with a larger filter $\widetilde{\Delta} = 2\overline{\Delta}$, we define: $T_{ij} = \widetilde{\overline{u_i u_j}} - \widetilde{\overline{u}}_i \widetilde{\overline{u}}_j$. Similary as τ_{ij}^{SGS}, T_{ij} is also expressed in function of C_s as:

$$T_{ij} - \frac{1}{3}T_{kk}\delta_{ij} = -2C_s \widetilde{\overline{\Delta}}^2 |\widetilde{\overline{S}}| \widetilde{\overline{S}}_{ij} + L_{ij}^T - \frac{1}{3}L_{kk}^T \delta_{ij} \tag{2.21}$$

with $L_{ij}^T = \widetilde{\overline{\overline{u}_i \overline{u}_j}} - \widetilde{\overline{\overline{u}}}_i \widetilde{\overline{\overline{u}}}_j$. Both T_{ij} and $\widetilde{\tau^{SGS}}_{ij}$ cannot be calculated explicitly however the difference $l_{ij} = T_{ij} - \widetilde{\tau^{SGS}}_{ij} = \widetilde{\overline{u}_i \overline{u}_j} - \widetilde{\overline{u}}_i \widetilde{\overline{u}}_j$ can be and allows to find the local coefficient C_s:

$$l_{ij} - \frac{1}{3}l_{kk}\delta_{ij} = -2C_s(\widetilde{\overline{\Delta}}^2 |\widetilde{\overline{S}}| \widetilde{\overline{S}}_{ij} - \widetilde{\overline{\Delta}}^2 \widetilde{|\overline{S}|\overline{S}_{ij}}) - \widetilde{\overline{u}}_i \widetilde{\overline{u}}_j + \widetilde{\overline{u}_i \overline{u}_j} + \frac{1}{3}(\widetilde{\overline{u}}_k \widetilde{\overline{u}}_k - \widetilde{\overline{u}_k \overline{u}_k})\delta_{ij} \tag{2.22}$$

C_s is then:

$$C_s = -\frac{(l_{ij} - h_{ij})M_{ij}}{2M_{ij}M_{ij}} \tag{2.23}$$

with $M_{ij} = \widetilde{\overline{\Delta}}^2 |\widetilde{\overline{S}}| \widetilde{\overline{S}}_{ij} - \widetilde{\overline{\Delta}}^2 \widetilde{|\overline{S}|\overline{S}_{ij}}$ and $h_{ij} = \widetilde{\overline{u}_i \overline{u}_j} - \widetilde{\overline{u}}_i \widetilde{\overline{u}}_j$
Unlike the classical Smagorinsky model, in which C_s is an empirical constant in all

the domain, the dynamic model by Germano [30] allows a local calculation of C_s to take into account the local turbulence in the flow. However, it is subject to numerical instabilities due to possible negative values of C_s resulting in negative total viscosity $\nu+\nu_t$. The mixed dynamic Smagorinsky model, considered in the current study[18], reduces the number of cells with a negative C_s in comparison with the dynamic Smagorinsky model [30] to less than 1% through its way of decomposing the sub-grid scale tensor and explicitly calculating the Leonard term as well as locally filtering C_s on the test-volume surrounding each cell. The very rare remaining negative values of the total viscosity are eliminated by locally clipping $\nu + \nu_t$ to 0.

2.4 CFD for fluid solid interaction

2.4.1 Introduction

Turbulent flows in applications often occur in complex geometries. For instance, in inline fluid separation, the swirl element has a complex geometry and is placed inside the flow which makes it in continuous interaction with the fluid. Therefore, the best way to avoid the use of complicated and demanding mesh is to model the fluid-structure interaction. Various methods can be found in the literature such as:
• Distributed lagrange multiplier [31, 32]: the fow inside, and on, each solid boundary is constrained to be a rigid-body motion using a distributed Lagrange multiplier. This multiplier represents the additional body force per unit volume needed to maintain the rigid-body motion inside the solid boundary, and is analogous to the pressure in incompressible fluid fow, whose gradient is the force required to maintain the constraint of incompressibility. In other terms, The rigidity constraint produces a stress field inside the solid that is a function of a scalar Lagrange multiplier.
• Penalty method [33]: a penalty term is added to the conservation equation, its expression depends on the approach that is used since there are various penalty methods: Volumic penalty method, Sub mesh penalty method...
• Lattice Boltzmann method [34]: the fluid phase is treated as a group of imaginary fluid particles which are allowed to move to the adjacent lattice nodes or stay at rest. The solid is also represented using lattice nodes. The surface of the solid is located in the boundary nodes where the bounce-back rule is applied so that the incoming fluid components from fluid nodes are reflected back.
• Ghost fluid method [35]: it creates a ghost artificial cells which implicitly induces the proper conditions at the interface solid/fluid through the interpolation of the parameters in those nodes.
• Immersed boundary method [36, 37]: it was first introduced by Peskin to study flow patterns around heart valves and has evolved into a generally useful method for problems of fluid/structure interaction. Peskin used Eulerian variables defined on a fixed cartesian mesh, and Lagrangian variables defined on a curvilinear mesh that moves freely through the fixed cartesian mesh without being constrained to adapt to it in any way at all.
In the current study, an Immersed Boundary Method developed by Bigot [23] is used, the equations are detailed in the following subsection.

2.4.2 Immersed Boundary Method (IBM)

As mentioned before, IBM was first introduced by Peskin[36], then developed for other applications. It consists in adding the force applied by the solid on the fluid to the Navier-Stokes equations at the interface fluid/solid. Two types of IBM are generally distinguished: sharp IBM, in which the solid boundary is located within one cell but then is experiencing possible spatial and temporal discontinuities while diffusive IBM overcomes this problem by providing a smooth transition between the fluid and the solid across three to four cells.
A different diffusive approach was developed [23] in JADIM which does not need the Lagrangian marking on the solid. A solid volume fraction α_{IBM} is defined equals 1 in the solid cell,0 in the fluid cell and between 0 and 1 in the transition region between the solid and the fluid. The solid-fluid interaction is then presented by a forcing term added to Navier-Stokes equations as a contribution in the volumetric force $\mathbf{f}$:

$$f^k_{IBM,i} = \alpha_{IBM} \frac{v^{k-1}_{s,i} - \widehat{u}^k_i}{\Delta t} \tag{2.24}$$

where Δt is the time step used for time advancement, $v_{s,i}$ is the local velocity imposed to the immersed solid object and $\widehat{u}_i$ is a predictor velocity without considering the immersed object.
For a static IB solid, the velocity $v_{s,i}$ is set to 0 and the IB force is then reduced to:

$$f^k_{IBM,i} = -\alpha_{IBM} \frac{\widehat{u}^k_i}{\Delta t} \tag{2.25}$$

Now, when it comes to α_{IBM}, the solid indicator, it is defined using a mathematical formula by Yuki [38] which decribes the form of the solid geometry. For instance, when the object is a spherical of center $\mathbf{x}_p$ and radius R, α_{IBM} is expressed as:

$$\alpha_{IBM}(\mathbf{x}) = \frac{1}{2}\left[1 - \tanh\left(\frac{\|\mathbf{x} - \mathbf{x}_p\| - R}{\lambda \eta \Delta_c}\right)\right] \tag{2.26}$$

with Δ_c is a characteristic grid size equals $\sqrt{2}\Delta$ for a regular mesh.
$\lambda = \mid n_x \mid + \mid n_y \mid + \mid n_z \mid$ calculated using the coordinates of $\mathbf{n}$ the normal outward unit vector at the surface.
$\eta = 0.065(1 - \lambda^2) + 0.39$ is a parameter controlling the thickness of the transition region $0 < \alpha_{IBM} < 1$. This relation for λ suppresses parasitic fluctuations of the forces applied to the object when the latter crosses a numerical cell [23].

2.4.3 Immersed Boundary Method for CAD complex geometries

The IBM as developed by Bigot [23] and implemented in JADIM requires an explicit expression of α_{IBM} such as equation 2.26. This is only working for simple geometries such as: cylinders, squares, spheres ... but when it comes to complex solids, like the swirl element created by a CAD softtware, there is no mathematical equation to describe it and thus the direct calculation of α_{IBM} is not possible. A new method is proposed to define $\alpha_{IBM}(\mathbf{x})$ which consists first to have the CAD file under the STL format, then import it to the program 'distance' of the the Open source CFD code BASILISK, this function 'distance' serves to build a distance field

representation of a 3D CAD file and all it needs as inputs from our side is the STL file and the number of grids we want which should be a power of 2. Now practically when 'distance' is runned, it starts by reading the STL file, computes the bounding box of the geometry, calculates the domain center and size, initializes the distance field on the mesh grids, constructs a vertex field interpolated from the centered field and then calls the appropriate VOF functions which computes the volume fraction (which is the solid fraction α_{IBM}) from the distance field. The output from 'distance' is saved in a file 'Alpha ibm.dat' containing the position (x, y, z) of each cell and the corresponding α_{IBM}. Finally the file 'Alpha ibm.dat' is sorted by ascending x, y and z using MATLAB and imported by JADIM to attribute the variable α_{IBM} for the swirl element. The procedure to calculate α_{IBM} for the IBM solver from a CAD geometry is briefly summerized in Fig. 2.2 showing the inputs and outputs at each step.

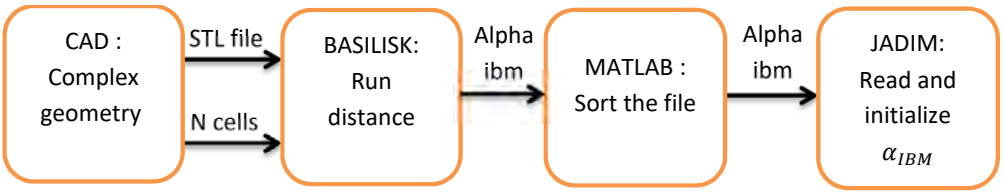

Figure 2.2: Steps to generate α_{IBM} from a CAD file

We should note that this procedure is applied only once to define α_{IBM} for the swirl element then the IBM forcing of Navier-Stokes equations is kept the same as done in equation 2.24.

2.4.4 Validation of IBM for complex geometries: inline fluid separator

To test the solver for a complex geometry and the proposed method to generate α_{IBM} from a CAD file, we simulate the inline separator using IBM, in which α_{IBM} of both the pipe and the pick up tube is defined by equation 2.26 and is calculated using the above procedure for the swirl element. The numerical domain is a box of size $L_x \times L_y \times L_z = 0.92m \times 0.1m \times 0.1m$ made of $N_x \times N_y \times N_z = 800 \times 92 \times 92$ cells along the e_x, e_y and e_z directions. The mesh is then regular Cartesian and the pipe diameter equals $D = 0.092m$. Figure 2.3 shows the contour $\alpha_{IBM} = 0.5$ of the separator. The latter is well described and the swirl element is successfully simulated.

Figure 2.3: 3D visualization of the separator using IBM: contour $\alpha_{IBM} = 0.5$

A DNS of single-phase flow in the separator is performed for $Re = Du_b/\nu = 4,600$, the flow is generated by a uniform velocity u_b at the inlet and a condition on the pressure at the outlet. Figure 2.4 shows the streamlines of the flow which

follow perfectly the shape of the swirl element. Moreover, the velocity reaches its maximum at the position of the blades. Chapter 4 is dedicated to the investigation of swirling single-phase flow in the separator where further results are presented.

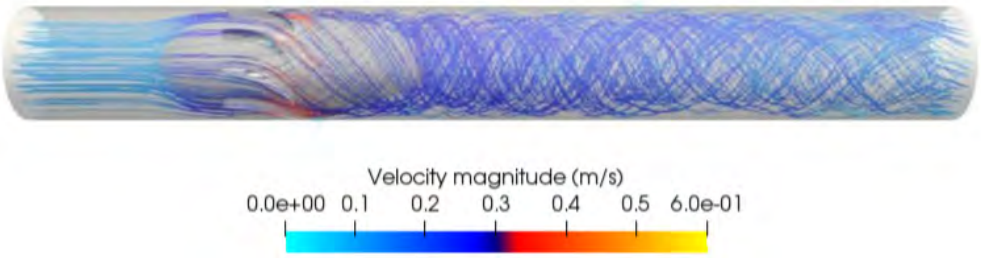

Figure 2.4: Streamlines of single-phase flow in the separator of Reynolds number $Re = 4,600$

It remains to mention that the separator is meant to operate on highly turbulent flows for which the Reynolds number can reach $Re = 200,000$ which justifies the need to use LES and consequently to develop a wall model for hybrid LES/IBM approach (see chapter 3).

2.5 Lagrangian Tracking (LT)

Lagrangian Tracking (LT) is an efficient CFD method in the current study to simulate the dispersed phase at the inlet especially that we have two different length scales, one of the dispersed phase (bubble or droplet) diameter which is in the order of millimeters and the other one in the order of meters for the separator. Having a diameter smaller than the mesh size, the bubbles/droplets are geometrically considered as points. The Lagrangian Tracking solver in JADIM [24] calculates the trajectory of each bubble/droplet based on the forces applied on it.
Let's consider now a spherical non deformable bubble/droplet (dispersed phase) of diameter d_d, volume V_d, velocity $\mathbf{v}_d$ inside a flow that has a velocity $\mathbf{u}$ and a kinematic viscosity ν_c. The Reynolds number is defined as:

$$Re_d = \frac{d_d \|\mathbf{u} - \mathbf{v}_d\|}{\nu_c} \tag{2.27}$$

2.5.1 Buoyancy

It is an upward force exerted by the continuous phase to oppose the weight of the immerged dispersed phase, it is the result of the gravity effect and the densities difference. The sum of buoyancy and weight of the dispersed phase is written as:

$$F_B = (m_d - m_c)\mathbf{g} \tag{2.28}$$

with m_d and m_c are respectively the dispersed phase and continuous phase masses.

2.5.2 Drag force

It is a force acting in the opposite direction to the relative motion between the dispersed phase and the continuous phase, it is calculated as:

$$F_D = C_D \rho_c \frac{\pi r_d^2}{2} \|\mathbf{u} - \mathbf{v}_d\| (\mathbf{u} - \mathbf{v}_d) \tag{2.29}$$

with C_D is a dimensionless drag coefficient which depends on the Reynolds number, the ratio of densities $\rho^* = \rho_d/\rho_c$ and the ratio of viscosities $\mu^* = \mu_d/\mu_c$.
For clean bubbles with free slip at the interface, Mei [39] found a correlation for C_D that is a function only of Reynolds number regardless of the latter's range variation.

$$C_D^{bubble} = \frac{16}{Re_d} \left[1 + \left(\frac{8}{Re_d} + \frac{1}{2} \left(1 + \frac{3.315}{Re_d^{1/2}} \right) \right)^{-1} \right] \tag{2.30}$$

For a droplet, Rachih et al. [25] have recently proposed a correlation for C_D which depends only on the viscosity ratio and is available for Reynolds numbers up to 200:

$$C_D^{droplet} = \frac{C_D^{bubble} + \mu^* C_D^{solid}}{1 + \mu^*} \tag{2.31}$$

with C_D^{solid} is the drag coefficient for a solid particle calculated from the work of Schiller and Naumann [40] as:

$$C_D^{solid} = \begin{cases} 24(1 + 0.15 Re_d^{0.687}) & \text{if } Re_d \leq 1000 \\ 0.44 & \text{if } Re_d > 1000 \end{cases} \tag{2.32}$$

2.5.3 Lift force

It is the result of the circulation of the continuous phase around the dispersed one. Its general expression is:

$$F_L = C_L \rho_c V_d (\mathbf{u} - \mathbf{v}_d) \wedge \Omega \tag{2.33}$$

with $\Omega = \nabla \times \mathbf{u}$ is the vorticity and C_L is the lift coefficient calculated for a bubble based on the work of Legendre and Magnaudet [19]:

$$C_L = \left[\left(\frac{13.53}{\pi^2 \sqrt{Sr Re_d} (1 + 0.2 Re_d/Sr)^{3/2}} \right)^2 + \left(\frac{1}{2} \frac{1 + 16/Re_d}{1 + 29/Re_d} \right)^2 \right]^{1/2} \tag{2.34}$$

where Sr is the shear rate.

2.5.4 Added (or virtual) mass and Tchen forces

Due to the acceleration of the dispersed phase, some of the continuous phase volume surrounding it is accelerated as well yielding to this force:

$$F_{VM} = C_M \rho_c V_d \left(\frac{D\mathbf{u}}{Dt} - \frac{d\mathbf{v}_d}{dt} \right) \tag{2.35}$$

with C_M is the virtual mass coefficient which equals 0.5 for a sphere [41].
Related to the virtual mass force, Tchen force is added to represent the inertia of the fluid in the absence of the bubble/droplet.

$$F_{Tchen} = \rho_c V_d \frac{D\mathbf{u}}{Dt} \tag{2.36}$$

2.5.5 Basset (or history) force

When the continuous phase accelerates, the inertial forces do not allow the viscous forces to establish instanteneously, so to take into account this effect, Basset force is introduced as a correction of the steady drag force. It is the history of successive time delays between the application of instantaneous viscous forces and those of a quasi-static pseudo movement and expressed as:

$$F_H = 6\pi\mu_c r_d \int_0^t K\frac{\tau}{t_{nu}}\left(\frac{d\mathbf{u}}{d\tau} - \frac{d\mathbf{v}_d}{d\tau}\right)d\tau \tag{2.37}$$

where K is the kernel of the history force depends on the type of the dispersed phase and $t_\nu = r_d^2/\nu$ is a characteristic time of the history effect controlled by the viscous diffusion.
In the case of bubbles, for high Reynolds numbers Re_d, this force is negligible compared to the drag force [42].

2.5.6 Force balance

With no history force, the force balance is expressed as:

$$\begin{aligned}(\rho_d + C_M\rho_c)V_d\frac{d\mathbf{v}_d}{dt} = (\rho_d - \rho_c)V_d\mathbf{g} + \\ C_D\rho_c\frac{\pi r_d^2}{2}\|\mathbf{u}_{x_d} - \mathbf{v}_d\|(\mathbf{u}_{x_d} - \mathbf{v}_d) + C_L\rho_c V_d(\mathbf{u}_{x_d} - \mathbf{v}_d)\wedge\Omega + \\ \rho_c V_d(1 + C_M)\frac{D\mathbf{u}}{Dt}|_{x_d}\end{aligned} \tag{2.38}$$

Each bubble/droplet trajectory is obtained by solving:

$$\frac{d\mathbf{x}_d}{dt} = \mathbf{v}_{x_d} \tag{2.39}$$

When considering the LES approach, the fluid velocity $\mathbf{u}_{x_d}$ and acceleration $D\mathbf{u}/Dt|_{x_d}$ at the bubble/droplet location $\mathbf{x} = \mathbf{x}_d$ are obtained by a second order interpolation of the filtered velocity $\overline{\mathbf{u}}$ with neglecting the SGS fluctuations [43].
The time integration of the trajectory of each bubble/droplet is done through a Runge Kutta 2. To satisfy the stability condition on the time step for the Lagrangian solver, the Lagrangian time dt_{traj} is set to the minimum of three characteristic times: the continuous phase time step Δt used for the integration of Navier-Stokes equations, the relaxation time of the bubble/droplet $\frac{r_d^2 C_D}{6\nu_c}$ and the Lagrangian time $\frac{\Delta}{max(v_d)}$ to ensure that the influence of the continuous phase dynamics on the bubbles/droplets is taken into account in the force balance.

$$dt_{traj} = min(\Delta t, \frac{r_d^2 C_D}{6\nu_c}, \frac{\Delta}{max(\mathbf{v}_d)}) \tag{2.40}$$

For large number or large size of bubbles/droplets, it is possible to consider the effect of the dispered phase on the continuous phase through a two-way coupling approach, a force F_{lag} is added to Navier-Stokes equations. When the concentration of the dispersed phase is high that the bubbles/droplets interact with each others,

one can incoporate a four-way coupling by including a collision/coalescence models in the Lagrangian Tracking solver. It is clear that both the complexity of the physics and the computational time increase as we move from one-way to four-way coupling at the expense of accuracy. The choice of the adequat approach depends on the studied two-phase flow. In our case, since the fraction of the dispersed phase is not high (less than 10%) and not kept in the Lagrangian framework during the whole simulation, one-way coupling is chosen.

2.5.7 Validation: bubble in a solid body rotation using LT

To check the Lagrangian Tracking solver in a situation close to the configuration considered in this work, 2D simulation of a bubble of radius r_b in a solid body rotation are conducted. The objective of this simple test case is to verify the calculation of the different forces and in particular those responsible of the bubble migration towards the pipe center, because they are of great importance for the process studied in this work.
The flow is generated by the rotation of a cylinder simulated using Immersed Boundary Method (IBM) of a radius $R = 0.046m$ with (OZ) as a rotation axis and ω is the constant angular velocity as shown in Fig. 2.5. The dimentionless number characterizing the system is $Re_\omega = \frac{(2r_b)^2\omega}{\nu}$ equals 10 in this case. The numerical domain is a box of size $L_x \times L_y = 0.14m \times 0.14m$ made of $N_x \times N_y = 44 \times 44$ cells along the e_x and e_y directions. Once the flow is developed inside the cylinder, a bubble is injected at the center (0,0) with the fluid velocity and its trajectory is calculated using the Lagrangian Tracking solver. Figure 2.5 represents the force balance (buoyancy, drag, lift, virtual mass and Tchen) of a bubble and its radial and tangential position in the cylinder.

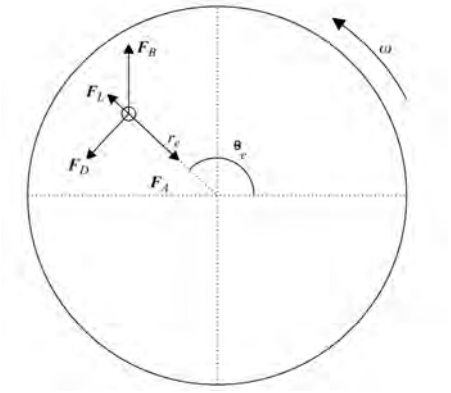

Figure 2.5: Geometry definition and sketch of the forces applied on the bubble

The bubble reaches the equilibrium position (r_e, θ_e) when the sum of the forces applied on it is 0. Figure 2.6 shows the trajectory of the bubble, the latter has a spiral form similar to the one reported by Nierop et al. [44] for the same considered Re_ω. From the simulations, the Reynolds number at equilibrium $Re_e = 2r_b r_e \omega/\nu$ equals 150, slightly different from the experimental results $Re_e^{exp} = 108$ measured by Nierop et al. [44] since in the numerical simulations, correlations for the drag and lift coefficients are fixed and are not exactly the same as the ones obtained from the experimental measurements.

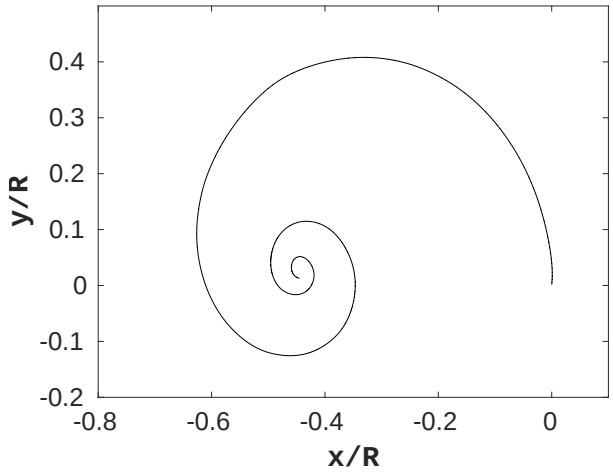

Figure 2.6: Trajectory of a bubble in a rotating flow

2.5.8 Lagrangian Tracking/ Immersed Boundary Method: collision model

Inside the separator, the dispersed phase is not only transported by the continuous phase but can also be in interaction with the solid part of the device namely the pipe, the swirl element or eventually the pick-up tube. This is why a coupling between IBM and Lagrangian Tracking is needed to make sure that the bubbles/droplets are not going to be trapped in a cell with $\alpha_{IBM} > 0$.
Inspired by the rebound of a particle on a solid surface, a collision model is then introduced to consider the rebound on the IB wall according to the normal $\mathbf{n}_{IBM}$ with a restitution coefficient e set to 1 for full restitution of the kinetic energy. The new bubble/droplet velocity in contact with the IB wall is therefore calculated as:

$$\mathbf{v}_d^{new} = \mathbf{v}_d - (1+e)(\mathbf{n}_{IBM}.\mathbf{v}_d)\mathbf{n}_{IBM} \tag{2.41}$$

where $\mathbf{n}_{IBM}$ is the solid surface normal oriented to the fluid calculated as:

$$\mathbf{n}_{IBM} = \frac{\nabla\alpha_{IBM}}{\|\nabla\alpha_{IBM}\|} \tag{2.42}$$

The activation of the collision model goes through three steps. Figure 2.7 illustrates them as the following: first we check if a bubble/droplet is located in a cell where $\alpha_{IBM} > 0$ after each trajectory integration (see Fig. 2.7a and 2.7b), if it is the case, the new velocity is calculated as 2.41. Finally, as the bubble/droplet was not supposed to be in an IB cell in the first place, its current position is set to its previous position just before the trajectory integration $\mathbf{x}_d = \mathbf{x}_d^{old}$ as shown in Fig. 2.7c. This also allows to make sure that the bubble/droplet is not again trapped in another IB cell after the collision model but located in a fluid cell.

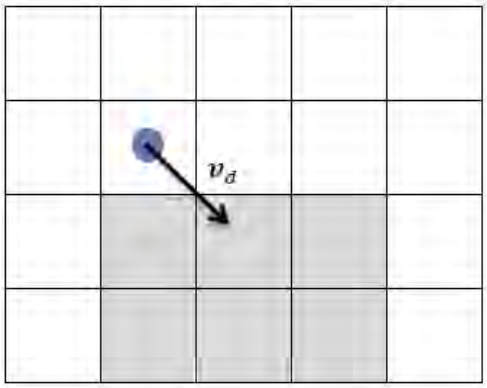

(a) Bubble/droplet heading towards an IB cell (in grey)

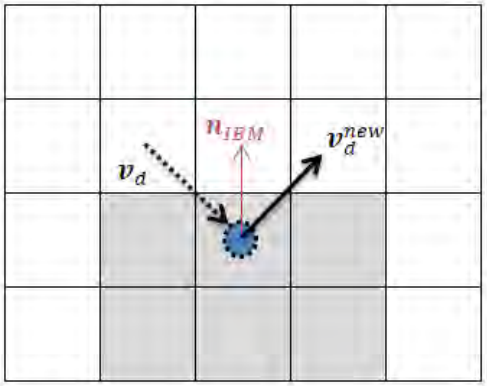

(b) Calculation of the new velocity according to 2.41

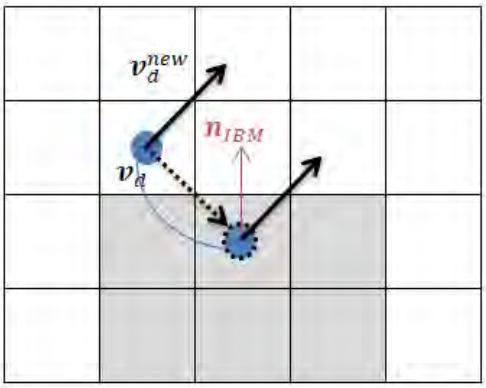

(c) Returning the bubble/droplet to its previous position with the new rebound velocity

Figure 2.7: Sketch of the steps for the activation of the collision model for hybrid IBM/LT

2.5.9 Validation of the collision model for hybrid IBM/LT: inline fluid separator

To see the interaction between the Lagrangian Tracking and the IBM solver, we consider 3D simulation of two-phase flow for $Re = 4,600$ in the separator. The numerical domain is a box of size $L_x \times L_y \times L_z = 0.92m \times 0.1m \times 0.1m$ made of $N_x \times N_y \times N_z = 400 \times 46 \times 46$ cells along the e_x, e_y and e_z directions. The gravity is $\mathbf{g} = -9.81\mathbf{e}_x$ and the flow is along the pipe axis generated by a uniform velocity at the inlet and a condition on the pressure at the outlet. When the swirling flow is developed, a set of 1000 bubbles of radius $r_b = 1mm$ are injected randomly upstream the swirl element with the fluid velocity. Figure 2.8 shows the initialisation of the bubbles in the separator, no contact with IB cells is yet taking place. Two configurations are tested: without the collision model and with the collision model.

Figure 2.8: Injection of a set of 1000 bubbles in the separator

First, we run the simulation without introducing the collision method. Figure 2.9 shows that the bubbles, when arriving at the IB cells, are moving inside the swirl element where $\alpha_{IBM} > 0$ and this justify the need to model the interaction between IBM and Lagrangian Tracking.

Figure 2.9: Two-phase flow simulation using LT and IBM without the collision model

Now, we run the same simulation, but this time with the proposed collision model activated. Figure 2.10 shows that the bubbles do not go inside the IB cells inside the swirl element but rebound on the latter's surface and the same happens to the bubbles in contact with the pipe wall at the blades. The magnitude of their velocity is of course conserved since the restitution coefficient e is set to 1. All the bubbles remain inside the fluid domain in particular when they are located in the small gap between the swirl element and the pipe wall.

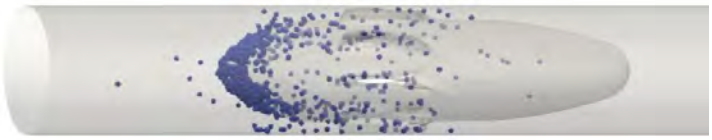

Figure 2.10: Two-phase flow simulation using hybrid LT/IBM: with the collision model

2.6 Volume of Fluid (VoF)

To simulate the interface in two-phase flows, one can either track the interface or capture it. The interface tracking method localises sharply the interface using for instance a front tracking method with fictive markers to define a moving embedded mesh [45] or a volume tracking with interface reconstruction [46]. In interface capturing approach, the interface is diffused over a number of cells and is defined using a distance function as in Level Set (LS) method or a volume fraction indicator as in Volume of Fluid (VoF). In the current work, since Lagrangian bubbles/droplets are switching their volume into the Eulerian framework which can directly be interpreted as a volume fraction indicator for VoF then the latter is chosen for the resolution of the light core which forms around the pipe center.

2.6.1 Transport equation

Volume of fluid was first introduced by Hirt and Nichols [47] to replace the Lagrangian markers used in interface tracking. A scalar C (volume fraction) is defined which equals to 1 in one phase, 0 in the other phase and varies between 0 and 1 at the interface. C is governed by the following transport equation:

$$\frac{\partial C}{\partial t} + u_i \frac{\partial C}{\partial x_i} = 0 \tag{2.43}$$

The two fluids are assumed to be Newtonian and incompressible with no phase change. The surface tension σ is constant and uniform at the interface between the two fluids. In such conditions, the velocity field u and the pressure p satisfy the classical one-fluid formulation of Navier-Stokes equations. The local density and dynamic viscosity are deduced from the value of C by a linear interpolation:

$$\rho = C\rho_1 + (1 - C)\rho_2 \tag{2.44}$$

$$\mu = C\mu_1 + (1 - C)\mu_2 \tag{2.45}$$

The transport equation 2.43 for C is solved using the Flux Corrected Transport (FCT) algorithm proposed by Benkenida [20]. It is based on a direction split approach when three intermediate equations 2.46,2.47,2.48 corresponding to the three directions are solved successively taking as initial condition the solution of previous equation. The order of the resolution of the equations changes at each time step so not to privilege a direction over another.

$$\frac{\partial C}{\partial t} + \frac{\partial C u_1}{\partial x_1} = C\frac{\partial u_1}{\partial x_1} \tag{2.46}$$

$$\frac{\partial C}{\partial t} + \frac{\partial C u_2}{\partial x_2} = C\frac{\partial u_2}{\partial x_2} \tag{2.47}$$

$$\frac{\partial C}{\partial t} + \frac{\partial C u_3}{\partial x_3} = C\frac{\partial u_3}{\partial x_3} \tag{2.48}$$

No interface reconstruction or redistance techniques are introduced. The problem of the numerical diffusion of the interface which leads to its thickness of about 2 to 3 grid cells is controled through the work of Bonometti[21, 48]. It briefly consists in making the velocity, used to transport the interface and defined locally over 2 to 3 cells, constant. A new velocity $\underline{\mathbf{u}}(\mathbf{x})$ is then used in solving the transport equation in the i direction, defined for cells with the coordinate $\mathbf{x}$ located in the interface and equals $\mathbf{u}(\mathbf{x}_0)$. The point $\mathbf{x}_0$ should satisfy two conditions:
- $C(\mathbf{x}_0) = 0.5$
- $\mathbf{x}_0$ is on the same streamline as $\mathbf{x}$ if the angle $\beta_1 = \widehat{(\mathbf{n}_C, \mathbf{u})}$ is higher than the angle $\beta_2 = \widehat{(\mathbf{e}_i, \mathbf{n}_C)}$, otherwise, $\mathbf{x}_0$ is on the same direction as the mesh line i that goes through $\mathbf{x}$ (see Fig. 2.11)

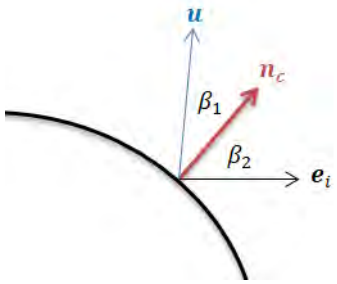

Figure 2.11: Sketch of the angles β_1 and β_2

This method was validated in the work of Bonometti [21] through diverse flow configurations.

2.6.2 Surface tension force

Surface tension force occurs at the interface between two different fluids. In fact, molecules of the same fluid are attracted to each other by an attractive force which is higher than the one that attract the molecules at the interface to those of the other fluid. Surface tension force is then produced at the interface minimising the interface area. When using an interface capturing method, VoF for instance, the interface is not located within one cell but spread over 2 to 3 control volumes. To handle this constraint, Brackbill [49] developed the Continuum Surface Force (CSF) model to express this force as a function of the volume fraction gradient:

$$f_\sigma = \sigma k_{cur} \nabla C = -\sigma \nabla . \left(\frac{\nabla C}{\|\nabla C\|} \right) \nabla C \tag{2.49}$$

with σ is the surface tension and $k_{cur} = -\nabla . \left(\frac{\nabla C}{\|\nabla C\|} \right)$ is the curvature of the interface. Since this force is added to Navier-Stokes equations to take into account the capillary effects, another condition on the time step Δt has to be respected:

$$\Delta t \leq \sqrt{\frac{(\rho_1 + \rho_2)\Delta^3}{8\sigma}} \tag{2.50}$$

2.6.3 Spurious currents

Despite the use of central difference scheme in the calculation of the surface tension force, it has been observed that the CSF suffers from the generation of non-physical spurious currents due to errors in the discretization of the interface curvature, those errors are advected and are possibly amplified along with the interface leading to incorrect velocity, pressure pics at the interface and an additional source term in the vorticity production. This numerical problem can be tackled to some extent by introducing a successive smoothing procedure using a weighted volume fraction average $\widehat{C}$ instead of C in the calculation of the interface curvature. For instance, it is expressed in 2D as:

$$\widehat{C}^{nf}_{i,j} = \frac{3}{4}\widehat{C}^{nf-1}_{i,j} + \frac{1}{16}(\widehat{C}^{nf-1}_{i+1,j} + \widehat{C}^{nf-1}_{i-1,j} + \widehat{C}^{nf-1}_{i,j+1} + \widehat{C}^{nf-1}_{i,j-1}) \tag{2.51}$$

with $\widehat{C}^{0}_{i,j} = C_{i,j}$ and $n_f = 1, ..., N$ N being the number of iterations. Dupont and Legendre [50] have shown that it is better to use a higher number of iterations for

the calculation of the interface curvature set to 12 since the aim is to reduce the variations in the curvature and a lower number of iterations set to 8 for the volume fraction gradient which define the force localization so to keep a sharp capillary force.
Now when it comes to the characterization of the intensity of the spurious currents. Francois et al. [51] introduces the norm l_1 corresponding to the averaged spurious velocity in the domain and Renardy et al. [52] defines the norm l_∞ as the maximum spurious velocity:

$$l_1 = \frac{1}{N_1 N_2 N_3} \sum_{i,j,k} \|\mathbf{u}_{i,j,k} - \mathbf{u}^{th}_{i,j,k}\| \tag{2.52}$$

$$l_\infty = max(\|\mathbf{u}_{i,j,k} - \mathbf{u}^{th}_{i,j,k}\|) \tag{2.53}$$

with $\mathbf{u}_{i,j,k}$ and $\mathbf{u}^{th}_{i,j,k}$ are respectively the velocity from the simulation and the one from the theoretical solution. The norm l_∞ can be normalized to build the dimensionless capillary number defined as:

$$Ca_{max} = \frac{\mu l_\infty}{\sigma} \tag{2.54}$$

This number is relevant when the viscous effects are dominant and the spurious currents resulting from the vorticity source term are balanced by the viscous term. However, when inertia is the dominating effect, the velocity used to characterize the spurious currents is defined as:

$$u_{inertia} = \sqrt{\frac{\sigma}{\rho D}} \tag{2.55}$$

with D is a length scale.
By normalizing the above velocity, the Laplace number is introduced as:

$$La = \frac{\rho D \sigma}{\mu^2} \tag{2.56}$$

One can eventually link the spurious velocity based on the viscous term to the one based on the inertia term as:

$$l_\infty = u_{inertia} \sqrt{La} \tag{2.57}$$

Dupont el al. [50] performed 2D numerical simulation of a circular drop at equilibrium for water/air system, zero velocity was imposed on the boundries of the numerical domain, the results have shown a deformation of the drop and a motion due to the spurious velocities. The evaluation of the spurious currents magnitude has given that $Ca_{max} \approx 0.004$. A comparable value was later found by Abadie et al. [53] through numerical simulations of a 2D Taylor bubble. Furthermore, both Dupont et al. [50] and Abadie et al. [53] did a mesh sensitivity of l_∞ and have shown that the intensity of spurious currents is slightly decreased by the mesh refinement.

2.6.4 Validation: gas core in a solid body rotation using VoF

To investigate the ability of the CSF to handle spurious currents in a situation close to the one we have in the inline separator, we simulate a gas core inside a solid body rotation, we consider a two-phase flow of water/air with the following physical properties:
water ($\rho_w = 1000kg/m^3, \mu_w = 0.0001Pa.s$), air ($\rho_g = 1kg/m^3, \mu_g = 2.10^{-5}Pa.s$), surface tension $\sigma = 0.072N/m$.
We perform 3D simulation of a VoF gas cylindrical core in a rotating IB pipe with (OX) as a rotation axis and ω is the constant angular velocity. The numerical domain is a box of size $L_x \times L_y \times L_z = 0.45m \times 0.1m \times 0.1m$ made of $N_x \times N_y \times N_z = 200 \times 46 \times 46$ cells along the e_x, e_y and e_z directions. Periodic conditions are imposed at the inlet and outlet of the pipe.
The diameter of the pipe is set to $R = 23\Delta$ and the initial gas core radius to $R_{core} = 13\Delta$ with Δ is the mesh size. The Reynolds number is defined as $Re = R^2\omega/\nu_w$ and is fixed to $4,600$. Laplace number equals $La = 18.10^5$, l_∞ is then used to characterize the spurious currents.
Figure 2.12 illustrates the gas core behaviour from the initialization of the gas core to the generation of spurious currents and finally the breakage of the core. The interface in blue corresponds to $C = 0.5$ and the velocity is presented by red arrows. We can see that at the beginning, the magnitude of the velocity varies with the radial position r as ωr, then high velocities are generated at the interface which is a direct indicator of spurious currents.

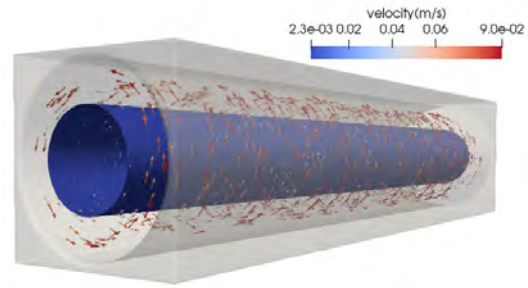

(a) Initialisation of the gas core at $t^* = 0$

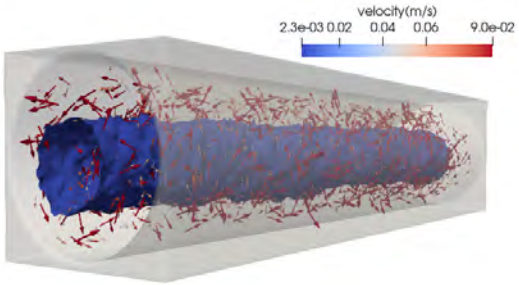

(b) Appearance of spurious currents at $t^* = 0.3$

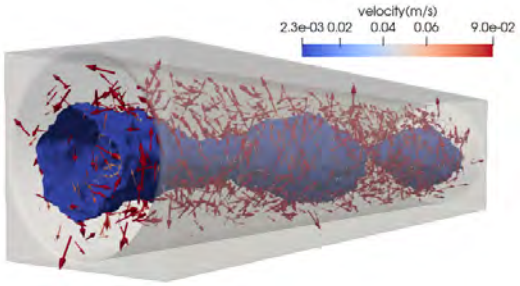

(c) Instability of the gas core at $t^* = 0.6$

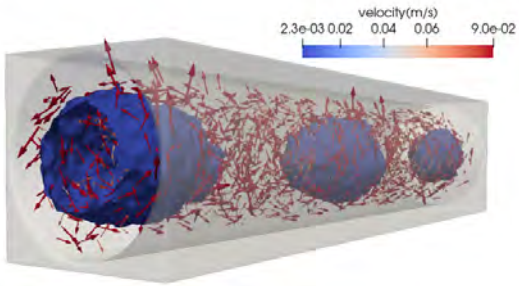

(d) breakage of the gas core at $t^* = 0.9$

Figure 2.12: Simulation of air core in a rotating water flow

To characterize the intensity of the spurious currents observed above, we calculate the capillary number defined as:

$$Ca_{max} = \mu_w l_\infty / \sigma \tag{2.58}$$

Figure 2.13 represents the variation of the capillary number as a function of the dimentionless time $t^* = t/t_\sigma$ such as $t_\sigma = \sqrt{(2R)^3\rho_w/\sigma}$ is the capillary time scale. Ca_{max} is almost zero at the initialization of the gas core when the spurious currents are not yet generated then Ca_{max} increases as spurious currents appear to reach a steady state when $Ca_{max} \approx 0.004$, the same order of magnitude is reported in [50, 53].

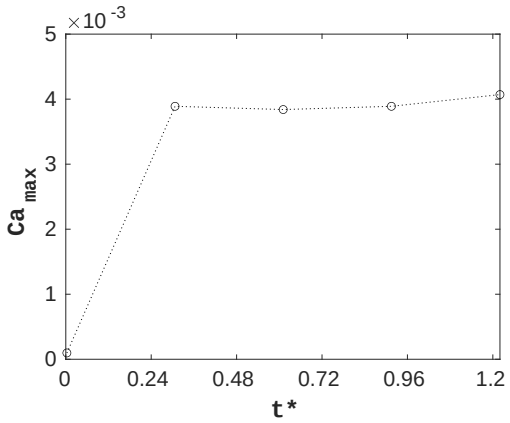

Figure 2.13: Evolution of the spurious currents intensity over time

Therefore, to avoid this unphysical velocities, we have to reduce the ratio σ/μ_w while keeping the same dimensionless numbers which characterize the system.
The Buckingham Π theorem is applied to find non-dimensional groups of parameters to describe the flow. The system has 8 physical parameters $(R, R_{core}, \omega, \sigma, \rho_w, \mu_w, \rho_g, \mu_g)$ and 3 independent dimensions (mass, length, time). 5 dimensionless numbers are then constructed:

$$R^* = R_{core}/R \tag{2.59}$$

$$\rho^* = \rho_w/\rho_g \tag{2.60}$$

$$\mu^* = \mu_w/\mu_g \tag{2.61}$$

$$Re = R^2\omega/\nu_w \tag{2.62}$$

$$We = \rho_w\omega^2R^3/\sigma \tag{2.63}$$

For a fixed R^*, the following table 2.2 summarizes the calculation of the dimensionless numbers for the previous gas/water system which leads to an intensity of the spurious currents proportional to $\sigma/\mu_w = 72$, another equivalent numerical gas/water system is found which gives the same dimentionless numbers and in the same time reduces the ratio σ/μ_w to 1.

Variables (SI)	gas/water system	numerical gas/water
ρ_w	1000	726
μ_w	0.001	10^{-5}
ρ_g	1	0.726
μ_g	2.10^{-5}	2.10^{-7}
ω	2.17	2.10^{-2}
σ	0.072	10^{-5}
ρ^*	1000	1000
μ^*	50	50
Re	4,600	4,600
We	6.37	6.37
σ/μ_w	72	1

Table 2.2: Dimension analysis for two self-similarity gas/water system

Finally, we run the same simulation of a VoF gas core in a rotating flow using the values of the numerical gas/water system presented in table 2.2. Figure 2.14 shows the gas interface $C = 0.5$ at $t^* = 0.9$ equivalent to the same time when a breakage of the core was observed in 2.12d, the numerical simulation reveals that the gas core remains stable and is rotating following the rotation of the pipe. Furthermore, no spurious velocities are observed at the interface proving that the instability we observed in figure 2.12 is effectively due to spurious currents.

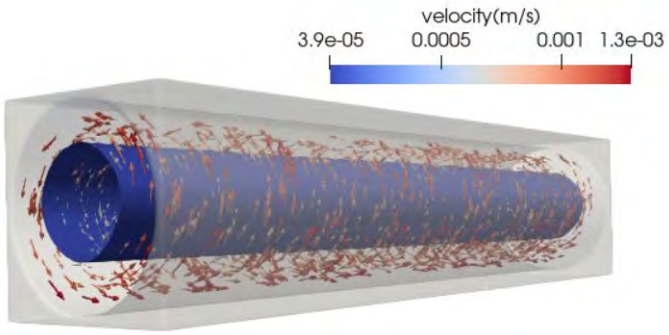

Figure 2.14: Gas core stability in a rotating flow at $t^* = 0.9$ using the numerical gas/water systems

To directly compare the intensities of the spurious currents between the two gas/water systems, we plot l_∞ in both cases over time t^*. Figure 2.15 shows the decrease of spurious velocity when moving from an air/water system to an equivalent system with a lower ratio σ/μ_w.

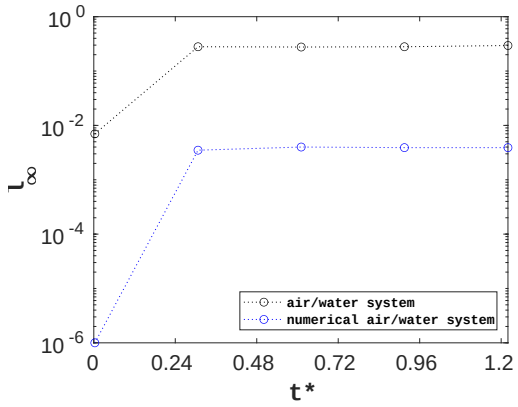

Figure 2.15: l_∞ in (m/s) over time for two self-similarity air/water system

Moreover, by calculating Ca_{max} for the numerical gas/water system and compare it to air/water system as presented in Fig. 2.16 we confirm once again that $Ca_{max} \approx 0.004$ and that the two systems are in perfect similarity.

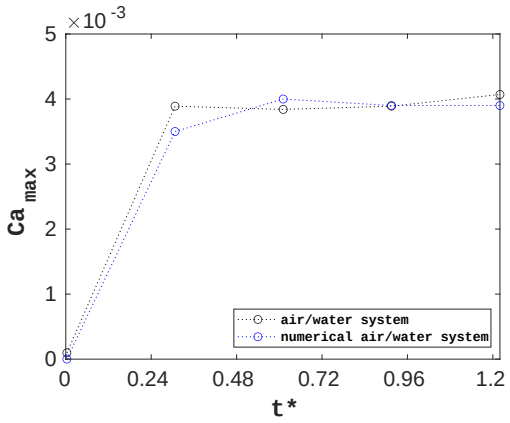

Figure 2.16: Ca_{max} over time for both air/water systems

2.7 Hybrid Lagrangian Tracking/Volume of Fluid (LT/VOF)

2.7.1 Introduction

As previously mentionned, in the separator, the interface presents a variation over a wide range of length scales. The ratio between the largest scale (the length of the core) and the smallest scale (bubble/droplet) is of order 1000. On one hand, the Lagrangian Tracking is efficient to track the light phase when it is dispersed but is not adequat to investigate the stability of the core after the separation. On the other hand, Volume of Fluid is not the convenient method to simulate the dispersed phase which has a size of milimeters as it needs very fine meshes to capture the interface. The solution is to develop a hybrid approach where a switch from Lagrangian Tracking to VoF takes place once the coalescence occurs without introducing any effictive coalescence model since we are not interested into the micro scale. This type of hybrid LT/VoF has been recently a subject of interest to some researchers working

on applications which involves multi-scale fluid structures (separation, atomization, cavitation...). Yu et al.[2] coupled Volume of Fluid and Lagrangian Tracking to simulate diesel spray using a Region Coupling Method (RCM), the latter consists in defining three regions which characterize the atomization, in the first and third regions, only VoF and Lagrangian Tracking are employed respectively while the second region is the coupling region where the two methods overlap, the criteria to move fluid parcels from VoF to LT is to have a volume less than 20% of the host cell and being discretised by less than 5 elements, figure illustrates an exemple of a simulation by Yu [2] using the RCM approach, the brown contour represents the 0.1 liquid volume fraction while the Lagrangian droplets are scaled to their diameters.

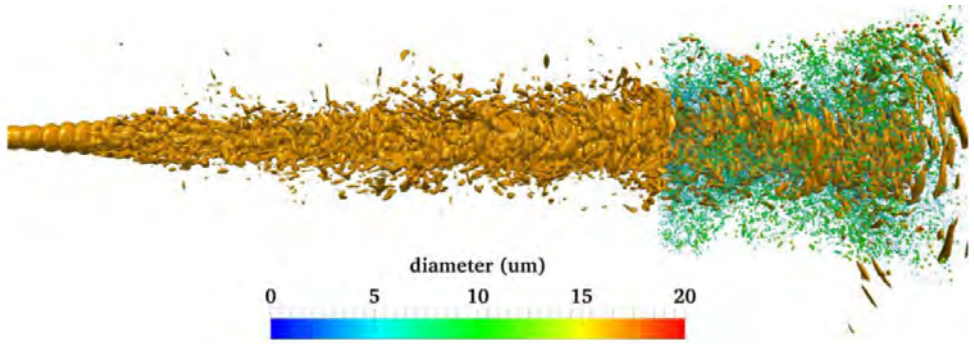

Figure 2.17: Simulation by Yu [2] for the atomization of a spay using hybrid VoF/LT

Within the same subject of atomization, Anez et al. [54] used an Eulerian–Lagrangian spray atomization model (ELSA) in which the switching strategy is based on the evaluation of the interface resolution as well as the curvature of the interface. the first criteria concerns the minimum resolved interface area while the second criteria assesses the ability of the LES filter to give a low interface curvature. Hence, when the interface fluctuations become significant at subgrid scale for instance in LES framework, the interface capturing method is droped and Euler-Lagrange method is adopted.
Peters et al.[3] developed a hybrid VoF/LT to simulate the cavitation phenomenon, a critical number of cells is defined beyond which a fluid is considered as sufficienly resolved to be treated by VoF and vice-versa to switch the unresolved fluid into the Lagrangian framework. Figure 2.18 depicts a snapshot in which Lagrangian bubbles are progressively growing and switching to VoF.

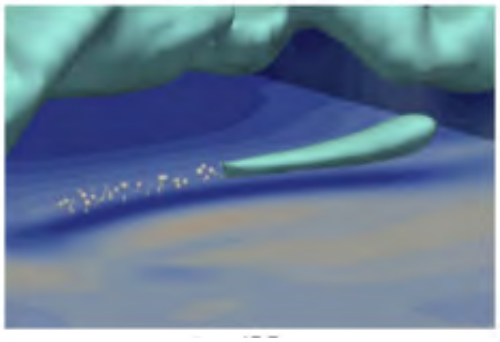

Figure 2.18: Simulation by Peters [3] where Lagrangian bubbles are growing and forming a larger Eulerian vapour structure

In short, developing a hybrid LT/VoF goes through certain steps: first, defining a criteria for the activation of the switch from VoF to LT or vice-versa, and this depends mainly on the simulated two-phase flow. Then, identifying the elligible fluid parcel which is subject to moving from one framework to the other. Finally, updating the volume fraction with the dispersed phase volume or specifying the number, volume and velocity of the new bubble/droplet to introduce when moving from VoF to LT. In the next subsection 2.7.2, an adequat hybrid LT/VoF for the inline fluid separation is proposed.

2.7.2 Switching from LT to VoF

In the inline fluid separator, since the core is formed downstream the swirl element, the hybrid LT/VoF is activated only in this region and this is the first condition. We also know that the bubbles/droplets migrate to the center of the pipe due to the centripetal force thus thoses bubbles/droplets trapped in cells located at the pipe center represent the starting point in the process of core formation. Thus, the second condition is to transform any dispersed phase located in the center of the separator or in contact with a filled cell $C > 0$ to VoF.
Figure 2.19 summerizes the steps to switch from the LT to VoF: - First, at each section x indexed by i along the separator, we detect bubbles/droplets located in $(i, N_y/2, N_z/2)$ which corresponds to the center of the separator, then we tag them, to do that, a flag variable is associated to each bubbles/droplets and equals 0 by default. If the bubbles/droplet is verifying the condition to move to the Eulerian framework, the tag is set to 1 and their velocity and accelaration is set to 0 (see Fig. 2.19a)
- The tagged bubbles/droplets are removed from the Lagrangian framework, in other terms, no force balance or trajectory equation is solved for them. Then at each section x indexed by i, a cylindrical core of length Δ (the mesh size) is constructed (see Fig. 2.19b). The details on how to define the cylinder and initialize the volume fraction $C_{i,j,k}$ is in the following paragraph.
- When a bubble/droplet is located in a cell (i, j, k) where $C_{i,j,k} > 0$, its flag is set to 1 and it undergoes the same treatment to move to VoF (see Fig. 2.19c).

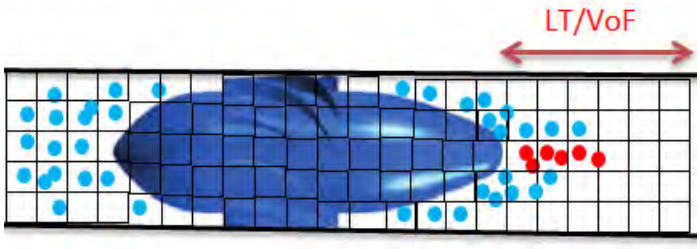

(a) Bubbles/droplets (in red) are positioned in cells at the center of the pipe

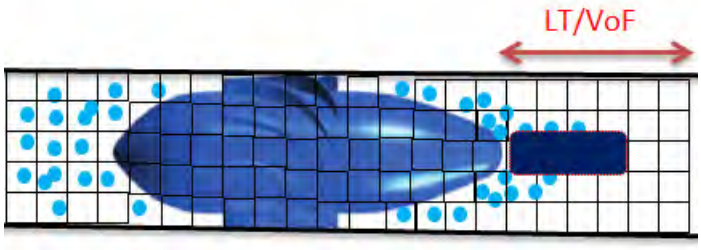

(b) Bubbles/droplets are transformed into the Eulerian framework and the VoF core is formed

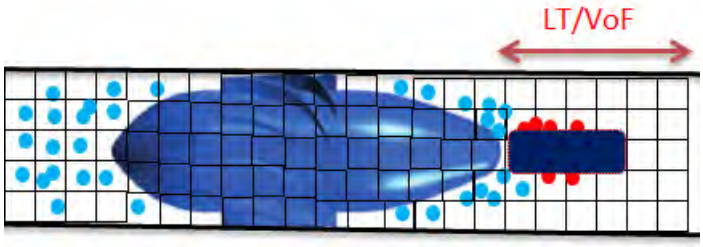

(c) Bubbles/droplets (in red) are located in a VoF cell $C > 0$ and therefore subject to switching to VoF

Figure 2.19: Sketch of the conditions to switch the dispersed phase from LT to VoF

Now that the conditions of when the hybrid LT/VoF is activated are detailed, we move to explaining how to construct the core and initialize the volume fraction for the VoF solver from the tagged bubbles/droplets.
As previously introduced, at each section x indexed by i, we know the bubbles/droplets located at each section x which are subject to the switch to VoF since they are tagged with flag=1, their total volume is therefore calculated as:

$$V_i^{LT} = \sum_i \frac{4}{3}\pi r_{d,tagged}^3 \tag{2.64}$$

And because the tagged bubbles/droplets are moving to the Eulerian framework, the Eulerian volume has to be updated by adding V_i^{LT} as following:

$$V_i^{VoF} = V_i^{LT} + \sum_{j,k} C_{i,j,k} V_{i,j,k} \tag{2.65}$$

with $V_{i,j,k}$ is the volume of the cell (i, j, k).
To locally form the core, a cylinder of length Δ is reconstructed at each section

where the switching criteria is verified, its radius is calculated as:

$$r_{i,cyl}^{VoF} = (\frac{V_i^{VoF}}{\pi\Delta})^{1/2} \tag{2.66}$$

To calculate the new volume fraction in the cell (i, j, k), four radii are defined:

$$\begin{aligned} r_{i,j,k} &= (y_{i,j,k}^2 + z_{i,j,k}^2) \\ r_{i,j+1,k} &= (y_{i,j+1,k}^2 + z_{i,j,k}^2) \\ r_{i,j,k+1} &= (y_{i,j,k}^2 + z_{i,j,k+1}^2) \\ r_{i,j+1,k+1} &= (y_{i,j+1,k}^2 + z_{i,j,k+1}^2) \end{aligned}$$

Where y and z are the cell Cartesian coordinates along $\mathbf{e}_y$ and $\mathbf{e}_z$ directions respectively.
Then, the minimum and maximum of these distances are determined:

$$r_{i,min} = min(r_{i,j,k}, r_{i,j+1,k}, r_{i,j,k+1}, r_{i,j+1,k+1}) \tag{2.67}$$

$$r_{i,max} = max(r_{i,j,k}, r_{i,j+1,k}, r_{i,j,k+1}, r_{i,j+1,k+1}) \tag{2.68}$$

Finally, the volume fraction resulting from the LT is $C_{i,j,k}^{LT}$:

$$C_{i,j,k}^{LT} = \begin{cases} 1 & \text{if } r_{i,max} \leq r_{i,cyl}^{VoF} \\ \frac{r_{i,cyl}^{VoF} - r_{i,min}}{r_{i,max} - r_{i,min}} & \text{if } r_{i,min} < r_{i,cyl}^{VoF} \& r_{i,max} > r_{i,cyl}^{VoF} \end{cases} \tag{2.69}$$

To make sure that the mass of the tagged dispersed phase is totally transformed into the Eulerian framework and that no mass loss or mass gain are taking place during the calculation of $C_{i,j,k}^{LT}$ locally at each section i. We recalculate the VoF volume as $V_i^{VoF,cylinder} = \sum_{j,k} C_{i,j,k}^{LT} V_{i,j,k}$ with $C_{i,j,k}^{LT}$ obtained from 2.69, and compare it to $V_i^{VoF,cylinder}$ from equation 2.65, if the relative error is of order 0.1% then $C_{i,j,k}^{LT}$ is final, otherwise, $C_{i,j,k}^{LT}$ is calculated in a loop until the condition on the relative error on the volume $\|E_{i,V}\|$ is less than 0.1%, the extra step in the algorithm after 2.69 is then:
For each section i, the initialization of $r_{i,test,max}$ and $r_{i,test,min}$:

$$\begin{aligned} r_{i,test,max} &= 1.5 r_{i,cyl}^{VoF} \\ r_{i,test,min} &= 0.5 r_{i,cyl}^{VoF} \end{aligned}$$

Then the loop starts:

$$\text{while}(\|E_{i,V}\| > 0.1\%)$$
$\text{if}(V_i^{VoF,cylinder} > V_i^{VoF})$ which means we have a mass gain then $r_{i,test,max} = r$
$\text{if}(V_i^{VoF,cylinder} < V_i^{VoF})$ which means we have a mass loss then $r_{i,test,min} = r$

The radius to test if it is resulting in the correct VoF volume is:

$$r_{i,test} = 0.5(r_{i,test,max} + r_{i,test,min}) \tag{2.70}$$

With this radius, we redistribute the volume fraction $C_{i,j,k}^{LT}$ as:

$$C_{i,j,k}^{LT} = \begin{cases} 1 & \text{if } r_{i,max} \leq r_{i,test} \\ \frac{r_{i,test} - r_{i,min}}{r_{i,max} - r_{i,min}} & \text{if } r_{i,min} < r_{i,test} \& r_{i,max} > r_{i,test} \end{cases} \tag{2.71}$$

We finally recalculate $\|E_{i,V}\| > 0.1\%$ to check the exit condition of the loop.
At the end of the switching algorithm (which starts from the bubbles/droplets detection step to equation 2.71), a verification if any other bubble/droplet is located in the updated C^{LT} is needed, if there is any, then the switching algorithm is called until no bubble/droplet is trapped in a cell with $C^{LT} > 0$. This case can eventually occur when, at the same time step, the interface of the formed core $C^{LT} > 0$ reaches some bubbles/droplets which where not concerned by the hybrid LT/VoF (see Fig. 2.20.

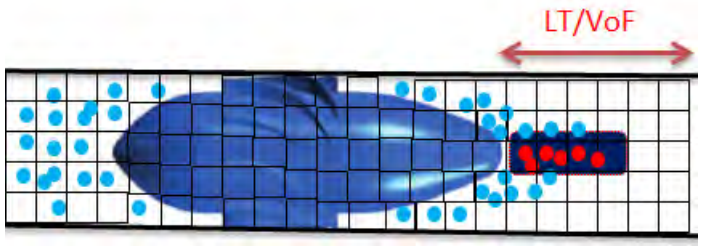

(a) The core is formed from the bubbles/droplets located at the center of the pipe (in red) at time t^n and the volume fraction C^{LT} is calculated

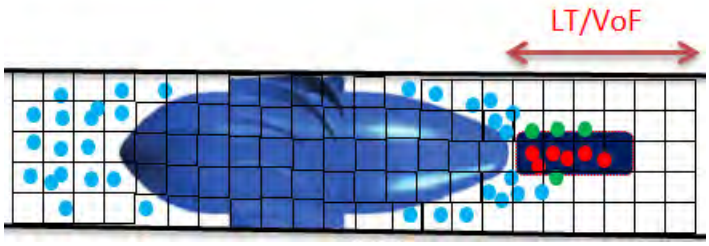

(b) The core characterized by the volume fraction C^{LT} reaches other bubbles/droplets (in green) at time t^n, thus, they become subject to LT/VoF

Figure 2.20: Sketch of the case when the constructed C^{LT} reaches other bubbles/droplets tagged with 0

Now, the volume fraction $C_{i,j,k}$ which will be used as initial condition in the next time step for the FCT is updated as $C_{i,j,k} = C^{lag}_{i,j,k}$ (see Fig. 2.24) if $C^{lag}_{i,j,k} \neq 0$ which means only in sections where a switch LT/VoF has happened. After the FCT and before the Lagrangian solver, another special case is treated to wit when the interface is transported and reaches another bubble/droplet with a flag=0, in this situation, the flag of this bubble/droplet is set to 2 so to avoid solving its trajectory equation and its contribution to C^{Lag} is taken into account during the following call of the hybrid LT/VoF. Figure 2.21 briefly summerizes the steps intervening in the hybrid LT/VoF inside the temporal loop.

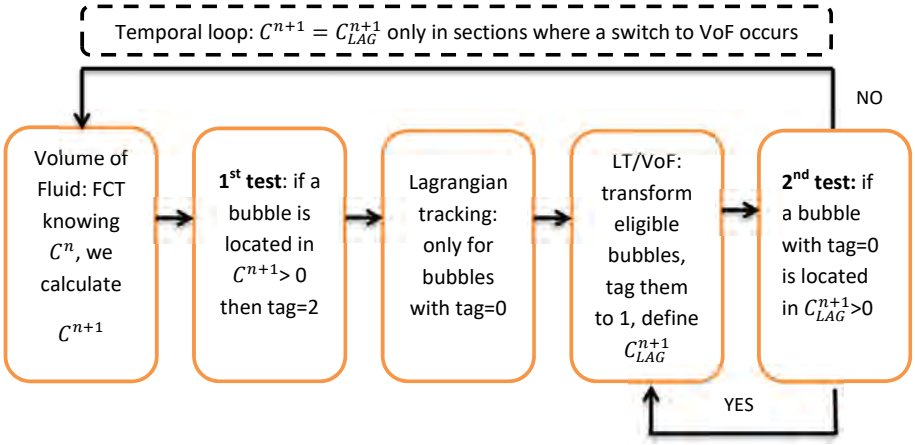

Figure 2.21: Algorithm of the hybrid LT/VoF

2.7.3 Validation: bubbles accumulation and core formation in a rotating flow using LT/VoF

To validate the new LT/VoF coupling algorithm, we simulate the accumulation of bubbles in a rotating flow, this configuration mimics, to some extent, the formation of the gas core in the separator. The two-phase flow is composed of the numerical air/water system previously introduced in table 2.2 to avoid spurious currents.
A rotating pipe with (OX) as a rotation axis and $\omega = 0.3rad/s$ the constant angular velocity is simulated using IBM. The numerical domain is a box of size $L_x \times L_y \times L_z = 0.23m \times 0.1m \times 0.1m$ made of $N_x \times N_y \times N_z = 100 \times 46 \times 46$ cells along the e_x, e_y and e_z directions. Periodic conditions are imposed at the inlet and outlet of the pipe. Once the flow is developed, a set of 1000 bubbles of radius $r_b = 1mm$ are injected randomly inside the tube with the fluid velocity (see Fig. 2.22a). The hybrid LT/VoF is activated inside the pipe. Figure 2.22 shows three different instants. First when the bubbles are injected and are still all in the Lagrangian framework. Then, the bubbles start to migrate towards the center of the pipe and once the criteria for switching to VoF is verified, the tagged bubbles are not any more resolved by LT and their total volume is transformed into a volume fraction C. In Fig. 2.22b, the interface corresponding to the contour $C = 0.5$ is visualized. After that, arriving bubbles are reaching the gas core, therefore they are switching to VoF. At the end, only the VoF is activated. Figure 2.22d represents the gas volume fraction C in a section $z = 0$, the interface $0 < C < 1$ is well resolved by VoF, C is no more updated by the hybrid LT/VoF and the Lagrangian Tracking solver is turned off.

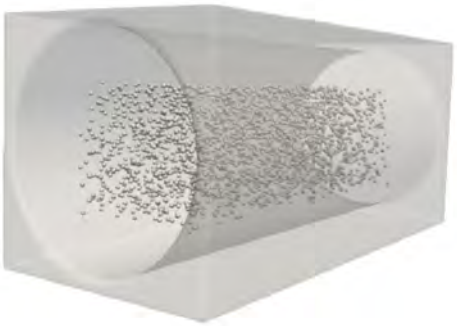

(a) Initialisation of the bubbles: only LT is activated

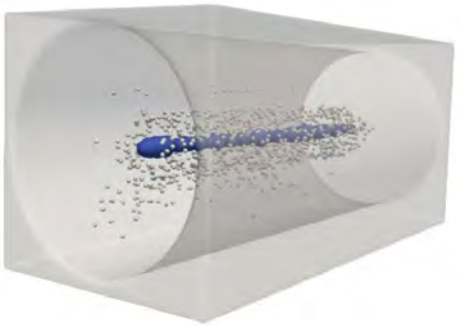

(b) Beginning of the core formation: LT/VoF is activated

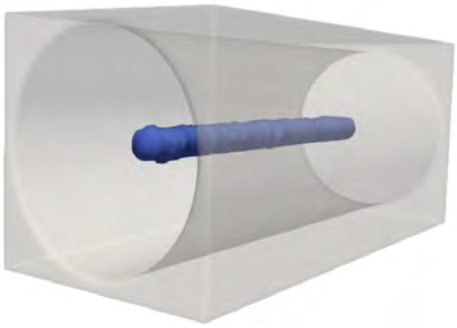

(c) End of the core formation: only VoF is activated

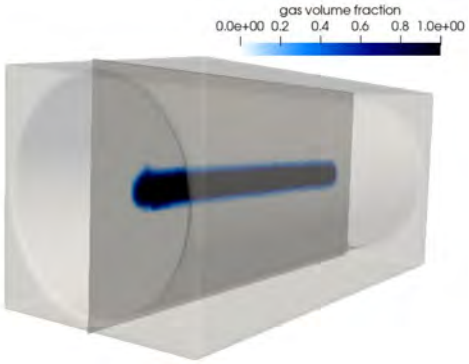

(d) The gas volume fraction in a section along the pipe

Figure 2.22: Simulation of two-phase flow: bubbles accumulation and core formation in a solid body rotation using hybrid LT/VoF

A close-up view on how the bubbles are progressively forming the gas core at a cross-section over time is given in Fig. 2.23. The bubbles are colored with their velocity and as previously explained, when the bubbles move to the Eulerian framework, their velocity is set to 0 so the red points represent the transformed bubbles. In each section, we also visualize the cylindrical core as it grows.

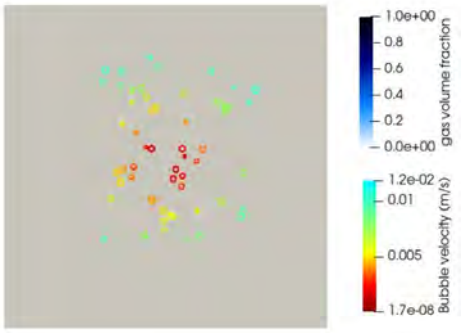

(a) Initial position of bubbles located at a cross-section of the pipe

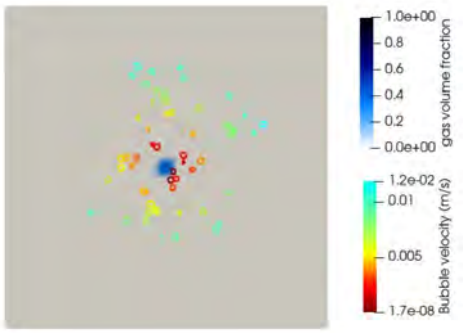

(b) Bubbles are migrating to the center and the gas core is appearing in blue

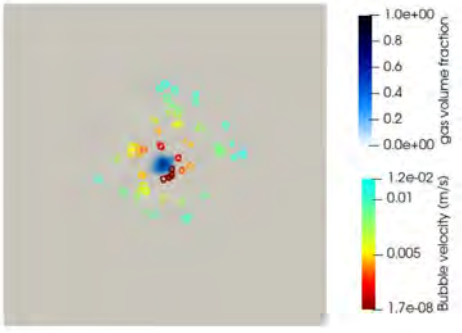

(c) Some bubbles are in contact with the core interface and therefore moved to VoF

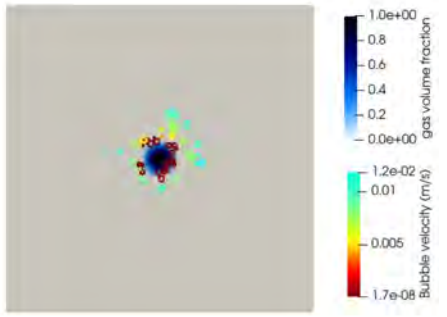

(d) The core is growning as more bubbles are switching to VoF

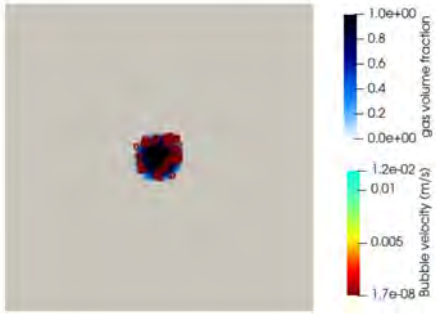

(e) All bubbles in the section have switched and only the VoF is active

Figure 2.23: Simulation of two-phase flow: bubbles accumulation and core formation at a cross-section using hybrid LT/VoF

2.8 Global algorithm and HPC performance

To summarize the over-all algorithm, Figure 2.24 illustrates step by step the order of the resolution of equations for the whole hybrid approach.

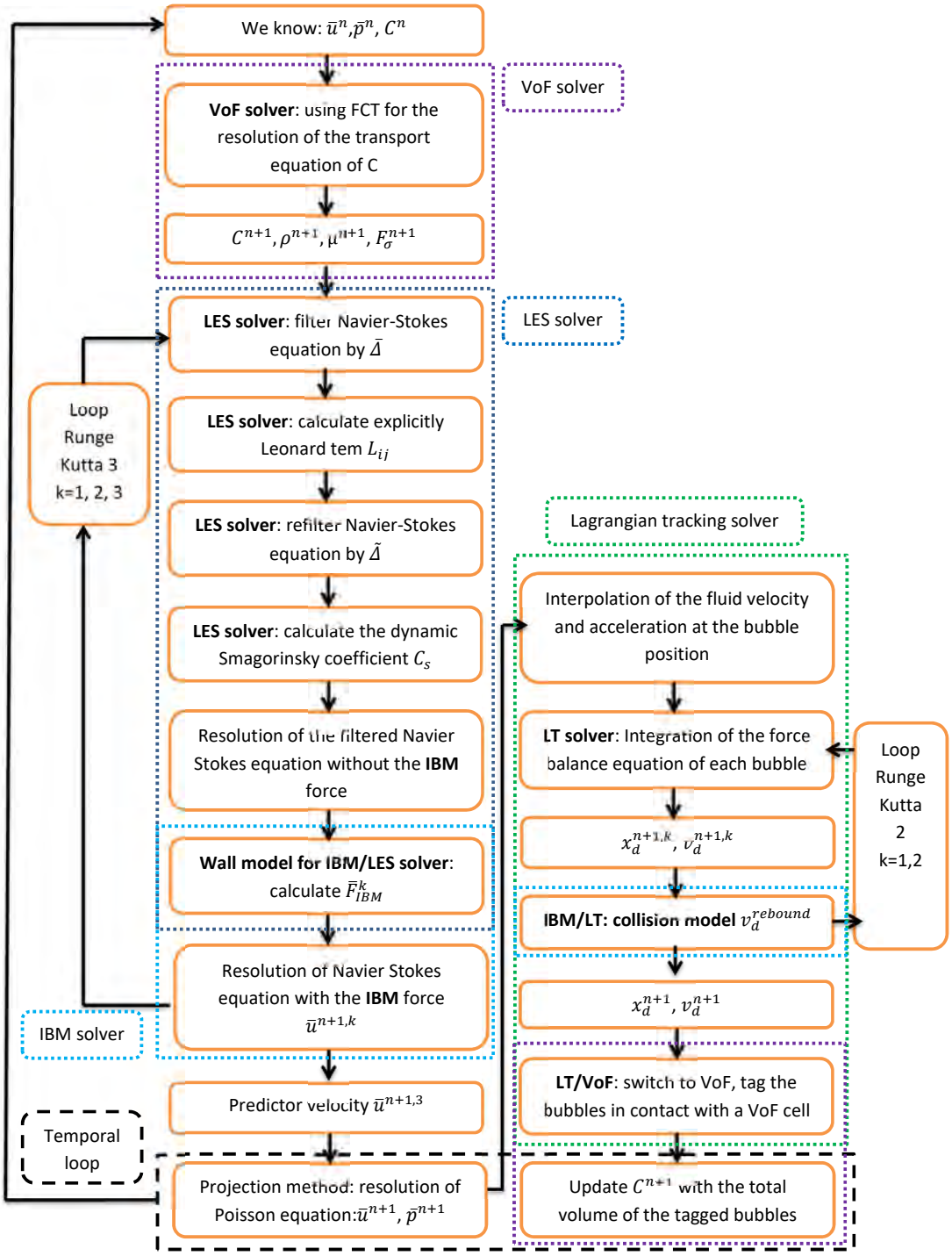

Figure 2.24: Over-all algorithm of the numerical resolution

We should note that parallel computing is used to run the simulations. And to check the achieved HPC performance of the code, we consider a 3D simulation of the separator in a numerical domain of size $L_x \times L_y \times L_z = 0.92m \times 0.1m \times 0.1m$ made of $N_x \times N_y \times N_z = 800 \times 92 \times 92$ cells along the e_x, e_y and e_z directions. We run the simulations on the supercomputer Olympe from CALMIP at the University

of Toulouse on N cores. In Fig.2.25, T_{32} is the time needed to run one time step on 32 cores and T_N is the time needed on N cores. This time is plotted as a function of the number of cores both for a single-phase flow simulation of $Re = 50,000$ when LES, IBM and the wall model are activated and for two-phase flow simulation of the same Reynolds number with the injection of a set of 70000 bubbles and the activation of whole hybrid approach summarized in Fig. 2.24. The achieved HPC performance is compared in the two cases to an ideal linear performance. Single-phase flow scales good up to 64 cores, then, the communication time between the cores starts to be relevant. For the two-phase flow case, it is worth noting that only the solvers for the continuous phase are runned in parallel (IBM, LES, VoF) while the Lagrangian Tracking is in series since the number of bubbles is not very high and that the tagged bubbles are removed from Lagrangian framework which further reduces the number of trajectory equations solved by the LT solver. The achieved performance is lower than the single-phase flow which is a normal response of the code. In short, parallel computing is favorable in the two cases as it helps getting the results in an acceptable time of such an important calculation domain.

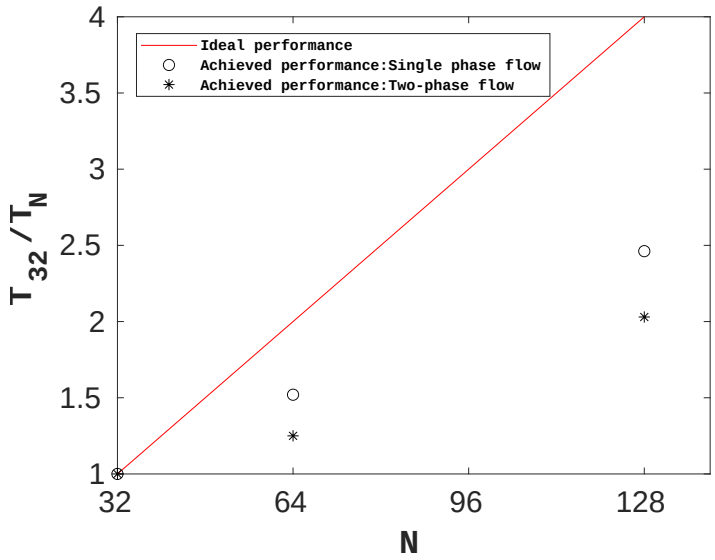

Figure 2.25: Comparison of the HPC performance for single-phase and two-phase flows on Olympe

2.9 Conclusion

In this chapter, the hybrid CFD approach to simulate the inline fluid separation is introduced, it involves four main CFD methods namely: Immersed Boundary Method (IBM) for simulating the comlex geometry of the swirl element, Large Eddy Simulation (LES) for turbulence using the mixed Dynamic Smagorinsky model, Lagrangian Tracking (LT) to calculate the trajectory of the dispersed phase and Volume of Fluid (VoF) for the core simulation. The discretization and intergation of the equations for each method are presented as it had been before developed in JADIM. However, to activate the four solvers, hybrid models need to be developed to ensure a correct interaction between them. IBM is successfully used for a CAD file for a complex geometry. Then a collision model is introduced for IBM/LT to allow the bubbles/droplets to rebound on the surface of IB solids and finally a hybrid

LT/VoF is developed to switch from the Lagrangian framework to the Eulerian one when the tracked bubbles/droplets accumulate in the center of the pipe after the swirl element to form a core, the latter is then simulated using VoF. It remains to mention that the LES solver as previously developed and used in JADIM requires a mesh refinement next to the wall to capture the viscous sub-layer, this condition becomes more and more constraining as the Reynolds number increases, that is why we are interesed in developing a special wall model for LES/IBM which will allow to use LES on coarse meshes. Chapter 3 introduces an orignal wall model for LES/IBM, the model is detailed and validated via a study of the classical turbulent pipe flow.

Chapter 3

Wall model for hybrid Immersed Boundary Method and Large Eddy Simulations IBM/LES

3.1 Introduction

The IBM solver in JADIM has been validated in many studies of flows around IB objects [23, 55]. Similarly, the LES solver has been implemanted and tested for different turbulent flows: channel flows [18] and pipe flows [22] with respect to the constraint of mesh refinment next to the wall to capture the viscous sub-layer. Yet, our objectif is to use both solvers within one simulation on a coarse mesh through the development of new wall models for hybrid IBM/LES method [56].
In this chapter, we first investigate the capacity of IBM to solve a flow inside an IB solid and for that we simulate Poiseuille flow and conclude how the model should be formulated and implemented. Then, turbulent pipe flow is studied, two wall models named: mean velocity model and stochastic model are proposed and validated, the effect of Reynolds number and the mesh size is analyzed and it is shown that with the wall model, correct mean velocity and fluctuations can be obtained.

3.2 Poiseuille flow

To evaluate the ability of IBM to predict the flow inside an IB solid, we start with studying the classical Poiseuille flow, for which the exact solution for the velocity U and shear stress τ in function of the radial position r are:

$$U(r) = -\frac{1}{4\mu}\frac{dp}{dx}\left(R^2 - r^2\right) , \quad \tau(r) = -\frac{1}{2}\frac{dp}{dx}r \tag{3.1}$$

We consider a pipe, simulated using IBM and defined by 2.26, of diameter $D = 2R$ and axis (Ox) inside a box of size $L_x \times L_y \times L_z$ along the e_x, e_y and e_z directions (Fig. 3.1).

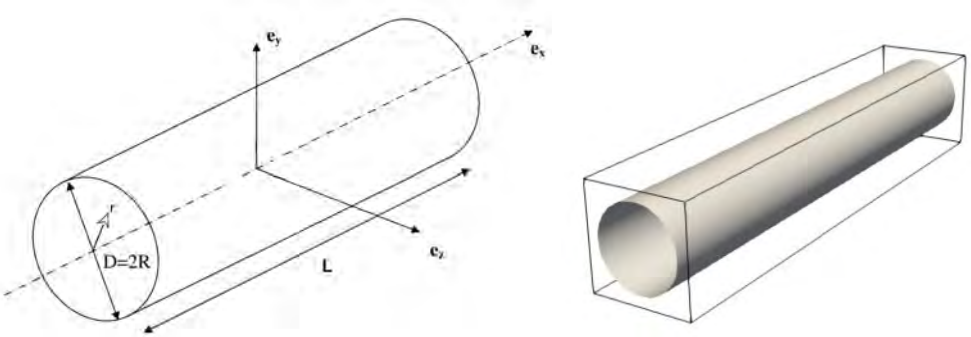

Figure 3.1: Sketch of the geometry (left). Numerical domain and wall pipe shown using the iso-contour $\alpha_{IBM} = 0.5$ (right).

The mesh is Cartesian and regular of size Δ and three different meshes $m1, m2$ and $m3$ are considered corresponding to the number of cells per pipe radius $R/\Delta = 8$, $R/\Delta = 16$ and $R/\Delta = 32$, respectively. Figure 3.2 represents the mesh on a cross section of the pipe. As shown, the solid wall thickness decreases when the mesh is refined.

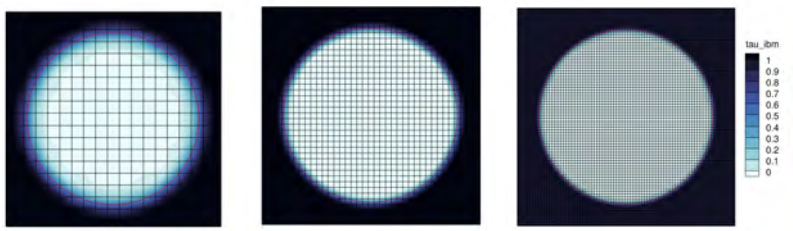

Figure 3.2: Pipe cross-section for the three meshes $m1$, $m2$, and $m3$ from left to right.

The flow is driven by a fixed pressure drop dp/dx along the x-direction. Periodic conditions at the inlet and outlet of the pipe are imposed. The flow is characterized by the Reynolds number $Re = Du_b/\nu$ with u_b the bulk velocity. At the beginning, numerical simulations are carried out using the standard IBM expression (2.25) to prescribe the presence of the wall. Figure 3.3 compares the velocity profile $U(r)$ and the shear stress $\tau(r)$ to the exact solution for the three meshes $m1$, $m2$ and $m3$. $U(r)$ and $\tau(r)$ are respectively made dimensionless by the maximum central velocity $U_{max} = -\frac{1}{4\mu}\, dp/dx R^2$ and the wall shear stress $\tau_{wall} = -\frac{1}{2}\, dp/dx R$ given by the exact solution (3.1).
To evaluate the convergence of the error at the IB wall, we calculate the relative error of the velocity at the IB wall as:

$$\epsilon_{U(R)} = \frac{U(R)^{analytical} - U(R)^{simulation}}{U(0)^{analytical}} \tag{3.2}$$

And relative error of the shear stress at two positions: at the IB wall $r = R$ and in a fluid cell $r = R/2$.

$$\epsilon_{\tau(r)} = \frac{\tau(r)^{analytical} - \tau(r)^{simulation}}{\tau(r)^{analytical}} \tag{3.3}$$

As shown in Fig. 3.4, the velocity and shear stress at the IB wall using IBM with no model is lower than a second order. The IBM does not conserve the second order accuracy because of its diffusive aspect.

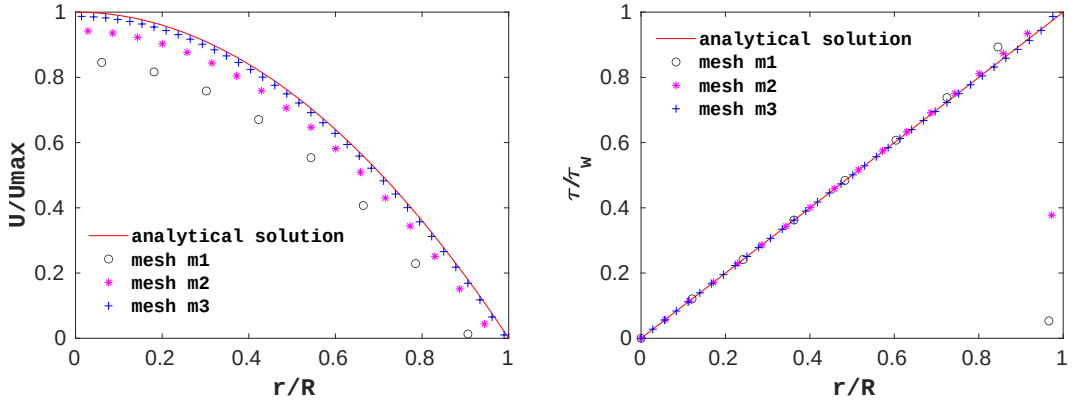

Figure 3.3: Dimensionless radial profiles of the velocity (left) and the shear stress (right) for the three meshes compared to the exact solution eq. 3.1.

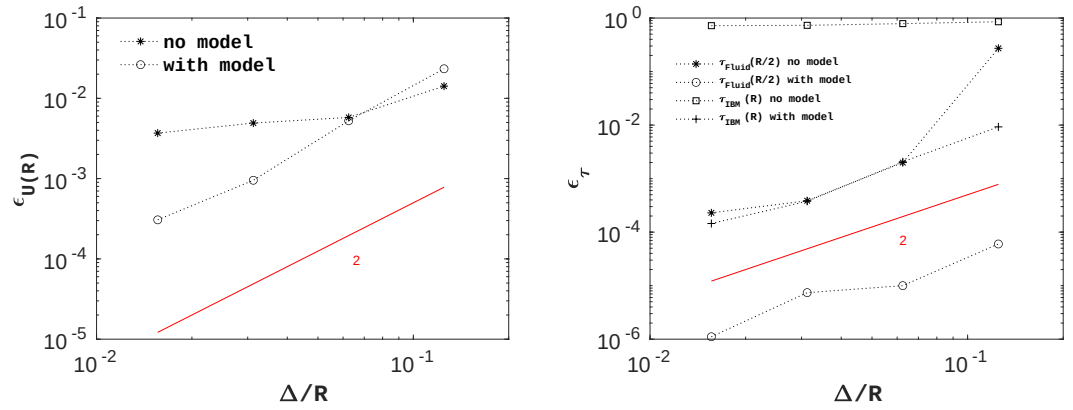

Figure 3.4: Grid convergence of the relative error on the velocity at the IB wall: $U(R)$ (left), the shear stress at the IB wall: $\tau_{IBM}(R)$ and in the fluid at $R/2$: $\tau_{Fluid}(R/2)$.

The significant loss of accuracy close to the wall is the direct consequence of the IBM solid-fluid interaction description used for the simulation. In the standard method first applied here, a zero velocity is considered across the entire IBM wall thickness zone i.e. for $0 < \alpha_{IBM} \leq 1$. We clearly observe in Fig. 3.3 that the resulting viscous shear stress departs from the linear evolution in this region and this impacts the shear stress in the fluid close to the wall. The control of the velocity profile cannot be made with the IBM function given by equation 2.26 since it mainly controls the width of the IBM wall thickness. The proposed method consists in directly imposing the correct velocity evolution inside the IBM wall thickness. In the case of the Poiseuille flow, the exact solution is given by equation (3.1) therefore the corresponding velocity profile for the solid wall velocity v_s of the solid-fluid interaction is then:

$$v_{s,x}(r) = -\frac{1}{4\mu}\frac{dp}{dx}(R^2 - r^2)\,, \quad v_{s,y} = v_{s,z} = 0 \tag{3.4}$$

By the definition of f_{IBM}, this forcing is effective for $\alpha_{IBM} > 0$. The velocity profile in the IBM wall thickness cancels at the exact wall position $r = R$ corresponding to $\alpha_{IBM} = 0.5$. Note that the velocity for $r > R$ is then negative in order to respect the correct value of the velocity gradient, and thus the wall shear stress at $r = R$. Figure 3.5 represents the velocity and shear stress obtained with the new IBM condition (3.4). All the profiles are now very close to the analytical solution regardless of the mesh size. The corresponding errors on both the velocity and the viscous shear stress are reported in figure 3.4 as a function of the grid size. We observe that by correcting the IBM forcing following the proposed model, the magnitude of the error has been significantly reduced, the accuracy is improved and a second order convergence is obtained for both velocity and shear stress.

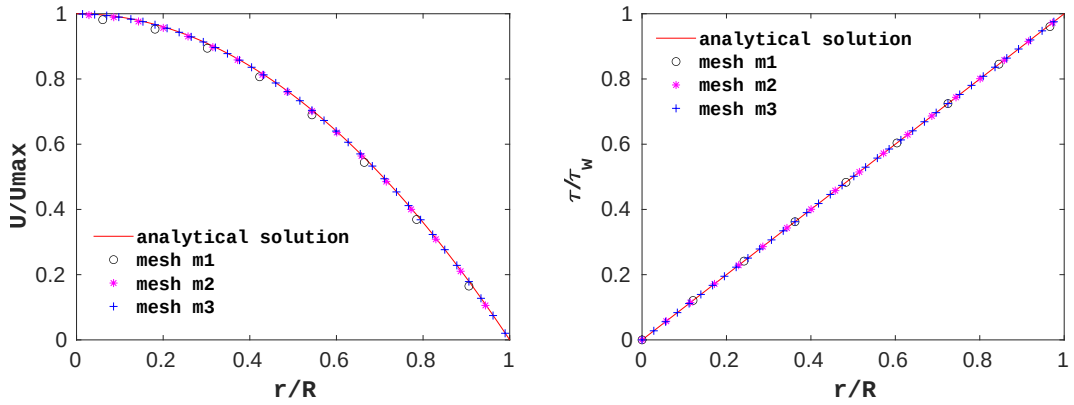

Figure 3.5: Dimensionless profiles of the velocity and the shear stress when using the IBM wall model (3.4)

From the DNS simulations of a Poiseuille pipe flow, we have demonstrated that the IBM method using the standard solid-fluid interaction is grid convergent. However the error with the exact solution can be significantly lowered with an appropriate condition applied inside the region of IBM wall thickness. The objective of the next section 3.3 is to consider turbulent pipe flow simulations via the IBM/LES solver.

3.3 Hybrid IBM/LES

Simulating turbulent flows by coupling IBM for complex geometries and LES for turbulence raises the question of adapting the wall boundary conditions for their coupling. The resolved LES can capture the viscous boundary layer therefore requires an adapted mesh refinement next to the wall. Specific wall conditions for IB walls to overcome that resolution constraint were proposed. Tessicini et al. [57] solved the LES equations up to the second grid cell away from the wall, then switched to solving the simplified turbulent boundary-layer equations on an embedded refined wall mesh. The eddy viscosity is obtained from a simple blend of an eddy viscosity model with near wall damping function. Cristallo & Verzicco [58] have upgraded the work of Tessini et al. [57] by using LES till the first grid point at the wall while the wall shear stress is deduced from a boundary layer approximation. Roman et al. [59] used a prediction of the velocity at the first fluid grid point in contact with the IB solid boundary assuming the classical log-law evolution and imposed a RANS-like

eddy viscosity. We note that these methods have been developed in the context of sharp immersed boundaries when the IB wall is well located in the Eulerian grid. Using a diffusive IBM with Lagrangian markers, Ma et al. [60] solved the boundary layer equation on an embedded mesh and used the local wall shear stress calculated on the Eulerian points to correct the sub-grid scale viscosity.
In our case, the IBM/LES coupling consists in applying the numerical procedure described for the IBM method to the governing equations considered for LES simulations. The IBM coupling term is then expressed using the filtered velocity field:

$$\overline{f}^k_{IBM,i} = \alpha_{IBM} \frac{v^{k-1}_{s,i} - \overline{u}^k_i}{\Delta t} \tag{3.5}$$

Now, we simulate turbulent pipe flow with the use of the IBM/LES method on the same numerical domain used in the Poiseuille flow study. The flow is again driven by a constant pressure drop. We note $\tau^* = \frac{R}{2}|dp/dx|$ the mean wall shear stress, $< u^* >= \sqrt{\tau^*/\rho}$ the mean friction velocity, $\ell^* =< u^* > /\nu$ the wall unit length and $Re^* = R < u^* > /\nu$ the friction Reynolds number. Three high Reynolds numbers flow $Re = u_b D/\nu$ are simulated: $Re = 50,000$, $Re = 100,000$ and $Re = 500,000$. Discussion on the results will be first conducted for $Re = 100,000$ because of the availability of several reference results for the mean axial velocity profile U^+ and the root mean square (rms) velocities u_x^+, u_r^+, u_θ^+ along the x, r and θ directions normalized by $< u^* >$, respectively. The corresponding references, values of Re and Re^* are reported in table 3.1.

Method	References	Re	Re^*	Available data	Symbol in graphs
LES/RANS	[61]	100,000	2350	U^+	$\times$
Experiments	[62]	98,000	2315	U^+	$\wedge$
DNS	[63]	83,000	2000	U^+, u_x^+, u_r^+, u_θ^+	$\diamond$
Experiments	[64]	81,000	1960	U^+, u_x^+	$+$

Table 3.1: References used for comparison and corresponding symbols in the figures.

The simulations are performed using the three meshes $m1$, $m2$ and $m3$. The ratio Δ/ℓ^* is reported in Table 3.2 for the three considered Reynolds numbers. With regard to high turbulent pipe flows, these meshes are coarse and none of them is adapted for a full resolution of the viscous sub-layer, justifying the need of an appropriate wall modeling. This is clearly shown in Fig. 3.6 where the simulations performed using mesh $m2$ are compared to the data referenced in Table 3.2 for $Re = 100,000$. As reported, all the data from literature are collapsing on a similar evolution for the mean velocity U^+. The IBM/LES simulation using the standard IBM solid-fluid interaction presented by circles is significantly under-estimating the mean velocity indicating that the wall friction is not correctly predicted. This response of IBM/LES is very similar to what we observed for a laminar flow. Considering the velocity fluctuations, thanks to the LES solver, their order of magnitude is correctly captured inside the pipe but not close to the wall.
The objective is now to propose a modified IBM solid-fluid interaction in order to improve the results and in particular to recover a correct magnitude for the mean velocity. Two approaches will be proposed in the following: the first one is based on the mean velocity profile while the second makes use of a stochastic model for the velocity to impose in the IBM wall thickness.

R/Δ - Re	50,000	100,000	500,000
8 $(m1)$	160	292	1260
16 $(m2)$	80	146	630
32 $(m3)$	40	73	315

Table 3.2: Value of ratio Δ/ℓ^* for the meshes and Reynolds numbers considered

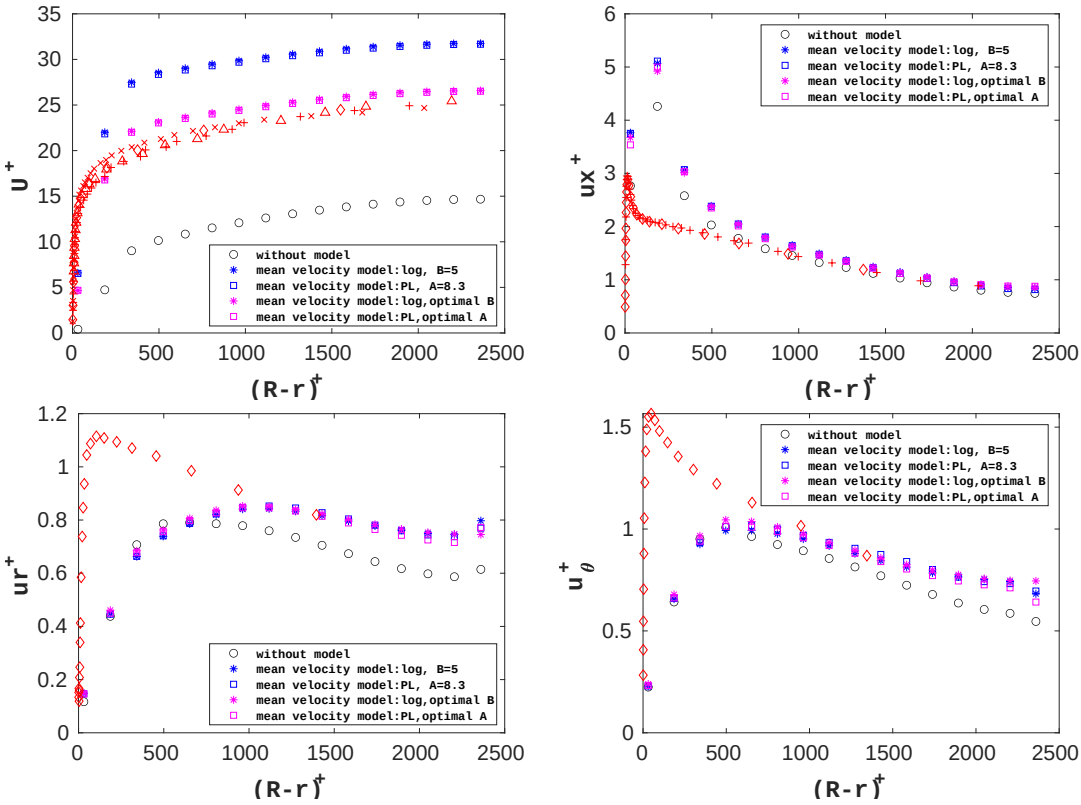

Figure 3.6: Profiles of the mean velocity and rms velocity for simulations using the standard IBM solid-fluid interaction and the IBM solid-fluid interaction based on the mean velocity models for $Re = 100,000$. Red symbols stand for the reference studies (see Table 3.1). The "log-law" and "power law" modeling are considered with the constants $(k = 0.41\ ;\ B = 5)$ and $(A = 8.3\ ;\ C = 1/7)$, respectively.

3.4 Mean velocity wall model

In the case of turbulent pipe flow, no exact solution for the velocity profile is available to make possible an unsteady and local control of the velocity field inside the IBM wall thickness as done in the previous section for the laminar Poiseuille flow. However the mean velocity profile close to a turbulent wall in a pipe has been characterized for a large range of Reynolds numbers. In particular the mean velocity can be described by the classical log-law evolution or can be fitted by a power law. Both laws have been considered at high Reynolds number regimes in experimental and numerical studies. See for example [65] where both laws compare well with LES simulation over a large range of Reynolds numbers varying from 10^4 to 10^{11}.

In this section, both the "log-law" and "power law" modeling are regarded to control the velocity description inside the IBM wall thickness. Since the model has to

be implemented in all the IBM thickness, a velocity condition also has to be imposed for $0.5 < \alpha_{IBM} < 1$, i.e. for negative values of the wall unit distance $r^+ = (R-r)/\ell^*$. In order to respect the condition $v_s(r^+ = 0) = 0$ and the continuity of the velocity for discretization purposes in the viscous shear calculation, the velocity field is extended for $r^+ < 0$ (i.e. $r > R$). Under these considerations, the "log law" modeling consists in imposing in the IBM forcing term f_{IBM} defined by (3.5) the velocity field v_s following:

$$v_{s,x} = \begin{cases} r^+ \ < u^* > & \text{if } \mid r^+ \mid \leq 11 \\ \text{sign}(r^+) \, (\frac{1}{k} log(\mid r^+ \mid) + B) \ < u^* > & \text{if } \mid r^+ \mid > 11 \end{cases}, \quad v_{s,r} = v_{s,\theta} = 0 \tag{3.6}$$

with $k = 0.41$ and $B = 5$ [66], while the "power law" modeling considers:

$$v_{s,x} = \begin{cases} r^+ \ < u^* > & \text{if } \mid r^+ \mid \leq 11 \\ \text{sign}(r^+) \, A \mid r^+ \mid^C < u^* > & \text{if } \mid r^+ \mid > 11 \end{cases}, \quad v_{s,r} = v_{s,\theta} = 0 \tag{3.7}$$

with $A = 8.3$ and $C = 1/7$ [67].

To analyze the effect of such control of the velocity in the IBM wall thickness, numerical simulations are first performed for $Re = 100,000$ using mesh $m2$. Figure 3.6 illustrates the mean and rms profiles normalized by $< u^* >$ as a function of the radial position normalized by the wall unit length ℓ^*. The two models ("log law" and "power law") provide very similar results for both the mean and the rms velocities. The mean velocity profile is now over-estimated in comparison with the previous data from literature. The impact on the rms velocity differs depending on each components. The velocity fluctuation in the streamwise direction increases close to the wall and is corrected far from it in the two other directions. The peak of the streamwise fluctuation generally located around $15\ell^*$, considered as a feature of turbulent pipe flow, cannot be detected with such a mesh resolution (see Table 3.2). However we see a peak in our curves which is shifted away from the near wall with a higher intensity. Similar behavior of the peak location is reported by Ma [60] using a dynamic wall model for IBM/LES simulations. Besides, the simulations on other meshes reveal that the peak gets closer to the wall as we refine the mesh.
The results obtained with the model follow the expectations but still need to be adapted and one possible solution to do so is through the modification of the wall law coefficients. An adjustment of the coefficients B for the log-law and A for the power law is performed aiming at minimizing the error on the bulk velocity. Figure 3.7 depicts the relative error on the bulk velocity as a function of the wall law coefficients for the mesh $m2$. The reported error E_U is calculated as:

$$E_U = \frac{U^{expected} - U^{simulation}}{U^{expected}} \tag{3.8}$$

where $U^{expected}$ is the expected value of the bulk velocity based on the pressure drop imposed to the pipe flow and $U^{simulation}$ is the one given by the simulation. Positive values represent the case of an underestimate of the bulk velocity as observed with no wall model giving $E_U = 55\%$. As shown in Fig. 3.6, the use of the two considered wall models induces an over-compensation of the mean velocity with a relative error $E_U = -20\%$. Thus, by adjusting the values of the model coefficients, an optimal value of $B \approx 0$ and $A \approx 5.8$ for the log and power models, respectively, can be found with a relative error less than 1%. The flow statistics when using these coefficients are reported in Fig. 3.6 and discussed more in section 3.6.

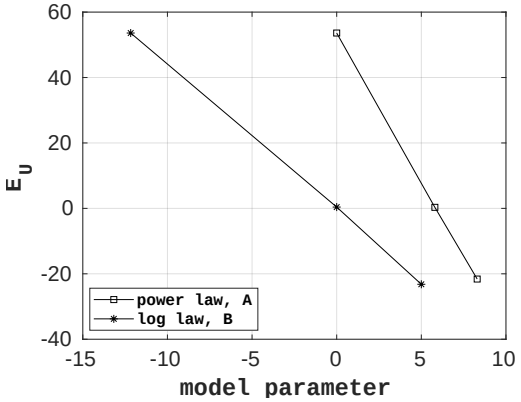

Figure 3.7: Relative error E_U on the bulk velocity as a function of the wall law coefficients B and A for the log and power laws, respectively.

As shown, with the adapted wall law coefficient, one is able to obtain the accurate mean velocity profiles. However, in terms of velocity fluctuations, the model does not improve remarkably the rms in comparison with the basic model. This is explained by the fact that the model uses only a constant friction velocity without introducing any source of fluctuations. And this can justify two main features of this model:
- the need of adjusting the wall law coefficient. For instance, the simulation using the classical law coefficients yields to higher bulk velocity because it does not have enough fluctuations, the latter contributing to the mean shear and can bring back the correct mean velocity profile. In short, it is not just about controlling the bulk velocity but also acting on the fluctuations.
- the rms velocities remain unchanged for different values of the wall law coefficients which means that tuning the wall law coefficients may not be the relevant approach if we are interested in reproducing the fluctuations as well, keeping in mind that a perfect fluctuation remains challenging if considering coarse meshes.
Therefore, we can conclude that the model based on the mean friction velocity overestimates the bulk velocity and needs to be corrected by an appropriate modeling for the fluctuations. Indeed, if we manage to increase the fluctuations, the mean velocity will decrease and it will be automatically corrected with no need of tuning the wall law coefficients. This is the objective of the stochastic wall model proposed in the next section 3.5.

3.5 Stochastic wall model

The previous model based on the mean friction velocity needs to be corrected by taking into account the fluctuations in the velocity imposed in the IBM wall thickness. Indeed, the wall region is known to present significant fluctuations with characteristic spatial and temporal correlations resulting from the regeneration cycle of turbulent structures as well as from the interaction with the outer flow [68, 69]. It has been pointed out [70] that the complex flow structure is strongly correlated to the wall shear stress which thus presents large scale fluctuations [71, 70, 72].

To mimic the effect of the unresolved turbulent wall structures, we propose to use a stochastic field which reproduces the fluctuations of the wall shear stress, for the definition of the solid velocity field v_s used for IBM forcing term f_{IBM} (3.5). Reflecting the view of the momentum cascade taking place in the logarithmic layer

as a self-similar hierarchy of wall-attached eddies [73, 74], we express the local IBM velocity from the law of the wall, but substituting the average friction velocity by a random friction velocity:

$$v_{s,x}(r,\theta,x,t) = \begin{cases} r^+ \; u^*(\theta,x,t) & \text{if } \mid r^+ \mid \leq 11 \\ \text{sign}(r^+)\,(\frac{1}{k} log(\mid r^+ \mid) + B)\; u^*(\theta,x,t) & \text{if } \mid r^+ \mid > 11 \end{cases} \tag{3.9}$$

$v_{s,r} = v_{s,\theta} = 0$
while keeping the original values of $k = 0.41$ and $B = 5.0$.
Note that the length scale l^* used to normalize r remains constant and is based on the average friction velocity. This model is supported by the self-similarity of large scales leading the velocity profile to scale with u^* as reported in [71, 72]. In order to reproduce the very large deviations of the wall shear stress [70], we assume that the stochastic field $u^*(\theta,x,t)$ presents a log-normal distribution [75, 76]. Thus, the variable $f = \ln(u^*/\langle u^* \rangle)$ has a normal distribution with average μ and variance σ^2. From the expression of the moments of log-normal variables ($\langle\langle (e^f)^q \rangle\rangle = e^{q\mu + q^2\sigma^2/2}$), we impose for its average $\mu = -\sigma^2/2$ to have $\langle e^f \rangle = 1$ and balance the global momentum budget. Considering that the variance of u^* is commensurate with the square of its mean, we introduce the ratio $\alpha_h = \langle u'^{*2} \rangle / \langle u^* \rangle^2$ which is related to σ as $\sigma^2 = \ln(1+\alpha_h)$. Indeed [77] showed that the standard deviation of u^* is between 15% and 40% of its mean value from experimental and DNS data and is probably Reynolds number dependent. We also want to impose the spatial correlation lengths in the streamwise and spanwise directions as well as the temporal correlation to account for both lifetime of the turbulent structures and their advection by the mean flow. These spatio-temporal correlations of the wall shear stress have been reported in [72, 71, 70]. It has been observed that the correlation lengths in the streamwise and spanwise directions are around 1000 and 100 wall units respectively, similarly to the near wall flow structures [78, 79, 80, 81]. We expect the convection velocity of the wall friction to be scale-dependent [82, 71, 83]. Indeed, the large scales of the wall friction, which are related to events taking place in the logarithmic region have been reported to be convected at a velocity that is much faster than the average velocity in the near-wall region [71, 84], while the smaller scales which are due to the near-wall cycle appending in the buffer layer are convected with the characteristic velocity of the buffer layer [82, 83]. Overall, the convection velocity, in wall unit, is estimated to stand in the range $u^+_{adv} = 10 - 20$ [71, 83].

To model the wall friction velocity field, we generate initially a field without spatial correlations (delta-correlated in space) but presenting a temporal correlation obtained by the resolution of a stochastic differential equation. Then, in a second step this field is convoluted with a spatial kernel to impose the adequate spatial correlation prescribed by the shape of the convolution kernel. The last step consists in taking the exponential of the field to obtain a log-normal field.

According to this procedure, we have:

$$f(t,\mathbf{x}) = \int G(\mathbf{x} - \mathbf{x'})\chi(t,\mathbf{x'})d\mathbf{x'} \tag{3.10}$$

where the stochastic process with delta-correlation in space is noted χ and G is a convolution kernel with $\mathbf{x}(x_x, x_\theta)$ and $\mathbf{x'}(x'_x, x'_\theta)$ position vectors. Note that the spatial autocorrelation of f is only set by G since χ is delta-correlated $\rho_f(\mathbf{x}) = G \star G$ where $\star$ denotes the convolution product.

To deem the advection, we decompose the convolution kernel into two parts: $G = G_s \star \delta(\mathbf{x} - \mathbf{u}_{adv}t)$, the second contribution representing the spatial translation due to the advection at a constant speed $\mathbf{u}_{adv}$. We propose to model the spatial contribution G_s as:

$$G_s(\mathbf{x}) = \beta \exp\left[-\left(\frac{x_x}{L_{cx}}\right)^2 - \left(\frac{x_\theta}{L_{c\theta}}\right)^2\right] \tag{3.11}$$

and β is a pre-factor for normalization purpose. L_{cx} and $L_{c\theta}$ are the characteristic lengths in the streamwise and the spanwise directions respectively and are set to $L_{cx} = 1000\ell^*$ and $L_{c\theta} = 100\ell^*$. In the current study, we take the advection velocity in the streamwise direction with a magnitude set to $u_{adv} = 20\langle u^* \rangle$.

We consider that the field χ is the solution of a stochastic differential Langevin equation defined and solved for each cell in the domain and at each time step:

$$d\chi = -\frac{\chi - \mu_\chi}{T_c}dt + \sqrt{\frac{2\sigma_\chi^2}{T_c}}dW \tag{3.12}$$

where dW is an increment of the Wiener process, a normal variable generated for each cell at each time step with $< dW >= 0$ and $< dW(t, \mathbf{x})dW(s, \mathbf{x'}) >= \delta(t - s)\delta(\mathbf{x}\text{-}\mathbf{x'})$. In equation (3.12) the parameter μ_χ and σ_χ^2 are respectively the mean and the variance of χ, while T_c corresponds to the correlation time of χ. Here we have estimated the lifetime of the wall friction events as $T_c = L_{cx}/u_{adv}$. From (4.24) the moments of f and χ are related, therefore we impose for μ_χ and σ_χ^2:

$$\mu_\chi =< f > (\int G(r)dr)^{-1} = -\frac{1}{2}\ln(1 + \alpha_h)(\int G(r)dr)^{-1} \tag{3.13}$$

$$\sigma_\chi^2 =< f'^2 > (\int G^2(r)dr)^{-1} = \ln(1 + \alpha_h)(\int G^2(r)dr)^{-1} \tag{3.14}$$

Taking advantage of the periodicity in the x and θ directions, we compute the convolution product in the spectral space through the Fourier transform making the calculation much faster:

$$\mathcal{F}(f) = \mathcal{F}(G_s)\exp(i\mathbf{k}.\mathbf{u}_{adv}t)\mathcal{F}(\chi) \tag{3.15}$$

with $i^2 = -1$ and $\mathbf{k}$ the wave vector. The inverse Fourier transform allows us to obtain f and finally the friction velocity field is as follows:

$$u^* =< u^* > exp(f) \tag{3.16}$$

We present in figure 3.8 a realization of the field obtained with this stochastic model (see also the movie in supplementary materiel). We observe that the model reproduces elongated structures moving with the prescribed velocity $\mathbf{u}_{adv}$ as expected.

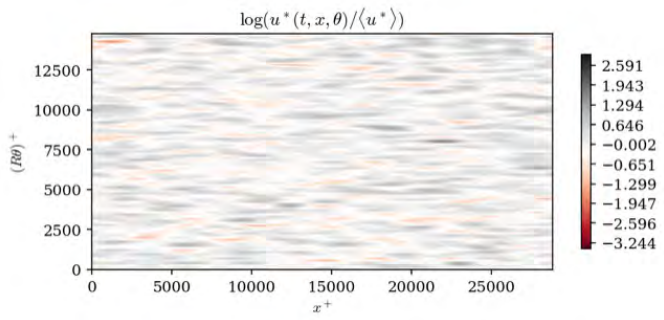

Figure 3.8: Realization of the stochastic process to predict the friction velocity field at the wall.

The main control parameter of the stochastic model is α_h which controls the magnitude of the imposed fluctuations. It is to note that α_h being the variance of $u^*/< u^* >$, setting $\alpha_h = 0$ restores the model with constant friction velocity presented in the previous section. To study the effect of α_h on the flow statistics, we carried out simulations of the turbulent pipe flow with an expected value of $Re = 100,000$ on the mesh $m2$ with $\alpha_h = 1$, $\alpha_h = 0.3$ and $\alpha_h = 0.07$. Figure 3.9 shows the mean velocity and the velocity fluctuations as a function of the distance from the wall normalized by $\langle u^* \rangle$ and ℓ^*. As expected, the stochastic IBM velocity is effectively acting on the velocity fluctuations. Increasing α_h leads to a significant increase of the rms of the three components of the velocity all across the pipe section. In particular, we notice the presence of a near-wall peak for both spanwise and radial components which was not present in the simulation without model. For $\alpha_h = 0.07$ we observe that the profile of the rms of the various velocity components are in good agreement with the experimental data, expected for the first two points next to the wall.

Adding fluctuations in IBM region enhances the shear stress and consequently it leads to a flattened mean velocity profile and causes a reduction of the bulk velocity. For the largest values of α_h it is clear that the level of fluctuation is too high and gives and under-prediction of the bulk velocity, but for $\alpha_h = 0.07$, the mean velocity appears to match fairly well the experimental data. This is confirmed in figure 3.10 that presents the relative error on the bulk velocity E_U defined by relation (3.8) as a function of α_h. For $\alpha_h = 0$, one recovers an overestimate of the bulk velocity with $E_U = -22\%$, as already obtained with the mean velocity model (3.6) (see figure 3.7), while for $\alpha_h = 0.07$, which is consistent with the value reported in [77], the relative error is less than 1%.

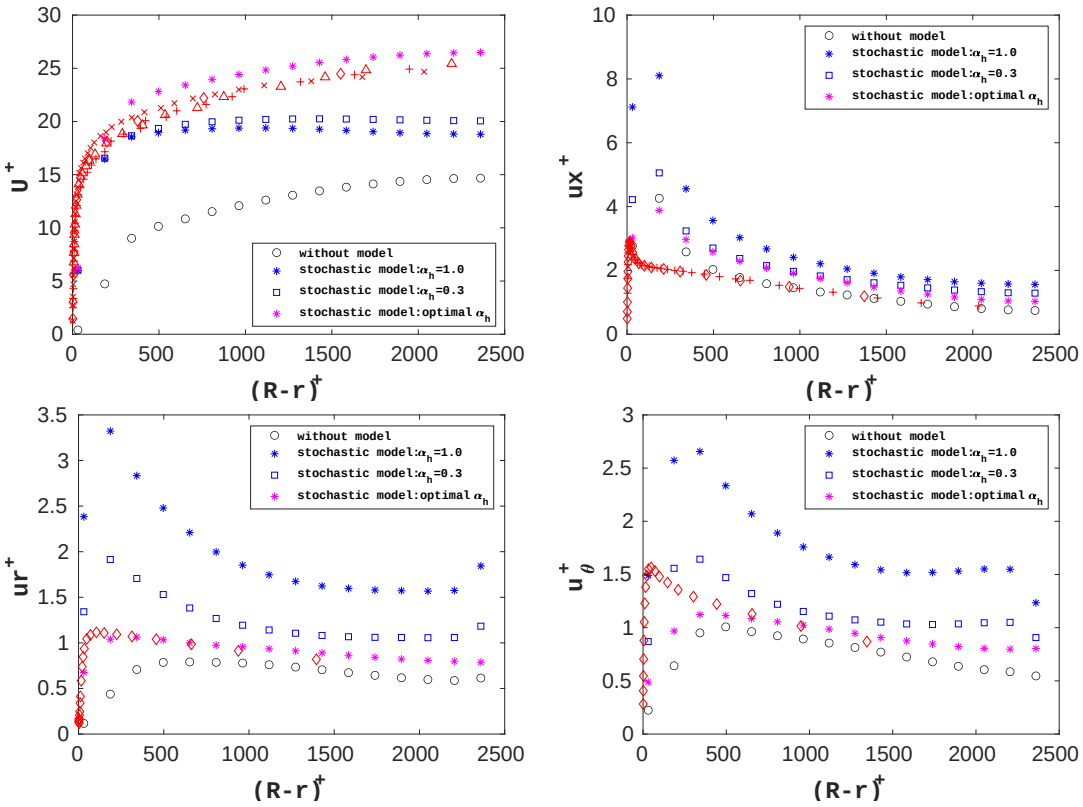

Figure 3.9: Mean velocity and rms using the stochastic model for $Re = 100,000$. Red symbols stand for the reference studies (see Table 3.1).

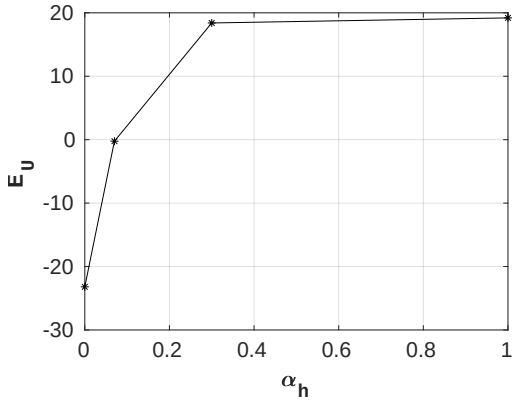

Figure 3.10: Relative error E_U on the bulk velocity as a function of the wall law coefficients.

3.6 Validation of the wall model for hybrid IBM-LES: turbulent pipe flow

3.6.1 Model comparison

We first compare the different modeling proposed in this work. The results are summarized in Fig. 3.11 in order to make a direct comparison between the basic IBM (without a wall model), the mean velocity model based on the log law and the

stochastic model. Flow statistics are reported for the value of $B = 0$ for the model (3.6) and $\alpha_h = 0.07$ for the model (3.9) that reproduces for each model the correct bulk velocity for the conducted simulations on mesh $m2$. These models are giving the same mean velocity profile and are providing a good agreement with previous data as well as the log law relation (3.6) and the power law relation (3.7) plotted in blue and red lines, respectively. As observed, the fluctuations can be adjusted thanks to the use of a stochastic model. In particular, the intensity of the peaks in the near wall region is improved: the peak is reduced in the streamwise direction while its magnitude is increased in the radial and azimuthal directions. The stochastic approach seems to provide a better prediction of the fluctuating flow structures along the three spatial directions.

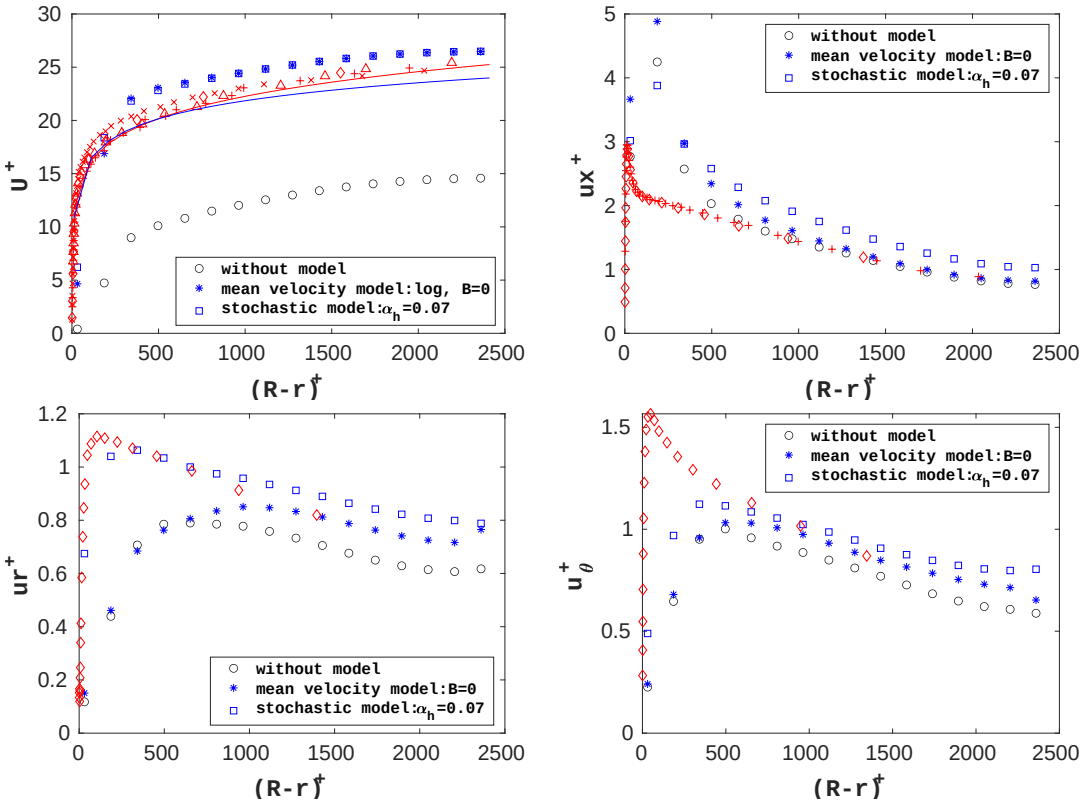

Figure 3.11: Comparison between the mean velocity models and the stochastic model for $Re = 100,000$. Red symbols stand for the studies of reference (see Table 1). Blue line: relation (3.6) for the "log law". Red line: relation (3.7) "power law".

3.6.2 Sensitivity of model parameters to grid resolution and Reynolds number

The previous analysis has been conducted for a selected Reynolds number $Re = 100,000$ and a given grid resolution (mesh $m2$). Each model has been optimized to provide the correct bulk velocity and optimized parameters have been proposed: $B = 0$, $A = 5.8$ and $\alpha_h = 0.07$ for the log law model, the power law model and the stochastic model, respectively. A similar investigation can be conducted for different Reynolds numbers and grid resolutions. The objective is now to discuss the effects of both the grid resolution and the pipe Reynolds number on the optimized values for

B, A and α_h. For that purpose, numerical simulations are carried out for the three Reynolds numbers $Re = 50,000$, $100,000$ and $500,000$ and the three meshes $m1, m2$ and $m3$. For each case, each model is considered and the corresponding model parameter (B, A or α_h) is adjusted in order to obtain the correct bulk velocity (with a relative difference on E_U less than 1%), while imposing a constant value to the mean pressure drop as specified before.
Figure 3.12 (left) reports the evolution of the optimized values of A and B as a function of the grid resolution for the three Reynolds numbers. Both A and B have to be increased when the mesh is getting coarser, because the underestimation of the bulk velocity is enhanced resulting in the need of larger solid velocity in the forcing inside the IBM wall region. A linear evolution with the grid size is observed for both A and B. The origin of the linear evolution for A (power law) needs to be adjusted for each Reynolds number while the linear fit of B (log law) is unchanged for the three different Reynolds numbers, outlining the relevance of the use of the log-law in the mean velocity model.
As shown in Fig. 3.12, the evolution of A can be simply described using the relation:

$$A = 20.5 \frac{\Delta}{R} + X(Re) \tag{3.17}$$

with the evolution of $X(Re)$ versus Re reported in Fig. 3.12 (right).
The evolution of B can be described using the relation:

$$B = 37.6 \frac{\Delta}{R} - 2.23 \tag{3.18}$$

Note that while the value of the coefficient B becomes negative for sufficiently fine mesh, the IBM velocity $v_{s,x}$ for $r^+ > 11$ remains positive. Indeed, for consistency the IBM velocity needs to tends to 0 as the mesh is refined.

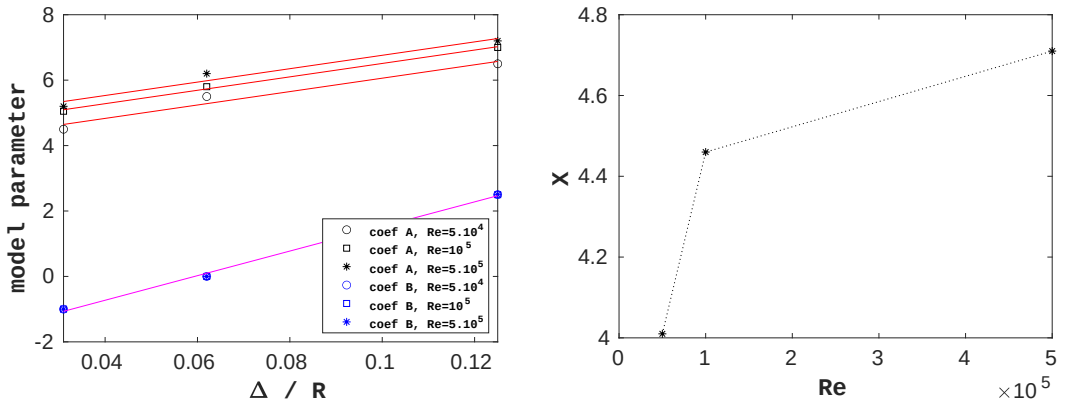

Figure 3.12: Optimal values for A and B as a function of the mesh resolution R/Δ for different Reynolds numbers Re (left). Lines stand for the linear fits 3.17 and 3.18. Evolution of $X(Re)$ (see relation 3.17) (right).

The variation of the parametr of the stochastic model α_h is reported in Fig. 3.13. α_h is found to decrease with the grid spacing. In fact, as the mesh gets coarser, the simulated bulk velocity is decreased and wall friction has to be reduced. This can be directly controlled with a reduction of the magnitude of the fluctuations imposed inside the IBM wall region. However, the same order of magnitude $\alpha_h = O(0.1)$ is

observed for the different Reynolds numbers and grid resolutions considered. A first rough estimate of the evolution of α_h can be described with:

$$\alpha_h = 0.00025 \left(\frac{\Delta}{R}\right)^{-2} \tag{3.19}$$

for the range of Reynolds number we considered.

The stochastic model is based on an instantaneous log law description ($B = 5$ being imposed) of the velocity inside the IBM wall thickness (see relation (3.9)). As shown above, changing B when using the log model only and α_h when using the stochastic forcing (B being set fixed) have both a clear impact on the bulk velocity. A better optimization of the combination of B and α_h in the stochastic model may certainly provide a better description of the fluctuation level and peak location.

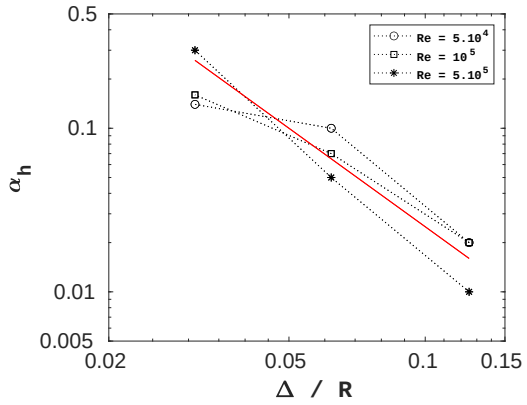

Figure 3.13: Optimal α_h as a function of the mesh resolution Δ/R for different Reynolds numbers Re. The solid red line represents the relation (3.19)

3.6.3 Flow streaks

The turbulent flow fields obtained with the different approaches are now compared. The Reynolds number is $Re = 100,000$, the mesh is $m2$ and numerical simulations with the optimized parameters ($B = 0$, $A = 5.8$ and $\alpha_h = 0.07$) are compared to the basic IBM wall forcing.

Figure 3.14 represents an instantaneous snapshot of the axial fluctuations u'_x normalized by the bulk velocity u_b at a section along the pipe axis. The fluctuations seem to have almost the same structures in the four cases. No noticeable difference can be observed and a zoom close to the wall is proposed in figure 3.15 where u'_x/u_b is plotted at a distance of 100 ℓ^* away from the wall.

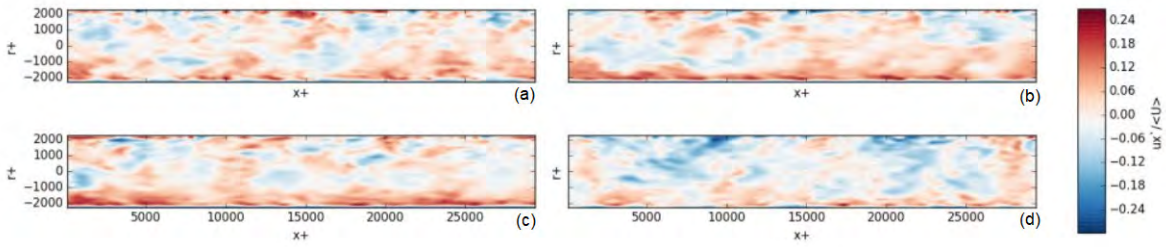

Figure 3.14: Normalized instantaneous axial fluctuations u'_x/u_b. (a) basic IBM wall forcing, (b) mean velocity model: log law, (c) mean velocity model: power law, (d) stochastic model.

Figure 3.15 clearly points out a difference in the streaks organization close to the wall. As shown, basic IBM forcing, log law and power law models provide similar fluctuation structures close to the wall. The streaks in those cases are somehow suppressed yielding to a reduced turbulence intensity. On the opposite, the stochastic model enhances the flow fluctuations and typical highspeed and lowspeed streaks are observed in figure 3.15 (d).

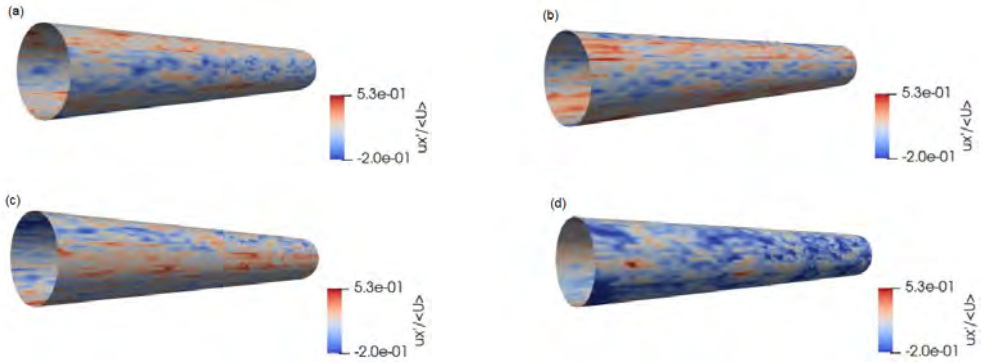

Figure 3.15: Streaks observation. Normalized instantaneous axial fluctuations u'_x/u_b at the distance $100\ell^*$ away from the wall. (a) Basic IBM wall forcing, (b) mean velocity model: log law, (c) mean velocity model: power law, (d) stochastic model.

We also compare the impact on the LES resolution of the different IBM wall models. For that purpose the total viscosity $\nu_{total} = \nu + \nu_T$ is considered. Figure 3.16 reports an instantaneous field of ν_{total} made dimensionless by the fluid viscosity ν in a pipe section. As shown, the intensity of ν_t is enhanced when using the stochastic model. From a LES modeling point of view, this can be explained by the induced effect of the fluctuations on the strain rate tensor and the local Smagorinsky coefficient C_s used to calculate the sub-grid viscosity ν_T.

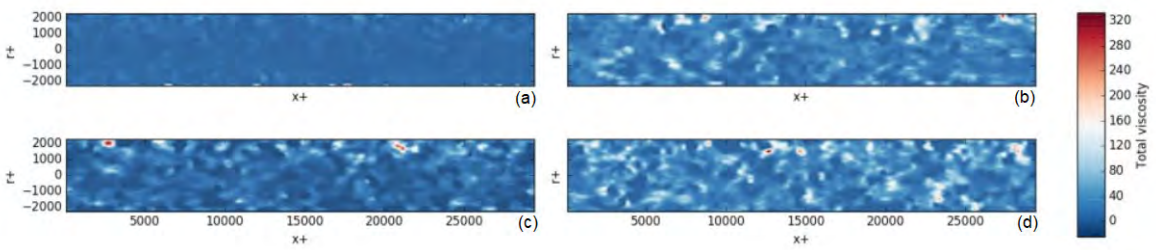

Figure 3.16: Normalized total viscosity ν_{total}/ν: (a) basic IBM wall forcing, (b) mean velocity model: log law, (c) mean velocity model: power law, (d) stochastic model.

3.6.4 Effect of the models on the pressure

Finally, it is worthwhile to check the effect of the models on the pressure. For that, we plot the mean and rms of the pressure for $Re = 50,000$ and compare it to a previous DNS [85] of $Re = 37,700$. Figure 3.17 represents the pressure normalized by $0.5\rho u^{*2}$ in function of the distance from the wall. The mean pressure profile is reported by considering the mean wall pressure as the reference pressure, we can see that the simulations without and with the mean velocity model give closer results to the DNS both for the mean as well as the rms of the pressure. However, the stochastic model with the optimal α_h which is able to reproduce the correct bulk velocity introduces higher pressure fluctuations. Figure 3.18 shows the normalized instantaneous pressure for each case, a different distribution and higher extreme values for the pressure are obtained with the stochastic model. Further investigations on this model points that the observed pressure jumps are a result of potential jumps when solving the Poisson equation and that the values increases with the incease of α_h. This is attributed to the fact that the imposed local solid velocity in the IBM forcing is not divergence free and is varying roughly both in time and especially in space.

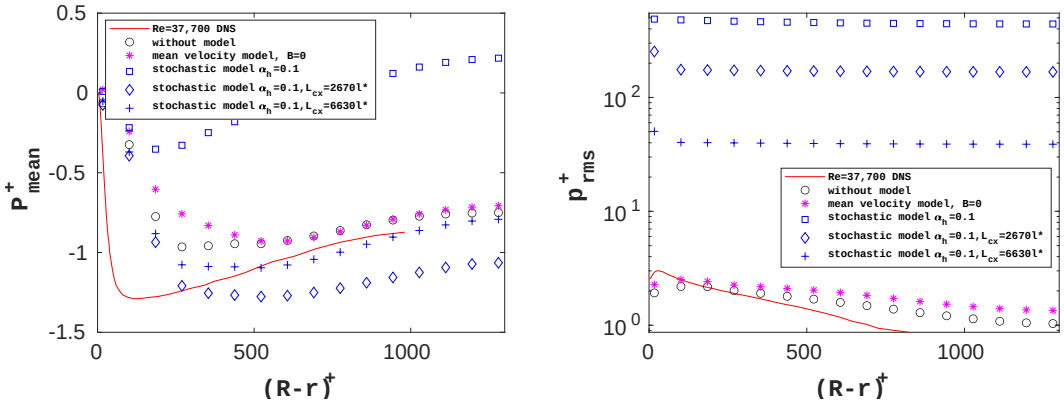

Figure 3.17: Pressure statistics for $Re = 50,000$

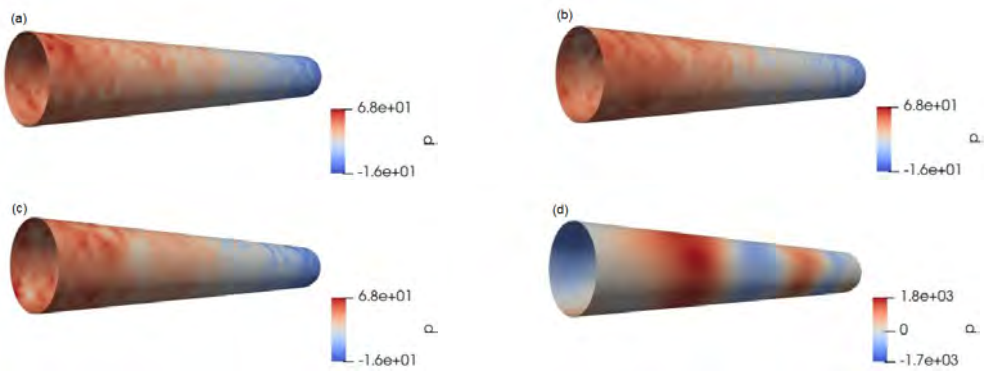

Figure 3.18: Normalized instanteneous pressure for $Re = 50,000$ at $100l^*$ away from the wall. (a) Basic IBM wall forcing, (b) mean velocity model: log law, (c) mean velocity model: power law, (d) stochastic model.

Now, going back to our stochastic model, two parameters are linked to the space-time correlation, namely, T_c and L_{cx}. Simulations considering a fixed α_h have shown that acting only on T_c does not influence on the pressure, while using higher length correlation L_{cx}, the mean pressure is corrected, the rms are reduced, the instantanous pressure is impoved but the bulk velocity is overestimated. This is illustrated via the pressure statistics in Fig. 3.17 and figure 3.19 which compares the normalized instantaneous pressure field when taking $L_{cx} = 2570l^*$ and $L_{cx} = 6630l^*$ instead of $L_{cx} = 1000l^*$ (Fig.3.18-d). An improvement is spotted with the highest correlation length but again the error on the bulk velocity surpasses 1%.

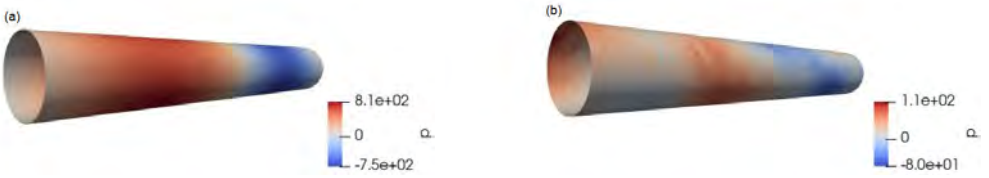

Figure 3.19: Normalized instanteneous pressure for $Re = 50,000$ at $100l^*$ away from the wall using the stochastic model $\alpha_h = 0.1$. (a) $L_{cx} = 2570l^*$, (b) $L_{cx} = 6630l^*$

We conclude that increasing the correlation length decreases the pressure fluctuations and increases the bulk velocity, and if we want to recover (decrease) in this case the mean velocity, we will have to increase α_h which will directly raise the pressure fluctuations. Finding the couple (α_h, L_{cx}) which can reproduce in the same time both the correct bulk velocity and the pressure fluctuation does not seem to be that easy and quick. This is why we consider as a perspective of this work the development of a stochastic zero divergence velocity vector with keeping α_h as the model parameter and aiming at getting an intermediate fluid velocity close to the one respecting the zero divergence condition.

3.7 Conclusion

A hybrid IBM/LES method has been presented addressing the challenge to simulate high Reynolds number pipe flows on coarse Cartesian meshes. Firstly, IBM method

is used to simulate a laminar pipe flow and numerical results demonstrate a second order convergence to the exact solution. By introducing the correct solid velocity condition in the forcing term inside the IBM wall thickness, the convergence is remarkably improved and the method inderlines its efficiency. Then, turbulent pipe flows of Reynolds numbers in the range 50,000 to 500,000 are considered coupling the IBM method and a LES solver. As expected, the use of a coarse grid resolution does not allow to reproduce both the mean bulk velocity and the fluctuations. Extending the IBM wall modeling introduced for the simulation of the laminar pipe flow, an IBM wall forcing scheme is developed based on the classical turbulent wall laws, namely the log-law and the power law, able to give the mean velocity profile. We show that adjusting the control parameters of these two models allows to recover the correct bulk velocity and mean velocity profile. With the aim of improving the fluctuations and spatial distribution of streaks inside the pipe, the log law modeling is coupled with a stochastic wall model to generate an unsteady and non-uniform forcing within the IBM wall thickness. The level of fluctuation is then corrected close to the wall approaching the reference data. The effect of both the Reynolds number and grid resolution are then discussed and empiric correlations for the model parameters are established.
We can consider further development of the stochastic modeling for the velocity in the IBM wall region, in particular reconstructing the three components of the free divergence velocity field should ameliorate the prediction of the velocity and pressure rms in the near wall region.
The main interest of the hybrid IBM/LES presented here is to demonstrate that simulations coupling LES and IBM can be performed for highly turbulent pipe flows with a coarse Cartesian resolution though a wall model. This is of great interest for the simulation of high Reynolds number flows not only in simple geometries but also in complex geometries. We can finally say that all the CFD development are done and that the solver is fully ready to simulate the inline fluid separation.

Chapter 4

CFD simulations of swirling single-phase flow in the separator

4.1 Introduction

The separator is designed and meant to be used for two-phase flows however it is interesting or even essential to first investigate single-phase flow especially that the swirling flow generated by the swirl element is complex and was not extensively studied. Moreover the simulations do not require all the hybrid approach reducing then the computational cost.
Therefore, in this chapter, we first introduce the design of the swirl element and give some general aspects of the swirling flow generated by the separator namely the swirl number, the centrifugal force and the flow split. Then, a mesh sensitivity study is carried out to find the optimal mesh size to be used in the rest of this PhD work. An original numerical procedure is later introduced to simulate the valve condition at the pick-up tube and finally we present the results of our numerical simulations of swirling single-phase flow in the separator for different Reynolds numbers and flow splits.

4.2 Description of swirling flow in the separator

4.2.1 Swirl element

The inline fluid separation, as briefly introduced in the first chapter, consists in separating two fluids of different densities by generating a centrifugal force. This force pushes the heavy phase towards the outer wall while leaving the light one in the center to be sucked up by a pick-up tube installed at the outlet of the pipe. The particularity of this separation technology comes from the way this centrifugal force is generated, a static swirl element is designed to create a swirling flow from the incoming axial flow. In fact, the swirl element has blades (or vanes) on its surface which deflect the flow and thus convert part of the axial velocity into an azimuthal velocity. The first reported separator prototype was modelled by Dirkzwager [12] in 1996 then Delfos [13] updated the swirl element previousely used by [12] and recently Slot [1] reconstructed new swirl element geometries. In each of the previous studies, the objective was to optimise the shape of the swirl element which will yield to a reduction of the pressure drop and an increase of the separation efficiency. Figure

4.1 shows the key design features of the swirl element to wit: the nose section, the vane section and the tail section.

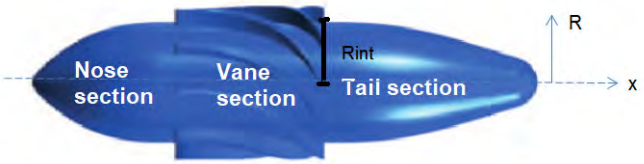

Figure 4.1: Layout of the swirl element with the definition of its different parts

In the current TOMOCON project and consequently this PhD work, since our focus is the investigation of separation and not the design itself, we will use directly one of the geometries created by Slot [1]. It is worth mentioning that each swirl element is characterized by a deflection angle. In fact, at the trailing edge of the vane section, the geometrical angle of deflection is formulated as:

$$\alpha_{def} = \arctan\left(\frac{u_{\theta,te}}{u_{x,te}}\right) \tag{4.1}$$

with $u_{\theta,te}$ and $u_{x,te}$ are the azimuthal and axial velocities at the trailing edge respectively which can eventually be expressed in function of the bulk velocity.
From mass conservation, we have:

$$u_{x,te} = u_b \frac{R^2}{R^2 - R_{int}^2} \tag{4.2}$$

with R_{int} is the radius of the internal vane section (see Fig. 4.1) calculated from the center of the pipe till the beginning of the blades, where there is no flow.
Similary, the conservation of the axial flux of the angular momentum in the vane section and after the swirl element is expressed as:

$$\int_{R_{int}}^{R} u_{x,te}\rho r u_{\theta,te} 2\pi r dr = \int_{0}^{R} u_b \rho r u_{\theta,0} 2\pi r dr \tag{4.3}$$

where $u_{\theta,0}$ is the azimuthal velocity right after the swirl element which depends on the radial position r.
By replacing $u_{x,te}$ from 4.2 in 4.3 and taking into account the angular momentum loss coefficient $c_{loss} \approx 0.5$ measured in [12] between the vane section and right after the swirl element, $u_{\theta,te}$ is:

$$u_{\theta,te} = \frac{3(R^3 - R_{int}^2)(R^2 - R_{int}^2)}{(1 - c_{loss})R^2} \int_{0}^{R} u_{\theta,0} r^2 dr \tag{4.4}$$

Now, it remains to determine $u_{\theta,0}$ to express $u_{\theta,te}$. From the experimental results of Dirkzwager [12], it was found that the radial distribution of the average-azimuthal velocity can be approximated by a Rankine vortex defined as:

$$u_\theta(x,r) = \begin{cases} U_\theta(x)\frac{r}{R_c} & \text{if } 0 < r < R_c \\ U_\theta(x) & \text{if } R_c < r < R \end{cases} \tag{4.5}$$

with $U_\theta(x)$ is an azimuthal velocity scale in each section x along the pipe, R is the pipe radius and R_c is the characteristic radius of the solid-body rotation in the

Rankine vortex.
We replace 4.5 in 4.4, we get $u_{\theta,te}$:

$$u_{\theta,te} = U_\theta(0)\frac{(R^3 - 1/4R_c^3)(R^2 - R_{int}^2)}{(1 - c_{loss})R^2(R^3 - R_{int}^3)} \tag{4.6}$$

Finally, from 4.2 and 4.6, the angle of deflection defined by 4.1 is:

$$\alpha_{def} = \arctan\left(\frac{U_\theta(0)(R^3 - 1/4R_c^3)}{u_b(1 - c_{loss})(R^3 - 1/4R_c^3)}\right) \tag{4.7}$$

In the work of Slot [1], designing a swirl element consisted in fixing a value for the deflection angle and this is what makes the difference between the prototypes used in [1][5], higher α_{def} leads to higher swirl intensity, the swirl element tends to be stronger. In this PhD work, the swirl element used is characterized by a an internal radius $R_{int} = 0.04m$ and a deflection angle $\alpha_{def} = 63°$ and the separator has a radius of $R = 0.046m$.

4.2.2 Swirl number

The intensity of swirling flows in general can be quantified by a swirl number S. This number is nothing else but the dimensionless angular momentum in the flow. In our case, for instance, the intensity of the swirl is 0 upstream the swirl element since the azimuthal velocity is zero then it goes up in the vane section and decreases downstream as we go far from the swirl element.
In the present work, we define the swirl number as the axial flux of the angular momentum normalized by the bulk velocity and the pipe radius. It is expressed as [12][1]:

$$S(x) = \frac{\int_A \rho u_x u_\theta r dA}{\rho R u_b^2 A} \tag{4.8}$$

with u_x, u_θ, u_b are the axial, azimuthal and bulk velocities respectively, r is the radial position, R is the pipe radius, ρ is the fluid density and A is the area of the pipe cross-section.

This number varies as a function of x. From velocity measurements, Dirkzwager [12] calculted this swirl number downstream the swirl element and found that $S(x)$ has an exponential decay:

$$S(x) = S_0 \exp\left(-C_{sw}\frac{(x - x_0)}{D}\right) \tag{4.9}$$

with S_0 is the swirl number at the reference axial position x_0 usually located at the end of the tail section and C_{sw} is a swirl decay coefficient which depends on the pipe Reynolds number $Re = 2Ru_b/\nu$, the swirl element and the wall roughness. Figure 4.2 shows the variation of the swirl decay coefficient denoted by β in function of Reynolds number from the measurement of Steebergen [4] on the same swirl element as used in [12]. Scattered of values for swirl decay coefficients are observed yet they almost all tend to decrease with the increase of Reynolds number. The typical order of magnitude of C_{sw} is between 0.01 and 0.7. From numerical simulations, Slot [1] plotted the swirl number along the separator for a stronger swirl element and found the same exponential decay.

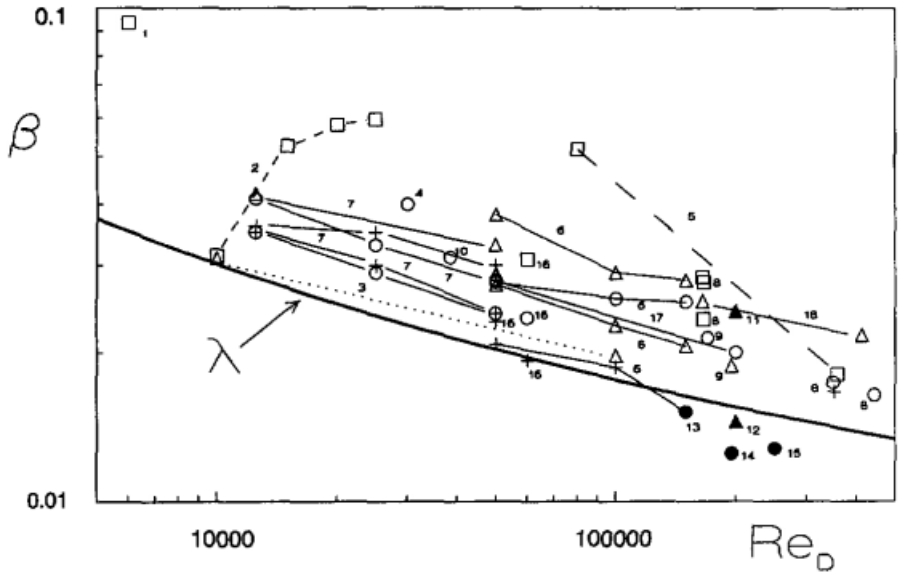

Figure 4.2: Swirl decay coefficient C_{sw} by [4] denoted here by β, the lines connect measurements done on the same set-up

4.2.3 Centrifugal force

The centrifugal force per unit of mass, generated by the swirl element, which is the driving force of the separation process is expressed as:

$$f_c = \frac{u_\theta^2}{r} \tag{4.10}$$

with u_θ is the azimuthal velocity and r is the radial position.
Slot [1] compared the time θ-averaged centrifugal acceleration $\frac{u_\theta^2}{r}$ to the gravity acceleration g and showed that for a Reynolds number of 200,000 and using a stronger swirl element characterized by $\alpha_{def} = 73°$, the force generated can reach $1{,}200g$.
Furthermore, the time θ-averaged centrifugal force can eventually be linked to the averaged radial pressure gradient. In fact, if we consider the time θ-averaging of Navier-Stokes equations in the radial direction in cylindrical coordinates expressed as:

$$\frac{\partial u_r}{\partial t} + u_r\frac{\partial u_r}{\partial r} + \frac{u_\theta}{r}\frac{\partial u_r}{\partial \theta} + u_x\frac{\partial u_r}{\partial x} - \frac{u_\theta^2}{r} = -\frac{1}{\rho}\frac{\partial p}{\partial r} + \nu\left[\frac{\partial^2 u_r}{\partial r^2} + \frac{1}{r}\frac{\partial u_r}{\partial r} - \frac{u_r}{r^2} + \frac{1}{r^2}\frac{\partial^2 u_r}{\partial \theta^2} + \frac{\partial^2 u_r}{\partial x^2} - \frac{2}{r^2}\frac{\partial u_\theta}{\partial \theta}\right] \tag{4.11}$$

This equation can be simplified by neglecting u_r in front of u_θ and u_x. The remaining terms which are time and θ-averaged lead to:

$$\frac{u_\theta^2}{r} \approx \frac{1}{\rho}\frac{\partial p}{\partial r} \tag{4.12}$$

showing the direct relation at first order between the mean centrifugal acceleration and the radial pressure gradient.

4.2.4 Flow split

At the exit of the separator, two outlets can be distinguished, one for the pick-up tube which is supposed to recover the core, we call it then the Light Phase Outlet (LPO) and the other outlet that is the surrounding annular region between the pipe and the pick-up tube from where the heavy phase exits and we therefore call it the Heavy Phase Outlet (HPO) (see Fig. 4.3). The same notation will be used for single-phase flow to refer to the outlet of the pick-up tube even though we do not have two separate phases.

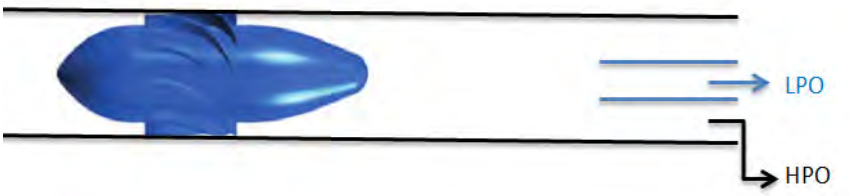

Figure 4.3: Sketch of HPO and LPO

Following this configuration, we introduce the inlet volumetric flow rate Q_{inlet} which is the total flow rate, the volumetric flow rate at the light phase outlet Q_{LPO} and the volumetric flow rate at the heavy phase outlet Q_{HPO}. The ratio between Q_{LPO} and Q_{inlet} is called the flow split:

$$FS = Q_{LPO}/Q_{inlet} \tag{4.13}$$

This parameter FS can also be interpreted as the condition on the valve acting on the pick-up tube. For instance, $FS = 0.5$ corresponds to a situation when the valve allows the pick-up tube to recover half of the inlet flow rate. The effect of the flow split on the velocity profile was studied numerically [1] and experimentally [5]. Both studies have shown that only the central part of the radial distribution of the axial and azimuthal velocities across the separator section close to the pick-up tube is affected, in this region, the velocities increases with the increase of the flow split.

4.3 Mesh sensitivity

The objective of conducting a mesh sensitivity analysis is to find the optimal mesh size which is simultaneously less demanding in terms of the total cells number and capable of capturing the swirling flow features. Therefore, we consider 3D simulations of single-phase flow using three mesh sizes. The numerical domain is a box of size $L_x \times L_y \times L_z = 0.92m \times 0.104m \times 0.104m$ made of $N_x \times N_y \times N_z$ cells. The mesh is regular with uniform cell distribution of width Δ in all directions.

Mesh	m1	m2	m3
R/Δ	20	40	80

4.3.1 Qualitative convergence

First, qualitatively from Fig. 4.4, the visualization of the contours α_{IBM} shows the effect of the grid size on the description of the swirl element, In fact, at the vane

section (see Fig. 4.5), we can notice that for the coarse mesh $m1$, the resolution of the tip of the blades is lower, their length is reduced as well as their curvature. This influences directly the flow deflection and the swirl intensity. As we refine the mesh, the resolution becomes higher.

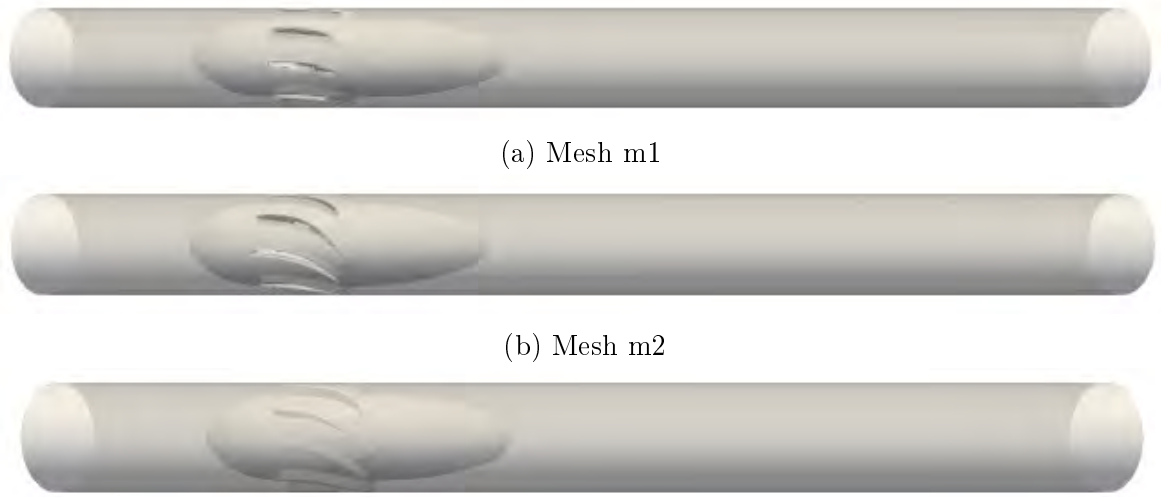

(a) Mesh m1

(b) Mesh m2

(c) Mesh m3

Figure 4.4: Visualization of the separator on three different meshes

Figure 4.5: Vizualization of the swirl element on three different meshes: m1 (left), m2 (middle), m3 (right)

On the three considered meshes, we perform single-phase flow simulations in the separator for Reynolds number $Re = 2Ru_b/\nu = 200,000$ (R is the pipe radius, ν is the fluid kinematic viscosity and u_b is the bulk velocity). To ensure that the turbulence at the inlet of the separator is fully developped, we impose at each time step an instantenous velocity field obtained from a turbulent pipe flow simulation with the same Reynolds number $Re = 200,000$ on the same mesh size. (OX) is the separator axis. Figure 4.6 illustrates the streamlines of the flow using the three meshes. With meshes $m2$ and $m3$, the swirling feature is more highlighted and by comparing the velocity at the vane section, we can see that the maximum velocity attained on the coarse mesh $m1$ is lower than the one on the other meshes. This is due to the resolution of the blades which generates the swirling flow.

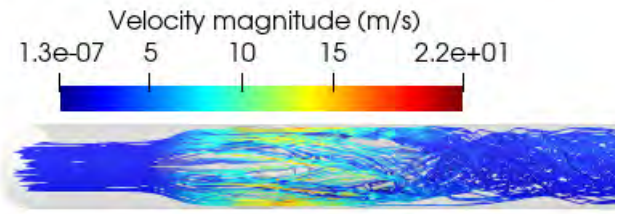

(a) Mesh m1

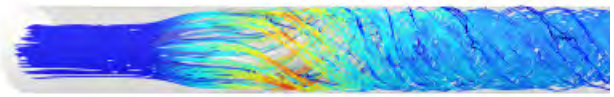

(b) Mesh m2

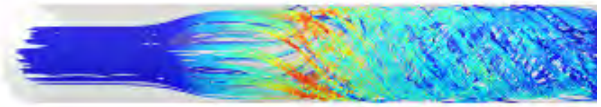

(c) Mesh m3

Figure 4.6: Streamlines of single-phase flow for $Re = 200,000$ on three meshes.

From this qualitative comparison, we can already estimate the following subsection 4.3.2, the convergence of the mesh sensitivity is quantified based on the deflection angle.

4.3.2 Quantitative convergence

From subsection 4.3.1, since the mesh resolution has an influence on the blade description and consequently on the deflection angle. We will evaluate the mesh convergence through the calculation of this angle. By postprocessing the numerical results from the three presented single-phase flow simulations, the azimuthal velocity U_θ right after the swirl element equals $2m/s$, $5.7m/s$ and $6.01m/s$ for the meshes $m1$, $m2$ and $m3$ respectively, the bulk velocity is $u_b = 2.17m/s$. Then we can calculate the deflection angle using equation 4.7. The obtained value is compared to the theoritical value $\alpha_{def}^{geometrical} = 63°$ fixed by construction of the CAD. The deviation from $\alpha_{def}^{geometrical}$ is then expressed as:

$$E_{\alpha_{def}} = \frac{|\alpha_{def}^{geometrical} - \alpha_{def}^{simulation}|}{\alpha_{def}^{geometrical}} \tag{4.14}$$

In Fig. 4.7 , the deviation is plotted as a function of Δ/R. It is of order 60% for the coarse mesh, then it remarkably decreases to 1.77% by multiplying the number of cells by a factor of 2^3, the final error is 1.66% for the finnest mesh. We notice a fast convergence with the resolution, this result confirms the effect of the mesh resolution on the blades seen in subsection 4.3.1.

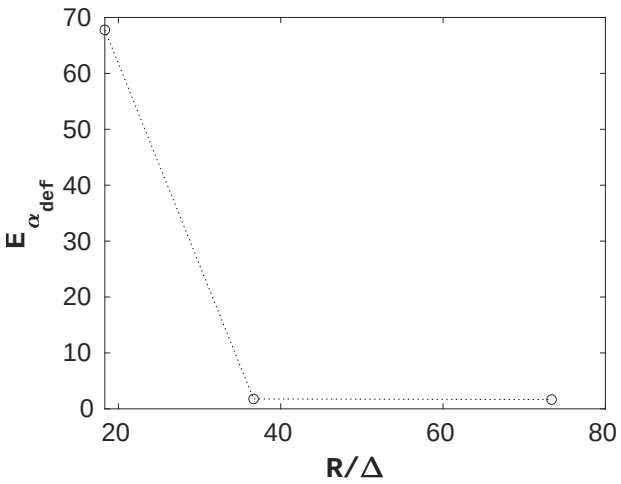

Figure 4.7: Deviation from the geometrical deflection angle as a function of the grid resolution

We conclude that the coarse mesh introduces an important error on the velocity and thus on the deflection angle. The deviation converges for the two other meshes, we will therefore choose the mesh size $m2$ for all the rest of the simulations.

4.4 Modelling of the valve condition in the pick-up tube

In addition to the pick-up tube installed at the outlet of the separator, a flow straightener is placed in the annular region between the pick-up tube and the pipe to eliminate the swirl in the HPO. In real situation, it is a porous medium which has a honeycomb form (see Fig. 4.8).

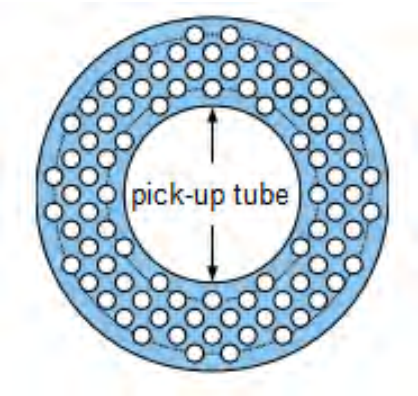

Figure 4.8: Sketch of a cross section of the flow straightener [5]

4.4.1 IBM for the flow straightener

To numerically model the flow straightener, Slot [1] defined a porosity in this region and added a momentum loss term to Navier-Stokes equations which depends on a loss coefficient that needs to be calibrated. In the current study, we propose to use Immersed Boundary Method (IBM) introduced in chapter 2 to model the flow

straightener. In fact, $(1 - \alpha_{IBM})$ can be seen as the opposite of the porosity. At every cross section x along the flow strainghtener, we can distinguish three regions for which an expression of α_{IBM} is attributed. Figure 4.9 represents how α_{IBM} varies across the section:
- $\alpha_{IBM} = 0$ inside the pick-up tube, no IBM forcing is added to Navier-Stokes equations.
- $0 < \alpha_{IBM} < 1$ at the pick-up tube wall, the expression 2.26 [38] is used based on the radius of the pick-up tube. The IBM forcing of Navier-Stokes is active.
- $\alpha_{IBM} = constant$ (0.2 in Fig.4.9) in the flow straightener. The IBM forcing of Navier-Stokes equations is active. The choice of how to set α_{IBM} in this region is discussed in the following subsection.
- $0 < \alpha_{IBM} < 1$ at pipe wall, the expression 2.26 [38] is again used based on the radius of the pipe. The IBM forcing of Navier-Stokes equations is active.
- $\alpha_{IBM} = 1$ outside the pipe since there is no flow.

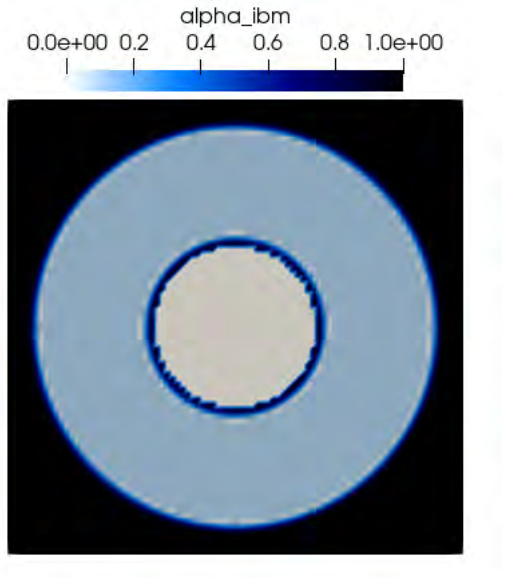

Figure 4.9: Visualisation of a cross section at the outlet of the separator with corresponding value of the IBM function

Therefore, IBM allows us to represent the porous region at the flow straightener, in the next subsection 4.4.2, we make use of this method to simultaneously implement the flow condition at the LPO.

4.4.2 Valve condition at the pick-up tube

In experiments, a valve is installed at the outlet of the pick-up tube and regulated by the control unit. It can be totally opened, closed or in between. The corresponding condition on the valve is what we eventually represent by the flow split FS previousely defined in 4.13.
From a CFD perspective, we will take advantage of the IBM forcing used to model the flow straightener to impose the condition on the flow split FS. De facto, we can control the flow rate going through the pick-up tube by setting the flow rate which

goes through the flow straightener. In this region the IBM force is expressed as:

$$f_{IBM,i} = \alpha_{IBM} \frac{v_{s,i} - u_i}{\Delta t} \tag{4.15}$$

with α_{IBM} is the solid volume fraction, Δt is the time step, u_i is the fluid velocity and $v_{s,i}$ is the expected velocity along the i direction $i = (x, y, z)$ with the objective to force the fluid outside the pick-up tube (inside the flow straightener in light blue in Fig. 4.9) to the imposed velocity.
For simplification purposes, if we neglect the spatial acceleration, the pressure gradient and the viscous term in the axial direction compared to the IBM force in the flow straightener, the Navier-Stokes equation becomes:

$$\frac{\partial u_x}{\partial t} \approx f_{IBM,x} \tag{4.16}$$

A first order differential equation is then obtained:

$$\frac{\partial u_x}{\partial t} \approx \alpha_{IBM} \frac{v_{s,x} - u_x}{\Delta t} \tag{4.17}$$

This reveals a characteristic time t_c:

$$t_c = \frac{\Delta t}{\alpha_{IBM}} \tag{4.18}$$

We are interested in the permenant regime with the objective that the fluid velocity in the flow straightener reaches the velocity $v_{s,x}$. The solution of equation 4.17 $u_x = v_{s,x}(1 - exp(-t/t_c))$ shows that the expected velocity is reached after some time steps. This means that we can directly set the condition on the flow split FS through $v_{s,x}$ and after a certain response time nt_c the condition is fulfilled. The steps to set the valve condition can be summarized as the following:
- Fix the FS target.
- Calculate the flow rate through the heavy phase outlet:

$$Q_{HPO} = Q_{inlet}(1 - FS) \tag{4.19}$$

- Calculate the solid velocity to impose in the IBM force as:

$$v_{s,x} = Q_{HPO}/(A_{pipe} - A_{LPO}) \tag{4.20}$$

with A_{pipe} and A_{LPO} the pipe and the pick-up tube areas respectively.

4.4.3 Validation of using IBM to impose the valve condition

To validate the proposed method in subsections 4.4.1 and 4.4.2, we perform simulations of single-phase flow in the separator for $Re = 50,000$ with a pick-up tube of radius $R_{pt} = 0.44R$. This value is fixed according to the experimental set-up in TU Delft. The pick-up tube is of length $2.6R$ and placed after the swirl element at a distance of $9R$. Two values of α_{IBM} in the flow straightener are tested to wit: 0.01 and 0.02, this corresponds respectively to two characteristic times tc: 1.0 and 0.5 and for each of t_c, two conditions on the flow split

are simulated: $FS = 0.5$ and $FS = 0.3$. In short, four simulations are done: $(FS = 0.5, t_c = 1), (FS = 0.5, t_c = 0.5), (FS = 0.3, t_c = 1), (FS = 0.3, t_c = 0.5)$. Figure 4.10 depicts the streamlines in the separator for the two cases $FS = 0.5$ (a) and $FS = 0.3$ (b) for the characteristic time $t_c = 1$. We see that in both cases the swirling flow is damped in the HPO where the streamlines are parallel to the axial direction and this is the effect of the flow straightener. Furthermore, in comparison to $FS = 0.5$, more fluid goes through the HPO for $FS = 0.3$ since the pick-up tube recovers only 30% of the inlet flow rate.

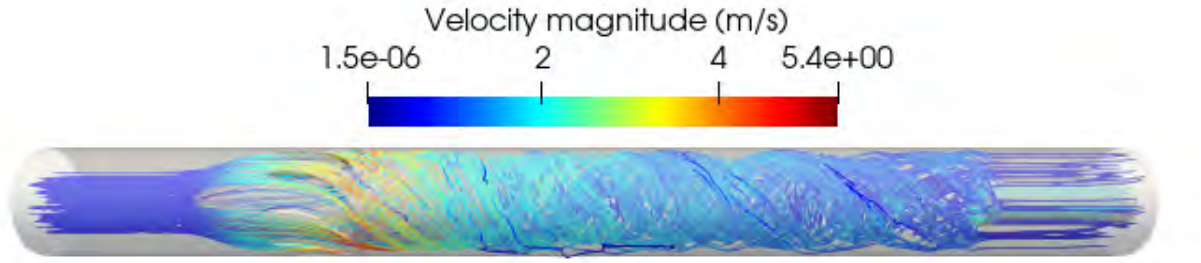

(a) $(FS = 0.5, t_c = 1)$

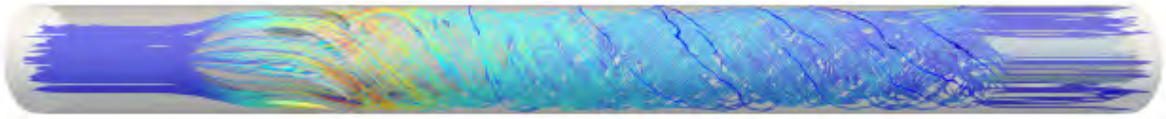

(b) $(FS = 0.3, t_c = 1)$

Figure 4.10: Streamlines of swirling single-phase flow for $Re = 50,000$ in the separator for two flow splits FS

Figure 4.11 represents the velocity contours in a cross section both at the pick-up tube and right after the swirl element. As expected, the flow rate in the LPO is higher when imposing a flow split of $FS = 0.5$ than that of a flow split $FS = 0.3$. Moreover, the ratio between the velocities at the center of the pick-up tube scales very well with the ratio of their flow splits respectively. In comparison with the flow at a cross-section right after the swirl element (see Fig.4.11c), we can see that the swirling flow is cancelled in the flow straightener. It is worth noting that for the same flow split, we got the same flow features for two different characteristic times t_c. More details are given in the next paragraph.

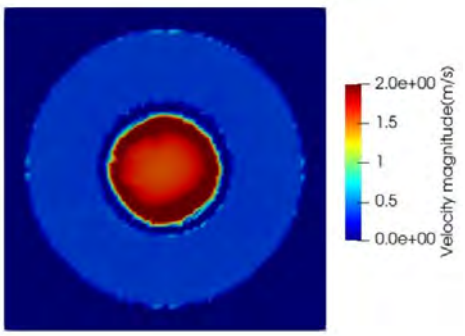

(a) $(FS = 0.5, t_c = 1)$

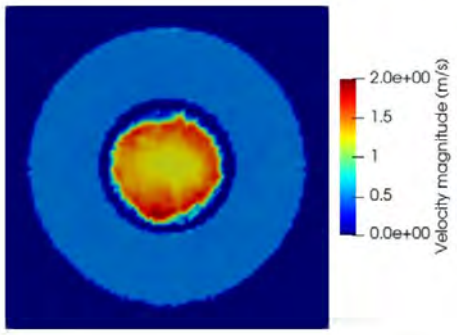

(b) $(FS = 0.3, t_c = 1)$

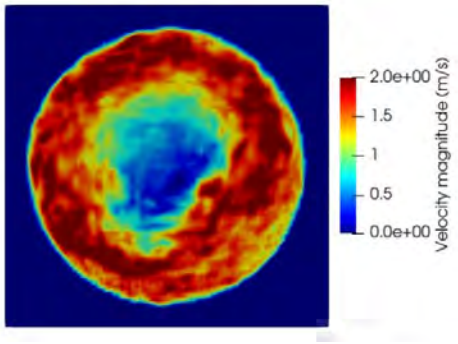

(c) Right after the swirl element

Figure 4.11: The velocity magnitude in (m/s) in cross-section at the pick-up tube for two FS: (a)=0.5, (b)=0.3 and right after the tail section of the swirl element (c)

Now, from the four numerical simulations, we calculate the flow split $FS(t) = Q_{LPO}(t)/Q_{inlet}$ over time. Figure shows its variation in function of the dimensionless time t/t_c. To begin with, we confirm that for the same flow split FS, varying t_c does not change the flow response to the imposed condition. Then, for both FS values, a transient regime is first observed then a permanent one is reached after $5t_c$, this defines the response time to the condition on $v_{s,x}$ and provides us with an interesting ability in CFD to mimic not only static conditions but also dynamic conditions on the valve if any. For instance, by just increasing α_{IBM} in the flow straightener or decreasing the time step Δt, the response time to the valve becomes faster and one can even follow the controller instruction. Finally, by resolving equation 4.17, we can express the temporal evolution of the flow split in function of the input parameters as:

$$FS(t) = \left(1 - \frac{v_{s,x}(A_{pipe} - A_{LPO})}{Q_{inlet}}\right)(1 - \exp(-t/t_c)) \tag{4.21}$$

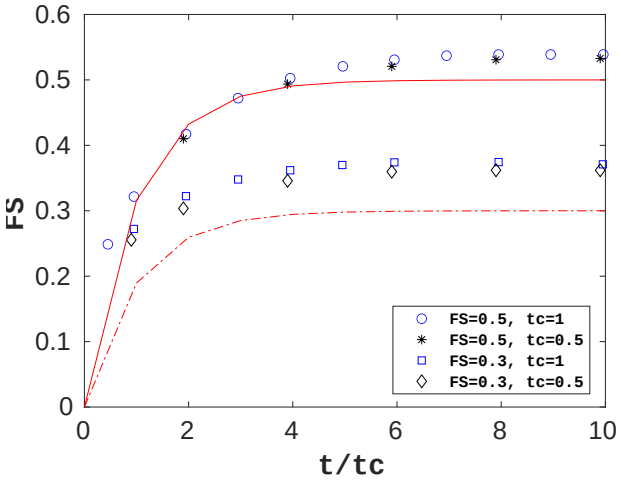

Figure 4.12: Evolution of the flow split over time: equation 4.13 for FS=0.5 (equation 4.13 for FS=0.3) is represented by a solid (dashed) red line, respectively.

A difference between the expected FS and the numerical results is observed which might be due to the flow streamlines inside the pick-up tube which are not totally parallel to the streamwise direction.
In general, we conclude that using Immersed Boundary Method to model the flow straightener and modifying the IBM forcing in this porous region is an efficient way to impose and control the condition on the flow split at the LPO and eventually mimic a dynamic change of this condition if necessary.

4.5 Numerical simulations of single-phase flow in the separator

In this section, we present the numerical results of 3D simulations of single-phase flow in the separator using the hybrid solvers: LES/IBM with a mean wall model. The numerical domain and boundary conditions are the same as decribed in 4.3 and the mesh is again $m2$. In subsections 4.5.1 and 4.5.5, the Reynolds number based on the bulk velocity $Re = Du_b/\nu$ is fixed to 50,000. The parameters used for the simulation are: $D = 0.092m$, $\nu = 10^{-6}m^2/s$ and $u_b = 0.54m/s$.

4.5.1 Velocity profiles

When the incoming axial flow is deflected by the swirl element, an azimuthal velocity is generated. After the swirl element, this velocity depends eventually on the radial position and decays along the axial direction. Therefore, to investigate its evolution, we choose sections after the swirl element and plot the radial distribution of the time and θ-averaged azimuthal and axial velocities normalized by the bulk velocity as a function of the radial position r normalized by the pipe radius R.

Figure 4.13 compares the azimuthal velocity at four different sections located at 0.08R, 2.5R, 5R, 7.5R after the swirl element. At $0.08R$, the azimuthal velocity reaches 2.8 times the bulk velocity generating thus a centrifugal acceleration 10 times larger than the gravity g. And as we move downstream from the swirl element, the azimuthal velocity decreases due to the wall friction but keeps the same radial

evolution which is 0 at the center of the separator, then a linear increase up to radial position noted R_c, an almost constant velocity and finally u_θ is 0 to respect the no-slip condition at the wall. The radial position R_c seems to shift towards the center of the pipe as we move along the separator with a conservation of the slope representing the ratio of the angular velocity over R_c in the solid-body rotation zone. The same behaviour is observed in the velocity profiles reported by [1, 5] using a stronger swirl element.

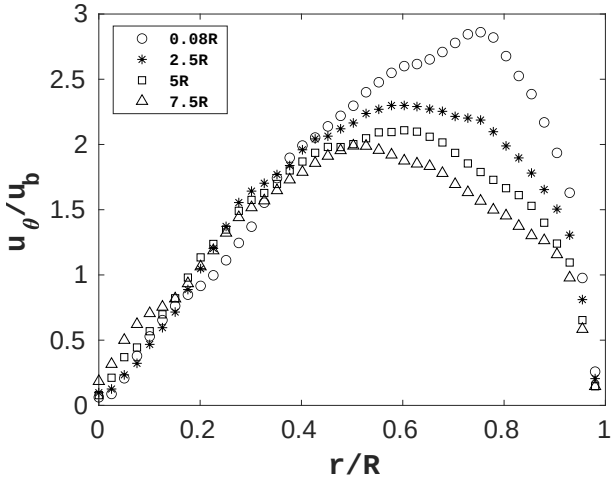

Figure 4.13: The radial distribution of the time-θ-averaged azimuthal velocity at four sections after the swirl element

Furthermore, the variation of the azimuthal velocity at each section is similar to Lamb-Ossen vortex or a more simple vortex: Rankine vortex. Figure 4.14 shows the Rankine profile fit to our simulations at $x = 0.08R$ of equation:

$$u_\theta(0.08R, r) = \begin{cases} 1.512\frac{r}{R_c} & \text{if } 0 < r < R_c \\ 1.521 & \text{if } R_c < r < R \end{cases} \tag{4.22}$$

It is decomposed of a solid body rotation for positions $r \leq R_c$ (equals 0.65R in this case) and a free vortex for $R_c \leq r < R$. This confirms once again the results of Dirkzwager in assuming the Rankine vortex for the velocity profile to determine the deflection angle.

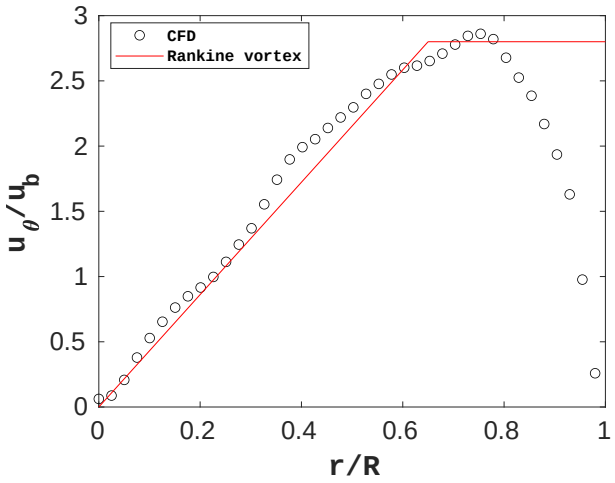

Figure 4.14: The Rankine vortex fit to the time-θ-averaged azimuthal velocity

Another interesting profile to check is the radial distribution of the axial velocity plotted in Fig. 4.15. The maximum attained by the axial velocity is $1.7u_b$ located around $r = 0.8R$ which is lower than the maximum azimuthal velocity $2.8u_b$. This is an expected results considering the value of the angle deflection 63° which is beyond 45° leading to more angular momentum than the axial one. Around the separator center, the velocity becomes negative, this a sign of the appearance of a reverse flow, a phenomenon which characterizes strong swirling flows in general [1][5]. The radial extension of the recirculation zone diminishes as we move away from the swirl element and this is illustrated in Fig. 4.16 which highlights regions with negative velocites in the separator.
In fact, the formation of a recirculation zone is caused by the pressure radial distribution in the separator over the concerned region (see Fig. 4.22). The pressure in the center close to the swirl element is lower than the one located at further axial positions. This defines the direction of the axial flow from high pressure zone (far from the swirl element) towards low pressure zone (close to the swirl element).

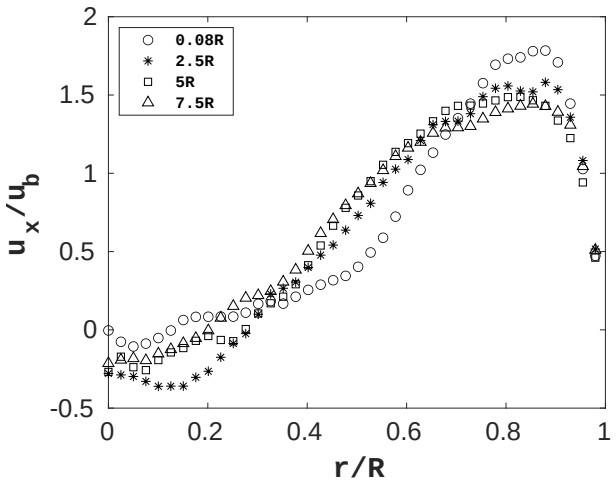

Figure 4.15: The radial distribution of the time-θ-averaged axial velocity at four sections after the swirl element

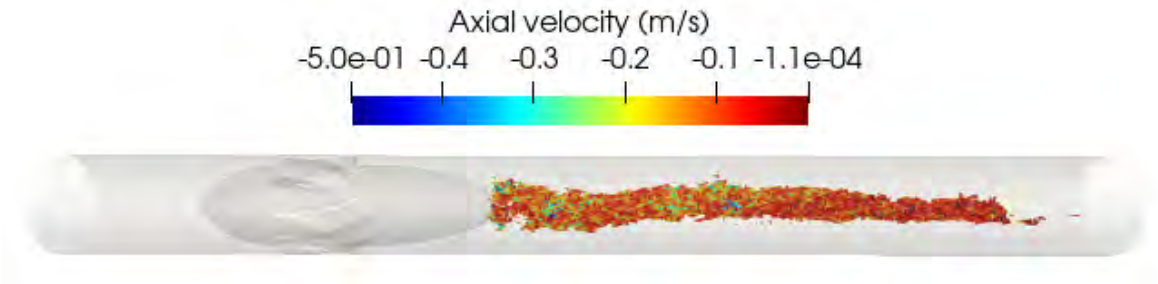

Figure 4.16: Instantenuous recirculation zone where the axial velocity is negative

In addition, figure 4.16 reveals an asymmetrical distribution of the velocity at each section along the separator, this comes from the asymmetrical shape of the swirl element which contains 9 blades. In Fig. 4.17 and 4.18 the time-averaged azimuthal and axial velocities along a line at the section $x = 0.08R$ are plotted and compared to the time θ-averaged velocities which suppose that the swirling flow is

axi-symmetrical. The velocities fluctuate slightly around the θ-average value. The extreme values are almost the same. However both the time-averaged axial and azimuthal velocities are not symmetrical with respect to the pipe center $(0, 0)$. The measurements of Campen [5] have also detected this behaviour.

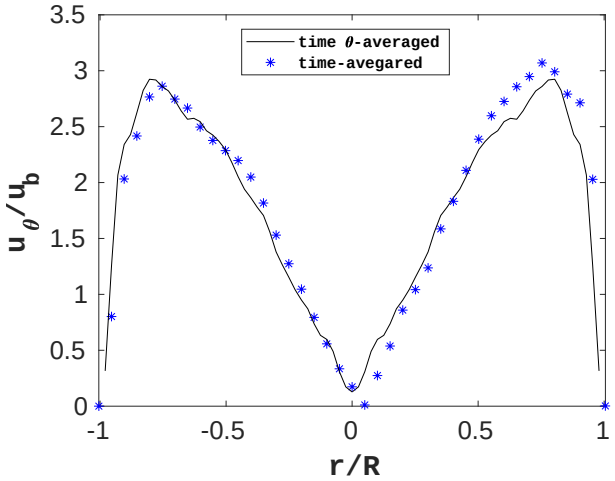

Figure 4.17: Time θ-averaged azimuthal velocity and time-averaged azimuthal velocity along a line across the section $x = 0.08R$

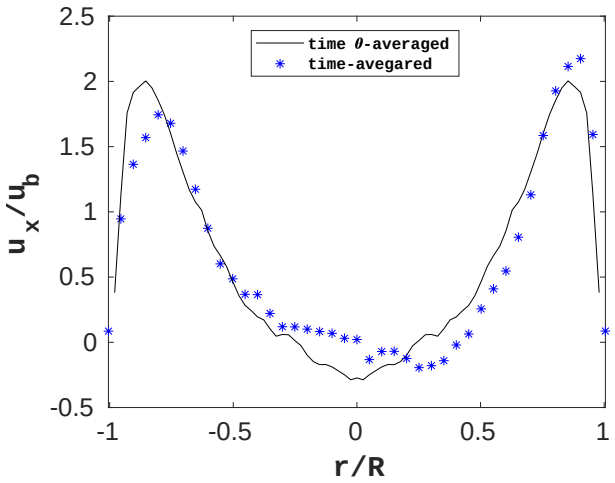

Figure 4.18: Time θ-averaged axial velocity and time-averaged axial velocity along a line across the section $x = 0.08R$

4.5.2 Swirl number profile

To quantify the intensity of the swirling flow, we calculate the swirl number using equation 4.8. Figure 4.19 shows its evolution along the separator as a function of the axial position normalized by the pipe diameter. Before the swirl element (up to $x/D = 2$), the centrifugal force is not yet generated, the swirl number is 0. Then, at the vane section, the flow is deflected and the azimuthal velocity is at its maximum, the swirl number reaches its highest value 3.4. From the tail section till the outlet of the separator, S decreases due to the wall friction. In the region after the swirl element, S is characterized by an exponentional decay following the empirical

correlation 4.9 given by Dirkzwager [12] for a swirl decay coefficient $C_{sw} = 0.15$. The curve is plotted in red in Fig. 4.19 and is defined as:

$$S(x) = 1.8 \exp(-0.15(x - 0.41)/D) \tag{4.23}$$

The swirl decay coefficient in this case is 0.15 which is a bit higher than the one reported in 4.2 for the same $Re = 50,000$. This is due to the difference of the swirl element geometry used for the separation and thus the swirl intensity which is one of the parameters influencing C_{sw}.

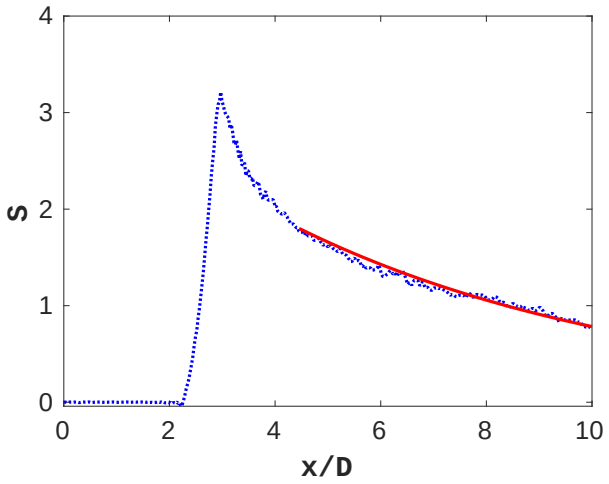

Figure 4.19: Evolution of the swirl number along the separator, solid red line represents the fit for the decay of S defined by 4.23

In the previous numerical simulation, the wall model proposed for hybrid LES-IBM and detailled in chapter 3 is activated to correct the velocity close to the wall, to see the effect of the wall model. The same simulation is performed without introducing a wall model. Figure 4.20 compares the evolution the swirl number along the separator obtained from the two simulations. The maximum of S located in the narrow zone of the vane section is slightly reduces when using the wall model, this can be justified by the fact that the latter acts on the axial velocity of the IB cells and not on the azimuthal one which is supposed to be the dominant one. Nevertheless, after the swirl element, the swirl number decays less strongly when using the wall model. In fact, the swirl decay coefficient C_{sw} decreases from 0.17 (without a wall model) to 0.15 (with a wall model).

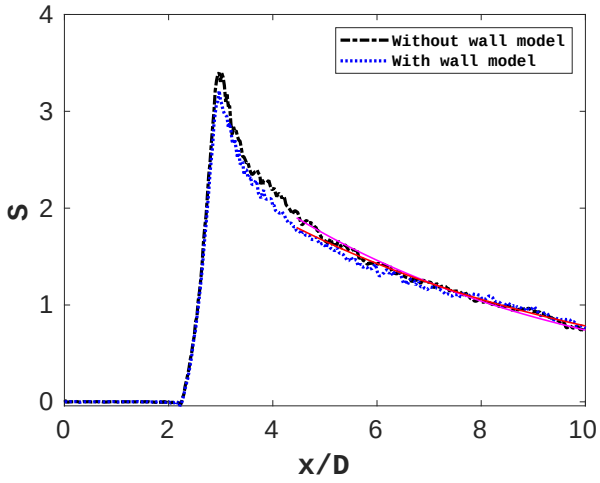

Figure 4.20: comparison of the swirl number in the two cases: without a wall model and with a wall model, the fits for the decay of S following 4.9 are represented with solid lines.

Figure 4.21 depicts the effect of the wall model on the time θ-averaged axial and azimuthal velocities at two different sections: 0.08R and 7.5R after the swirl element. Close to the latter, the simulation without a wall model gives a slightly higher negative axial velocity at the recirculation zone and the maximal azimuthal velocity is a bit decreased. However, at 7.5R after the swirl element, a significant improvement of the azimuthal velocity is obtained with the use of the wall model. The slope is conserved as observed by [1][5] unlike when no wall model is used. Furthermore, the decay of the centrifugal force is reduced and this is why the swirl decay coefficient C_{sw} is found to be lower than the one without the wall model. These results confirm the need of a wall model to perform the simulation to avoid the loss of the centrifugal force due to extra wall friction brought by the IBM method.

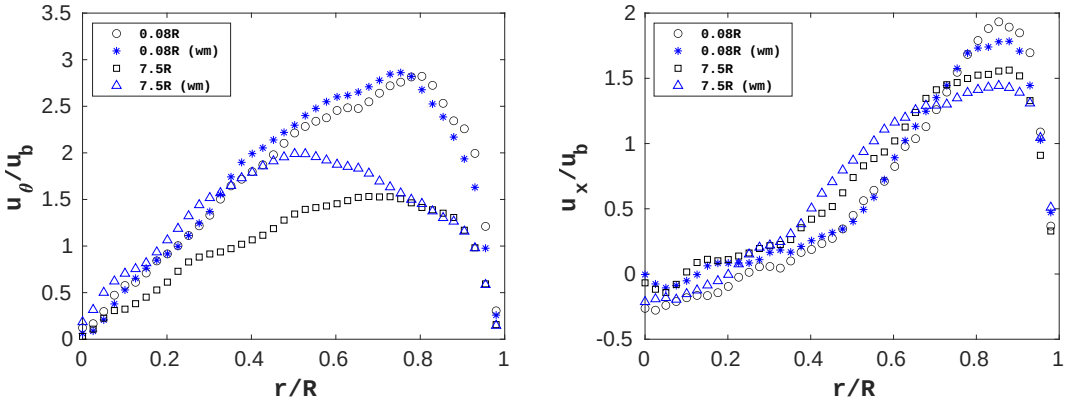

Figure 4.21: comparison of the time θ-averaged azimuthal velocity (right) and axial velocity (left) at $x = 0.08R$ for the two cases: without a wall model and with a wall model (wm).

4.5.3 Pressure and centrifugal force

When the centrifugal force pushes the fluid towards the wall, it creates a pressure drop at the center of the separator, this is depicted in Fig. 4.22 where the pressure

normalized by $1/2\rho u_b^2$ is plotted as a function of the radial position. By comparing the pressure at different axial positions, we see that p decreases along the separator due to friction except in the recirculation zone where the curves intersect leading to the reverse flow.

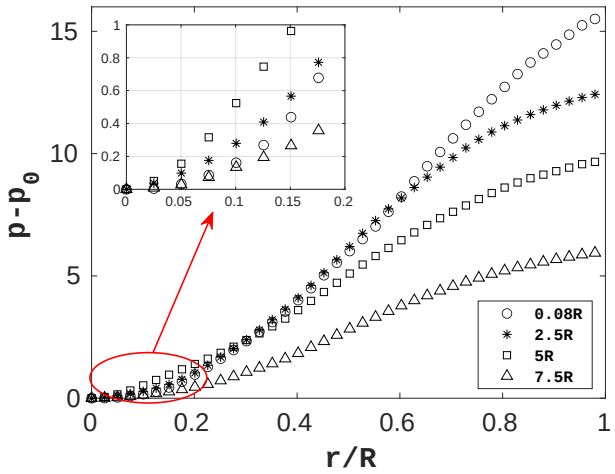

Figure 4.22: The radial distribution of the normalized pressure

As shown in subsection 4.2.3, the centrifugal force can be associated to the radial pressure gradient through equation 4.12. In Fig. 4.23 we represent separately the two terms: $\frac{u_\theta^2}{r}$ and $\frac{1}{\rho}\frac{\partial p}{\partial r}$ as a function of the radial position r at two sections $x = 0.08R$ and $x = 7.5R$ after the swirl element. At each of the axial positions, equation 4.12 is verified. The centrifugal force is 0 at the center of separator then it increases halfway between the center and the wall to finally decrease to 0 at the separator wall. The effect of the centrifugal force of great importance for the separation is thus observed to be maximum at a radial position $r \approx 0.7R$ and then decreases in magnitude along the separator.

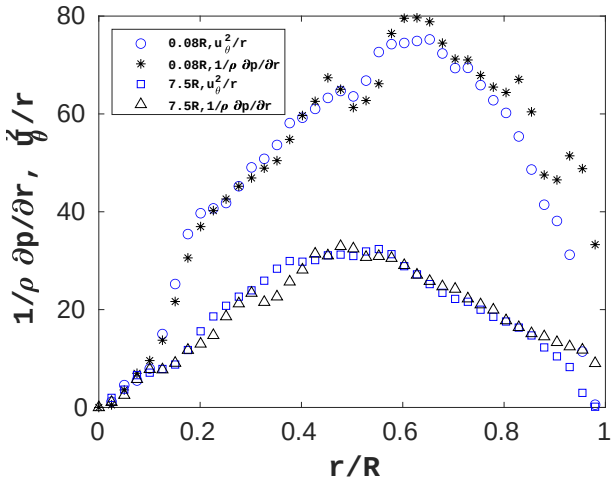

Figure 4.23: The radial distribution of the centrifugal force and pressure gradient

To evaluate the pressure drop along the separator, we calculate the time-averaged p_{wall} at the wall. Figure 4.24 illustrates the pressure normalized by $1/2\rho u_b^2$. Before

and after the swirl element, the pressure varies linearly with x/D, a friction coefficient similar to the one in non-swirling flow can be defined:

$$f_{wall} = \frac{\Delta p_{wall}}{1/2\rho u_b^2} \frac{D}{L} \tag{4.24}$$

It represents the slope of the curve for $x \in [0; 2D]$ and $x \in [4D; 10D]$ (in the regions before and after the swirl element) and equals 6.54 . Across the swirl element region, a remarkable pressure loss is introduced by this element and in which the local pressure loss coefficient equals $f_{swirl} = \frac{\Delta p_{wall}}{1/2\rho u_b^2} = 60.5$

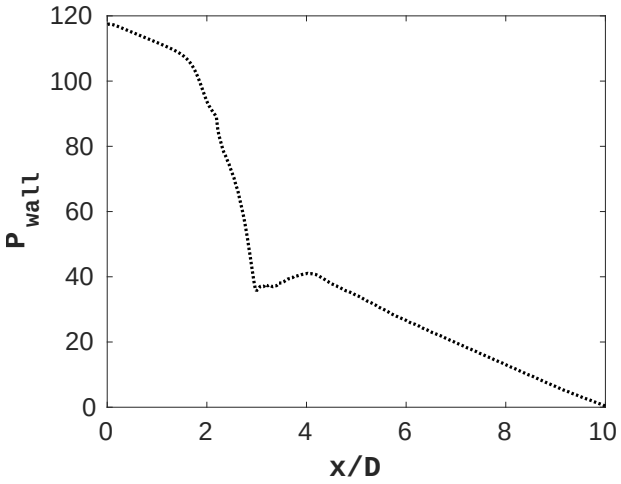

Figure 4.24: Time-averaged normalized pressure along the separator

4.5.4 Effect of the Reynolds number

Since the separator operates for different bulk velocities, Reynolds number is then considered as one of the parameters for which a sensitivity study should be done. Therefore, we compare the numerical results obtained from simulations of single-phase flow in the separator for $Re = 50,000$, $Re = 100,000$ and $Re = 200,000$, no pick-up tube is installed.
Figure 4.25 represents the swirl number for three Reynolds numbers. The maximum value is 3.4 located at the vane section and is independent of the Reynolds number. A slight difference exists in the decay of S. As the Reynolds number increases, the swirl number increases and its decay becomes weaker.

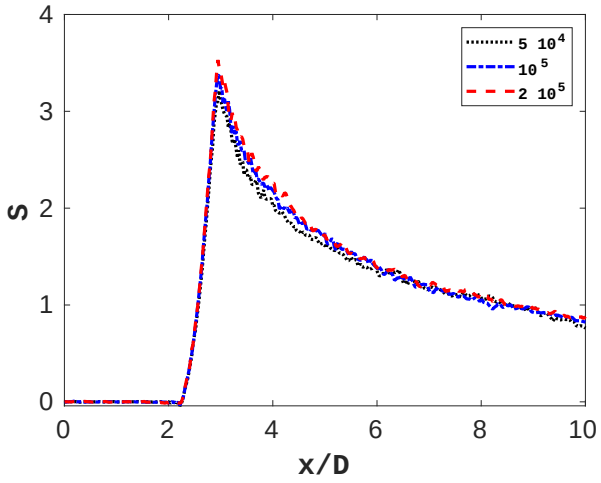

Figure 4.25: The swirl number for different Reynolds numbers

To calculate the swirl decay coefficient, we plot $ln(S/S_0)$ as a function of $(x - x_0)/D$ (see Fig.4.26: left). The slope represents therefore C_{sw}. Similary, the evolution of C_{sw} reported in [12] and shown in Fig. 4.2, figure 4.26 (right) points out that C_{sw} decreases as Re increases. A fitting for the variation of the swirl decay coefficient is found and expressed as:

$$C_{sw} = 0.3072 Re^{-0.067} \tag{4.25}$$

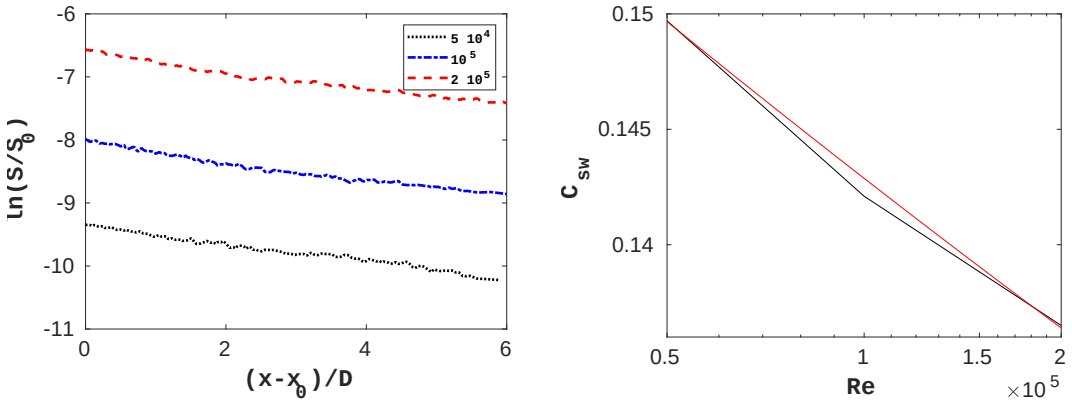

Figure 4.26: The variation of $ln(S/S_0)$ along the separator (right) and the swirl decay coefficient (left) for different Re, the solid red line represents the fit defined by 4.25

The radial distribution of the time θ-averaged azimuthal velocity at a section $x = 0.08R$ is shown in Fig. 4.27. All profiles are normalized by their corresponding bulk velocity. A minor dependence on the Reynolds number is observed for the normalized azimuthal velocity and the axial one except in the recirculation zone where increasing Re leads to an expansion of the reverse flow. For instance, for $Re = 200,000$, negative axial velocities are found up to $r = 0.3R$ while for $Re = 50,000$, the recirculation region exists only up to $r = 0.18R$.

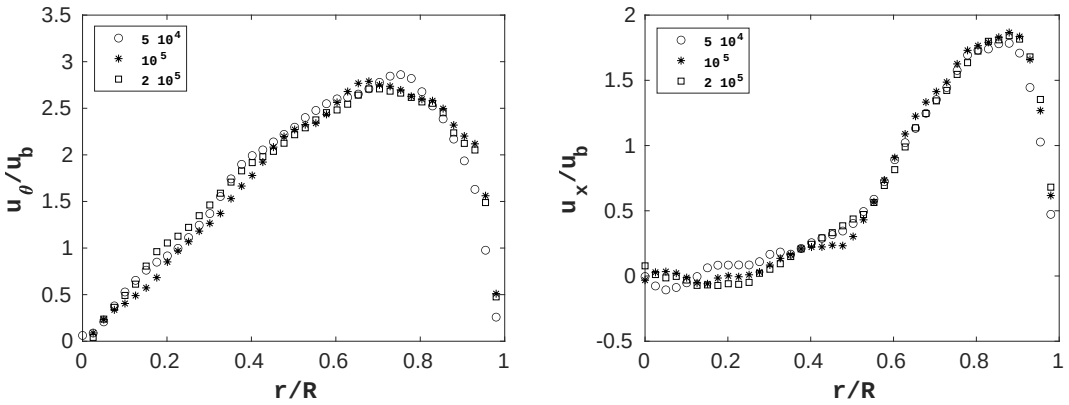

Figure 4.27: The radial distribution of time θ-averaged azimuthal and axial velocities normalized by their corresponding bulk velocity at 0.08R after the swirl element for different Reynolds numbers

Since the reverse flow is the main feature highly depending on the Reynolds number, we also plot the normalized axial velocity at a further section located at 7.5R after the swirl element. Figure 4.28 shows the effect of increasing Re in developing and spreading the reverse flow not only in the radial direction but also the axial one. A recirculation zone is still detected at this section for both $Re = 100,000$ and $Re = 200,000$ and this is a crucial information to consider when simulating two-phase flows in the separator in terms of bubble/droplet and eventually core dynamics if located in this region.

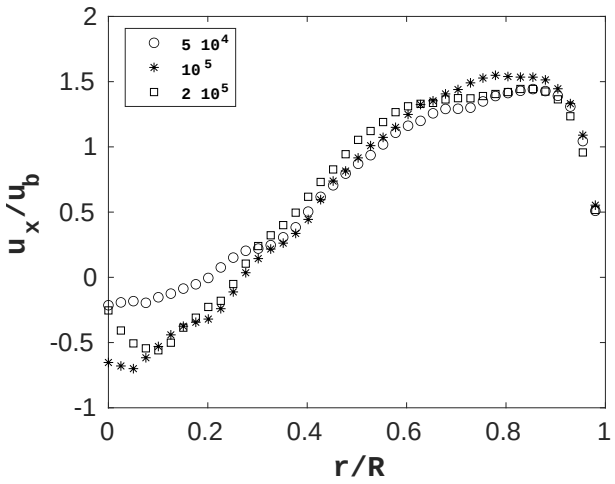

Figure 4.28: The radial distribution of time θ-averaged axial velocity at 7.5R after the swirl element for different Reynolds numbers

Figure 4.29 represents the time-averaged pressure along the separator for the three considered Re normalized by the corresponding $1/2\rho u_b^2$. The pressure drop introduced by the swirl element is almost the same for which the friction coefficient defined by equation 4.24 equals 21. Before and after the swirl element, the pressure variation is linear and depends on the Reynolds number.

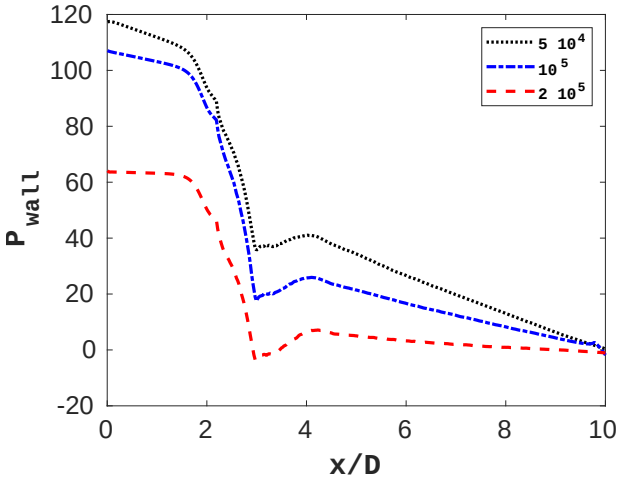

Figure 4.29: Time-averaged normalized pressure along the separator

Figure 4.30 shows the evolution of the friction coefficient calculted from the end of the tail of the swirl element to the separator outlet for different Reynolds numbers. f_{wall} decreases linearly with the increase of Re and the numerical results can be fitted to:

$$f_{wall} = -3.10^{-5} Re + 7.97 \tag{4.26}$$

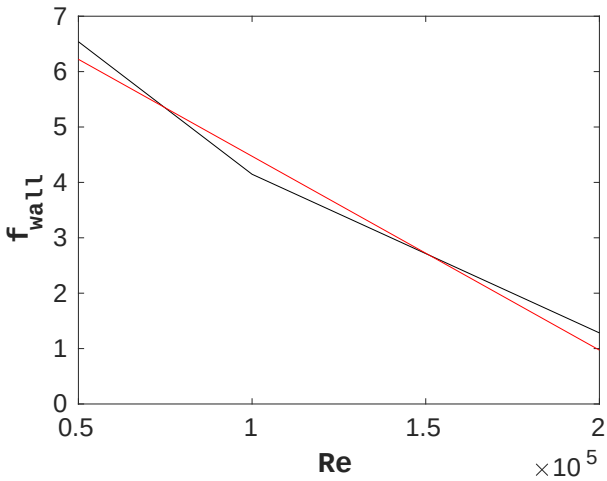

Figure 4.30: The friction coefficient f_{wall} as a function of Reynolds number, the red line represents the fit defined by 4.26

To sum up, the dimensionless azimuthal velocity is found to be slightly dependant of the Reynolds number. This means that by doubling the bulk velocity while keeping all other parameters constant, the generated centrifugal force is raised to the power 2 surpassing easily the gravitational force in highly turbulent flows. For the normalized axial velocity, the Reynolds number influences the expansion of the recirculation zone radially and axially. In subsection 4.5.5, we are interested in the effect of the flow split FS.

4.5.5 Effect of the flow split

In previous numerical simulations, the flow was investigated without any influence of the pick-up tube. In this subsection, we present the numerical results when the pick-up tube is also simulated and a condition on the flow split FS is imposed. The objective is to study the effect of the flow split on the flow features. Therefore, for the same Reynolds number $Re = 50,000$, two flow splits are considered: $FS = 0.3$ and $FS = 0.5$ to be compared to the case when no pick-up tube is installed.
Figure 4.31 represents the evolution of the swirl number along the separator for the three configurations. When no pick-up tube is installed, the swirl number continues its exponential decay until the outlet of the separator. In the region up to $x = 7.3D$, the swirl number is independent of the flow split FS. The use of the flow straightener with a condition on the flow split FS eliminates the swirling flow inside the pick-up tube located at $8.7D$ resulting in $S = 0$ and does also influence the swirl strength upstream of the pick-up tube between $x = 7.3D$ and $8.7D$. In fact, the suction of the flow at the central part of the separator leads to an increase of the axial velocity on the expense of a decrease of the azimuthal one. To visualize this, velocity profiles are plotted.

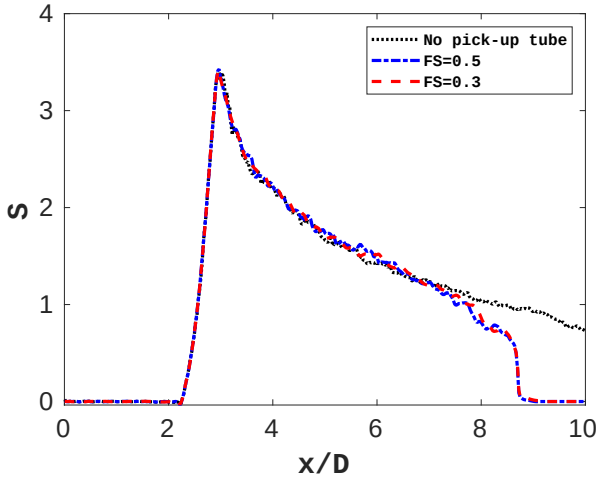

Figure 4.31: Effect of the flow split FS on the swirl number S

Figure 4.32 illustrates the effect of the flow split on the time θ-averaged azimuthal velocity at a distance $0.08R$ from the inlet of the pick-up tube. The wall of the pick-up tube is located at $r/R = 0.43$ and marks the begining of the flow straightener. In both these regions, the velocity is significantly lower than in the case of no use of the pick-up tube. It is also much reduced in the flow straightener in comparison to its evolution inside the pick-up tube. Furthermore, increasing the flow split FS results in an additional decrease of the centrifugal force.

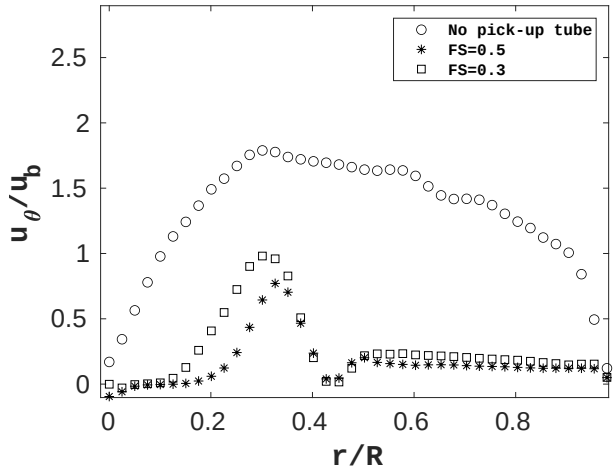

Figure 4.32: The radial distribution of time θ-averaged axial velocity across the pick-up tube for different flow splits

Besides, the time θ-averaged axial velocity is also affected by the condition on FS (see Fig.4.33). By imposing $FS = 0.5$, more fluid goes through the pick-up tube, the velocity is thus higher than in the case of imposing $FS = 0.3$. The suction of the flow, which is the aim of using the pick-up tube is then present. In the other way around, for low FS, the velocity is expected to be higher in the flow straightener, which is depicted and confirmed in the region $r > 0.43R$.

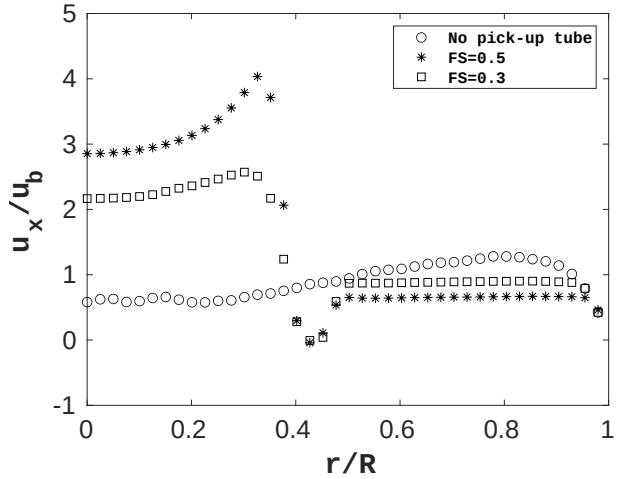

Figure 4.33: The radial distribution of time θ-averaged axial velocity across the pick-up tube for different flow splits

It is worth mentioning that the influence of the flow split is not limited only across the pick-up tube but also upstream of it at a distance 1.2R from the entrance of the pick-up tube. Figure 4.34 highlights the reduction of the azimuthal velocity when imposing FS especially far from the separator wall. The use of the pick-up tube does also eliminate the reverse flow since it forces the flow to move towards it and this is how the pick-up tube is able the recover the central core.

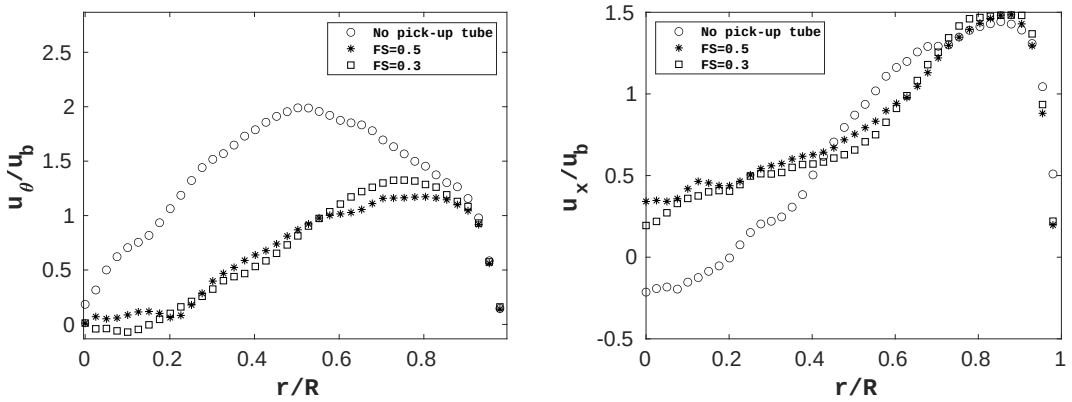

Figure 4.34: The radial distribution of time θ-averaged azimuthal and axial velocity upstream the pick-up tube at 7.5R after the swirl element for different flow splits

4.6 Conclusion

In this chapter, swirling single-phase flows in the separator are simulated using LES/IBM and the wall model and an investigation of the main features is done. A full description of the axial and azimuthal velocities, the pressure, the swirl number and the centrifugal force is given. The sensitivity to the Reynolds number is also presented. Furthermore, an original approach using IBM to model the flow straightener and to impose the condition on the valve at the pick-up tube is introduced and validated to finally study the effect of the flow split FS on the flow features. The next chapter will therefore be dedicated to simulating two-phase flows in the separator.

Chapter 5

CFD simulations of swirling two-phase flow in the separator

5.1 Introduction

As previously introduced in the first chapter, the inline fluid separation involves various flow features: turbulence, bubble migration and gas core formation, stability and recovery. The first experiments made within the TOMOCON project in TU Delft [6, 15, 86] give an overview of how the gas core is formed. In fact, three gas core patterns can be distinguished as shown in Fig.5.1: the swirling column, the swirling pulsating and the swirling burst. The pattern of the swirling gas core and the instability of its interface depend on the flow regime imposed upstream the swirl element.

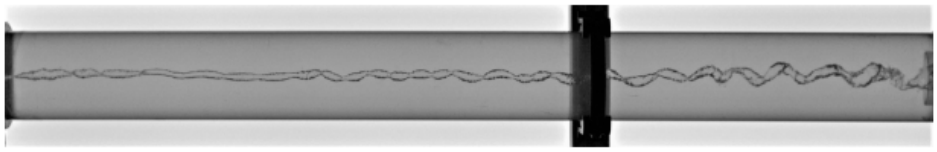

(a) Swirling column

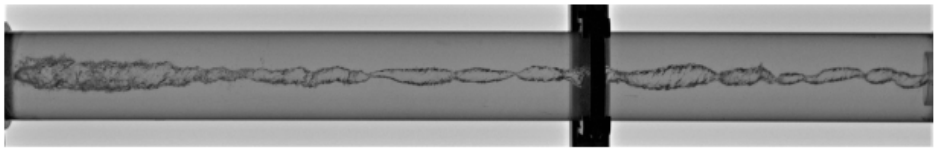

(b) Swirling pulsating

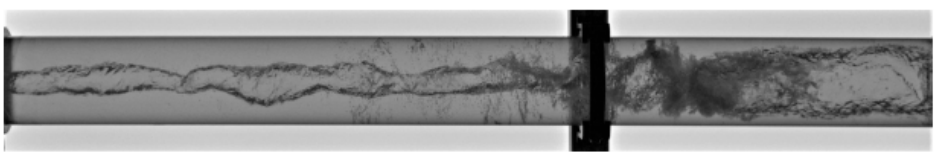

(c) Swirling burst

Figure 5.1: The different gas core patterns observed between the swirl element and the pick-up tube [6]. The flow is from the left to the right in the opposite direction to gravity.

The experiments of two-phase flow in the separator [6, 15] are conducted for different air and water bulk velocities. By observing the flow regime upstream the swirl element, the map presented in Fig. 5.2 is constructed, three flow regimes are tested (bubbly, churn, slug) and the transition between them is validated with a theoritical study by Taitel et al.[7] presented with a black line in Fig. 5.2.
Then, the flow is observed over 20cm downstream the swirl element to determine the gas core pattern. Figure 5.3 represents a map of the swirling gas core patterns. The experiments have shown that the core is formed only when the liquid velocity at the separator inlet is beyond a certain value (0.2m/s in this case) regardless of the gas velocity. This limit is marked by a black line in Fig. 5.3 and can be interpreted as a minimum needed centrifugal force capable of forming a gas core. For instance, for a gas velocity under 0.1m/s, the flow upstream the swirl element is bubbly according to the map 5.2, for liquid velocities below the black line in Fig. 5.3, the bubbles do not accumulate to form a core, the flow remains bubbly even downstream the swirl element. By increasing the liquid velocity over the black line, the flow upstream is still bubbly and the gas core is formed downstream and has a swirling column shape. Similary, the same goes for the slug flow which results in a swirling pulsating core and churn flow which gives the bursts breaking the gas core when the centrifugal force is enough to accumulate the dispersed phase. Overall, the bubbly flow regime upstream seems to lead to a stable core. We should note that the condition on pick-up tube influences the gas core behaviour as spotted in the right side of Fig. 5.1, which means that a different flow map is found for the core if observed at this location: close to the pick-up inlet (right side of Fig. 5.1).

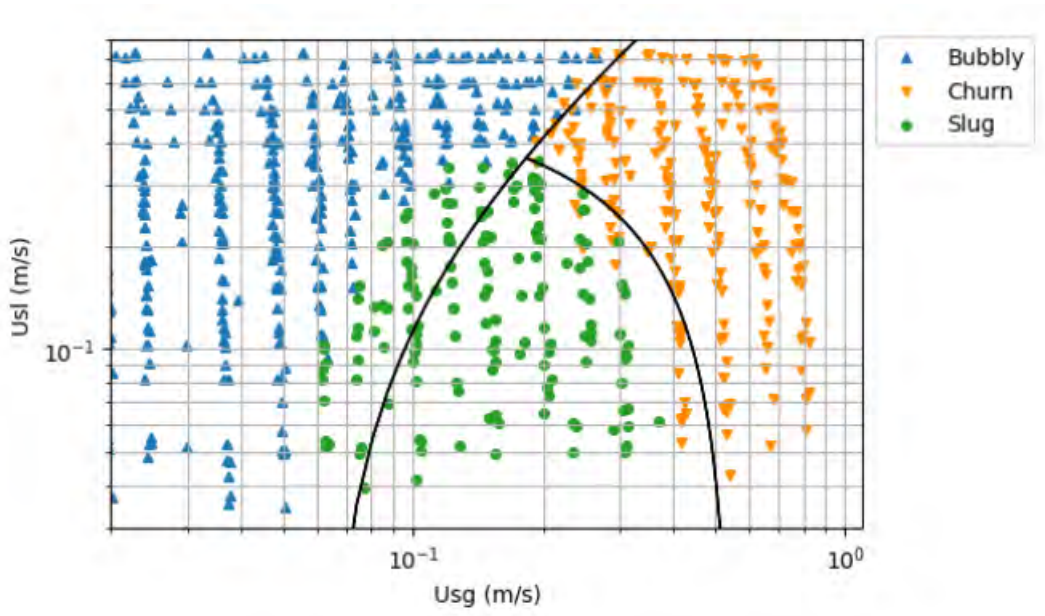

Figure 5.2: Map of two-phase flow regimes upstream the swirl element, the points are identified experimentally [6] while the black line marks the transition between bubbly-churn-slug found by Taitel et al. [7].

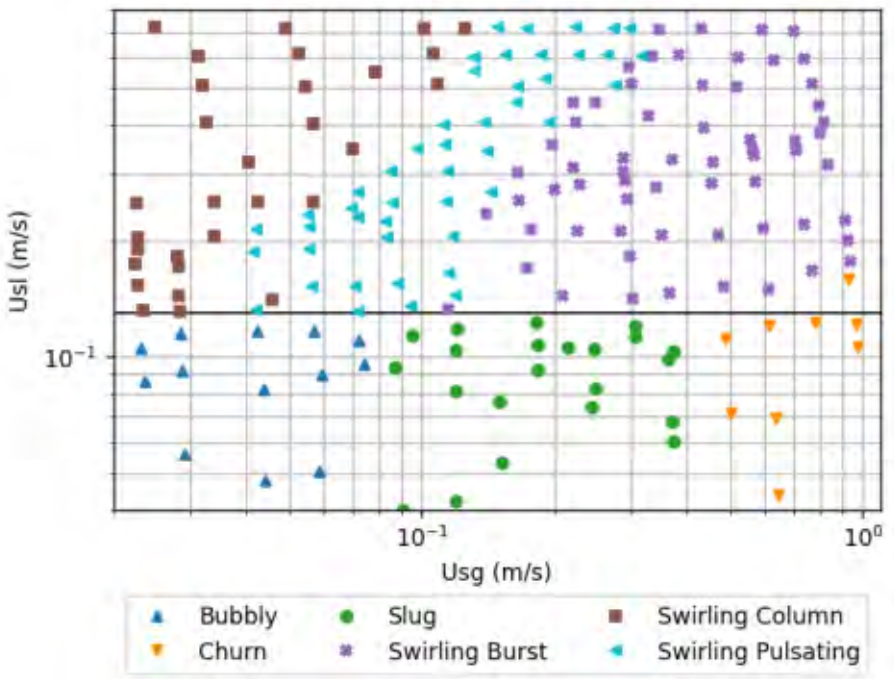

Figure 5.3: Map of the swirling gas core patterns observed just after the swirl element. A transition marked by a black line can be observed from the experiments which represents the liquid superficial velocity u_{sl} beyond which the gas core is formed and below which the generated centrifugal force is not enough to form the core and thus the flow regime downstream the swirl element is the same as the one upstream the swirl element [6].

While the experiments reveal some interesting aspects of the core formation and its various patterns depending on the upstream flow regime, the objective of this chapter is to investigate numerically the physical phenomena leading to the separation for upstream bubbly flow (left part of Fig. 5.2). For that purpose, we investigate bubble accumulation and core formation using the proposed hybrid CFD approach (LES-IBM-LT-VoF).

First, a simplified model of the force balance of a bubble in the separator is given. Then, the bubbles trajectories are calculated thanks to the Lagrangian Tracking method. The instantaneous, mean and RMS of the forces applied on the bubbles are analyzed to discuss the dominant force leading to the bubbles migration. The effects of the bubble size as well as the Reynolds number on this process are also studied. Additionally, we visualize the bubbles accumulation and calculate the separation efficiency. Finally, the hybrid approach (LT-VoF) is activated to simulate the gas core and discuss about its stability. A simplified study of a gas core in a rotating flow is also done to try to investigate the possible instabilities which can occur at the interface.

5.2 Description of bubble dynamics in swirling flow

In order to introduce the mechanisms involved in the separation process for a bubbly flow, we first consider the motion of an isolated bubble in a swirling flow region

during its migration to the pipe centerline. The motion of a bubble in a turbulent swirling flow in the separator is governed by the Newton's second law introduced in subsection2.5.6 and expressed by the force balance 5.1.

$$(\rho_d + C_M\rho_c)V_d\frac{d\mathbf{v}_d}{dt} = (\rho_d - \rho_c)V_d\mathbf{g}+ C_D\rho_c\frac{\pi r_d^2}{2}\|\mathbf{u}_{x_d} - \mathbf{v}_d\|(\mathbf{u}_{x_d} - \mathbf{v}_d) + C_L\rho_c V_d(\mathbf{u}_{x_d} - \mathbf{v}_d) \times \Omega+ \rho_c V_d(1 + C_M)\frac{D\mathbf{u}}{Dt}|_{x_d} \quad (5.1)$$

To integrate this equation and get the bubble trajectory in a complex flow as the one generated here by the swirl element, we use the Lagrangian Tracking method and this will be the subject of the next section. However, we can employ the single-phase flow study done in chapter 4 and propose assumptions to simplify the terms of equation 5.1 to be able to approximate and compare the different forces applied on the bubble in order to discuss the process of bubble migration. In fact, the numerical simulations of single-phase flow in the separator have shown that the fluid time θ-averaged azimuthal velocity has a Rankine vortex profile with a constant rotation rate ω in the solid rotation zone while the averaged radial fluid velocity is neglected in front of the two other velocity components. For simplification purposes, we consider that the fluid axial time and θ-averaged is constant and equal to bulk velocity u_b.
Therefore, this simplified fluid velocity field takes the form:

$$u_r = 0;\ u_\theta(r) = \omega r;\ u_x = u_b \quad (5.2)$$

This leads to:

$$\frac{D\mathbf{u}}{Dt}|_{x_d} = (-\frac{u_\theta^2}{r} = -\omega^2 r; 0; 0);\ \Omega = \nabla \times \mathbf{u} = (0; 0; 2\omega) \quad (5.3)$$

The gravity is $\mathbf{g} = -9.81\mathbf{e}_x$.
Considering that the bubble Reynolds number is much larger than unity, $Re_b = 2r_d\rho_c\|\mathbf{u} - \mathbf{v}_d\|/\mu_c >> 1$, we can first consider that $C_D \approx 48/Re_b$ (i.e. $\mathbf{F}_D \approx 12\pi\mu_c r_d(\mathbf{u} - \mathbf{v}_d)$) and $C_L \approx 1/2$. The bubble being assumed as spherical we have $C_M = 1/2$. With the additional condition $\rho_d << \rho_c$, the bubble relaxation time is $\tau_d = r_d^2/18\nu_c$. Typically, for a 1 mm diameter bubble in water, $\tau_d \approx 0.01$s.

Then, we can examine the radial components of the three forces (drag, lift and virtual mass) corresponding to the second and third lines in equation 5.1 which are involved in the process of bubble migration towards the pipe centre as:

$$F_{D,r} = -12\pi\mu_c r_d v_{d,r} \quad (5.4)$$

$$F_{L,r} = \rho_c V_d\omega(\omega r^* - v_{d,\theta}) \quad (5.5)$$

$$F_{VM,r} = -\frac{3}{2}\rho_c V_d r^*\omega^2 \quad (5.6)$$

where r^* is the radial bubble position.

Since a negative force induces a motion towards the pipe centre, the radial component of the virtual mass force always imposes the centripetal force leading to the

migration of the dispersed phase, the radial lift has a centrifugal effect proportional to the azimuthal relative velocity that is a priori expected to vanishes after some bubble relaxation time τ_d since the bubble adjusts to the swirling fluid flow, but this point will be discussed later. The radial drag force is opposite to the radial bubble velocity. Thus, it has a centripetal effect during the migration of the bubble.

Besides, we are also interested in the axial movement of the bubble which is being transported towards the outlet of the separator in order to check if the bubble is captured by the pick-up tube or not. For this, we investigate the axial components of buoyancy, drag, lift and virtual mass.

$$F_{B,x} = \rho_c V_d g \tag{5.7}$$

$$F_{D,x} = 12\pi\mu_c r_d(u_b - v_{d,x}) \tag{5.8}$$

$$F_{L,x} = 0 \tag{5.9}$$

$$F_{VM,x} = \frac{3}{2}\rho_c V_d u_x \frac{\partial u_x}{\partial x} \tag{5.10}$$

In the simplified situation where $u_x \approx u_b$ then $F_{VM,x} \approx 0$ and we see that along the axial direction, the bubble will reach after some relation times τ_d a velocity composed of the fluid bulk velocity u_b and the so called terminal velocity $\mathbf{v}_T = 2\tau_d\mathbf{g} = r_d^2/(9\nu_c)\mathbf{g}$. For a 1 mm diameter bubble in water, $v_T \approx 0.27\text{m/s}$.

The bubble is also subject to an azimuthal motion which describes its rotation movement and is governed by the azimuthal components of the drag, lift and virtual mass forces:

$$F_{D,\theta} = 12\pi\mu_c r_d(\omega r^* - v_{d,\theta}) \tag{5.11}$$

$$F_{L,\theta} = \rho_c V_d \omega v_{d,r} \tag{5.12}$$

$$F_{VM,\theta} = 0 \tag{5.13}$$

The lift induces an azimuthal contribution that may contribute to a slip azimuthal velocity depending on both solid body rotation and the bubble radial velocity.

In order to give an idea about the order of magnitude of these forces and their contribution in the migration and capture of the bubble in the separator, we consider, for instance, the numerical results obtained for swirling single-phase flow of $Re = 50,000$ detailed in chapter 4.5. From this simulation, the continuous phase velocities at a position $0.08R$ after the swirl element are: $\omega \approx 50s^{-1}$, $u_b \approx 0.54m/s$. We consider a bubble of radius $r_d = 1mm$ transported by the flow along the pipe axis with the velocity $\mathbf{u} + \mathbf{v}_T$ that is instantaneously submitted to the solid rotation. We consider an initial radial position $r_0^* = 0.035m$ and zero radial velocity when the bubbles enters inside the vortex.

Table 5.1 summarizes the order the magnitude of the different forces components. We can say that the buoyancy and drag are the dominant forces for transporting the bubble to the separator outlet while the virtual mass force is dominant in the radial direction leading to the radial migration of the bubble to the centre.

Components	F_B	F_D	F_L	F_{VM}
x	4.1×10^{-5}	-5.0×10^{-5}	0	0
r	0	0	3.6×10^{-4}	-5.5×10^{-4}
θ	0	6.6×10^{-5}	0	0

Table 5.1: Estimation of the magnitude of the forces components (N) applied on the bubble in the separator.

It is worth reminding that the force comparison done above does not take into account the effect of turbulence presented by the velocity fluctuations of the continuous phase since only time and θ-averaged velocities were considered with simplified profils.

When discussing the separation efficiency, three characteristic times of interest for the dispersed phase can be distinguished:
- The relaxation time $\tau_d = r_d^2/18\nu_c$ which is the response time of the bubble to the continuous phase, i.e. the characteristic time for a bubble to adjust its velocity to the carrier fluid as well as buoyancy.
- ω^{-1} which is a relevant time scale on its own according to 5.5. It can be interpreted as the relaxation rate for the lift force.
- The migration time $t_{migration}$ which is the time needed for a bubble to reach the centre of the separator.
- The capture time $t_{capture}$ which is the time needed to reach the outlet of the separator: the HPO or the LPO.

Based on the force magnitude presented above, a first attempt is made to provide an estimation of these characteristic times for the considered system. In order to determine the characteristic migration time $t_{migration}$ we consider the trajectory equation along the radial direction:

$$\frac{1}{2}\rho_c V_d\left(\frac{d^2r^*}{dt^2} - \frac{v_{d,\theta}^2}{r^*}\right) = -12\pi\mu_c r_d\frac{dr^*}{dt} + \rho_c V_d\omega(\omega r^* - v_{d,\theta}) - \frac{3}{2}\rho_c V_d r^*\omega^2 \tag{5.14}$$

Considering first that $dr^*/dt << r^*/\tau_d$ (which is expected for the bubble dynamics in the separator). The force balance in the azimuthal direction gives $v_{d,\theta} = \omega r^*$. From this, the trajectory along the radial direction can be simplified to:

$$\frac{d^2r^*}{dt^2} \approx -\frac{1}{\tau_d}\frac{dr^*}{dt} - \frac{1}{t_{VM}^2}r^* \tag{5.15}$$

where appears a characteristic time t_{VM} imposed by the virtual mass force:

$$t_{VM} = \frac{1}{\sqrt{2}\,\omega} \tag{5.16}$$

The solution of equation 5.15 is reported in Fig. 5.4 for three cases: ($r_d = 1mm, t_{VM} = 0.014s$), ($r_d = 0.5mm, t_{VM} = 0.014s$) and ($r_d = 1mm, t_{VM} = 0.007s$). As shown, for the same $\omega \approx 50s^{-1}$, the increase of the bubble radius leads to a decrease of the migration time from 0.035s to 0.024s. Then, for the same bubble size $r_d = 1mm$, the migration time is reduced to 0.011s by increasing ω from $50s^{-1}$ to $100s^{-1}$ which corresponds to $t_{VM} = 0.007s$.

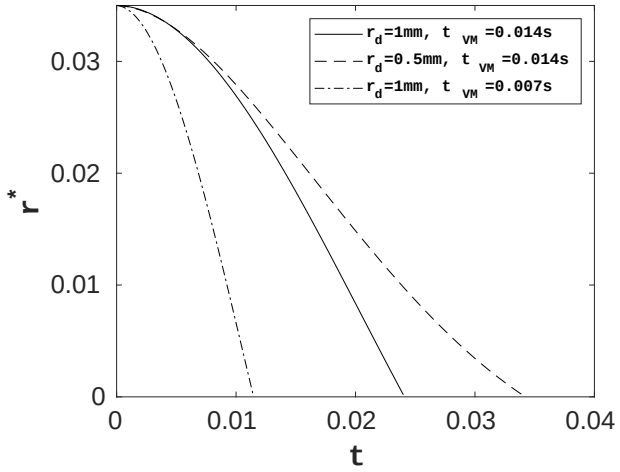

Figure 5.4: Comparison of the evolution of the bubble radial position obtained by solving equation 5.15 for $(r_d = 1mm, t_{VM} = 0.014s)$, $(r_d = 0.5mm, t_{VM} = 0.014s)$ and $(r_d = 1mm, t_{VM} = 0.007s)$.

Indeed the increase of the bubble radius decreases the migration time, however, it also increases the buoyancy force which speeds up the axial mouvement of the bubble. A bubble can, in some cases, be driven by the axial fluid velocity before it reaches the pipe centre. To evaluate the effect of the bubble size and Reynolds number on the capture process, we calculate the axial length over which the bubble gains the pipe centre using its axial velocity estimated to $u_b + v_T$. Figure 5.5 shows the bubble radial position as function of its axial position normalized by the pipe radius for the three cases: $(r_d = 1mm, t_{VM} = 0.014s)$, $(r_d = 0.5mm, t_{VM} = 0.014s)$ and $(r_d = 1mm, t_{VM} = 0.007s)$. We can see that although the increase of the bubble radius decreases the migration time from Fig. 5.4, the bubble crosses a distance of $0.8R$ in the axial direction which is larger than the one travelled by the bubble with lower radius. This can give an idea on where to position the pick-up tube to make sure that the bubbles have enough space and thus time to migrate. Furthermore, figure 5.5 reveals that for the same bubble radius, the increase of Reynolds number leads to a decrease of both the migration time and axial length, which means that it contributes more in the migration than in the capture. Numerical simulations using LT and LES will allow to determine precisely the role of each force and the effect of the turbulent dispersion.

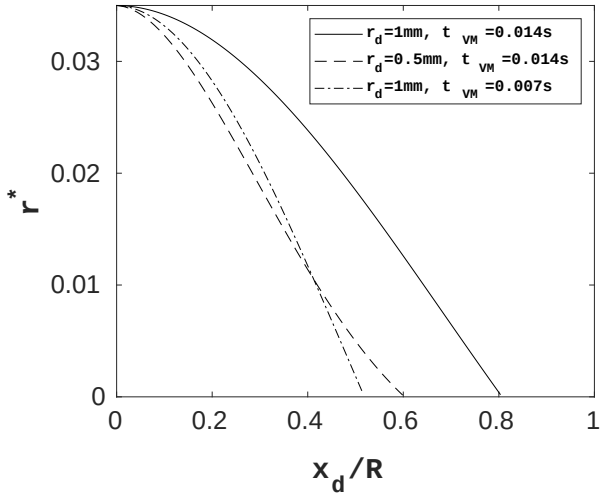

Figure 5.5: Comparison of the evolution of the bubble radial position as function of its axial position normalized by the pipe radius for ($r_d = 1mm, t_{VM} = 0.014s$), ($r_d = 0.5mm, t_{VM} = 0.014s$) and ($r_d = 1mm, t_{VM} = 0.007s$).

Considering the value of the forces reported in table 5.1, the lift force also contributes to the radial motion. The lift force has an opposite sign but its magnitude is smaller than the virtual mass force. The migration towards the pipe centre is still taking place but the time migration will be certainly increased due to the lift force. This will be discussed using the numerical simulations presented in the next section. The value of the migration time will be compared to the results obtained from the numerical simulations where all the effects are taken into account, and in particular the decay of the swirl strength and the unsteadiness and fluctuations of the flow turbulence.

5.3 Numerical results of bubble dynamics in the separator using Lagrangian Tracking

One of the advantages of using the Lagrangian Tracking solver for the dispersed phase is to accurately describe its dynamics during the process of bubble migration preceeding the core formation. In this section, 3D simulations of two-phase flows are perfomed on a numerical domain of size $L_x \times L_y \times L_z = 0.92m \times 0.104m \times 0.104m$ made of $N_x \times N_y \times N_z$ cells. The mesh size Δ is the same as the one retained from the mesh sensitivity study reported in the previous chapter 4 such as: $R/\Delta = 40$.

When the incoming bubbles located upstream the swirl element pass through the vane section, they are forced to move into the tiny space between the blades and the pipe wall to finally exit to the tail section. Therefore, to save the computationnal time needed to track the bubbles up to the vane section, the bubbles are injected at the tail section with the fluid velocity and the study focuses on the migration happening downstream the swirl element. In the following, a set of 5000 bubbles are injected continuousely over time with an averaged volumetric rate $q = 5 \times 10^{-4} m^3/s$. In fact, at each time step, the number of bubbles to inject is defined as a random integer N_{inj} which follows a Poisson distribution with the parameter $\mu_{poisson} =$

$q\Delta t/V_d$:

$$Pois(\mu_{poisson}) = \frac{\mu_{poisson}^{N_{inj}} e^{-N_{inj}}}{N_{inj}!} \tag{5.17}$$

In space, the bubbles are initialized at the same axial position $x_0 = 0.35m$ and at random different radial positions as illustrated in Fig. 5.6. The bubbles are considered non deformable clean spheres and the gravity is $\mathbf{g} = -9.81\mathbf{e}_x$ opposite to the flow direction.

Figure 5.6: Positions of a set of 5000 bubbles (in blue) at $t = 0.04s$ after the continuous injection is done.

At first, an analysis of the force balance on a single bubble is done to show the temporal evolution of the forces acting on it. Then, a mean force balance is calculated by averaging over the 5000 injected bubbles to determine the driving force leading to the migration. Finally, the effect of both the bubble size and the Reynolds number on the migration is studied.

5.3.1 Instantaneous force balance

A 3D simulation of a two-phase flow in the separator is performed for $Re = Du_b/\nu_c = 50,000$. A single bubble of radius $r_d = 1mm$ is tracked and its force balance is calculated.

Figure 5.7 represents the spatial 3D trajectory of the bubble. The bubble position in the (y, z) plane fluctuates between positive and negative values which indicates that the bubble is rotating around the pipe centre located at $(y_0 = 0, z_0 = 0)$ and marked by a red line in Fig. 5.7. In addition, the bubble is pushed towards the pipe centre, its radial position approaches $r^* = 0$, reaches it at several times and oscillates around it (see Fig. 5.8 (left)). The bubble can be ejected from the axis during its migration process due to turbulent fluctuations that develop in the flow, increasing the time for the bubble migration.

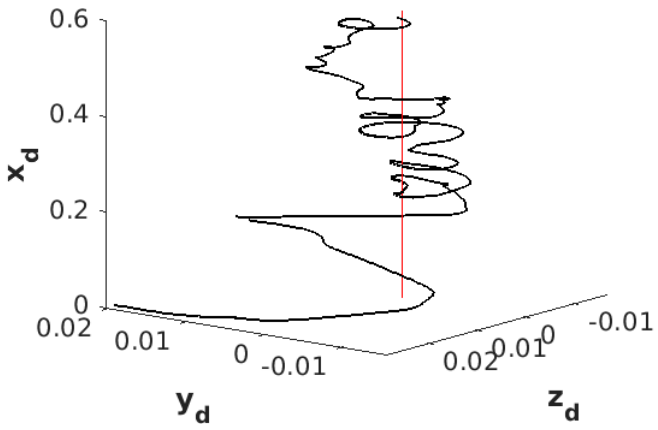

Figure 5.7: Trajectory of a 1mm radius bubble in the separator swirling flow for $Re = 50,000$. The red line represents the pipe centre $(y, z) = (0, 0)$, the gravity is $\mathbf{g} = -9.81\mathbf{e}_x$.

Figure 5.8 shows the temporal evolution of the radial and axial positions of the bubble. Fluctuations are observed for the radial position which might be a result of the turbulent dispersion intervening in the force balance via the velocity fluctuations of the continuous phase. On the other side, the axial position shows weak fluctuations since it is mainly controlled by the drag balanced by the buoyancy and weight which are independant of the fluid velocity. As revealed by the silmulation of the forces acting on a bubble in a turbulent pipe flow [22], turbulent fluctuations can provide some significant lift and virtual mass fluctuations while the drag force fluctuations remain around 5% of the mean drag force.

From Fig.5.8, we can calculate the characteristic time of migration corresponding to when the bubble reaches the pipe centre for the first time. In this case, we have $t_{migration} = 0.18s$ which is almost eight times higher than the time migration obtained from the simplified analysis presented in section 5.2 when neglecting the lift force effect in the migration. This is due to the decay of the centrifugal force (i.e the azimuthal velocity) which is not considered in the simplified analysis. Additional effects such as the radial turbulent dispersion may also be induced by the unsteadiness and spatial fluctuations of the continuous phase.

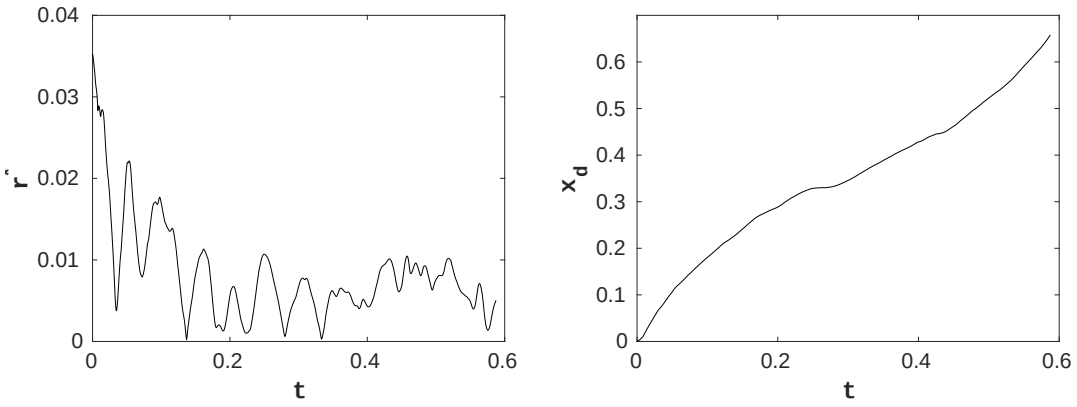

Figure 5.8: The radial (left) and axial (right) positions (m) of the bubble in (m) as function of time (s).

To evaluate the different forces applied on the bubble, we compare the magnitude of the drag, virtual mass and lift in Fig. 5.9 while keeping in mind that the sum of weight and buoyancy is constant and equals $F_B = 4.1 \times 10^{-5}$N. First, fluctuations are observed in all the forces due to turbulence which explain the fluctuations present in the bubble trajectory. The drag force is smaller than the lift and virtual mass forces which are relatively of the same order of magnitude found in the simplified study in section 5.2.

Now, in order to decipher the contribution of the drag, and virtual mass forces in the process of bubble migration, we plot separately in Fig.5.9 the three components of each force over time. In the radial direction, the virtual mass force is generally negative which corresponds to a centripetal effect while the lift force is constantly changing sign which means that it has both centrifugal and centripetal effects on the bubble. As the bubble moves far from the swirl element, the fluctuations and the magnitude of the forces are reduced due to the decay of the swirl strength. Finally, since the instantaneous force balance for only one bubble remains insufficient to adequately compare with the simplified analysis and conclude on the effect of the each force, a statistical study is conducted on the force balance in the next subsection 5.3.2.

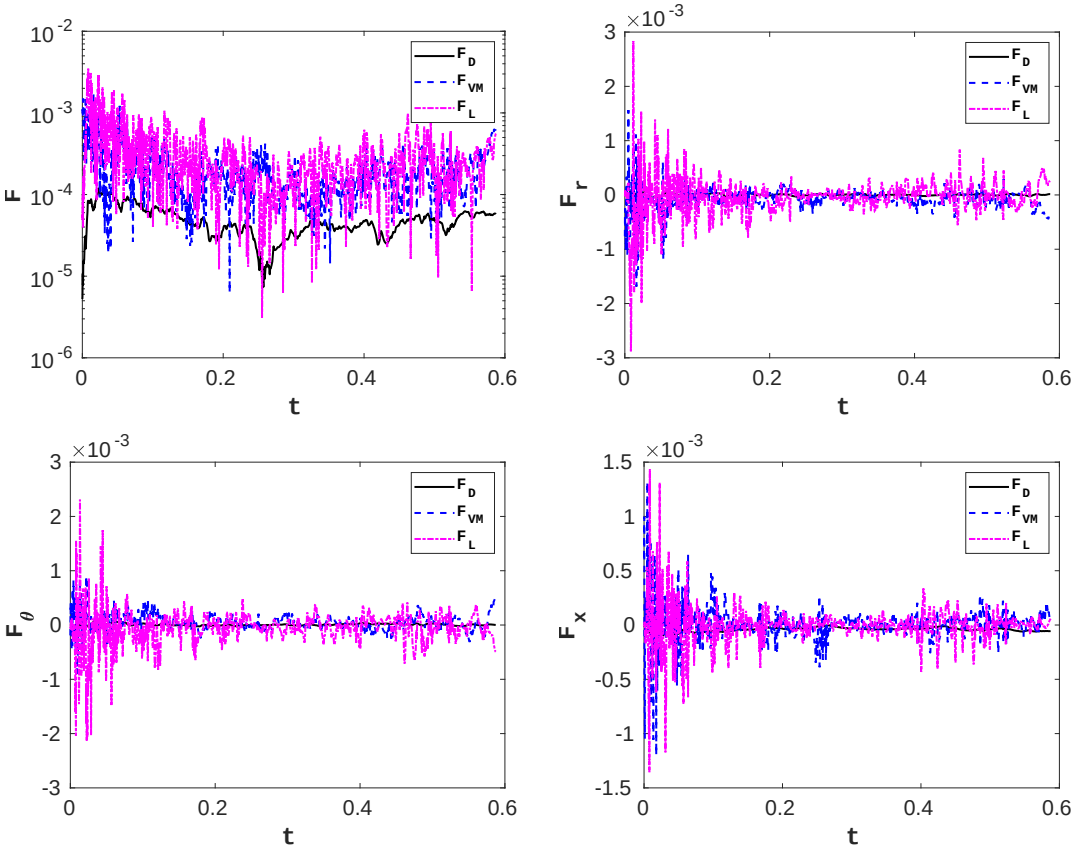

Figure 5.9: Time evolution of the magnitude and components of the forces acting on the bubble in (N).

5.3.2 Mean force balance

In the previous subsection 5.3.1, the analysis focuses on the instantaneous evolution of the forces over time to reveal strongly fluctuating forces, in particular the lift and

virtual mass forces in agreement with [22]. In this subsection, we will investigate the statistics of each force namely the mean and the RMS in order to characterize the fluctuations observed in subsection 5.3.1. Therefore, for the set of 5000 bubbles of radius $1mm$ injected continousely at the same axial position $x_0 = 0.35m$, we average the terms of the force balance at 50 axial positions vaying between x_0 and the separator outlet.

The mean of the forces magnitude and components as function of the axial position are reported in Fig.5.10. First, the range of values found for the magnitude of each force is consistent with the estimation calculated in table 5.1. The virtual mass is the dominant force, then comes the lift force. By taking a close look at the evolution of each force in each direction, we find that the radial virtual mass is negative leading to the migration of the bubbles and is maximum just after the swirl element where the azimuthal velocity is maximum. The radial lift contributes in the migration process right after the swirl element but also has a centrifugal effect on the bubbles which pushes them towards the pipe wall. The lift force is characterized by numerous fluctuations and peaks which are also illustrated later in the RMS profiles in Fig. 5.13 showing a sensitivity to the continuous phase velocity fluctuations. These peaks may after all get reduced if the number of bubbles is increased for statistical convergence. In the axial direction, considering the value of the weight and buoyancy force, the latter is the one transporting the bubbles towards the outlet. Therefore, by comparing between all the components of all the forces, we can say that the bubbles motion is first dominated by the migration then the azimuthal swirl of the continuous phase and finally the weight and buoyancy which lead to the capture of the bubbles.

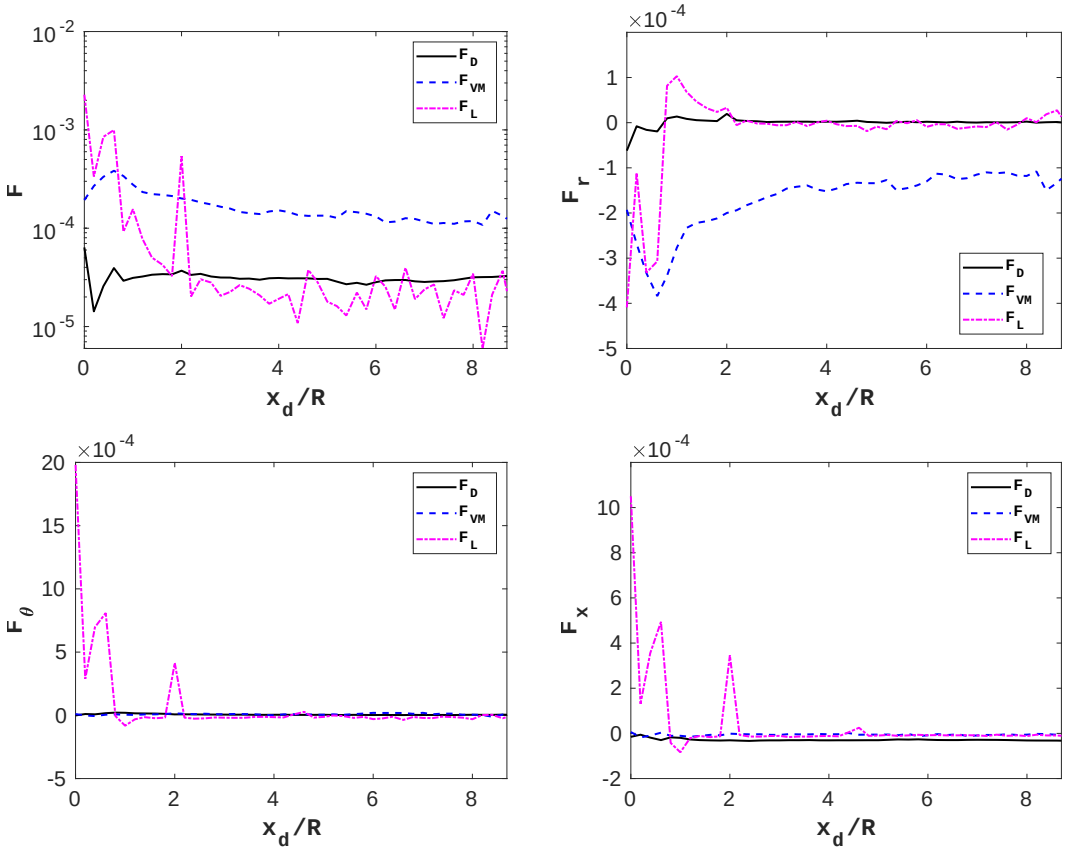

Figure 5.10: The averaged magnitude and components of the forces in (N) as function of the axial position normalized by the separator radius.

We eventually can compare the radial virtual mass force, responsible of the migration, obtained from the numerical simulation and the one calculated based on the simplified analysis presented in section 5.2 and using equation 5.18 with u_θ is the mean azimuthal velocity of the continueous velocity at the bubble position and r^* is the mean radial position of the dispersed phase given by the simulation. In figure 5.11, the mean value of $F_{VM,r}$ from the numerical simulation and the one calculated from relation 5.18 are close to each others, showing that the dominant term of the averaged radial acceleration of the continuous phase is indeed $-u_\theta^2/r$.

$$F_{VM,r} = -\frac{3}{2}\rho_c V_d \frac{u_\theta^2}{r^*} \tag{5.18}$$

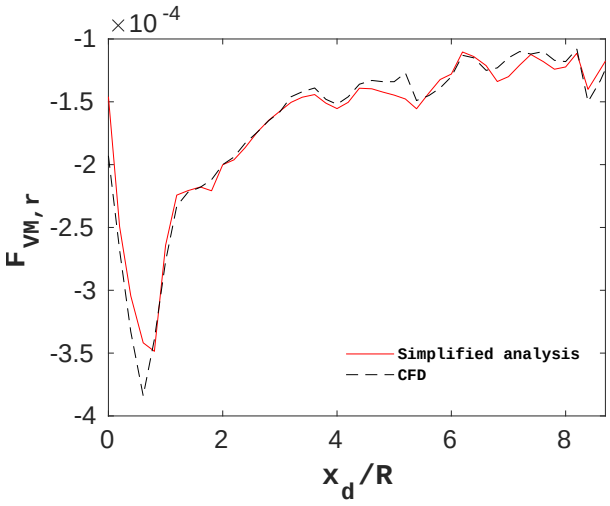

Figure 5.11: Comparison of the averaged radial virtual mass force in (N) obtained from the simulation and the one calculated using eq 5.18 as function of the axial position normalized by the separator radius.

The average of the bubbles radial position is plotted as function of the axial position in Fig.5.12 and compared to an instantaneous projection of a single bubble trajectory. The radial position r^* decreases significantly right after the swirl element and up to $x_d/R \approx 5$ where the virtual mass is maximal then it is stabilized at a radial position r^* around 0.008m. This equilibrium corresponds to a balance between the average and the fluctuating contribution in the radial force balance. An averaged migration time can be calculated based on the bubble averaged axial velocity as $t_{migration} = 5R/v_d$ equal to $0.37s$. It is around twenty times more than the one estimated from the simplified analysis given in section 5.2. The distance $5R$ can also be interpreted as the migration length needed for the bubbles to draw near the pipe centre. This value is higher than $0.8R$ reported in Fig. 5.5 since the axial lift contributes also in pushing the bubbles towards the separator outlet and the radial fluctuations delays the migration process. This is an important criteria to take into account in dimensionning the length of the separator and/or positionning the pick-up tube.

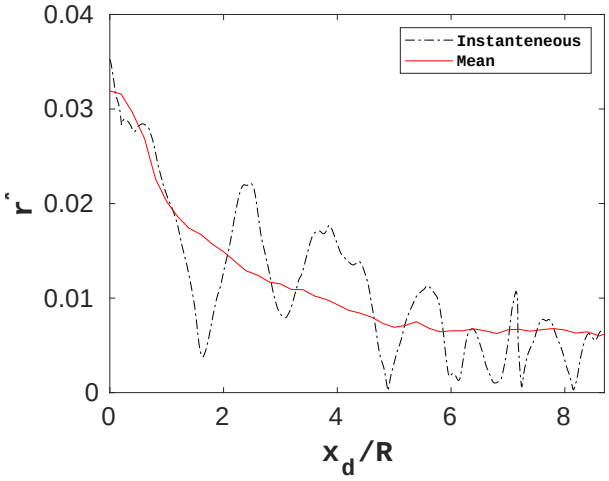

Figure 5.12: The mean radial position and a single bubble radial position in (m) as function of the axial position normalized by the separator radius.

Now, to characterize the forces fluctuations observed in the instantaneous profiles, the RMS are calculated for each force component.
First, to compare between all the RMS, the fluctuations are normalized by the magnitude of the averaged virtual mass. This is illustrated in Fig.5.13(left). The RMS of the lift and the virtual mass are higher than the drag RMS consistently with the important fluctuations observed in 5.9 for these two forces. This aspect of unsteadiness which was neglected in the simplified analysis, can be responsible for increasing the time migration since it can generate a centrifugal effect on the bubble as previousely mentionned. Indeed, it can be seen that the RMS are of the order of the averaged virtual mass which is the dominant force.
And in order to evaluate the contribution of the fluctuations of each force separately, we normalize each RMS by its corresponding force magnitude as illustrated in Fig.5.13(right). The fluctuations in the three directions represent an important part of the instantenueous lift force since turbulence intervenes in the continuous phase velocity and vorticity. The lift force as well as the virtual mass are then the dominant forces in the process of bubble migration through their means and fluctuations.

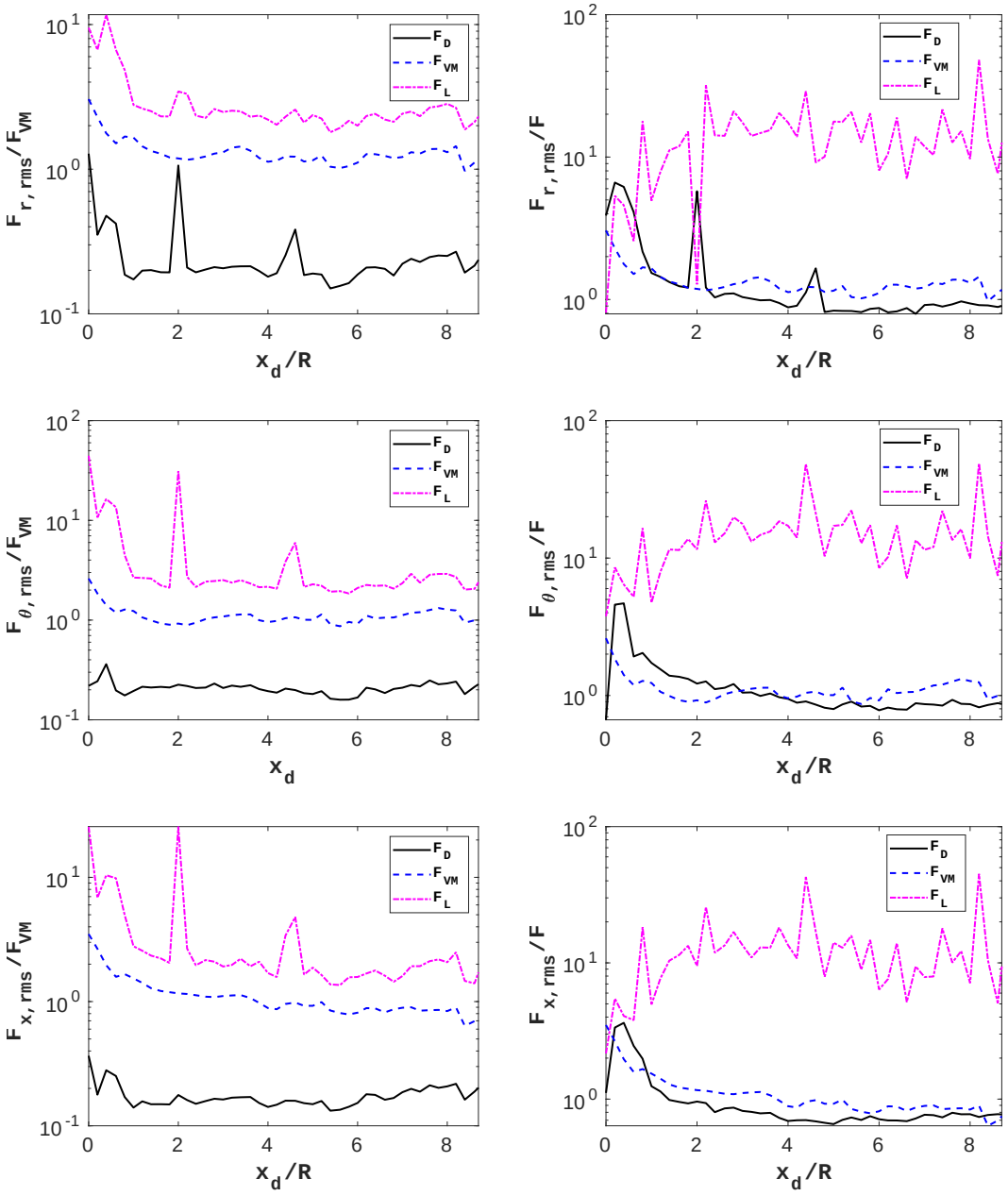

Figure 5.13: The RMS of the forces normalized by the averaged virtual mass force (left) and normalized by the averaged corresponding force (right) as function of the axial position normalized by the separator radius.

The study of the instantaneous and averaged force balance has proved that the virtual mass is the driving force of bubble migration and has highlighted that the lift force is also important in either promoting the migration or delaying it. The fluctuations of both these forces have also a significant role in agitating the bubbles and increasing the migration time. Finally, it is worth noting that the contribution of each force can eventually change depending on the properties on the continuous and dispersed phase (the bubble size and the Reynolds number). This will be discussed in the next subsections.

5.3.3 Effect of the bubble size

To investigate the effect of the bubble size on the migration process, the same simulation with $Re = 50,000$ is perfomed for 5000 bubbles of radius $r_d = 0.5mm$ injected continuousely at the axial position $x_0 = 0.35m$. The mean force balance is compared to the one of the previous case where the injected bubbles were of radius $r_d = 1mm$.

We compare in Fig. 5.14 (left) the temporal evolution of the bubble radial position as function of the normalized axial position of two single bubbles of different radius $r_d = 0.5mm$ and $r_d = 1mm$. Fluctuations are observed in both profiles but are intensified with the increase of the bubble size. The mean of the bubbles radial position is plotted in Fig. 5.14 (right), from which we can estimate a migration time of $0.52s$ calculated from the averaged velocity of the dispersed phase. This value is higher than the migration time obtained for $1mm$ radius bubbles. Thus, we can see the effect of decreasing the bubble size in delaying the migration process. To justify this, the radial components of the forces are investigated later on.

It is worth mentionning that in the axial direction, the big bubbles reaches the outlet of the separator in less time in comparison to the small bubbles since the buoyancy is higher which indicates that the capture time increases with the decrease of the bubble size. The migration length which is the axial distance travelled by the bubbles till stabilizing its radial position around the pipe centre decreases with the decrease of the bubble size similary to what is found in the simplified analysis in section 5.2.

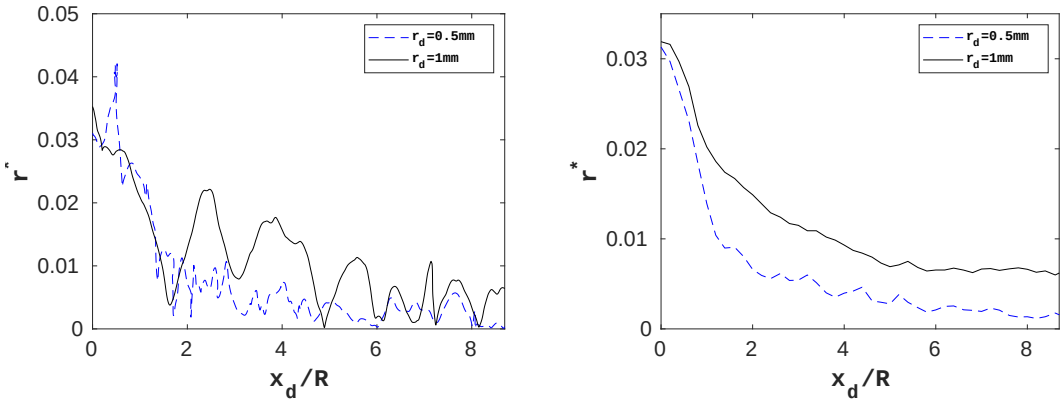

Figure 5.14: Comparison of the instantaneous (left) and mean (right) bubbles radial position in (m) as function of the axial position normalized by the pipe radius for bubbles of radius $r_d = 0.5mm$ vs $r_d = 1mm$.

Since we are interested in the migration process and that the radial drag force is found to be weaker than both the virtual mass and lift in the radial direction, we will focus on the evolution of the lift and virtual mass while comparing between the two cases $r_d = 0.5mm$ and $r_d = 1mm$. Figure 5.15 shows the mean radial lift and virtual mass normalized by the buoyancy force $F_B = g\rho_c V_d$ for bubbles of 1mm radius versus bubbles of 0.5mm radius. With decreasing the bubble size, the virtual mass decreases while keeping a negative sign to represent a centripetal effect. The lift force is mainly negative right after the swirl element and becomes weaker afterwards. The overall evolution of both forces for the two bubble sizes is the same in terms of centripetal/centrifugal effects but is propotional to the bubble

size in terms of magnitude as the lift and virtual mass are propotional to the bubble volume. And this is what explains the increase of the migration time due to the decrease of the magnitude of the radial forces linked to the bubble size.
The normalized forces do not collapse onto a single curve since the lift and virtual mass do not only depend on the bubble volume but also on the continuous phase velocity at the bubble position which is different between the two cases $r_d = 0.5mm$ and $r_d = 1mm$ (see Fig. 5.14).

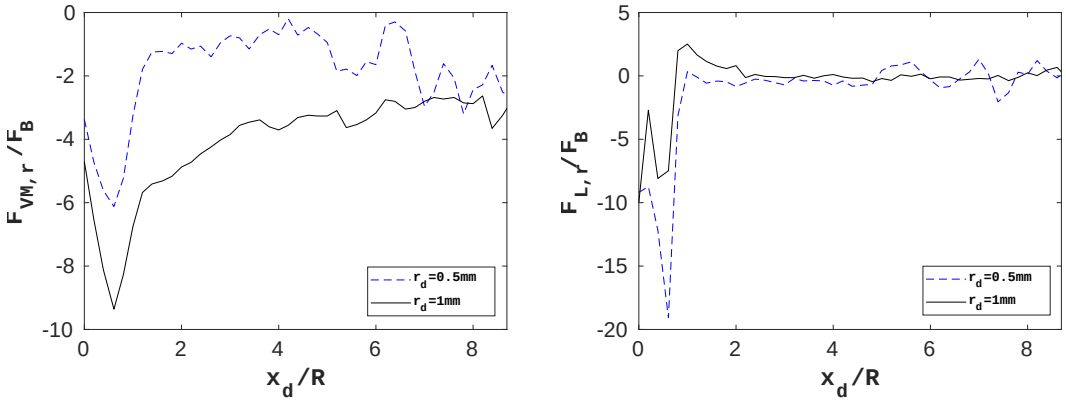

Figure 5.15: The averaged radial components of the lift and virtual mass normalized by the buoyancy F_B as function of the axial position normalized by the separator radius of two radius cases: $r_d = 0.5mm$ vs $r_d = 1mm$.

Regarding the fluctuations, the RMS of the radial lift and virtual mass normalized by the buoyancy F_B are plotted in Fig.5.16. The increase of the bubble size leads to a decay of the RMS and this is why the evolution of the instantaneous radial position of the bubble contains less fluctuations. The bubbles move slower thus they are not subject to high unsteadiness of the continuous phase. Similarly, the normalized radial lift and virtual mass RMS are not the same because the $1mm$ and $0.5mm$ do not have the same radial position at the same axial position, which means not the same continuous phase velocity used in the forces definition.

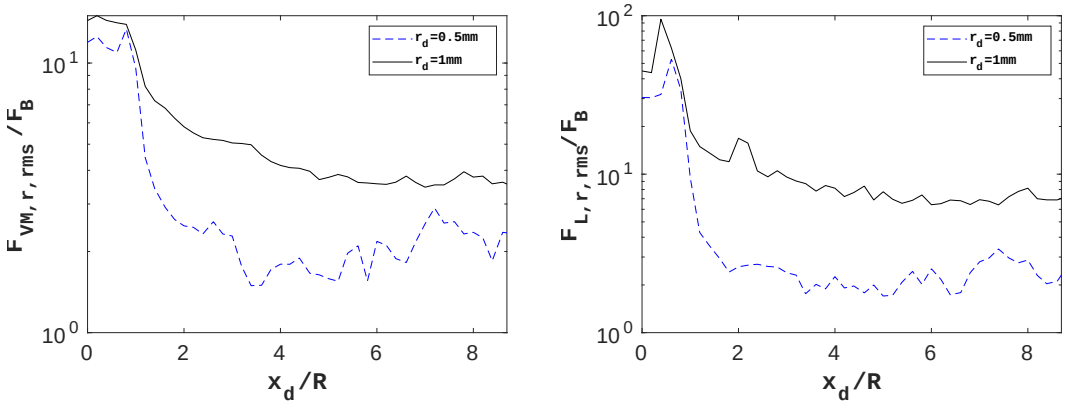

Figure 5.16: The RMS of the radial components of the lift and virtual mass normalized by the buoyancy F_B as function of the axial position normalized by the separator radius of two radius cases: $r_d = 0.5mm$ vs $r_d = 1mm$.

This study proves that the bubble size is an important parameter influencing the migration and capture times. A decrease of the bubble radius leads to a decrease of the mean and RMS of the radial lift and virtual mass as well as the buoyancy which increases the migration and capture times respectively. It is worth reminding, as previously discussed in subsection 5.3.2, that the migration motion overcomes the axial one in magnitude, which means that even though the increase of the bubble size speeds up the capture yet it contributes more in producing a centripetal effect ensuring the migration.

5.3.4 Effect of the flow Reynolds number

In chapter 4, we have observed from the numerical simulation of single-phase swirling flow that the centrifugal force normalized by the bulk velocity (i.e. u_θ^2/u_b^2) is independent of the Reynolds number. This implies that when increasing the flow rate, keeping all other parameters constant, leads to an increase of the centrifugal force. In this section we further study the effect of varying the Reynolds number (via the bulk velocity) on the bubble migration

A 3D simulation of a two-phase flow for $Re = 100,000$ in the separator is performed where the injected bubbles are of radius $r_d = 1mm$ ($r_d/R = 2.17 \times 10^{-2}$) and the results are again compared to the previous two-phase flow simulation with $Re = 50,000$ and the injected bubbles of the same radius $r_d = 1mm$ ($r_d/R = 2.17 \times 10^{-2}$).

Figure 5.17 represents the evolution of the instantaneous (left) and averaged (right) bubble radial position as function of the normalized axial position for both Reynolds numbers. Fluctuations are enhanced with the increase of Re which is also shown via the RMS profiles in Fig.5.19. The averaged radial position for $Re = 100,000$ is close to the one obtained for $Re = 50,000$. The averaged bubbles velocity, being higher in a flow with $Re = 100,000$, the calculated time migration, in this case, is $0.36s$. This means that the increase of Reynolds number accelerates the migration time. In fact, since the swirl strength is raised, the azimuthal velocity after the swirl element becomes more important and therefore the migration is faster. Moreover, the bubbles reach the outlet of the separator quicker than in the case of $Re = 50,000$.

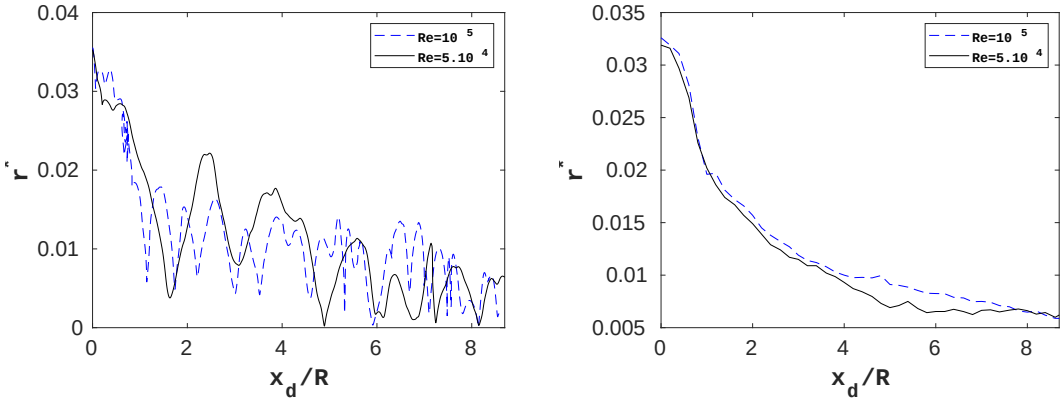

Figure 5.17: Comparison of the instantaneous (left) and mean (right) bubbles radial position in (m) as function of the axial position normalized by the pipe radius in a flow for $Re = 100,000$ vs $Re = 50,000$.

By plotting the mean radial components of the lift and virtual mass normalized

by $F_c = \rho_c V_d \omega^2 R$ with ω is the rotation velocity of the swirling flow in the separator, we can see that increasing the Reynolds number and by consequence the swirl strength, those forces are increased. Considering the sign and magnitude of each force, the centripetal effect of the virtual mass overcomes the centrifugal effect of the lift even when the latter becomes positive. Thus, the virtual mass is the dominant force.
The normalized radial profiles seem to be almost Re-independant where the averaged radial position is the same. The forces depends only on the rotation velocity since the bubbles size is unchanged between the two cases $Re = 100,000$ and $Re = 50,000$.

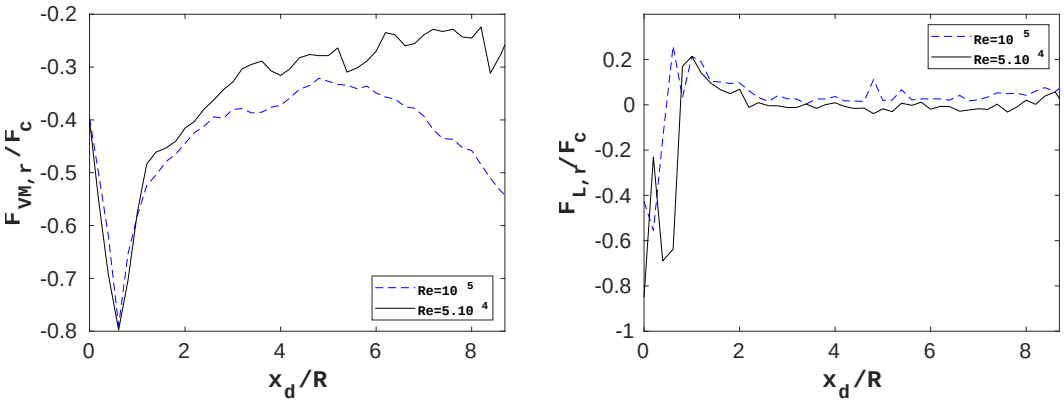

Figure 5.18: The averaged radial components of the lift and virtual mass normalized by F_c as function of the axial position normalized by the pipe radius in a flow of $Re = 100,000$ vs $Re = 50,000$.

Figure 5.19 shows the radial RMS of the lift and virtual mass normalized by $F_c = \rho_c V_d \omega^2 R$ as function of the axial position made dimensionless by the pipe radius. The intensity of the fluctuations increases with the increase of Reynolds number. The radial lift force fluctates more than the virtual mass and peaks are also observed similary to the case $Re = 50,000$. The dimensionless profiles are very close, allowing to predict the forces fluctuations for the same bubble size while varying Re.

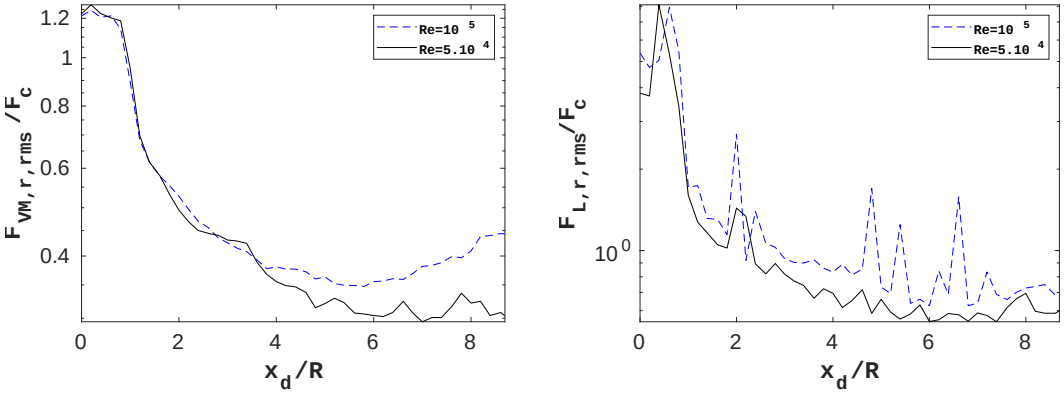

Figure 5.19: The RMS of the radial components of the lift and virtual mass normalized by F_c as function of the axial position normalized by the pipe radius in a flow of $Re = 100,000$ vs $Re = 50,000$.

As we have reported, the increase of the Reynolds number reduces the time migration which might be interesting from an industrial point of view as it gives an idea on when to activate the condition on the pick-up tube to recover the bubbles. However, one should consider the eventual instabilities of the gas core which can take place due to the high shear rate at the interface and the potential change of the flow regime as depicted in Fig. 5.1 and 5.3. In this section, we have characterized the process of bubble migration. Both the virtual mass and lift are found to be the controlling forces on the radial motion of the bubble. The intensity of the forces fluctuations proves the importance of taking into account the instantaneous and turbulent effect on the bubbles. Finally, the sensitivity study to the main parameters is done. An increase of the bubble size r_d leads to increasing the virtual mass and thus reducing the migration time. Similary, higher bulk velocity u_b gives higher swirl strength and therefore speeds up the migration. Tables 5.2 and 5.3 summarize the above conclusions:

Components	F_D	F_L	F_{VM}
Migration time	increase	increase	decrease

Table 5.2: Summary of the contribution of each force in the bubble migration process.

Parameter	r_d	u_b
Migration time	decrease	decrease
Capture time	decrease	decrease

Table 5.3: The effect of increasing r_d and u_b on the migration and capture times.

In the following, we first carry on the same simulation of two-phase flow of $Re = 50,000$ using Lagrangian Tracking with a continuous bubbles injection and we check out the performance of the separator. Later, the hybrid approach LT-VoF is activated to investigate the core formation and stability.

5.4 Numerical simulations of inline fluid separation

To study the inline separation, we first conduct the simulation using only the Lagrangian Traking and we evaluate the efficiency of separation. Then, the simulation is performed using the developed hybrid approach LT-VoF and the gas core is described.

Therefore, we consider 3D simulations of two-phase flow for which the numerical domain is the one previousely defined: a box of size $L_x \times L_y \times L_z = 0.92m \times 0.104m \times 0.104m$ made of $N_x \times N_y \times N_z$ cells. The mesh size Δ is the same as the one retained from the mesh sensitivity study reported in the previous chapter 4 such as: $R/\Delta = 40$. The flow is in the upwards direction, opposite to the gravity direction and the pick-up tube of radius $R_{pt} = 0.44R$ is located at $8R$ after the swirl element.

5.4.1 Simulations using Lagrangian Tracking

3D two-phase flow simulation of $Re = 50,000$ is performed using Lagrangian Tracking. A set of 1mm radius bubbles are injected continuously over the tail section $x_0 = 0.35m$ with a fixed volumetric rate $q = 5 \times 10^{-4} m^3/s$ following a Poisson distribution as already explained in 5.3.

Figure 5.20 visualizes snapshots of the two-phase flow simulation at different moments. The bubbles are colored in blue. Due to the centripetal force applied on them, they progressively migrate towards the pipe centre. All the bubbles with a radial position below the Light Phase Outlet (LPO) radius are colored in red. They are to be captured by the pick-up tube. In fact, at halfway between the swirl element tail section and the LPO, we can already observe that the majority of the bubbles are located within the operational zone of the pick-up tube. After $0.44s$ from the injection of the bubbles at the swirl tail section, we can see that the first set of bubbles reaches the pick-up tube which is the moment when the condition on the flow split should be activated in the pick-up tube to recover the light phase. This time may also serve as a characteristic time to take into consideration while building the controller since the valve should respond as fast as the separation process.

(a) $t = 0s$

(b) $t = 0.088s$

(c) $t = 0.176s$

(d) $t = 0.264s$

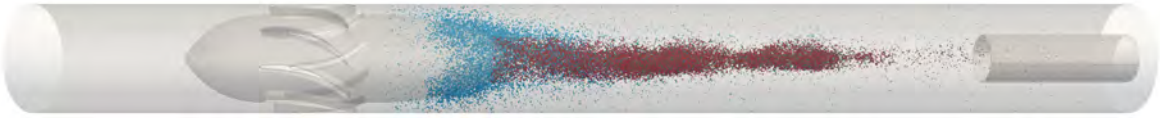

(e) $t = 0.352s$

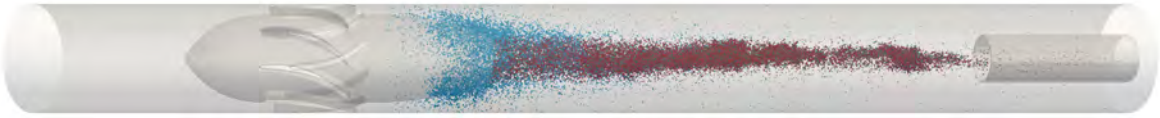

(f) $t = 0.44s$

Figure 5.20: Simulation of two-phase flow separation for $Re = 50,000$ using Lagrangian Tracking. The bubbles are presented in a blue color while those located at radial positions $r^* < R_{LPO}$ are colored in red.

Figure 5.21 illustrates trajectories of four bubbles in the separator. A quasi-spiral movement around the pipe centre is observed with a fluctuating and decreasing radial positions as the bubbles are being transported towards the LPO. Figure 5.22 shows the evolution of the radial positions of the four bubbles as function of the axial position normalized by the pipe radius. We notice that although the black and blue bubbles have the same initial radius and axial positions yet their trajectories are different due to the difference in their initial azimuthal position thus the effect of the unsteadiness and non-symmetry of the continuous phase velocity reported in chapter 4 on the bubbles force balance.
It is worth mentioning that the capture time depends on the pick-up tube positionning because by increasing the distance between the swirl element and LPO, the capture time systematically increases as well as the length of the separator. Therefore, from an industrial point of view, the position of the pick-up tube should be

chosen in a way to simultaneously reduce the separator size, respect the minimum needed response time of the tomographs and controller used in the experiments [15] and mainly assure a higher separation efficiency. The latter is evaluated in the following.

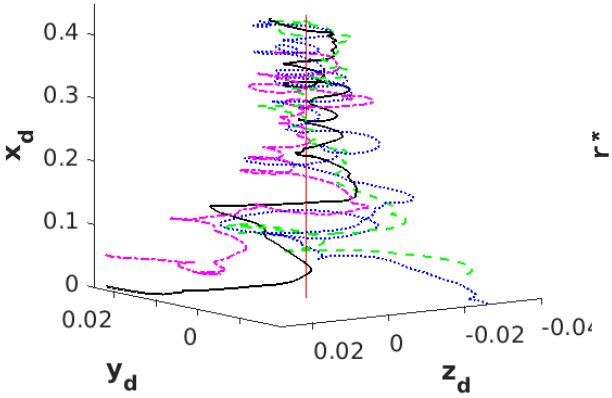

Figure 5.21: Trajectories of four bubbles in swirling flow in the separator.
The red line represents the pipe centre.

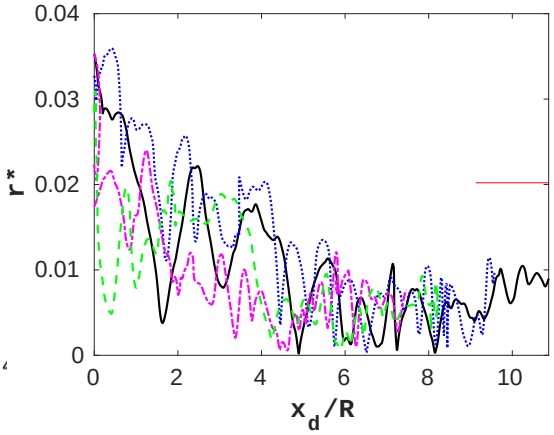

Figure 5.22: The bubbles radial positions in (m) as function of the normalized axial position. The red line represents the location of the pick-up tube.

5.4.1.1 Efficiency of separation

At $t = 0.44s$, we activate the condition on the flow split $FS = Q_{LPO}/Q_{inlet}$ at the pick-up tube to recover the light phase as explained in section 4.4. And in order to evaluate the performance of the inline separator, we introduce the efficiency of separation eff calculated at the pick-up tube inlet as the ratio of the cumulative volume of bubbles passing through the LPO over the cumulative volume of all the bubbles passing through the entire cross-section (LPO+HPO).

$$eff = \frac{\Sigma V_d^{LPO,inlet}}{\Sigma V_d^{LPO,inlet} + \Sigma V_d^{HPO,inlet}} \tag{5.19}$$

For the same simulation presented in subsection 5.4.1, we compare the separation efficiency obtained by imposing a flow split of $FS = 0.3$ to the one for a flow split of $FS = 0.5$. Figure 5.23 illustrates the suction of the bubbles by the pick-up tube for the two flow splits at $t = 0.5s$. With a higher flow split, the dispersed phase moves axially faster inside the LPO since the velocity is higher in this case than in the case of $FS = 0.3$ which reduces the capture time.

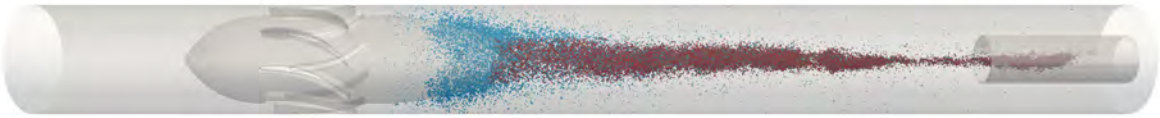

(a) $FS = 0.3$

(b) $FS = 0.5$

Figure 5.23: Simulation of two-phase flow separation. The bubbles are presented by a blue color while those situated at radial position $r^* < R_{LPO}$ are colored in red for FS=0.3 and FS=0.5

Figure 5.24 represents the time evolution of the separation efficiency for both flow splits averaged over $50\Delta t$. Indeed the decrease of the flow split increases the capture time, however it increases the efficiency of separation since the centrifugal force of the continuous phase which pushes the bubbles to the pipe centre is less influenced than in the case of a flow split $FS = 0.5$ close to the pick-up tube. This was reported in the study of the effect of FS on the azimuthal velocity profile for single-phase flow in the previous chapter. Bubbles located close to the LPO are then subject to a higher swirl strength for $FS = 0.3$ and might still be captured. Overall, by calculating the mean efficiency for both flow splits, we find that $eff(FS = 0.3) = 96\%$ and $eff(FS = 0.5) = 95\%$ which proves that the inline separator is efficient from an industrial point of view. It is also possible to consider imposing a dynamic condition on the flow split, which changes in time to further increase the efficiency of separation. Numerically, it can be simulated using the proposed approach in chapter 4 and experimentally it is doable using a controller which changes the condition on the valve depending on the arriving gas core at the pick-up tube.

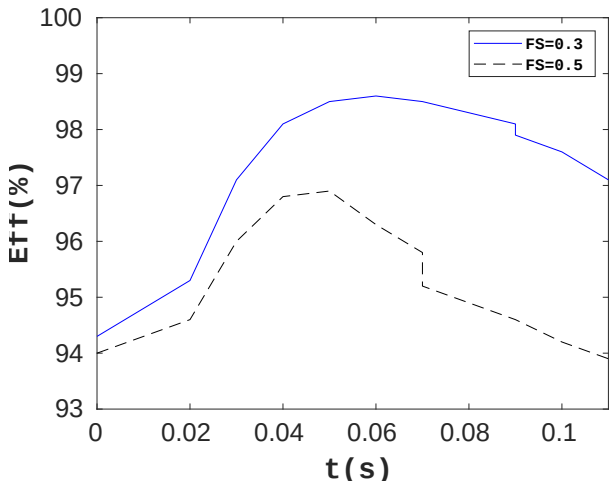

Figure 5.24: Comparison of the time-evolution of the separation efficiency for two flow splits: $FS = 0.3$ and $FS = 0.5$

The fact that the averaged efficiency does not attain 100% means that not all bubbles at the pick-up tube inlet are captured. This is due to the turbulent dis-

persion effect since the bubbles coalescence is not considered and no core is formed. This is why it is interesting to introduce a hybrid approach LT-VoF. Using the latter, the gas core formation and stability is simulated in the following.

5.4.2 Simulations using hybrid LT/VoF

In this subsection, numerical simulations of two-phase flow in the separator are carried out using the hybrid approach LT/VoF allowing to transform accumulated bubbles from the Lagrangian framework into a gas core and predict its dynamics using VoF as proposed in chapter 2. Since we are simulating an air/water two-phase flow, the problem of spurious current is present as detailed in subsection 2.6.3. To avoid it, we conduct a similarity simulation as proposed in 2.6.4 which consists in reducing σ/μ_w while keeping the same dimentionless numbers. In the case of the inline separator, the gravity is considered as a physical parameter thus an extra dimensionless number is added, namely the Bond number. The physical parameters representing the system are as follow:

$$R^* = r_d/R \tag{5.20}$$

$$\rho^* = \rho_w/\rho_g \tag{5.21}$$

$$\mu^* = \mu_w/\mu_g \tag{5.22}$$

$$Re = u_b D/\nu_w \tag{5.23}$$

$$We = \rho_w u_b^2 D/\sigma \tag{5.24}$$

$$Bo = (\rho_w - \rho_g) g D^2/\sigma \tag{5.25}$$

For a fixed R^*, Table 5.4 summarizes the calculation of the dimensionless numbers for two self-similarity gas/water systems characterizing the two-phase flow in the separator.

Variables (SI)	gas/water system	similarity simulation
ρ_w	1000	726
μ_w	0.001	10^{-5}
ρ_g	1	0.726
μ_g	2×10^{-5}	2×10^{-7}
u_b	0.54	7.5×10^{-3}
σ	0.072	10^{-5}
g	9.81	1.88×10^{-3}
ρ^*	1000	1000
μ^*	50	50
Re	50,000	50,000
We	$3.75 \times 10^{+2}$	$3.75 \times 10^{+2}$
Bo	$1.15 \times 10^{+3}$	$1.15 \times 10^{+3}$
σ/μ_w	72	1

Table 5.4: Dimensional analysis for similarity systems simulation of the separator.

Therefore, to simulate the two-phase flow separation using LT/VoF, the similarity system presented in 5.4 is considered in all the following. Both fluids are

considered incompressible. Results are made dimensionless, the time is normalized by D/u_b and the velocity by u_b.

The same 3D two-phase flow simulation for $Re = 50,000$ reported in subsection 5.4.1 is performed this time using the hybrid LT-VoF approach. Figure 5.25 shows the bubbles which are still in the Lagrangian framework in blue color, the formation of the gas core from the accumulated bubbles in red color, the gas volume fraction in a cross section at $x = 0.5R$ (right) after the swirl element and the gas core fraction in a section along the separator (bottom). At first, the bubbles continuousely injected are all simulated using the Lagrangian Tracking (Fig.5.25 (a)). Then, the bubbles reaching the pipe centre are transformed into VoF following the method described in section 2.7 (Fig.5.25 (b)). As other bubbles touch the gas core, the latter grows and its radius becomes important especially right after the separator since the bubbles are not constraint to reach the pipe centre to switch to VoF but only to be in contact with the core interface (Fig.5.25 (c)). The gas core has a form of a cone that is stretched in the axial direction towards the LPO due to buoyancy (Fig.5.25 (d)). As the injection continues, the gas core increases in size and progressively evolves to a cylindrical shape (Fig.5.25 (d) to (g)). An instability is observed at the interface along the gas core, it propagates radially and starts with small bursts at the interface leading to the divergence of the calculation at $t^* = 0.44$.

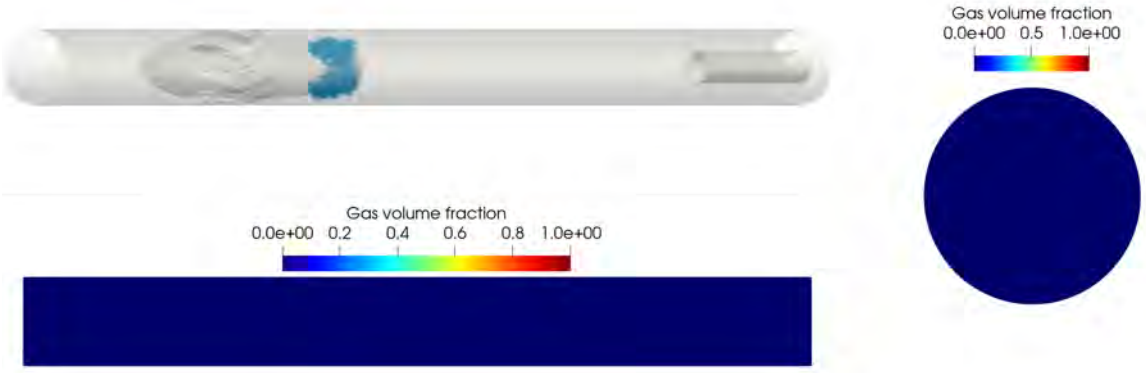

(a) $t^* = 0$

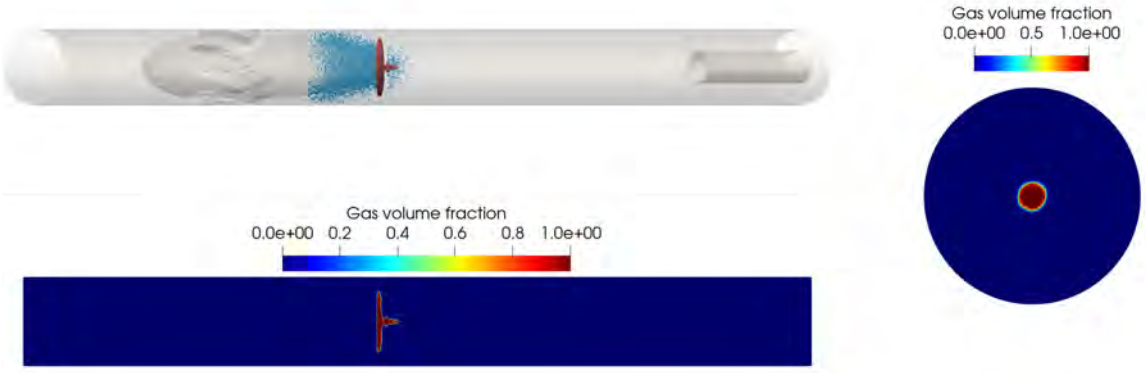

(b) $t^* = 0.19$

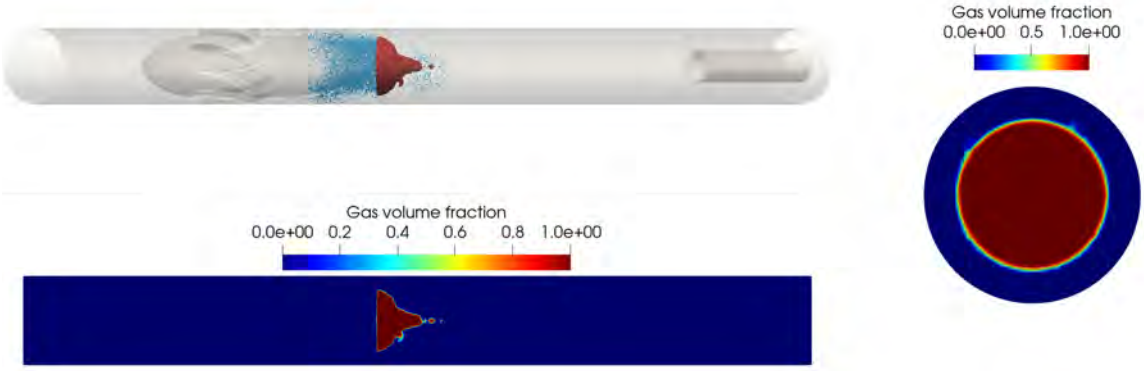

(c) $t^* = 0.27$

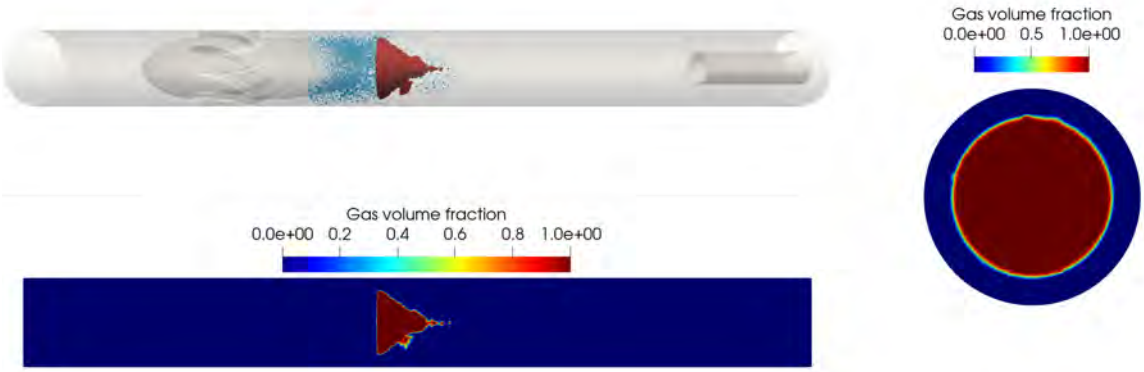

(d) $t^* = 0.31$

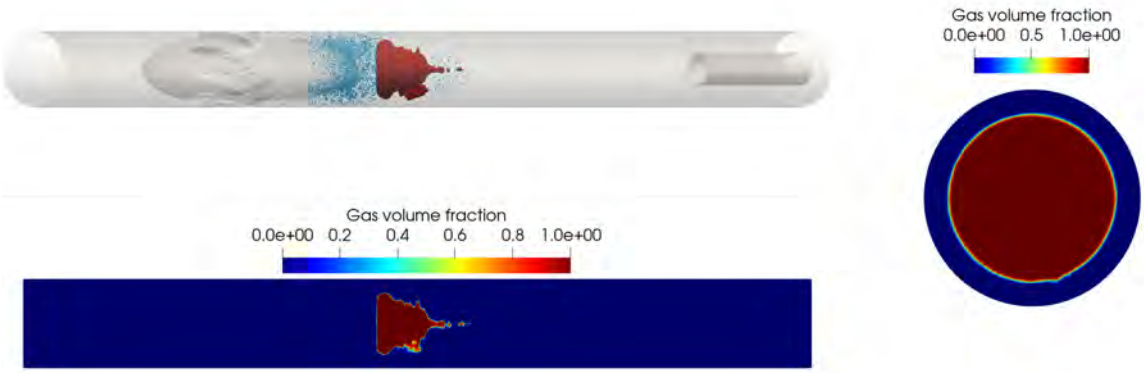

(e) $t^* = 0.34$

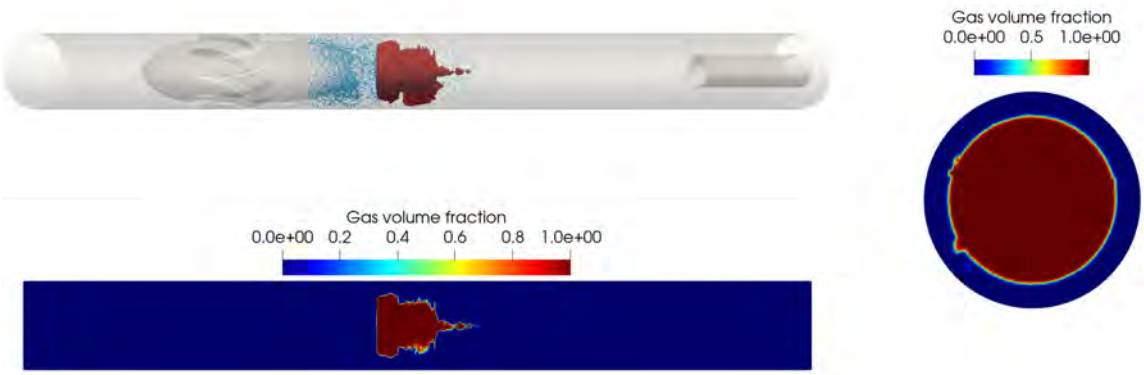

(f) $t^* = 0.4$

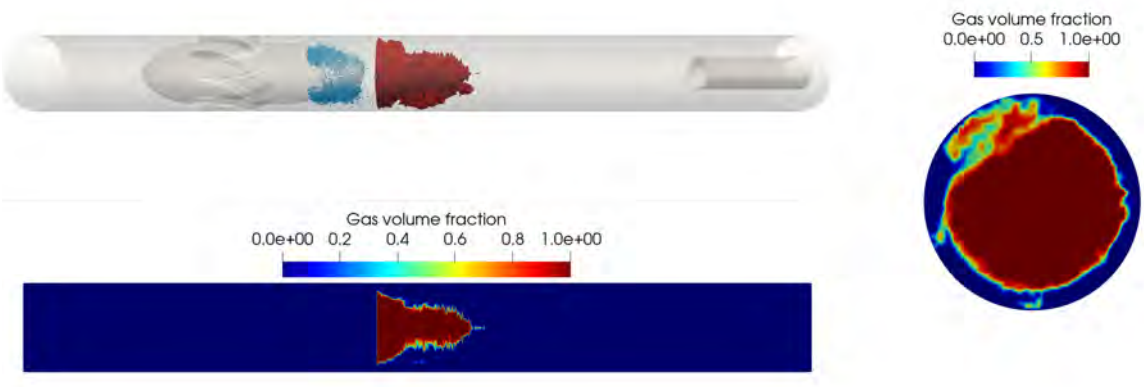

(g) $t^* = 0.44$

Figure 5.25: Simulation of two-phase flow separation for $Re = 50,000$ using hybrid LT-VoF with a continuous bubbles injection. The bubbles are presented by a blue color. The gas core is colored in red. The gas volume fraction over a cross section $x = 0.5R$ after the swirl element is showed on the right and along the separator in the bottom.

Figure 5.26 shows the distribution of the gas volume fraction (top) and the normalized velocity field (bottom) at $t^* = 0.4$ over four different sections along the separator located respectively from left to right at: $x = 0.76R$, $x = 1.2R$, $x = 1.41R$, $x = 1.52R$ after the swirl element. The instability is present in the four locations and has a similar pattern as the swirling burst observed in the experiments [6] and reported in Fig. 5.1 for higher gas volume fraction where the bursts spread radially till reaching the pipe wall. From the simulation, those instabilities are characterized by a high velocity magnitude which destablizes the simulation later than $t^* = 0.44$.

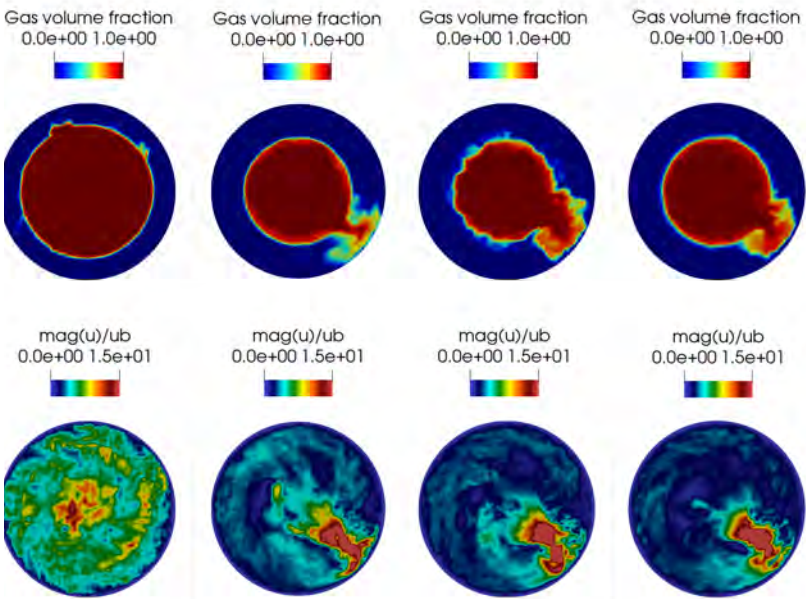

Figure 5.26: Gas volume fraction in different cross sections along the separator where an instability is developed with the corresponding velocity field normalized by the bulk velocity.

To reduce the growth of a significant core radius right after the separator (see Fig. 5.25(b)), we test a one-time bubbles injection all along the separator as illustrated in Fig. 5.27. The bubbles of radius 1mm are injected with the continuous phase velocity. The core is not yet formed.

Figure 5.27: A one-time injection of a set of 70,000 bubbles after the swirl element a swirling flow for $Re = 50,000$ in the separator.

Figure 5.28 shows the bubbles migration and core formation over time. We can see that the bubbles follow the swirling spiral shape of the continuous phase. The accumulated bubbles are transformed into a gas core resolved using VoF. Since the centrifugal force decreases along the separator, the accumulation of the bubbles is more significant close to the swirl element leading to a larger gas core radius at this location than far from it as shown in Fig. 5.28(a,b). As the migration of bubbles continues, the gas core grows, and while rotating, the core is transported towards the pick-up tube due to weight and buoyancy. Its size is also changing along the separator, more gas is flowing towards the LPO, the core radius increases close to the LPO and decreases close to the swirl element. By activating the condition on the flow split $FS = 0.3$ at the pick-up tube, the core is recovered by the LPO, but then gets diffused because of the high velocity inside the LPO.

The temporal evolution of the gas core fraction across the separator at $x = 0.5R$ presented on the right side of Fig. 5.28 illustrates that the core is cylindrical at the begining of the simulation following the proposed algorithm of the hybrid LT-VoF. Then, it gets slightly deformed while rotating yet it remains centered inside the separator.

Bursts are observed once the core radius is large enough inside the pipe. It induces the increase of the liquid velocity between the core and the pipe wall thus increasing the shear close to the core interface. This promotes the interface destabilisation both physically and numerically as shown in Fig. 5.28 (i). This is clearly illustrated in Fig. 5.29 (left) and further discussed in the following paragraph.

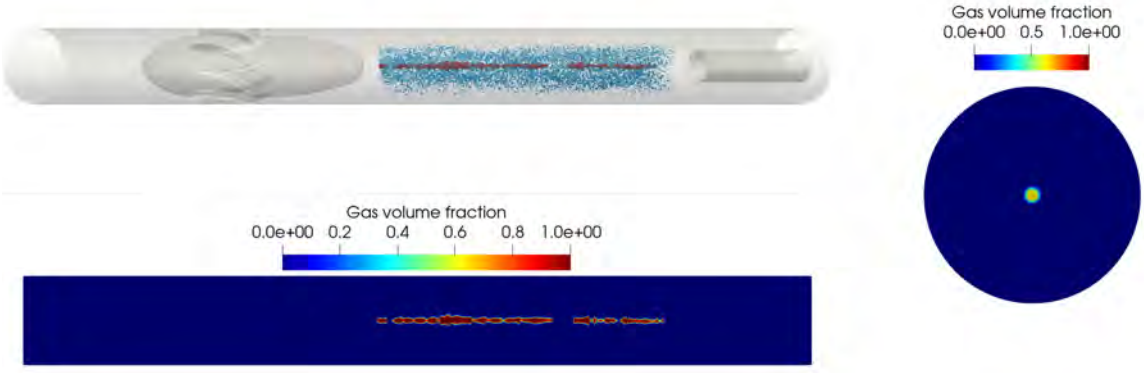

(a) $t^* = 0.086$

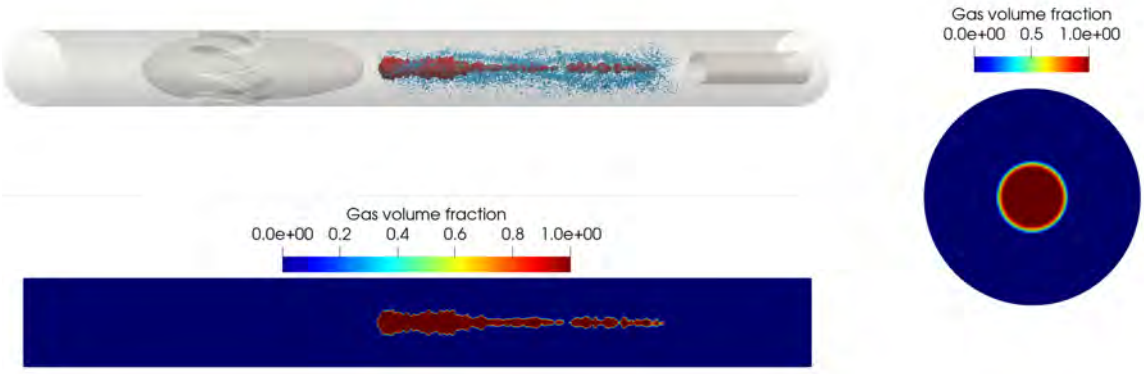

(b) $t^* = 0.11$

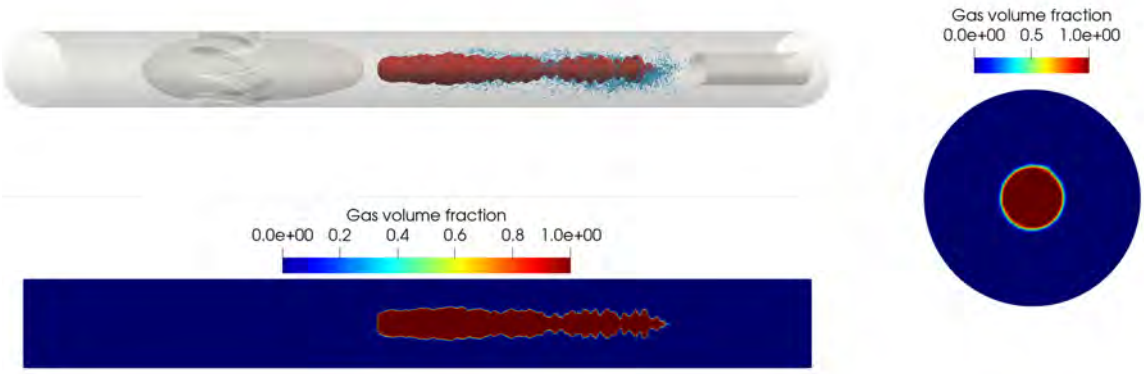

(c) $t^* = 0.17$

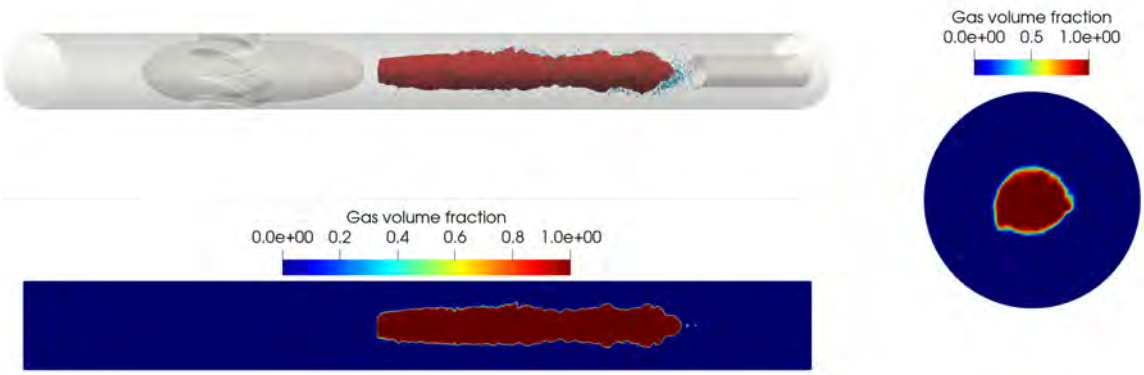

(d) $t^* = 0.3$

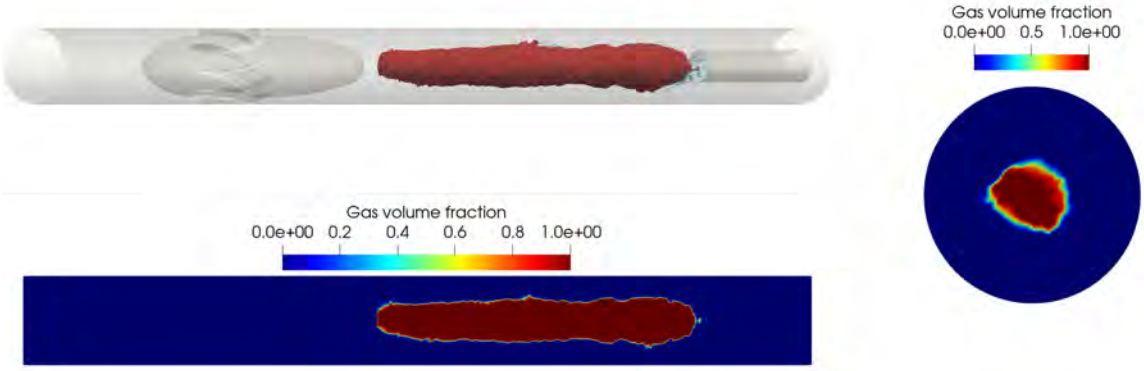

(e) $t^* = 0.42$

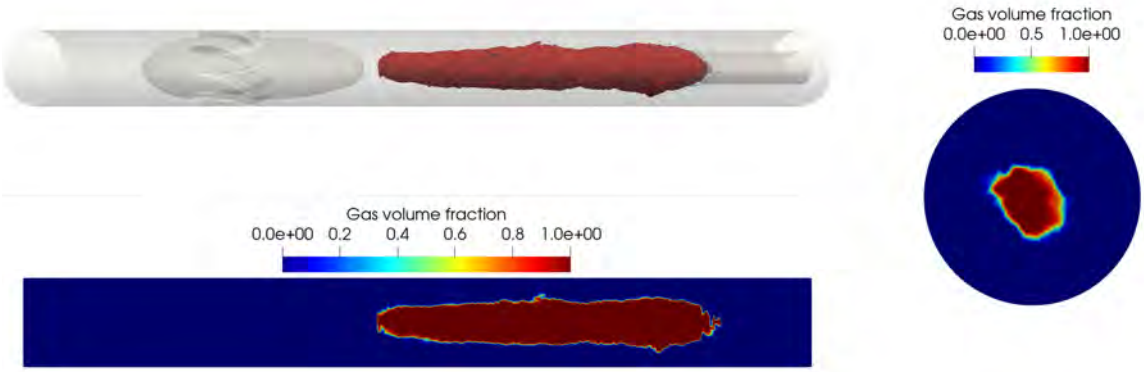

(f) $t^* = 0.46$

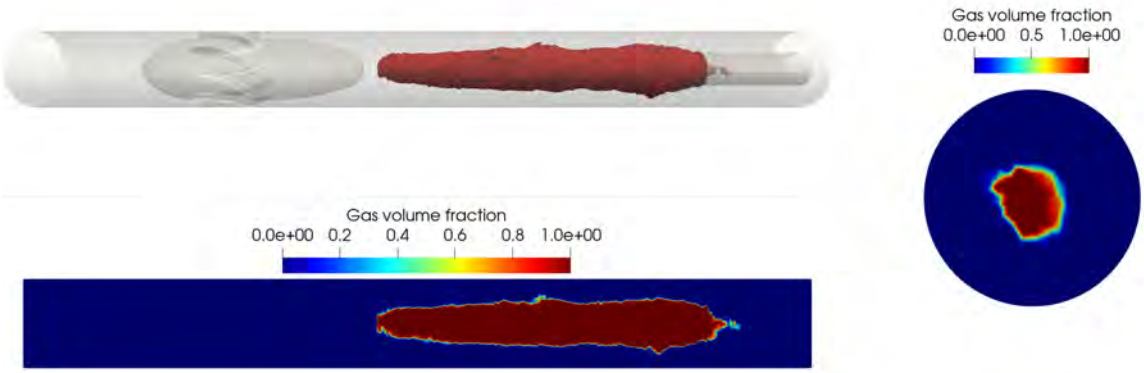

(g) $t^* = 0.47$

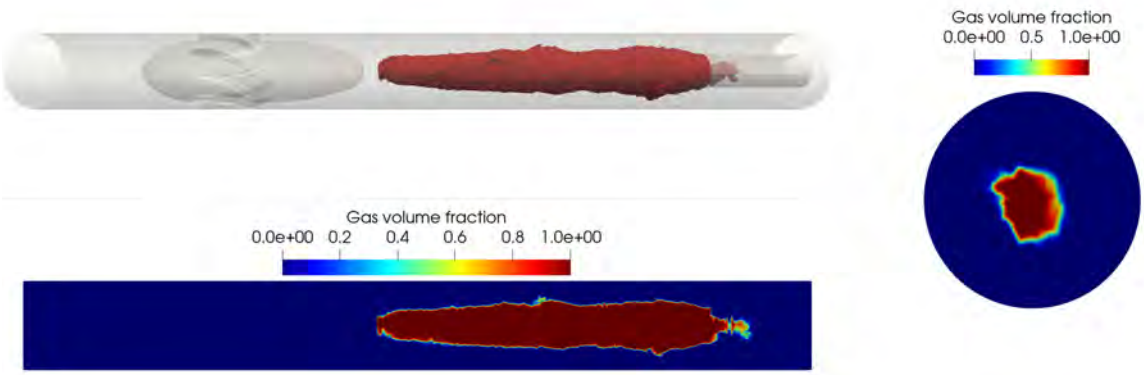

(h) $t^* = 0.48$

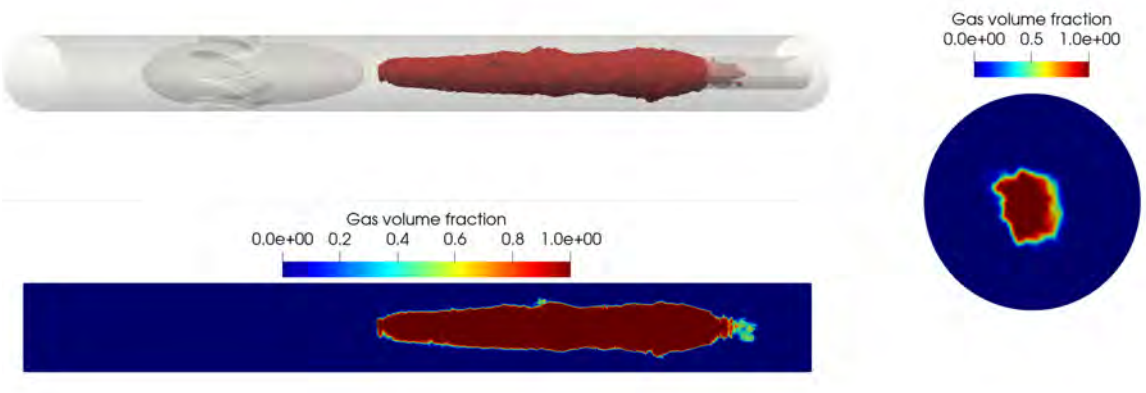

(i) $t^* = 0,486$

Figure 5.28: Simulation of two-phase flow separation for $Re = 50,000$ using hybrid LT-VoF with a one-time bubbles injection. The bubbles are presented by a blue color. The gas core is colored in red. The gas volume fraction over a cross section $x = 0.5R$ after the swirl element is showed on the right and along the separator in the bottom.

Figure 5.29 represents a zoom on the gas core interface which corresponds to $C = 0.5$ (on the left) and the axial velocity normalized by the bulk velocity at a cross section $2R$ after the swirl element (on the right). Up to $t^* = 0.17$, the gas fraction is about 8%, the core has a column shape which looks like the swirling column pattern 5.1(a). As the gas fraction increases, the core diameter increases, the core is deformed and small bursts are formed at the interface. The core keeps rotating in the same direction as the continuous phase as shown by the streamlines but moves towards the LPO. Its axial velocity is positive and is around 5 times the bulk velocity. By comparing this with the single-phase flow simulation of the same $Re = 50,000$ reported in chapter 4 in which a recirculation zone is detected and shown in Fig. 4.16 where the axial velocity is negative, we can say that the effect of the buoyancy of the gas core overcomes the effect of the reverse flow. This is also observed in the simulation of the inline separation using only the Lagragian Tracking in which the bubbles, although located in a recirculation zone, have a positive axial velocity.

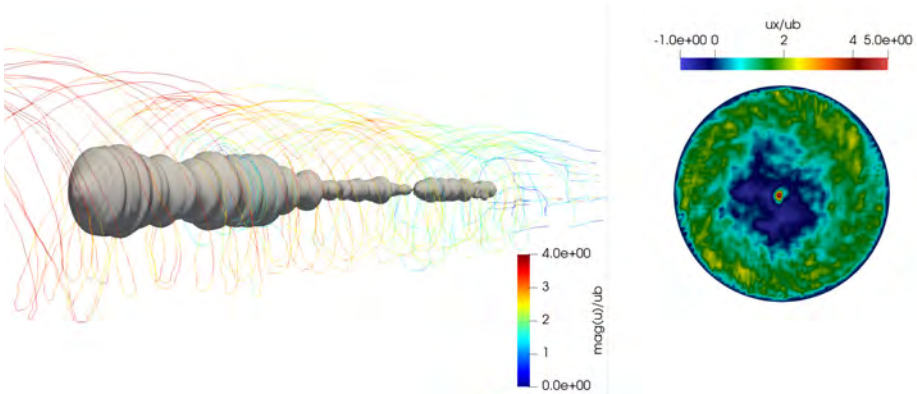

(a) $t^* = 0.11$

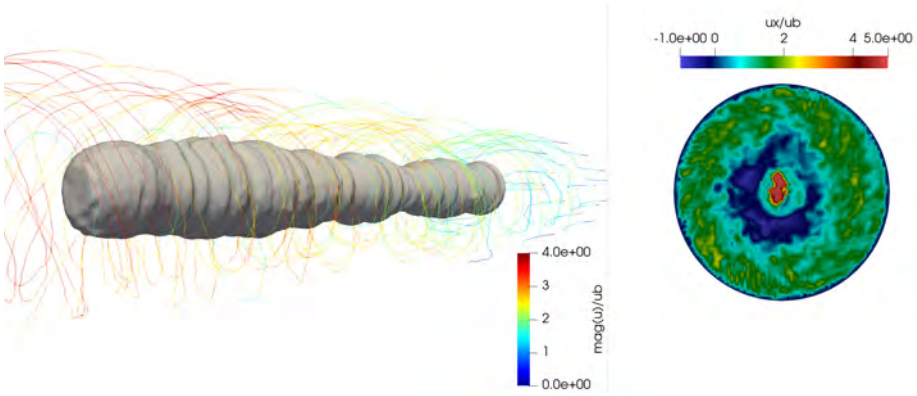

(b) $t^* = 0.17$

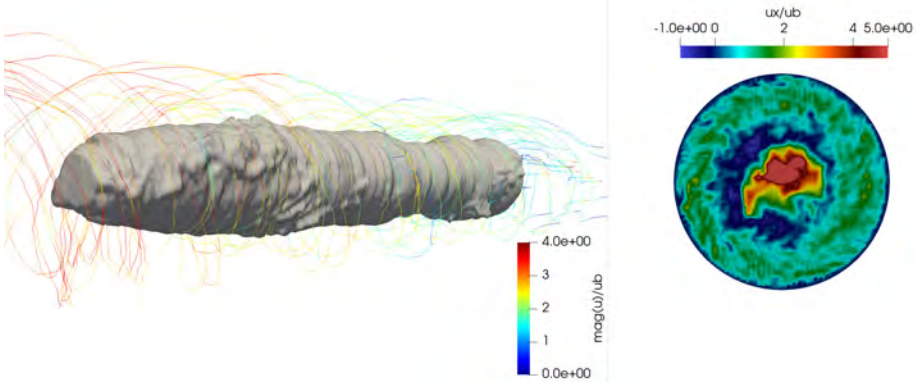

(c) $t^* = 0.3$

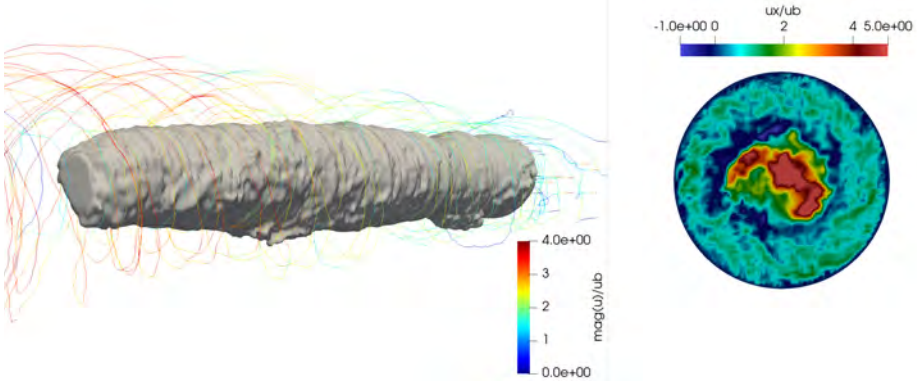

(d) $t^* = 0.42$

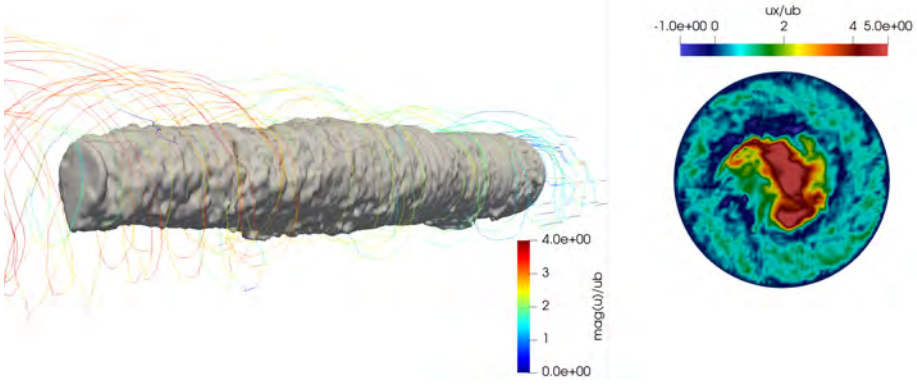

(e) $t^* = 0.46$

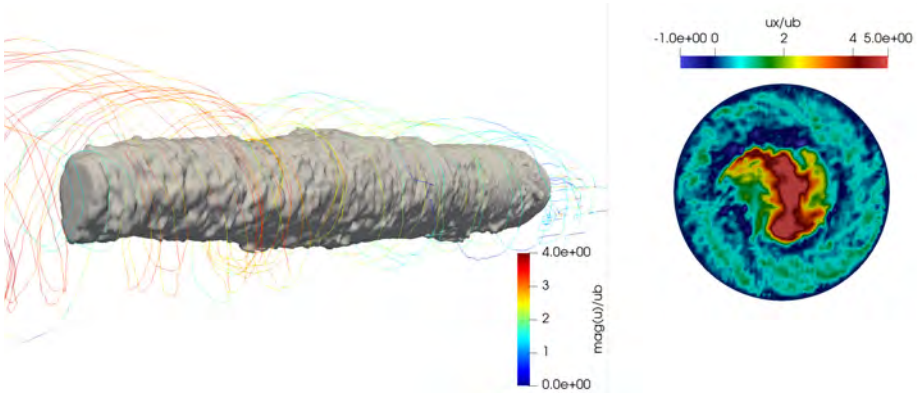

(f) $t^* = 0.47$

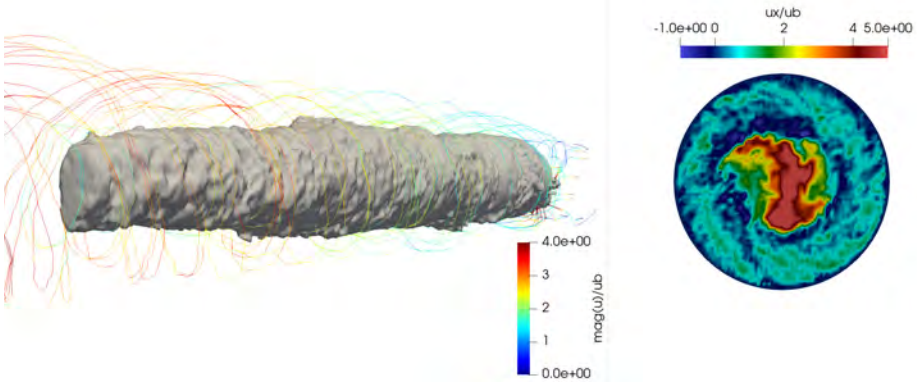

(g) $t^* = 0.48$

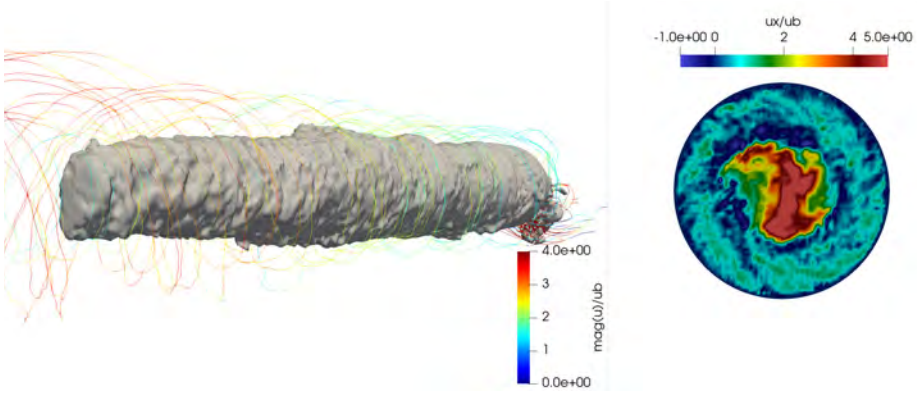

(h) $t^* = 0,486$

Figure 5.29: Simulation of two-phase flow separation for $Re = 50,000$: The gas core interface (left) with the streamlines. The axial velocity normalized by the bulk velocity u_b over a cross section located at $2R$ after the swirl element the gas core (right). The flow is from left to right in the opposite direction of gravity.

Finally, the same simulation is performed for a two-phase flow with $Re = 25,000$ to check the effect of the swirl strength on the gas core stability. The numerical simulation has showed that the bubbles accumulation is slower in comparison to the case of $Re = 50,000$ as expected and reported in subsection 5.3.4. The gas core is formed and is stable at first as illustrated for instance in Fig. 5.30, then small bursts appear at the interface. They are characterized by high velocites as presented in Fig. 5.31.

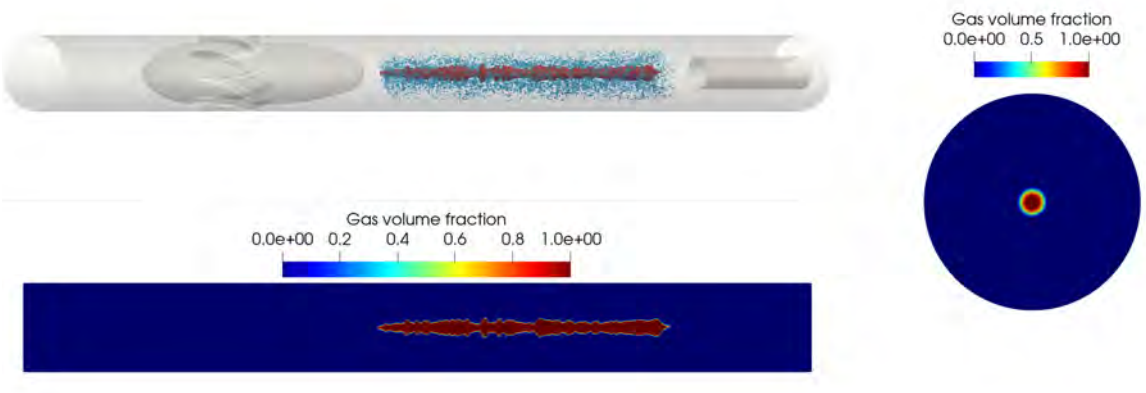

Figure 5.30: Simulation of two-phase flow separation for $Re = 25,000$ using hybrid LT-VoF with a one-time bubbles injection.

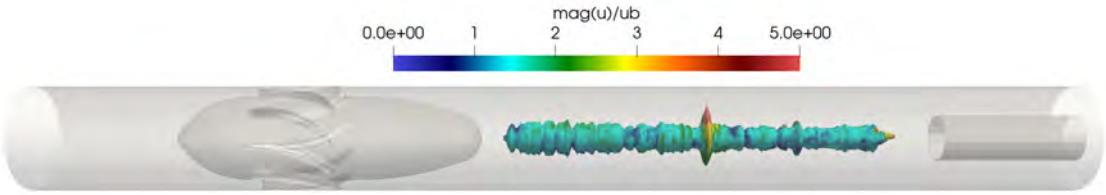

Figure 5.31: The normalized velocity magnitude at the gas core interface when the instability takes place.

The hybrid approach have allowed to simulate the two-phase flow inline separation and revealed the possible instabilities and core deformations which can happen inside the separator. Common patterns of the gas core are observed between the numerical simulations and the first experiments which confirms qualitatively the results. However, other numerical constraints are encountered while simulating such a complex process notably the resolution of the bursts at the interface both in time and space.

5.4.3 Investigation of the gas core instability in a swirling flow

In the process of investigating the reason behind the instability of the core interface in the separator, we consider the simplified test case of a cylindrical gas core in a rotating flow. The numerical and physical conditions are fixed in a way to match the closest flow configuration existing in the separator namely the same mesh resolution $R/\Delta = 40$, the use of the numerical gas/water system to avoid any possible spurious currents as detailled in subsection 2.6.3. The time is normalized by $t_\sigma = \sqrt{D^2\rho_w/\sigma}$. The rotation velocity of the cylinder ω is fixed to the one obtained in the separator right after the swirl element for $Re = Du_b/\nu_w = 50,000$. The Reynolds number of the flow in the rotating cylinder is defined based on ω as: $Re_\omega = \omega R^2/\nu_w$. The radius of the core corresponds to a gas volume fraction equal to 10% as the one previously simulated inside the separator, thus $R_{core}/R = 0.315$ which gives $R_{core}/\Delta \approx 12.5$. Furthermore, periodic boundary conditions at the inlet and outlet of the pipe are

imposed and the gravity is not considered. At first, a single-phase flow is simulated inside a rotating cylinder till the solid rotation velocity profile is established, then the core is initialized as shown in Fig.5.32. First, only the VoF solver is used then the need of a sub-grid model for turbulence is discussed.

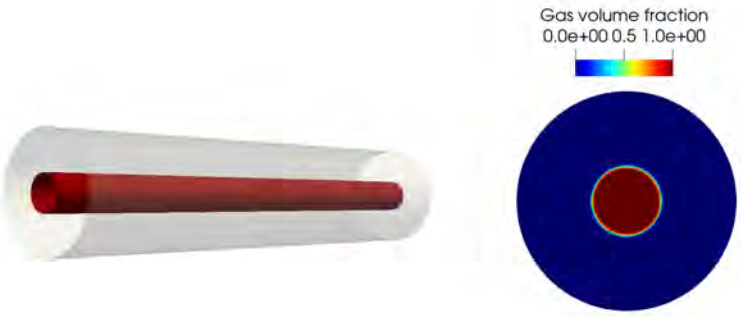

Figure 5.32: Initialisation of a gas core in a rotating flow, on the right is shown the gas volume fraction in a cross section.

Figure 5.33 illustrates the temporal evolution of the interface of an unstable gas core. At $t^* = 0.0016$, the interface is deformed following a polygonal shape. The core continues to rotate while the interface instability is being developped in the radial direction. Such a deformation was observed experimentally in a study of rotating polygon instability of a swirling free surface flow [87]. As time goes on, the instability spreads widely till the point when the interface is not resolved, the mass is lost and the simulation diverges at $t^* = 0.147$ which can be an indication of the developpement of a numerical instability. This seems to indicate that the first stage of interface deformation observed here, and certainly previously when bursts are developped, is captured by the solver. Then, the instabilities result in structures of size smaller than the interface (sub-grid phenomena which are not modelled here). This point will be discussed later.

Since the centrifugal force generated by the rotation velocity is a direct parameter which can be controlling the core deformation, an investigation of the behaviour of the core at lower rotation velocities is done to characterize the occurrence of the instability and find a case where the core is stable. The size of the core is kept the same $R_{core}/R = 0.315$.

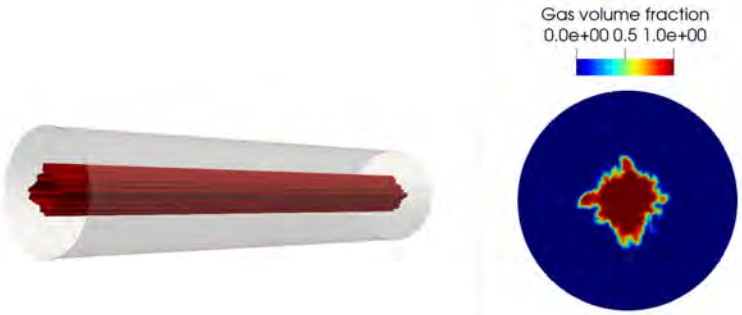

(a) $t^* = 0.0016$

(b) $t^* = 0.002$

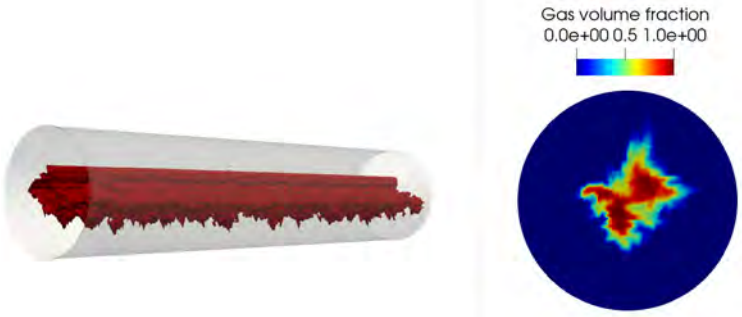

(c) $t^* = 0.003$

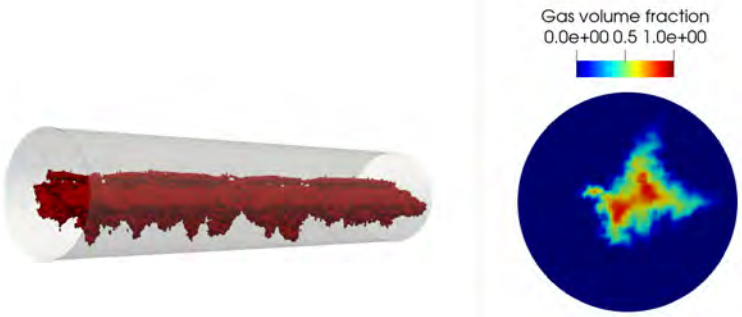

(d) $t^* = 0.0035$

Figure 5.33: Simulation of gas core in a rotating flow: $Re_\omega = 1.06 \times 10^5$, $R_{core}/R = 0.315$

Figure 5.34 represents the temporal evolution of the gas volume fraction for three different rotation velocities corresponding to: $Re_\omega = 2.12 \times 10^4$, $Re_\omega = 4.23 \times 10^4$ and $Re_\omega = 1.06 \times 10^5$ and for which the final gas core snapshots are at $t^* = 0.237$, $t^* = 0.0067$ and $t^* = 0.0035$ respectively.

For $Re_\omega = 4.23 \times 10^4$, the polygonal instability is observed at the beginning then the instability diffuses the interface similary to the case of $Re_\omega = 1.06 \times 10^5$. We

should note that by increasing the rotation velocity, the instability happens faster. Finally, by reducing the rotation velocity, the core remains stable while rotating and no deformation is obtained. This comparison shows the effect of increasing the rotation velocity in developping the instability and explains, to some extent, why the instabilities of the core in the separator take place with the considered Reynolds number.

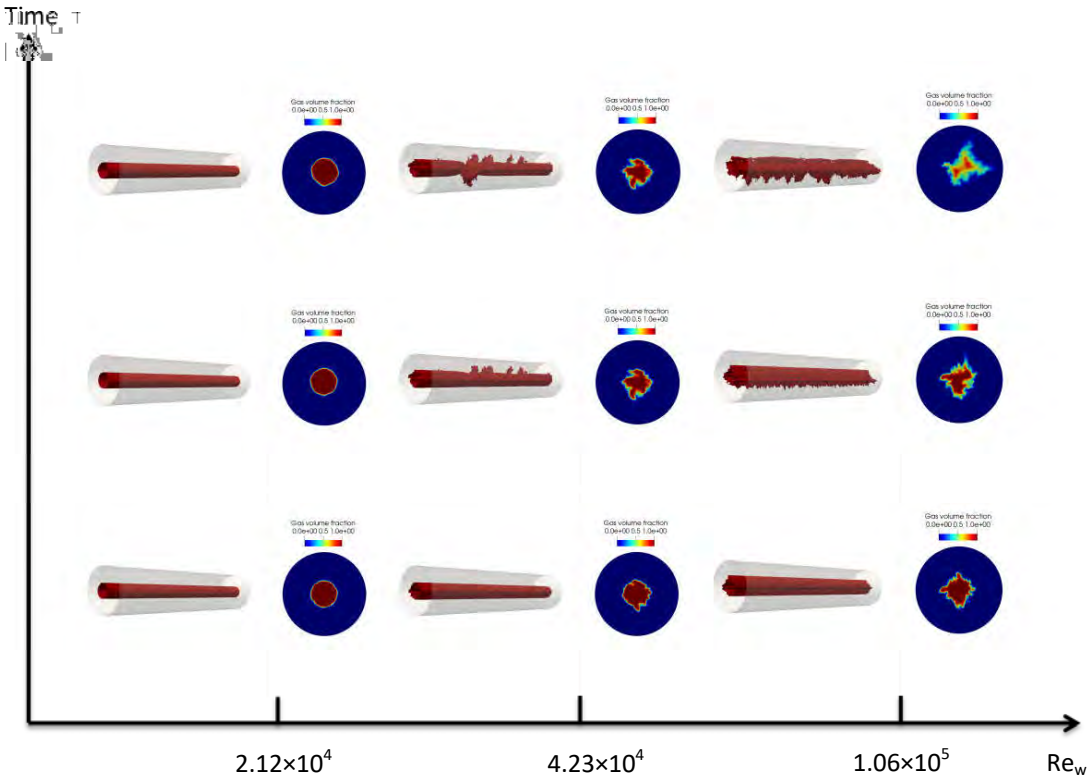

Figure 5.34: Map of the stability of a gas core of radius $R_{core} = 0.315R$ in a rotating flow with three different Re_ω: $Re_\omega = 2.12 \times 10^4$, $Re_\omega = 4.23 \times 10^4$ and $Re_\omega = 1.06 \times 10^5$ and for which the final gas core snapshots are at $t^* = 0.237$, $t^* = 0.0067$ and $t^* = 0.0035$ respectively.

To fairely compare between the numerical results of the swirling core in the separator for $Re = 50,000$ and the one inside the rotating cylinder, another detail should be taken into account to wit the turbulence modelling. In fact, the numerical simulations of the separator were done using LES, therefore, we conduct the same simulation of a gas core of radius $R_{core}/R = 0.315$ in a rotating flow using the mixed dynamic Smagorinsky model.

It is worth mentionning that with the CFD code we are using, only the transport of the volume fraction by the filtered velocity is done while the extra term appearing due to the filtering operation of the transport equation: $\overline{\mathbf{u} \cdot \nabla C} - \overline{\mathbf{u}} \cdot \overline{\nabla C}$ is neglected. The surface tension force considered is also not the filtered one which is expressed as: $\sigma(\overline{k_{cur} \nabla C} - \overline{k_{cur}}\ \overline{\nabla C})$. It is true that at this stage, the assumption of neglecting these terms are not physically justified but considered for the sake of simplification because the closure of these terms is still an open question. For instance, Vincent et al.[17] have investigated the modelling of LES for two-phase flow via the simulation of a phase inversion case. The convection, diffusion, surface tension and interface

advection subgrid terms are compared in magnitude and have shown a dependance on the type of the filter as well as the LES approach.

Figure 5.35 illustrates the temporal evolution of the gas core interface. The polygonal instability is slightly distinguished, it is not as sharp as it was with DNS case in Fig.5.33. Moreover, the interface diffusion which happens using DNS disappears when the LES in considered and the numerical results converges. The LES is then helping in stabilizing the calculation. The question now is how does the LES eliminates what looks like a small scale instability and to what extent it does.

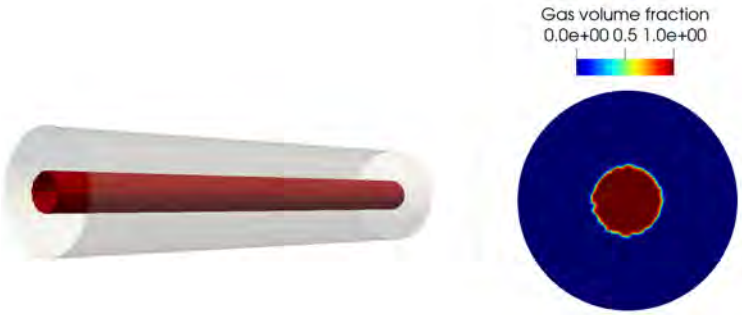

(a) $t^* = 0.001$

(b) $t^* = 0.01$

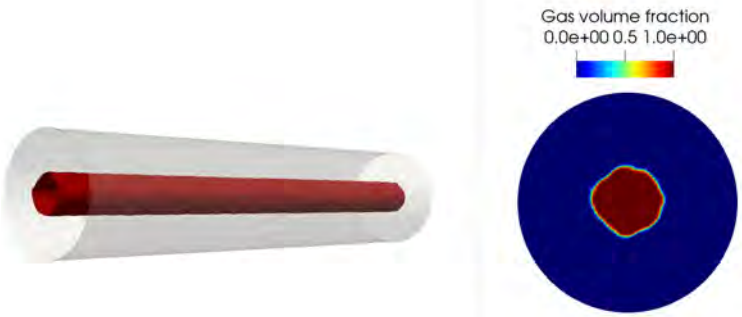

(c) $t^* = 0.05$

Figure 5.35: Simulation of gas core in a rotating flow: $Re_\omega = 1.06 \times 10^5$, $R_{core}/R = 0.315$ using the mixed dynamic Smagorinsky model.

In an attempt to explain the effect of LES on the core stability, and since the mixed dynamic Smagorinsky model acts in modelling sub-grid scale effect and in particular dissipation at small scales through the local turbulence viscosity, we show in Fig.5.36 the latter normalized by the kinematic viscosity of the gas in a cross-section. At initialisation $t^* = 0s$, the turbulent viscosity is zero, then at $t^* = 0.001$, the core is slightly deformed while rotating, the turbulent viscosity becomes

important and reaches $80\nu_g$ in region close to the interface where small scales are developed. This means that the turbulence is dissipated at the interface leading to a reduction of the intensity of the instability. This represents a transient regime because after that, the turbulent viscosity becomes more homogeneous even though the interface instability due to the swirling flow still exists.

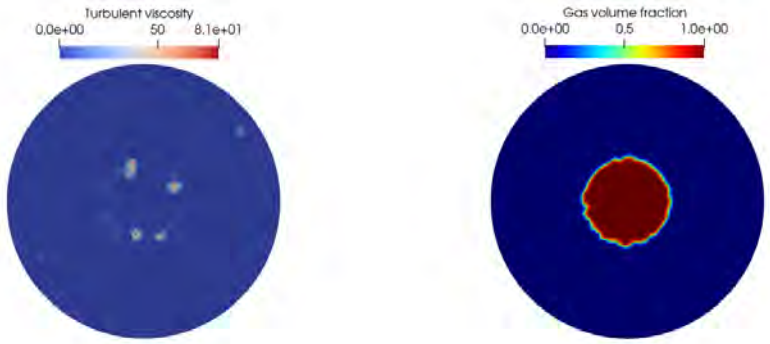

(a) $t^* = 0.001$

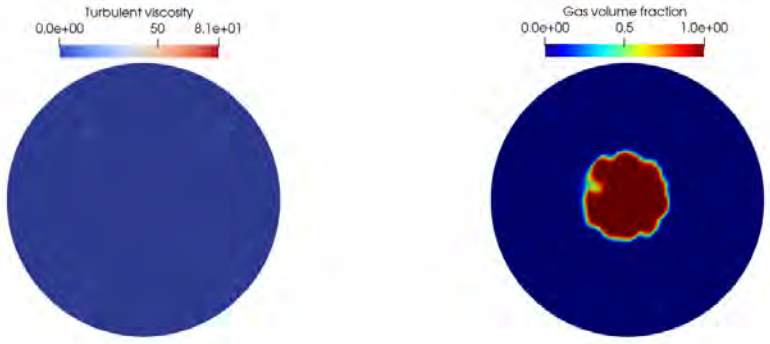

(b) $t^* = 0.03$

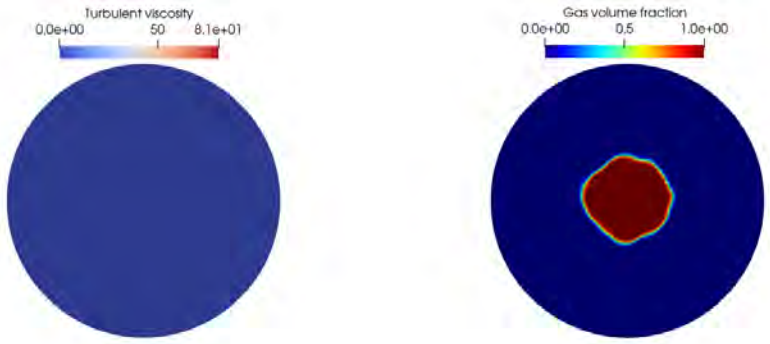

(c) $t^* = 0.05$

Figure 5.36: Turbulent viscosity (left) normalized by the kinematic viscosity over a cross section where the gas core is located (right) : $Re_\omega = 1.06\times10^5$, $R_{core}/R = 0.315$

Indeed the gas core of radius $R_{core} = 0.315R$ was found to be stable with LES, however, one can expect the behaviour to change if the core size increases since the interface will be subject to a higher centrifugal force similary to the case of a small radius in a high rotation velocity. Figure 5.37 represents the interface deformation over time for a core of radius $R_{core} = 0.547R$. At first, the polygonal instability is enhanced in comparison to a small radius. But after that, the interface is diffused and the core keeps rotating.

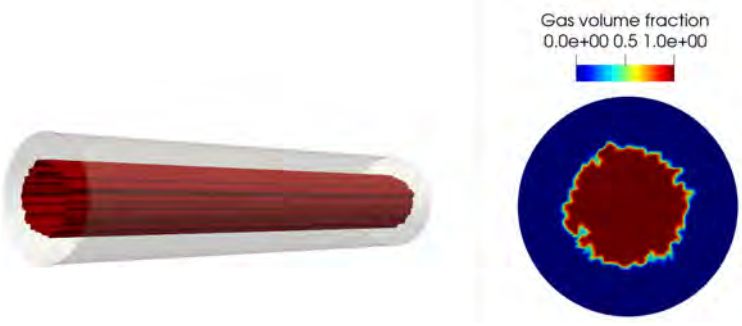

(a) $t^* = 0.001$

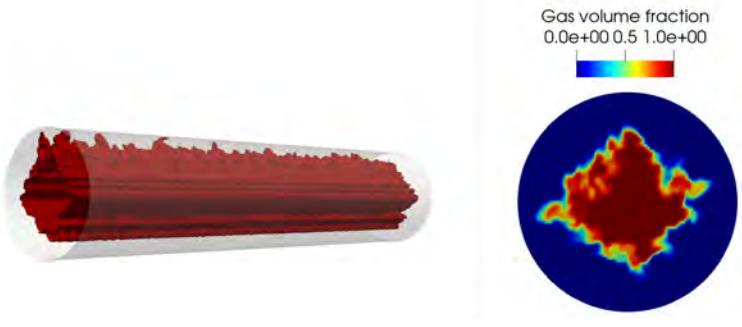

(b) $t^* = 0.003$

(c) $t^* = 0.007$

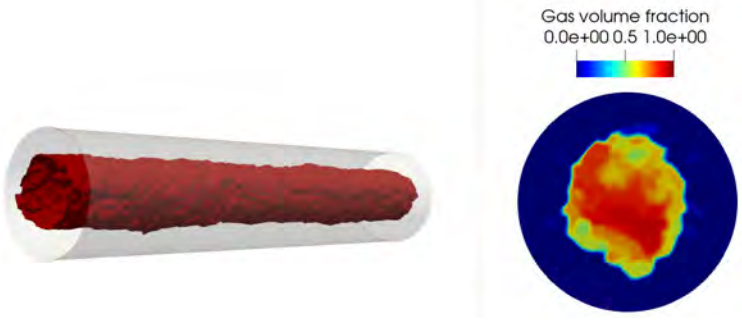

(d) $t^* = 0.1$

Figure 5.37: Simulation of gas core in a rotating flow: $Re_\omega = 1.06 \times 10^5$, $R_{core}/R = 0.547$ using the mixed dynamic Smagorinsky model.

In this section, we have tried to shed some lights on the instability of a gas core in a rotating flow in order to understand what occurs in the inline separator. There is no doubt that some numerical improvement are still to be introduced in the proposed numerical method coupling Lagrangian Tracking and VoF especially when coupled to LES.

5.5 Conclusion

Numerical simulations and results of two-phase flow inline separation are presented in this chapter. A simplified analysis of the migration of a bubble in swirling flow is first provided using the results of single-phase flow simulations from chapter 4. The comparison between the different forces applied on the bubble shows that the drag force can be neglected in front of the lift and added mass in the radial direction. An estimation of the migration time is also calculated. To take into account the effects of the flow unsteadiness and fluctuations, numerical simulations of a bubble in the separator using Lagrangian Tracking are performed. The results are discussed over various aspects: the bubble size, the flow Reynolds number and their influence on the migration time.

Once the migration and capture processes are described in details, the inline separation of gas/water flow is simulated first by considering only the Lagrangian Tracking solver and an evaluation of the separation efficiency is done proving the capacity of the inline separator. Then, the hybrid LT-VoF is activated. The formation of the gas core and its resolution using VoF from the accumulated Lagrangian bubbles enables to display the patterns on the core interface as the gas volume fraction increases and relates them to the experimental observations. Bursts are developed radially at the interface due to the centrifugal force and are characterized by high velocities. From a CFD point of view, these simulations reveal other open questions about the resolution of turbulent two-phase flow using LES and VoF. A simplified study of the instabilities of a gas core inside a rotating flow is conducted to make an openning statement on this topic for a future work.

Chapter 6

Conclusion and perspectives

6.1 Conclusions

This PhD work is about the development of a hybrid CFD approach based on four different CFD methods to wit: Immersed Boundary Method (IBM), Large Eddy Simulation (LES), Lagrangian Tracking (LT) and Volume of Fluid (VoF) to be able to simulate and understand a two-phase flow separation process investigated within the scope of the European project TOMOCON. The inline fluid separator makes use of a static swirl element which is fixed inside the pipeline and has blades on its surface to deflect part of the arriving axial flow into a swirling tangential flow generating then a centrifugal force. The latter pushes the heavy phase towards the wall, leaving the light phase in the centre to be recoverd afterward by a pick-up tube at the outlet of the separator. From a CFD standpoint, the simulation of such process represents many challenges taking into account the flow features present in the separator. In fact, the flow is highly turbulent, the geometry of the swirl element is complex and the interface length scales of the two-phase flow are varying from a millimeter (the size of the dispersed phase) to few meters (the size of the separator). Hence, a coupling between the different CFD methods is needed. In chapter 1, the inline fluid separation is detailed and the CFD approach proposed in this study is presented.

The rest of this thesis can be divided into two parts: chapters 2 and 3 which focuses on the CFD developements and chapters 4 and 5 which deals with the simulations and investigation of swirling single and two-phase flows in the separator.

As a matter of fact, in chapter 2, the CFD code JADIM used for the simulations is introduced and the independant LES [18], IBM [23], LT [24] and VoF [48] solvers as previously developed in JADIM and validated through many studies are described. New CFD developments are then proposed in the current work: first, the use of IBM for complex geometries (the swirl element in our case) constructed via a CAD solfware. Basilisk is used to generate the required solid fraction needed for the IBM solver [23]. This method is validated through the simulation of the separator. Then, IBM is coupled to LT by introducing a collision model to allow the dispersed phase to rebound on the IB solids (pipe, swirl element, pick-up tube) when a contact accurs according to the normal to the IB surface with a restitution coefficient set to 1 for full restitution of the kinetic energy. A 3D simulation of a set of bubbles injected at the fluid velocity upstream the swirl element in the separator is performed without the proposed collision model shows that the bubbles are trapped inside IB

cells and that by activating the hybrid IBM/LT model, they are able to rebound on the swirl element. Later, when the separation takes place and the dispersed phase accumulates in the centre to form the core, a switch from LT to VoF is done. The hybrid LT/VoF consists in moving any dispersed phase reaching the pipe centre or in contact with a VoF cell from the Lagrangian framework to the Eulerian one and update the phase indicator with the transformed dispersed phase fraction. This model is validated through the simulation of bubbles accumulation in a solid body rotating fluid. The core is formed and its interface is solved using VoF. For an air/water system, the problem of spurious currents in VoF is discussed and solved via a dimentionless study. Finally, an original stochastic wall model for hybrid LES/IBM is presented in chapter 3 with the objective to develop a wall model for the mixed dynamic Smagorinsky model coupled to IB solids in order to avoid the need of mesh refinment next to the wall to capture the viscous sub-layer. The development of the model has gone through three steps, Poiseuille flow is first simulated to check the ability of IBM to solve the flow since we already know the analytical solution, a model is therefore introduced in the IBM forcing. Then, turbulent pipe flow is simulated using just IBM/LES, an underestimation of the bulk velocity is found. Thus, a mean wall model based on the log law or the power law is implemented. With the adjustment of the model parameter, the wall model is able to recover the mean velocity but needs a source of fluctuations to act on the rms velocities. This is why, a stochastic wall model is finally proposed and is capable of correcting both the mean and velocity fluctuations.

Once the proposed hybrid CFD approach is presented and validated, numerical simulations of the inline fluid separation process are performed. Chapter 4 focuses on studying swirling single-phase flow in the separator using LES/IBM with the wall model. A general description of the swirling flow features in the separator is provided. The mesh sensitivity is done. Then, a single-phase flow in the separator for $Re = 50,000$ is investigated in terms of the axial and azimuthal velocities, the swirl element, the pressure and the centrifugal force. The effect of the Reynolds number on these quantities is also looked at. The normalized azimuthal velocity and the swirl element are found to be slightly dependent of the Reynolds number while the recirculation zone expansion is influenced by Re. Finally, to simulate the effect of the condition at the separator outlet, the pick up-tube and the flow straightner which eliminates the swirling flow between the separator and the pick-up tube are added using IBM. And to impose the condition of the flow split FS on the valve acting on the pick-up tube, an IBM forcing is introduced in the flow straightener. This allows to control directly the flow rate going through the LPO and eventually mimic a dynamic condition of the valve when it is the case. Similary, a comparison of the velocity profiles is done for different flow splits. The latter modifies the flow not only inside the pick-up tube but also upstream of it.

Chapter 5 represents the numerical results of the two-phase flow simulations in the separator. At the beginning, the dynamics of a bubble in the separator is described though its force balance. The objective is to understand the migration process and the forces which are behind it. A simplified trajectory equation is found based on the previous single-phase flow study. And characteristic times are introduced namely the relaxation time, the migration time and the capture time. Then, two-phase flow simulations of a set of bubbles using LT are carried out. This allows to take into account the flow fluctuations effect on the dispersed phase and

evaluate accurately the forces. The instantenuous and averaged forces are compared and the RMS are calculated. The migration process is found to be governed mainly by the radial virtual mass force and an eventual contribution of the lift force with either a centripetal or a centrifugal effect, the fluctuations of these forces have also a role in delaying the migration especially the lift force. Furthermore, an impact of the decrease of the bubble size is noticed on the increase of the migration time. A similar effect is observed when decreasing the Reynolds number. This detailed study of the forces on the bubbles and their sensitivity to the various parameters is important to estimate the migration time and therefore optimize the separator. The second part of the chapter deals with the bubbles accumulation and core formation. Using only the Lagrangian Tracking, the separator performance is evaluated. The inline separator proves to be an efficient technology to recover the gas. Finally, by activating the hybrid approach LT-VoF, the gas core is constructed and solved employing VoF. A rotation of the gas core following the continuous swirling phase as well as an axial motion towards the LPO are observed. At the interface, instabilities marked by high velocities occur in the form of bursts and relate qualitavely to experimental results from TU Delft. To further investigate the interface deformation, a study of gas core instabilities in a rotating flow is conducted and conclusions are drawn both from a physical and numerical views.

Figure 6.1 summarizes the numerical developments of this PhD work by presenting the complex flow features in the inline separator, the proposed hybrid CFD approach which consists of IBM/LES, IBM/LT and LT/VoF and illustrations of numerical simulations using this approach.

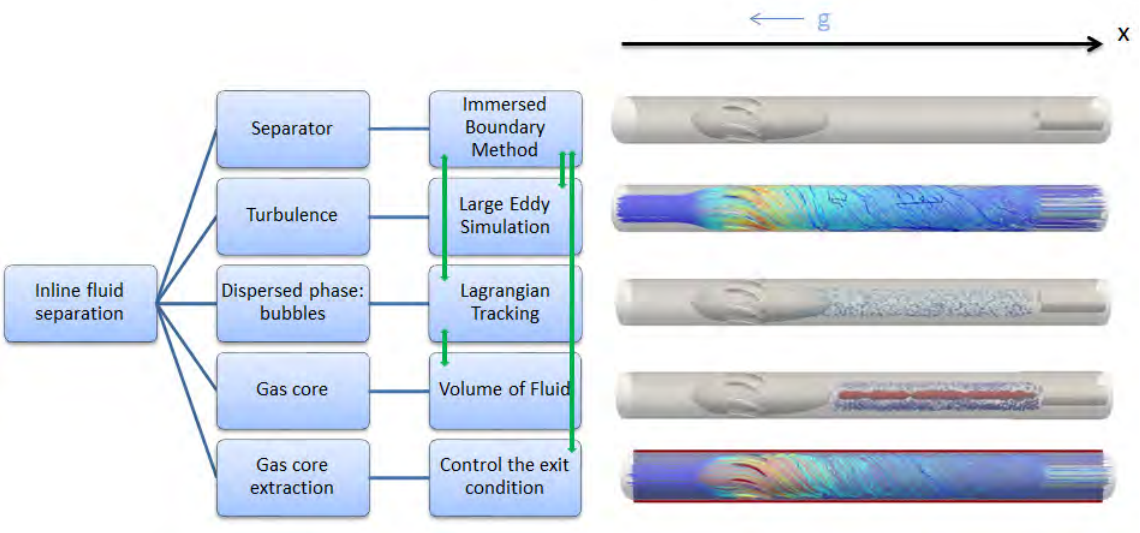

Figure 6.1: Illustration of the developed hybrid CFD approach for the simulation of inline fluid separation.

6.2 Perspectives

The short-term perspectives concern the ongoing work to extend the numerical domain to the same exact configuration used in the experimental study for a quantitative comparison this time. More scenarios of fixed and dynamic pick-up tube

conditions are to be simulated in a way to mimic the condition of the controller on the valve in experiments. In fact, by following the time evolution of the efficiency of separation, the condition on the flow rate at the HPO can be adapted depending on the coming gas fraction at the LPO to ensure a good efficiency. This is implemented in the CFD code by imposing the adequat IBM force defined in the flow straightener and the response time of the flow to the new condition can also be controlled. Moreover, the simplified model of the bubble migration can be upgraded by including the contribution of the fluctuations of the forces deduced from this PhD work to help predict the migration and capture time accurately. This can eventually contribute in adding some physics in the transfer function of the controller (see Fig. 6.2). The results are expected to be presented in future publications.

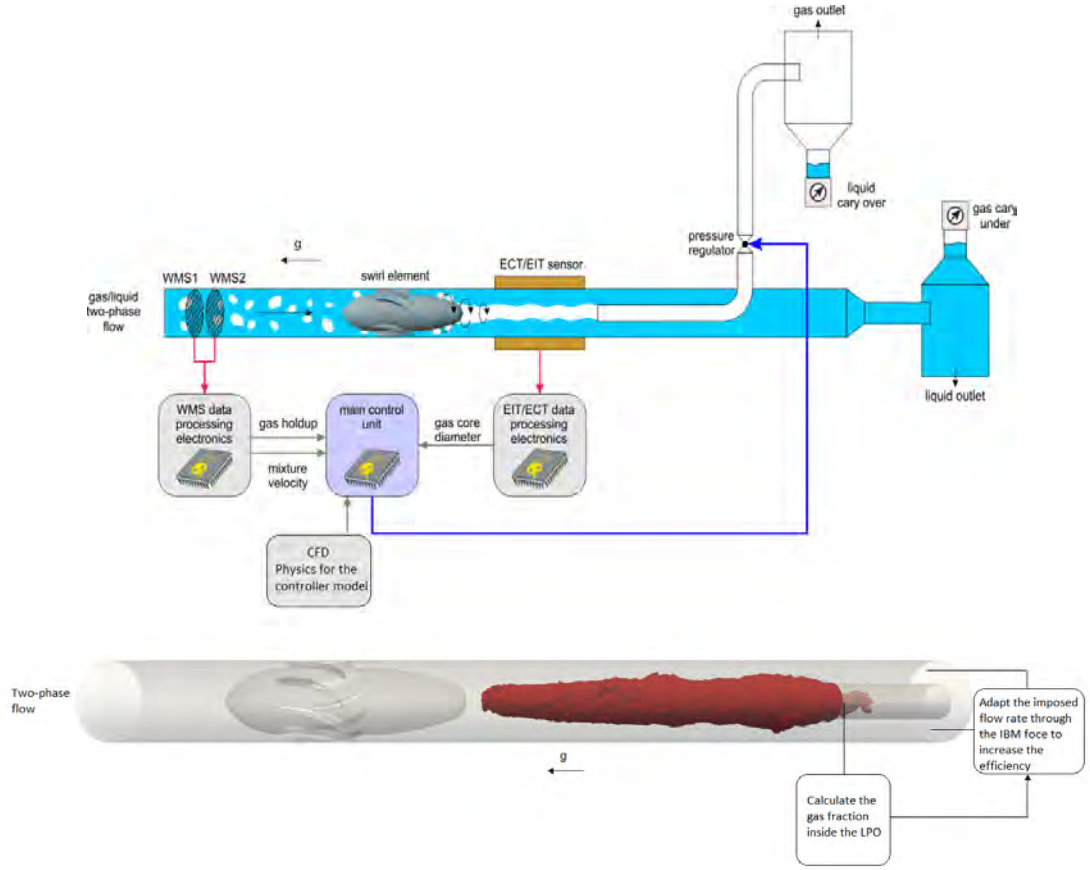

Figure 6.2: Sketch of the control of the inline fluid separation process with the contribution of tomography sensors as well as CFD (top) and how the control condition is implemented in the CFD simulations (bottom).

The same device of separation including a controller can also be tested on liquid liquid two-phase flow. This can represent an extension of the previous work [1, 5]. Numerically, the VoF solver will be more stable since the viscosity ratio of oil water two phase-flow is lower, the instabilities at the interface are then reduced. However, the drag coefficient should be adapted to droplets following the recent work of Rachih et al. [25] while the lift coefficient for droplets is less known and a correlation for solid particles could be used as a first approximation. The same study can be done on different swirl element geometries to determine the effect of its shape on

the separation.

Indeed the developed hybrid CFD approach has given a relevant proof of concept of its capacities in simulating inline fluid separation and which can also be used for other complex flows. But, it still has some aspects which can be done or improved in the long term. For instance, one can still ameliorate the collision model of hybrid IBM/LT to evaluate the restitution coefficient for different types of dispersed phase (bubble, droplet, solid particle). This may need information about the microscopic physics which we cannot be solved using LT but can eventually be deduced from existing experiments and included in the CFD model. Furthermore, as we are dealing with highly turbulent bubbly flow, it is also possible to investigate the variation of the force balance coefficients for drag, lift and virtual mass so to consider the deformation of the bubbles which might influence the separation process in our study.
Concerning the proposed wall model for IBM/LES. It has been observed that the stochastic model which is able to reproduce the mean and fluctuations velocities gives strong pressure fluctuations since the velocity imposed in the IBM forcing is not divergence free and this represents an interesting persective to bring more improvment to the model.
Finally, one of the outlooks of this thesis is the modelling of turbulence for VoF since a limited number of publications are present in litterature [17, 54] and the subject remains an open question in the domain of CFD modelling. A hybrid LES/VoF should discuss many aspects such as the effect of the LES approach, the formulation of the two-phase LES sub-grid terms and the robustness of the method to simulate different flow configurations. This is why, this represent an immense work in itself allowing to explain what happens to the interface in turbulent flows like what we observe in the inline fluid separation.

Bibliography

[1] Slot JJ. *Development of a centrifugal inline separator for oil/water flows.* PhD thesis, University of Twente, 2013.

[2] Yu H., Goldsworthy L., Ghiji M., Brandner P.A., and Garaniya V. A parallel volume of fluid-lagrangian parcel tracking coupling procedure for diesel spray modelling. *Computers and Fluids*, 2017.

[3] Peters A. and Ould el Moctar B. Numerical assessment of cavitation-induced erosion using a multi-scale euler-lagrange method. *J. Fluid Mech.*, 2020.

[4] Steebergen W. *Turbulent pipe flow with swirl.* PhD thesis, TU Eindhoven, 1995.

[5] Van Campen L. *Bulk Dynamics of Droplets in Liquid-Liquid Axial Cyclones.* PhD thesis, TU Delft, 2014.

[6] Ammerlaan D. Swirl effects on vertical gas-liquid flow regimes: Experiments and modelling. Master's thesis, TU Delft, 2020.

[7] Taitel Y., Bornea D., and Dukler AE. Modelling flow pattern transitions for steady upward gasliquid flow in vertical tubes. *AIChE Journal*, 1980.

[8] Sahovic B., Atmani H., Wiedemann P., Schleicher E., Legendre D., Climent E., Zamansky R., Pedrono A., and Hampel U. A study on the relationship between upstream and downstream conditions in swirling two-phase flow. *Flow Measurement and Instrumentation*, pages 74, 101767, 2020.

[9] Cullivan J.C, R.A. Williams R.A, and Cross C.R. Understanding the hydrocyclone separator through computational fuid dynamics. *Chemical Engineering Research and Design*, pages 455–466, 2003.

[10] Colman D.A. *The Hydrocyclone for Separating Light Dispersions.* PhD thesis, University of Southampton, 1981.

[11] Gomez L. and Molina R. Wet gas separation in gas-liquid cylindrical cyclone separator. *J. Energy Resour. Technol*, 2008.

[12] Dirkzwager M. *A new axial cyclone design for fluid fluid separation.* PhD thesis, TU Delft, 1996.

[13] Delfos R., Murphy S., Stanbridge D., Olujic Z, and Jansens P.J. A design tool for optimising axial liquid-liquid hydrocyclones. *Minerals Engineering*, 2004.

[14] Sahovic B., Atmani H., Sattar M. A., Martinez Garcia M., Schleicher E., Legendre D., Climent E., Zamansky R., Pedrono A., Babout B., Banasiak R., Portela L.M., and Hampel U. Controlled inline fluid separation based on smart process tomography sensors. *Chemie Ingenieur Technik*, pages 92/5, 1–11, 2020.

[15] Garcia M.M., Sahovic B., Sattar M.A., Atmani H., Schleicher E., Hampel U., Babout L., Legendre D., and Portela L.M. Control of a gas-liquid inline swirl separator based on tomographic measurements. *IFAC-PapersOnLine*, pages 53/2, 11483–11490, 2020.

[16] Atmani H., Zamansky R., Climent E., and Legendre D. Cfd approach to simulate two phase flow inline-separator coupling ibm, les, lagrangian tracking and vof methods. In *SINTEF Proceedings 6*, 2020.

[17] Vincent S., Tavares M., Fleau S., Mimouni S., Ould-Rouiss M., and Estivalezes J.L. A priori filtering and les modeling of turbulent two-phase flows application to phase separation. *Computers and Fluids*, pages 245–259, 2018.

[18] Calmet I. and Magnaudet J. Large eddy simulation of high schmidt number mass transfer in a turbulent channel flow. *Physics of Fluids*, 1997.

[19] Legendre D. and Magnaudet J. The lift force on a spherical body in a viscous linear shear flow. *J. Fluid Mech.*, 1998.

[20] Benkineda A. *Developpement and validation of a numerical method for two phase flow without the interface reconstruction : application to the dynamics of the Taylor bubbles.* PhD thesis, INPT, 1999.

[21] Bonometti T. *Development of a numerical method for the computation of incompressible two-phase flows with bubbles or drops.* PhD thesis, INPT, 2007.

[22] Merle A., Legendre D., and Magnaudet J. Forces on a high reynolds number spherical bubble in a turbulent flow. *J. Fluid Mech*, 2005.

[23] Bigot B., Bonometti T., Thual O., and Lacaze L. A simple immersed boundary method for solid fluid interaction in constant and stratified density flows. *Computers and Fluids*, 2014.

[24] Chouippe A., Climent E., Legendre D., and Gabillet C. Numerical simulations of bubble dispersion in turbulent taylor couette flow. *Physics of Fluids*, 2014.

[25] Rachih A., Legendre D., Climent E., and Charton S. Numerical study of conjugate mass transfer from a spherical droplet at moderate reynolds number. *Journal of heat and mass transfer*, 2020.

[26] Chorin A.J. The numerical solution of the navier-stokes equations for an incompressible fluid. *Bull. Am. Math. Soc.*, 73:928–931, 1967.

[27] Peyret R. and Taylor T. Computational methods for fluid flow. *Springer-Verlag*, 1983.

[28] Pope S. B. *Turbulent flows.* Cambridge University Press, 2000.

[29] Sagaut P. *Large eddy simulation for incompressible flows: an introduction.* Springer Verlag, 2nd edition, 2002.

[30] Germano M., Piomelli U., Moin P., and Cabot W. A dynamic subgridscale eddy viscosity model. *Phys. Fluids A*, 1991.

[31] Glowinski R., Pan T., Hesla T., and Joseph D.D. A distributed lagrange multiplier/ fictitious domain method for particulate flows. *International Journal of Multiphase Flow*, 1999.

[32] Singh P., Hesla T.I, and Joseph D.D. Distributed lagrange multiplier method for particulate flows with collisions. *International Journal of Multiphase Flow*, 2003.

[33] Sarthou A. and Vincent S. Eulerian lagrangian grid coupling and penalty methods for the simulation of multiphase flows interacting with complex objects. *Int. J. Numer.Meth. Fluids*, 2008.

[34] Wang M., Y.T. Feng Y.T, and Wang C.Y. Coupled bonded particle and lattice boltzmann method for modelling fluid solid interaction.int. *J. Numer. Anal. Meth. Geomech*, 2016.

[35] Fedkiw R.P. Coupling an eulerian fluid calculation to a lagrangian solid calculation with the ghost fluid method. *Journal of Computational Physics*, 2002.

[36] Peskin C.S. Numerical analysis of blood flow in the heart. *J. Comput. Phys*, 1977.

[37] Peskin C.S. The immersed boundary method. *Acta Numerica*, 2002.

[38] Yuki Y., Takeuchi S., and Kajishima T. Efficient immersed boundary method for strong interaction problem of arbitrary shape object with the self-induced flow. *Journal of Fluid Science and Technology*, 2007.

[39] Mei R., Klausner J., and Lawrence C. A note on the history force on a spherical bubble at finite reynolds number. *Phys. Fluids*, 1994.

[40] Schiller L. and Naumann A. A drag coefficient correlation. *Ver. Deut. Ing. Z*, 1933.

[41] Auton TR., Hunt JCR., and Prud'Homme M. The force exerted on a body in inviscid unsteady non-uniform rotational flow. *Journal of Fluid Mechanics*, 197:241–257, 1988.

[42] Magnaudet J., Rivero M., and Fabre J. Accelerated flows past a rigid sphere or a spherical bubble. *J. Fluid Mech.*, 1995.

[43] Zhang Z., Legendre D., and Zamansky R. Model for the dynamics of microbubbles in high reynolds number flows. *Journal of Fluid Mechanics*, 879:554–578, 2019.

[44] Nierop E., Luther S., Bluemink J., Magnaudet J., Prosperetti A., and Lohse D. Drag and lift forces on bubbles in a rotating flow. *J. Fluid Mech*, 2007.

[45] Unverdi S.O and Tryggvason G. A front-tracking method for viscous, incompressible, multi-fluid flows. *Journal of Computational Physics*, 1992.

[46] Weymouth G.D. and Yue P. Conservative volume-of-fluid method for free-surface simulations on cartesian-grids. *Journal of Computational Physics*, 2010.

[47] Hirt C.W and Nichols B.D. Volume of fluid (vof) method for the dynamics of free boundaries. *Journal of computational physics*, 1981.

[48] Bonometti T. and Magnaudet J. An interface capturing method for incompressible two-phase flows: Validation and application to bubble dynamics. *International Journal of Multiphase Flow*, 2007.

[49] Brackbill J., Kothe DB., and Zemach C. A continuum method for modeling surface tension. *J Comput Phys*, 1992.

[50] Dupont J.B. and Legendre D. Numerical simulation of static and sliding drop with contact angle hysteresis. *J. Comput. Phys.*, 2010.

[51] Francois MM., Cummins S.J, Dendy E.D, Kothe D.B, Sicilian J.M, and Willians M.W. A balanced-force algorithm for continuous and sharp interfacial surface tension models within a volume tracking framework. *J. Comput. Phys.*, 2006.

[52] Renardy Y and Renardy M. Prost: a parabolic reconstruction of surface tension for the volume-of-fluid method. *J. Comput. Phys.*, 2002.

[53] Abadie T., Aubin J., Legendre D, and Xuereb C. Hydrodynamics of gas-liquid taylor flow in rectangular microchannels. *Microfluid. Nanofluid.*, 2012.

[54] Anez J, Ahmed A, Hecht N, Duret B, Reveillon J, and F.X. Demoulin. Eulerian–lagrangian spray atomization model coupled with interface capturing method for diesel injectors. *International Journal of Multiphase Flow*, pages 325–342, 2019.

[55] Pierson J.L. *Settling of a sphere through a horizontal fluid-fluid interface*. PhD thesis, INPT, 2015.

[56] Atmani H., Zamansky R., Climent E., and Legendre D. Stochastic wall model for turbulent pipe flow using immersed boundary method and large eddy simulation. *Computers and Fluids*, pages 239,105419, 2022.

[57] Tessicini F., Iaccarino G., Fatica M., Wang M., and Verzicco R. Wall modeling for large-eddy simulation using an immersed boundary method. *Standford University. Annual Research Briefs*, 2002.

[58] Cristallo A. and Verzicco R. Combined immersed boundary/large-eddy-simulations of incompressible three dimensional complex flows. *Flow Turbulence Combust*, 2006.

[59] Roman F., Armenio V., and Frohlich J. A simple wall-layer model for large eddy simulation with immersed boundary method. *Physics of Fluids*, 2009.

[60] Ma M., Huang W., and Xu C. A dynamic wall model for large eddy simulation of turbulent flow over complex/ moving boundaries based on the immersed boundary method. *Physics of Fluids*, 2019.

[61] Vijiapurapu S. and Cui J. Performance of turbulence models for flows through rough pipes. *Applied Mathematical Modelling*, 2010.

[62] Zagarola M.V. and Smits A.J. Mean-flow scaling of turbulent pipe flow. *J. Fluid Mech*, 1998.

[63] Chin C., Monty J.P., and Ooi A. Reynolds number effects in dns of pipe flow and comparison with channels and boundary layers. *International Journal of Heat and Fluid Flow*, 2014.

[64] Hultmark M., Vallikivi M., Bailey S.C.C., and Smits S. Logarithmic scaling of turbulence in smoothand rough-wall pipe flow. *J. Fluid Mech*, 2013.

[65] Cheng W. and Samtaney R. Power law versus log law in wall bounded turbulence: A large eddy simulation perspective. *Physics of Fluids*, 2014.

[66] Karman Th. V. Mechanical similitude and turbulence. *Tech. Mem. NACA*, 1931.

[67] Werner H. and H. Wengle. *Large-eddy simulation of turbulent flow over and around a cube in a plate channel.* Turbulent Shear Flows, Springer-Verlag, editor, Munich, Germany, 1993.

[68] Jiménez J. and Pinelli A. The autonomous cycle of near-wall turbulence. *Journal of Fluid Mechanics*, 389:335–359, 1999.

[69] Smits A.J., B. J. McKeo, and Marusic I. High-Reynolds Number Wall Turbulence. *Annual Review of Fluid Mechanics*, 43:353–375, 2011.

[70] Pan C. and Kwon Y. Extremely high wall-shear stress events in a turbulent boundary layer. *J. Phys.: Conf. Ser.*, 1001:012004, 2018.

[71] Hutchin N., Monty J. P., Ganapathisubramani B., H. C. H. Ng, and Marusic I. Three-dimensional conditional structure of a high-reynolds-number turbulent boundary layer. *Journal of Fluid Mechanics*, 673:255–285, 2011.

[72] Gomit G., de Kat R., and Ganapathisubramani B. Structure of high and low shear-stress events in a turbulent boundary layer. *Physical Review Fluids*, 3(1), jan 2018.

[73] Townsend A. A. Equilibrium layers and wall-turbulence. *Journal of Fluid Mechanics*, 11:97–120, 1961.

[74] Perry A. E., S. Henbes, and Chong M. S. A theoretical and experimental study of wall turbulence. *Journal of Fluid Mechanics*, 165:163–199, 1986.

[75] Maniero R., Climent E., and Bacchin P. Adhesion and detachment fluxes of micro-particles from a permeable wall under turbulent flow conditions. *Chem. Eng. Sciences*, 2012.

[76] Sheng J., Malkiel E., and Katz J. Buffer layer structures associated with extreme wall stress events in a smooth wall turbulent boundary layer. *J. Fluid Mech.*, 2009.

[77] Alfredsson P. H., Johansson A. V., Haritonidis J. H., and Eckelmann H. The fluctuating wall-shear stress and the velocity field in the viscous sublayer. *Physics of Fluids*, 31(5):1026, 1988.

[78] Smith C.R and Metsler S.P. The characteristics of low speed streaks in the near wall region of turbulent boundary layer. *J. Fluid Mech*, 1983.

[79] Chernyshenko S.I. and Baig M.F. The mechanism of streak formation in near wall turbulence. *J. Fluid Mech*, 2005.

[80] Wallace J.M. Space-time correlations in turbulent flow: review. *Theoretical and applied mechanics letters*, 2014.

[81] He G., Jin G., and Yang Y. Space-time correlations and dynamic coupling in turbulent flows. *Annu. Rev. Fluid Mech*, 2017.

[82] Monty J. P. and Chong M. S. Turbulent channel flow: comparison of streamwise velocity data from experiments and direct numerical simulation. *Journal of Fluid Mechanics*, 633(-1):461–474, 2009.

[83] Del Álamo J. and Jiménez J. Estimation of turbulent convection velocities and corrections to taylor's approximation. *Journal of Fluid Mechanics*, 640:5–26, 2009.

[84] Kreplin H and Eckelmann H. Propagation of perturbations in the viscous sublayer and adjacent wall region. *Journal of Fluid Mechanics*, 95(2):305–322, 1979.

[85] El Khoury G., Schatther P., Noorani A., Fischer P., Geert Brethouwer G., and Johansson A. Direct numerical simulation of turbulent pipe flow at moderately high reynolds numbers. *Flow Turbulence Combust*, 2013.

[86] Garcia M.M. *Optimized controlled inline fluid separation.* PhD thesis, In progress,TU Delft, 2022.

[87] Tophoj L., Mougel J., Bohr T., and Fabre D. Rotating polygon instability of a swirling free surface flow. *Physical Review Letters*, pages 1–5, 2013.